FINE PARTICULATE FILLED POLYMERIC MATERIAL AND THE INVESTIGATION OF ITS FRICTION AND WEAR PROPERTIES

by

Kwai-Yung Benjamin Su

B.S., National Taiwan University
(1971)

S.M., Massachusetts Institute of Technology
(1976)

MechE, Massachusetts Institute of Technology
(1976)

SUBMITTED IN PARTIAL FULFILLMENT
OF THE REQUIREMENTS FOR THE
DEGREE OF

DOCTOR OF SCIENCE

at the

MASSACHUSETTS INSTITUTE OF TECHNOLOGY

May 1980

Signature of Author _____
Department of Mechanical Engineering, March 1980

Certified by _____
Thesis Supervisor

Acceted by _____
Chairman, Department Committee on Graduate Students

FINE PARTICULATE FILLED POLYMERIC MATERIAL AND THE INVESTIGATION OF ITS FRICTION AND WEAR PROPERTIES

by

Kwai-Yung Benjamin Su

Submitted to the Department of Mechanical Engineering
on March 21, 1980 in partial fulfillment of the
requirements for the degree of Doctor of Science

ABSTRACT

The effects of filler particle size on void nucleation in a particulate filled polymeric material is investigated. An analysis for determining criteria for void nucleation around filler particles shows that the energy criterion is dependent on the size of the filler particles. A critical particle size is defined as the particle size below which the amount of strain required to satisfy the energy criterion is greater than that to satisfy the strength criterion. This critical particle size is found to be about 3000 Å for a typical polymer matrix and inorganic filler system. If filler particles smaller than the critical particle size are used in a particulate filled polymeric material, the chance of failure caused by void nucleation can be reduced. Experiments were conducted to verify the particle size dependency of the energy criterion. Methods of dispersing fine particulate fillers in polymer resins were investigated. Dispersions with particle aggregates in the size range 500-1000 Å were successfully prepared with fumed silica dispersed in PMMA and epoxy. Wear studies were conducted to investigate the effects of filler particle size on sliding wear. The results are in agreement with the void nucleation arguments suggested in the delamination wear theory.

Thesis Supervisor: Nam P. Suh
Title: Professor of Mechanical Engineering

ACKNOWLEDGEMENTS

First, I wish to express my gratitude to Professor Nam P. Suh, my thesis supervisor, who has, as always, delivered inspiration, challenge, as well as criticism. But at critical moments, there is always a word of encouragement. To him, I give my highest appreciation for guiding me through my intellectual and professional development. I am also indebted to other members of my thesis committee: Professor Ali S. Argon and Professor Ernest Rabinowicz. Their efforts and criticisms have been of great benefit to me. I also wish to thank Professor Nathan H. Cook and Professor Bruce M. Kramer. With them, I begin my association with the Materials Processing Laboratory.

This research was sponsored by the M.I.T.-Industry Polymer Processing Program. The sponsors of the program include AMP Inc., Eastman Kodak Co., General Motors Corp., Goodyear Tire and Rubber Co., Instrumentation Laboratories, Inc., ITT Corp., Lord Corp., Rogers Corp. and Xerox Corp. I am grateful for the assistance received in my research from many individuals in these companies. Dr. Richard Traskos of Rogers Corp. and Messrs. David Raia and Joseph Steglemann of Xerox Corp. deserve special thanks for their efforts. I am also grateful to Professor Nak-Ho Sung and Mr. Ernest Crowell, who associated in the past with the Polymer Processing Program, for imparting me their knowledge on polymer and surface chemistry.

The staff of the Materials Processing Laboratory, Fred Anderson, Ralph Whittemore, Bob Kane, John Ford and Fred Cote have provided assistance in various stages of this research. They deserve my utmost appreciation for

their efforts. My fellow students in Building 35 must also receive their deserved credit. Ken Smith, Jim Rinderle and Kim Stelson are credited for preventing the multilation of the English language in this thesis. My officemates, Jim (again), Blair Allison, John Border and Sharon Shepard, with their good sense of humor have helped to preserve some sanity in our daily research pursuit. I also wish to thank our data processing crew, Raj Melville and Ted Ruegsegger for their kind assistance. It will be grossly unfair not to mention everyone associated with the Materials Processing Laboratory. If their names do not appear between the lines, it is not because they are forgotten in my mind.

My friends in other non-Mechanical Engineering departments have also provided me with help in my research. I especially want to thank Bor Jang and Sui-Ching Lui, who taught me the ABC's of microtoming and transmission electron microscopy. I am also very grateful to Rosalie Allen for the excellent job she did in typing this thesis.

Finally, I wish to express my most sincere gratitude to my parents and my financee, Li-fen Chen, their love and encouragement have always provided me with moral support.

To Li-fen, this thesis is dedicated.

TABLE OF CONTENTS

LIST OF TABLES

LIST OF FIGURES

I. INTRODUCTION

The rapid development of polymeric materials and polymer composites has resulted in a much greater utilization of these materials in engineering applications. In applications where friction and wear properties are important, the polymers possess some highly desirable and unique properties. Some of these properties are, oxidation and corrosion resistance, tolerance to wear debris, light weight, and in some cases, self lubrication. The improvements in mechanical strength and thermal properties further enhance the competitive position of polymers and composites in bearing applications. Many polymer based materials have replaced metals in bearing parts for light load services. There is little doubt that future developments will make polymer based materials competitive with metals in more critical service conditions. The future trend is toward greater use of polymer based composite materials. However, the science of understanding the tribological behavior of polymer composites lags far behind their acceptance in practical applications. There exists an urgent need for better understanding of the wear mechanism of composite materials and the development of some basic guidelines that designers can follow in materials selection, design, and problem solving.

In many cases, the adhesive wear model developed in the middle of this century for metallic materials can be successfully applied to unfilled polymeric materials. But the model is not satisfactory when applied to the more complex composite materials, where the principle wear mode is usually due to some kind of mechanical failure. The recently developed delamination theory of wear provides a new perspective for investigating

wear problems. Although the delamination wear theory was initially developed from studies on metallic materials, the analysis itself can be applied to any materials. The description of the delamination wear process in terms of subsurface crack nucleation and propagation resembles the wear observed in composite materials. Therefore, the delamination wear theory provides some insight to direct the investigation of the friction and wear behavior of composite materials.

Particulate fillers are commonly used in polymeric materials, with or without fiber reinforcement. It is pointed out in the delamination wear theory, that inclusions in the material have an important influence on the microvoid and microcrack nucleation process. The nucleated microvoids and microcracks are precursors for the formation of delaminated wear sheets through crack propagation and void growth. The simplest model of a composite system is that of a matrix phase filled with spherical inclusions. Therefore, the logical step to conduct investigations on the wear behavior of composites is to begin with the simple matrix and spherical inclusion model. The study of this simple model nevertheless encompasses one of the most important topics in connection with the delamination wear theory, microvoid nucleation.

In Chapter II, a brief review is conducted on the established theories of friction and wear, which include the classical adhesive wear model and the recently developed delamination wear model. One section is devoted to the discussion of polymeric materials and composites. It is interesting to notice how some unique phenomenon observed on some polymers intrigues the interest of researchers and occupies a large part of the research efforts in the study of the friction and wear of polymers.

One typical example is the transferred film found in the sliding of some polymers. The transferred film gives a successful explanation to the friction behavior of polytetrafluorethylene (PTFE) and high density polyethylene (HDPE). But the discussion on the transferred film phenomenon has extended to recognize it as an important form of polymer wear, and are subjected to extensive investigation. On the other hand, relatively little effort has been spent studying the lumpy fragmented type of wear observed on a larger class of polymers, which contributes to the massive wear loss of the material. A practical engineer would certainly consider the latter a more important problem to address, and would also exploit the transferred film phenomenon to reduce wear, instead of treating it as an undesirable form of wear. The historic survey on the subject of friction and wear highlights these ideas.

Chapter III discusses the failure mechanisms of materials, particularly materials that contain second phase inclusions. The discussion emphasizes the role of the nucleation of microvoids and microcracks in the material. Most of the theories were developed from studies of metallic materials, therefore, one section is devoted to the discussion of how and when these theories or models can be appropriately applied to polymeric materials. The last two sections discuss the mechanics of a matrix-inclusion system. Eshelby's method was used to analyze the problem. A simple transformation process is invented to solve for the elastic state after void formation at stress concentrated sites at the matrix inclusion interface. The criteria for void nucleation are also discussed. The analysis shows that the energy criterion for void nucleation is dependent on the size of the inclusion. Void nucleation is

favored when large inclusions are present in the material. The critical particle size is about 3000 Å for a typical polymer matrix and inorganic filler system. This finding promotes the interest in dispersing fine particulate fillers that are smaller than this critical particle size in a polymeric material, and investigate the validity of the analysis. Experiments of dispersing fumed silica in PMMA and epoxy are reported in Appendix D. The experiments resulted in a silica particle dispersion with particle aggregate size in the range of 500 to 1000 Å.

Chapter IV describes the uniaxial tensile test performed to verify the validity of the inclusion size dependent energy criterion for void nucleation derived in Chapter III. A method is invented that enables direct observation of the nucleated voids, using a large scale model. The method involves the increase of the critical particle size to above micron range by testing at elevated temperatures to reduce the matrix stiffness. Dispersions of three different sizes of spherical glass beads in epoxy were used in this large scale model investigation. The results show that void nucleation is dependent on the size of the inclusion.

Chapter V reports the wear test results of the fine particulate fumed silica filled epoxy material. An unfilled epoxy and a crushed silica gel filled epoxy, which has a large silica particle size, are also investigated. Using the same principle as in the large scale modeling study, wear tests were conducted at different temperatures. These results also show that the wear rate depends on inclusion size. The sliding conditions under which void nucleation is an important wear mechanism are also

discussed.

The results of the investigations are summarized and discussed in the final chapter. Suggestions are also made concerning implementation of the research findings in practical applications.

II. FRICTION AND WEAR OF MATERIALS

Wear may be defined as the removal of material from a pair of contacting bodies in relative motion with each other. The wear process is generally thought of as a harmful one. However, there are some important applications that make use of the wear phenomenon, such as (1) writing with a pencil or a piece of chalk, (2) abrading and polishing to produce a desired surface finish, and (3) breaking in a new automobile or a piece of new machinery. But in the majority of cases, wear is desired to be minimized and controlled.

Most of the literature on the subject of wear is either in reporting a specific observation, or in the investigation of a specific wear model or theory. There are very few articles that attempt to provide a unified perspective to the wear problem, or to establish relationships among different theories. As a matter of fact, this may be a very difficult if not impossible task. There are very few statements that can be made on the subject of wear without confronting oppositions, and hardly any wear model or theory is established without making some highly idealized assumptions. A historical account on the subject of friction and wear as well as systematic and scientific treatment on wear related topics can be found in the works of Bowden and Tabor [1] and Rabinowicz [2].

No matter how imperfect the presently available wear models and theories are, the extensive effort in the development of these theories has nevertheless made important contributions in practical applications. No longer is experience the only reliable tool a designer can rely on in attacking wear problems. Many problems were solved, or more importantly,

circumvented before designs were made, with the understanding of the basic mechanisms of wear and the application of the appropriate wear theory.

In the classical literature, wear is usually categorized in four major categories [2]:

(1) Adhesive Wear. This is the form of wear that occurs when two smooth bodies are sliding against each other. Fragments are pulled out from one surface and adhere to the other. Later, these fragments either transfer back to the original surface or come off as loose wear particles.

(2) Abrasive Wear. This form of wear occurs when a rough hard surface slides on a soft surface, or when hard particles are present at the sliding interface. The result is the ploughing of a series of grooves on the surface of the soft material. Wear particles are formed from material displaced from the grooves.

(3) Corrosive Wear. This is the form of wear that takes place in a corrosive environment. The corroded film on the surface is worn away by the sliding action, and fresh material is exposed to the environment, so that the corrosive attack can continue into the material.

(4) Surface Fatigue Wear. This type of wear occurs in systems where the same volume of material at the surface is stressed and unstressed a large number of times, and results in wear particles produced by fatigue cracking.

Ideally, the latter three types of wear can be prevented by thoughtful design and careful maintenance. Adhesive wear remains the one form of

wear that is most common and least preventable. Therefore, over the years, it was considered as the basic mechanism of wear and was subjected to extensive investigation.

A. ADHESIVE WEAR THEORY

When two surfaces are brought in contact with each other, the tendency for them to adhere arises from the attractive forces exist between the surface atoms of the two materials. As illustrated in figure II-1, when the adhesive junctions are separated normally or tangentially, the adhesive forces at the junctions attempt to pull material from one surface onto the other, which results in an adhesive wear fragment. The separation usually takes place in the weaker soft material. However, weak spots or defects in the hard material may also cause wear fragments to form from the hard sliding surface.

Quantitative laws of adhesive wear were developed based on the model presented by Archard [3]. The volume of transferred wear fragments formed in sliding through a distance of x is,

$$V = \frac{kLx}{3p} \qquad \text{(II-1)}$$

Where:

k = wear coefficient

L = normal load

x = sliding distance

p = hardness of the soft material

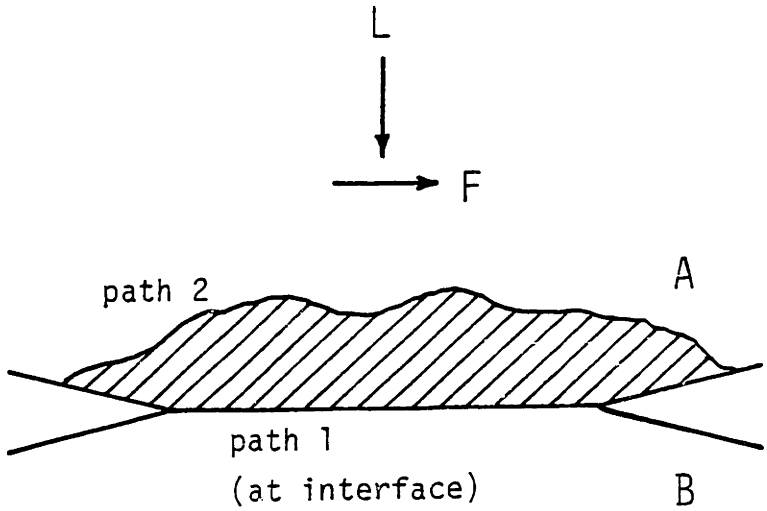

Figure II-1 Adhesive wear model. If the shear strength of the junction is higher than the bulk strength of the weaker material A, shear will take place in material A (path 2) instead of at the interface (path 1). (reference 2)

The wear coefficient, k, can be considered as a probability factor for establishing adhesive junctions. Other parameters not included in the above equation, such as friction coefficient, mechanical and metallurgical factors, can be considered as implicitly implied in the wear coefficient. The wear coefficient is used extensively to comparing the wear rates of different materials.

The development of the adhesive wear model and its success in many practical applications has made the study of wear a quantitative science. In the past ten to fifteen years, Rabinowicz [4] has initiated efforts in the direction of investigating the mechanisms of adhesion as well as the surface energies of solid materials. Vast quantities of information from the areas of surface chemistry and solid state physics were applied to supplement the adhesive wear theory. Unfortunately, with all the enthusiasm devoted to wear studies, the role of metallurgical parameters as well as mechanics of deformation and fracture were largely overlooked. One of the few exceptions which also has significant implication in practical applications, is the compatibility chart developed by Rabinowicz [5]. The study relates the adhesion (implied by static friction measurements) between material pairs of various combinations of pure elements to their ability to form solid solution or other metallurgical phases. It is found that the best combination for low friction and low wear applications is two hard single phase materials which are not chemically compatible.

In recent years, there is a general feeling of the need and interest to investigate the wear phenomenon in disciplines of science other than that of adhesion, particularly in relating wear to the mechanics of de-

formation and fracture. This interest is further stimulated by the introduction of the delamination theory of wear.

B. THE DELAMINATION THEORY OF WEAR

The adhesive wear theory has received a number of criticisms, largely because of the many highly idealized assumptions made in constructing the model. Also, some important experimental observations were overlooked or were treated as some extraneous behavior, even if their occurrence was commonplace. A list of the most commonly raised criticism can be found in reference [6]. We will try to illustrate here with an example; why, from a practical engineering point of view, there is the need to investigate other aspects of wear than that of the adhesive wear model. Figure II-2 shows a histogram of the distribution of wear particle size from a typical sliding wear test. The wear particle size is represented by the mass of the wear particles. It is noticed that the vast majority of the wear particles are small. Their dimensions approximates that predicted by the adhesive wear theory [2]. However, a higher percentage of the wear loss is contributed by the fewer number of large wear particles. The particle size of these large wear particles is not predicted by the adhesive wear theory. Also, the features of these large wear particles closely resemble the features of a fracture process. This example points out that, although the adhesive wear mechanism is indisputably in operation during the sliding wear, the real answer to the consequence of practical concern; the wear loss, is caused by some other wear mechanisms that is not emphasized or even discussed in adhesive wear theory.

The delamination theory of wear was introduced by Suh [7] in 1973,

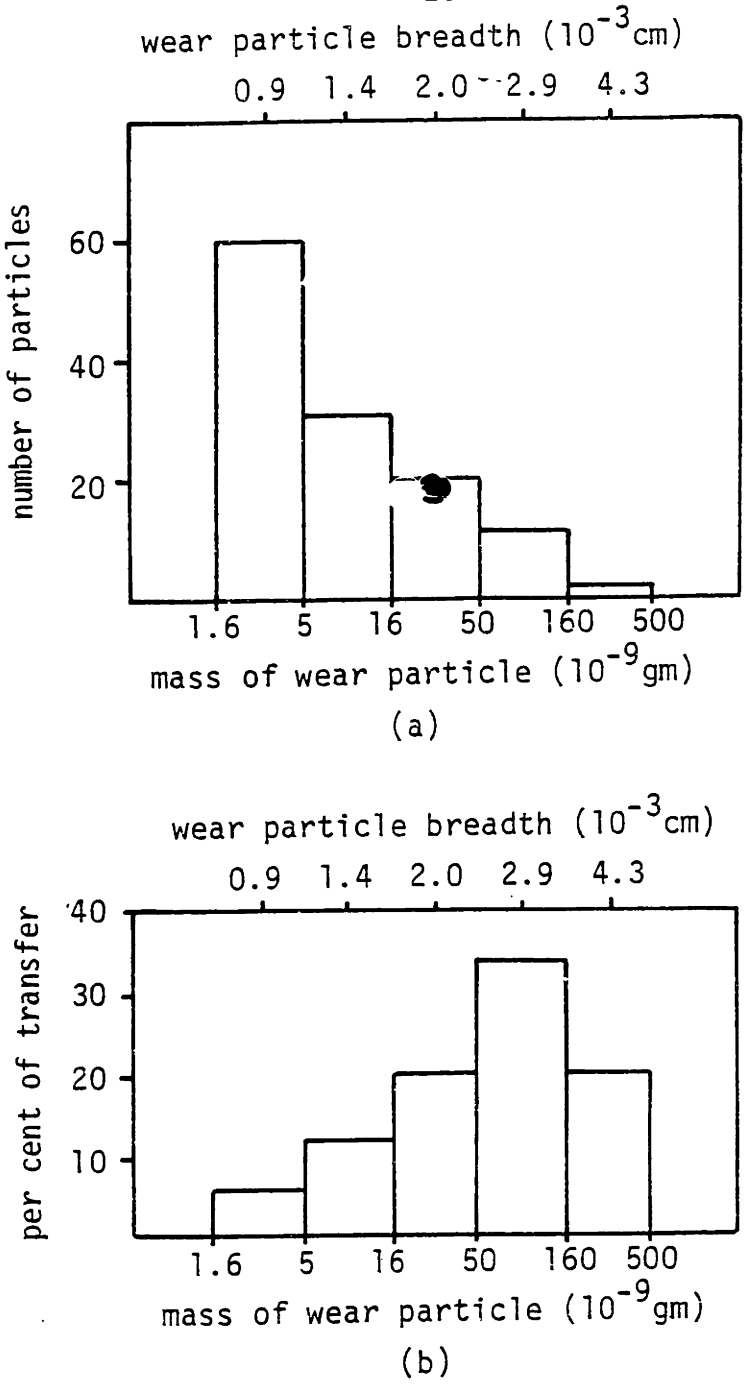

Figure II-2 Histogram of wear particle distribution (reference 2)

followed by extensive analytical and experimental investigations conducted at M.I.T. Most of these investigations were reported in volume 44 of the journal, Wear. They are also compiled into a single volume reference, published by Elisevier [8]. The significance implied in this theory is to provide a new perspective to examine the wear problem in an unified and consistant manner, rather than conducting case by case investigations, and apply one of the established wear models or theories that best describes the observation. Although the delamination wear theory place its emphasis on the mechanical aspects of wear, it is not in conflict with the classical theories. On the contrary, most of the classical theories are important contributing factors to the mechanics and materials parameters involved in the delamination theory of wear.

(1) THE DELAMINATION WEAR PROCESS

Referring to figure II-3, the delamination theory of wear describes the sliding wear process as follows:

(a) When two sliding surfaces come in contact, normal and tangential tractions are transmitted through the contact points by adhesive and mechanical interlocking actions. Asperities of the softer surface are deformed and some are fractured by the passage of the harder surface. This process is similar to that described in the adhesive wear model. The wear particles generated are of the size of the contact asperities.

(b) As the process continues, the surface becomes smooth and the plastic deformation is no longer limited to asperity contacts but extends deeper into the subsurface of the material. This subsurface plastic shear deformation accumulates as a consequence of repetitive loading. The

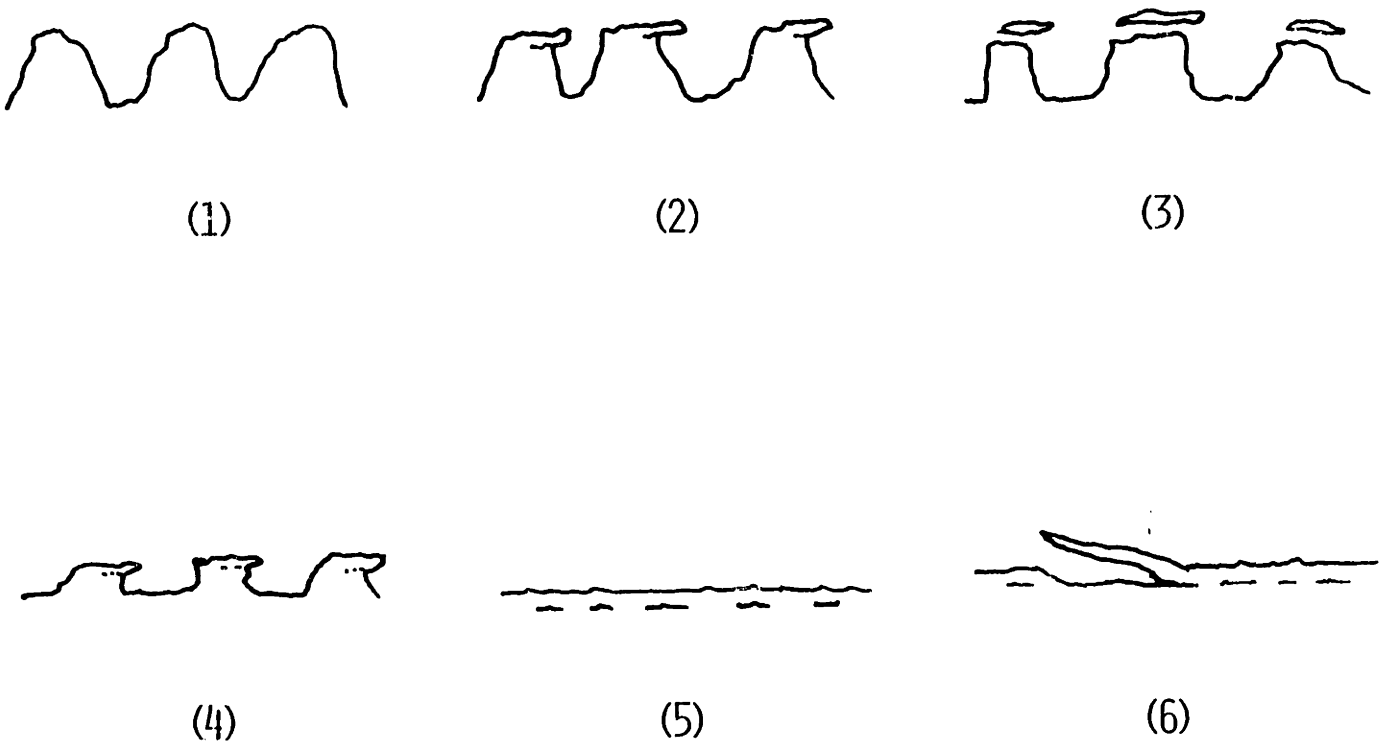

Figure II-3 Delaminaltion wear process. (reference 6)

maximum shear deformation occurs at some distance below the surface. The depth depends on the magnitude of the normal and tangential surface tractions, and is usually within the same order of magnitude as the contact size.

(c) As the subsurface deformation continues, cracks are nucleated below the surface. Crack nucleation very near the surface is not favored because of the high compressive stresses in that region.

(d) Once subsurface cracks are nucleated or there are pre-existing cracks or voids in the subsurface, further loading and deformation leads to the extension and propagation of these cracks. The crack propagation rate and the direction of the running cracks depend on the stress state in the subsurface.

(e) When the propagated cracks finally extends to the surface, a plate or sheet like wear particle is produced, as shown in figure II-4, which is very different from the asperity wear particles produced in stage (a).

(2) STRESS STATE UNDER THE SLIDING CONTACT

From the above description of the delamination wear process, it is shown that the stress state under the sliding contact is the most important factor that effects the delamination process. The elastic stress state of this problem was investigated by Smith and Liu [9], and Poritsky [10]. Their solution is based on a Hertzian contact stress distribution on the surface, and assumes a friction coefficient for the tangential traction. The elastic solution of the principle stresses and the maximum shear stress under the sliding contact are shown in figures II-5 and II-6, assuming a friction coefficient of 0.3. It is noticed that the maximum shear stress

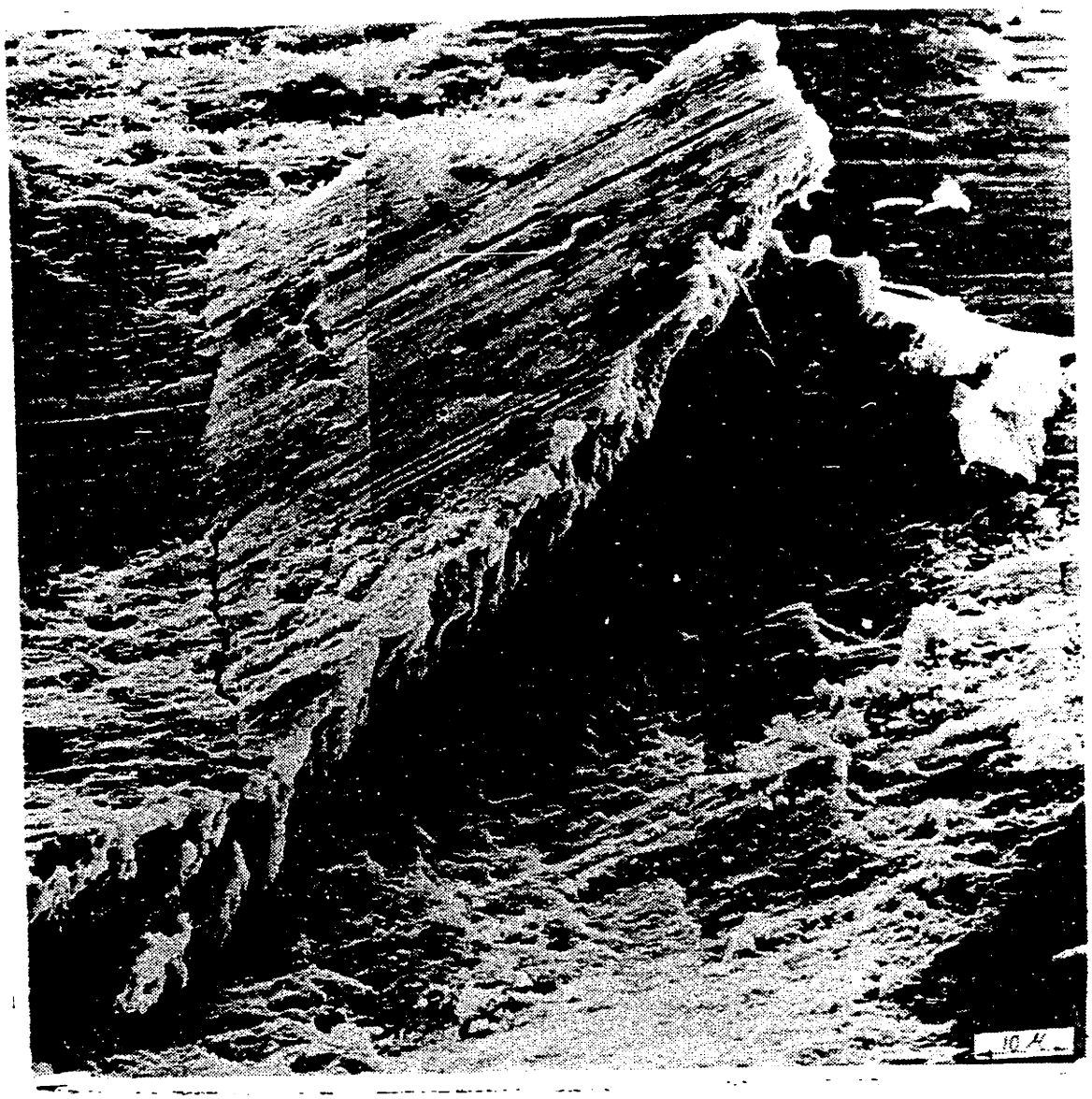

Figure II-4 Delaminated wear sheet on wear track of iron solid solution. (reference 6)

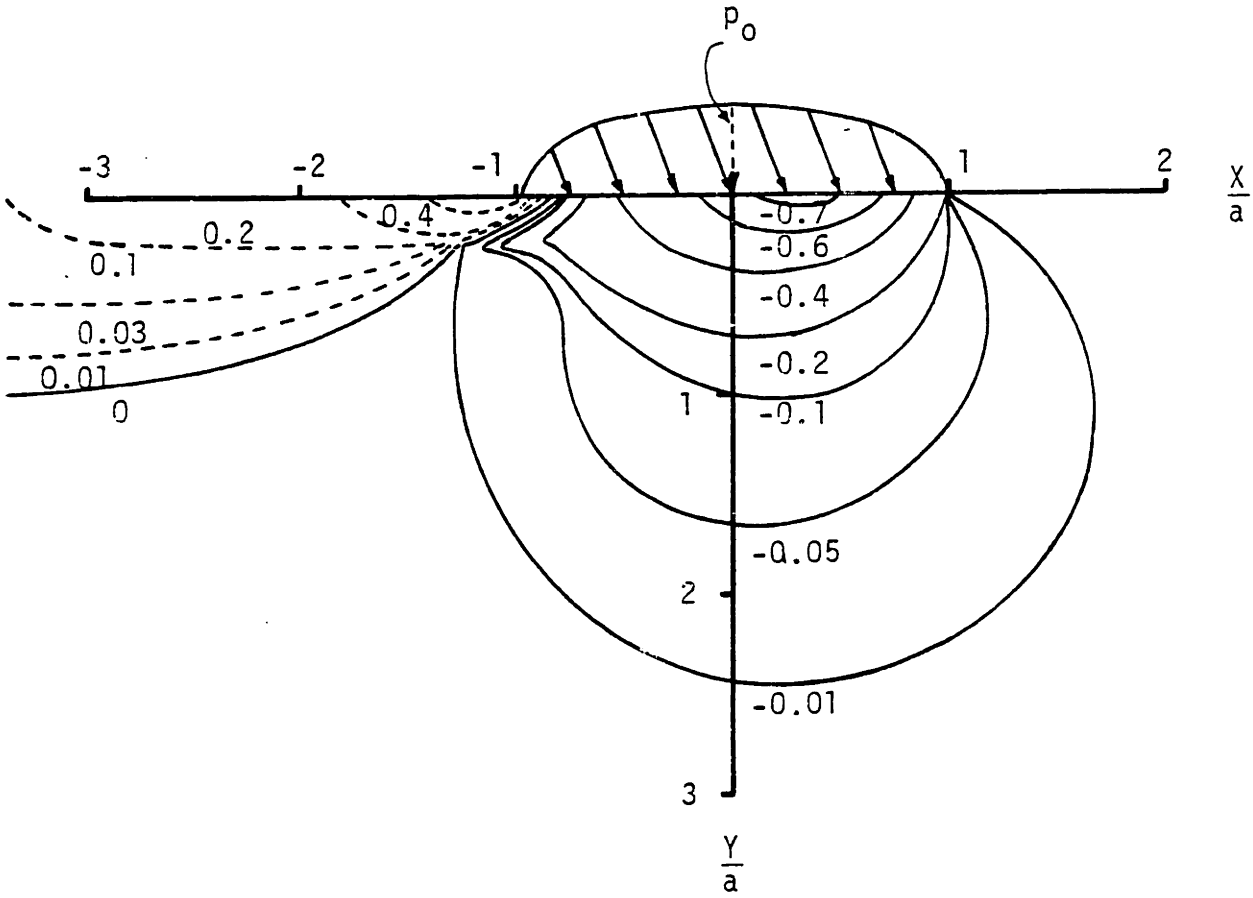

Figure II-5 One of the principal stresses in the X-Y plane under the sliding contacts. Stress is normalized by the maximum Hertzian contact stress p_o. Friction coefficient is assumed to be 0.3. Solid lines represent compression, broken lines represents tension. (reference 9)

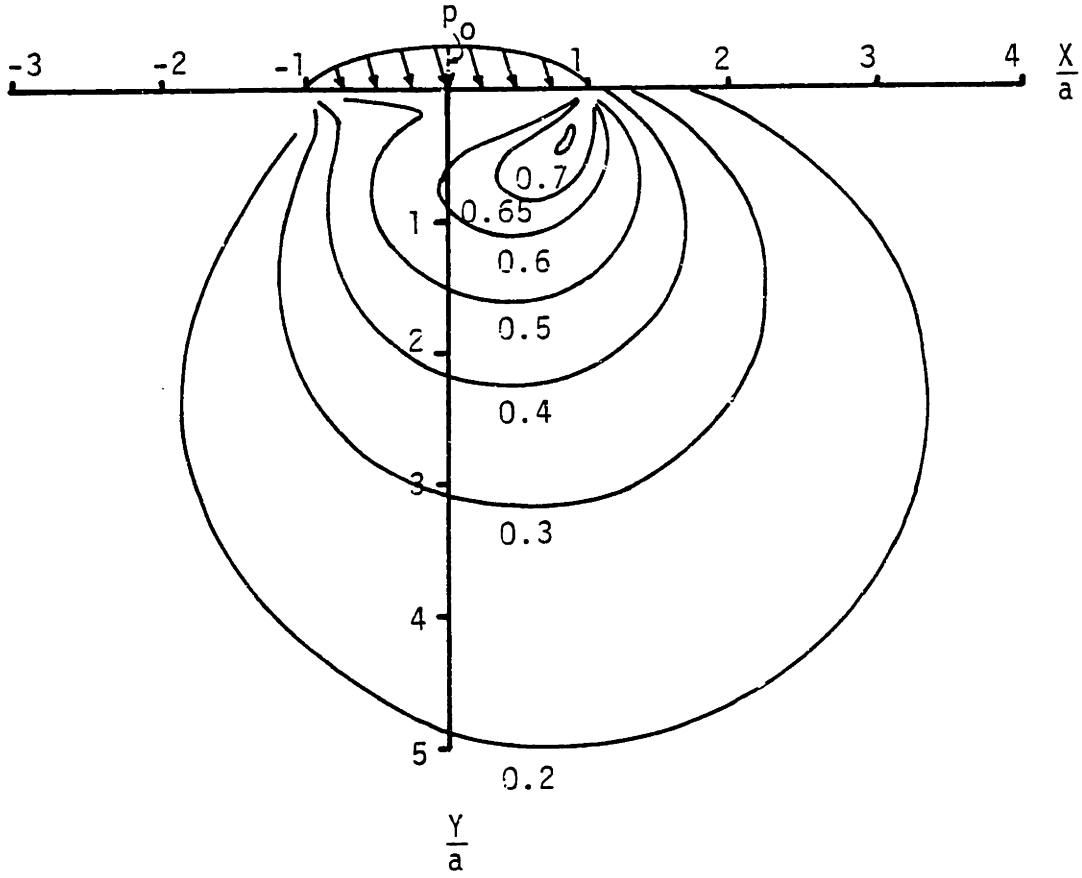

Figure II-6 Maximum shear stress in the X-Y plane under the sliding contact. Stress is normalized by the maximum Hertzian contact stress p_o. Friction coefficient is assumed to be 0.3. (reference 10)

developed in front of the slider at a distance below the surface, and the principle stresses under the slider are mainly compressive, except at a region trailing behind the slider, where tensile stresses are developed.

Suh and Jahanmir [11] studied the size of the plastically deformed zone under a sliding contact, using an approximated elastic-plastic analysis by Marwin and Johnson [12]. The results are shown in figure II-7, with an assumed maximum Hertzian contact stress of $p_o = 4k$, where k is the shear yield stress, and friction coefficient ranging from 0.25 to 1.0. It is shown that the size of the plastically deformed zone is expanded significantly with the increase of the friction coefficient.

(3) EFFECTS OF INCLUSIONS ON THE DELAMINATION WEAR PROCESS

The most important effect of hard inclusions in the material on the delamination wear process is that they serve as preferential sites for void and crack nucleation. Mechanisms of void and crack nucleation around inclusions are discussed in the next chapter. In the particular case of wear, the existence of inclusions in the material further amplifies the stress level of the maximum shear stress in the subsurface because of stress concentration. Therefore, microvoids are preferentially nucleated in areas around the inclusions. Observations of this phenomenon was reported in the study by Jahanmir [6] as shown in figure II-8. The nucleated voids will then experience a repetitive local tensile stress developed by the trailing edge of each asperity passage. Under the influence of this repetitive tensile stress, the voids will either propagate as cracks or undergo slow growth, joining neighboring voids or cracks. Finally, the cracks extends to the surface and produce delaminated wear sheets.

Suh and Jahanmir [11] found that the number of asperity passages re-

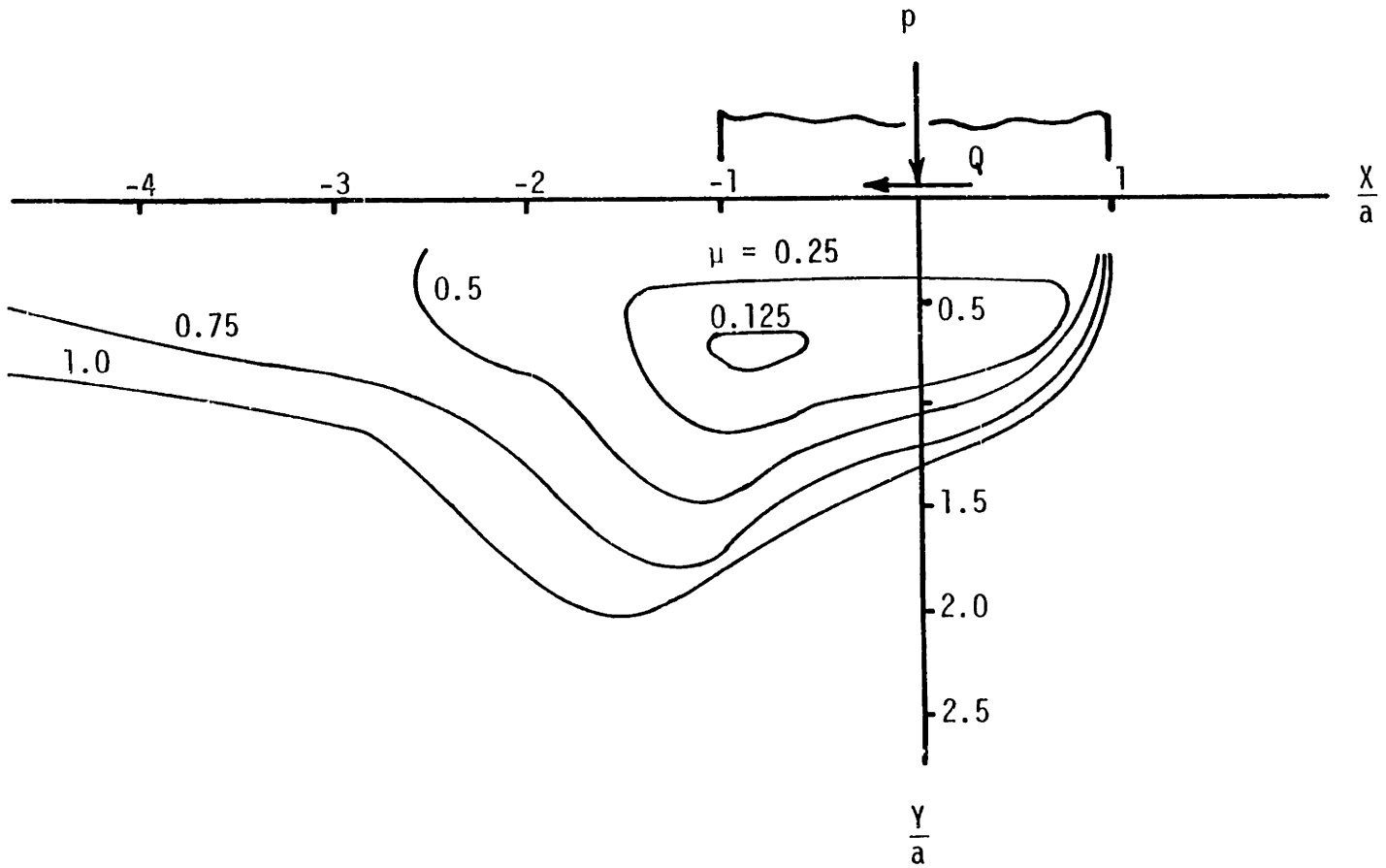

Figure II-7 The steady state plastic deformation regions in an elastic-perfectly plastic material under a sliding contact, for a maximum applied normal stress p_o = 4k and different friction coefficients. (reference 6)

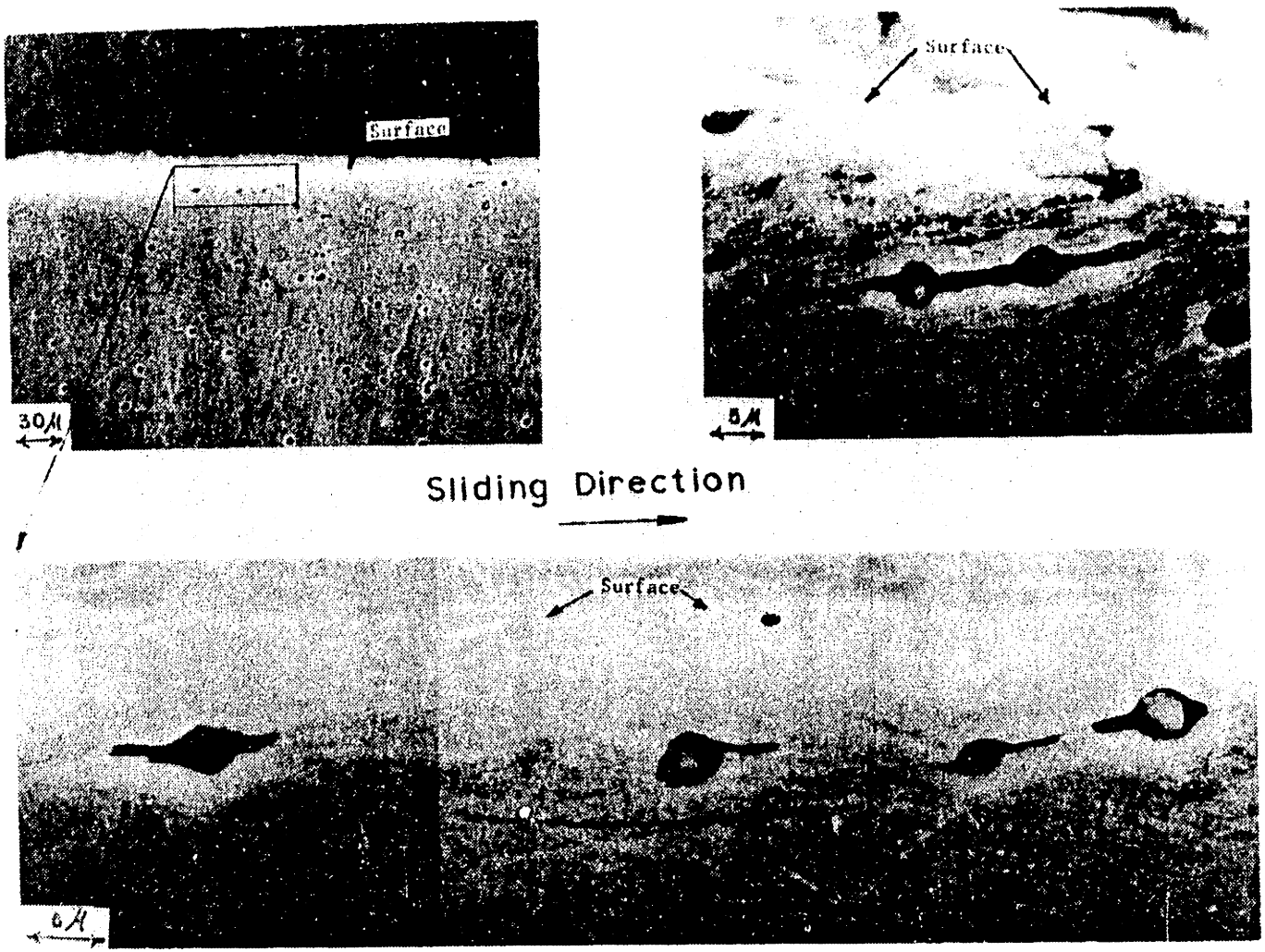

Figure II-8 Subsurface void nucleation and crack growth in Fe - 1.3% Mo under sliding contact. (reference 6)

quired for void nucleation is usually very small (fewer than 10). Since these nucleated voids are an important origin for the later crack propagation process, if the material is brittle, where crack propagates easily, the wear rate will be governed by how fast these subsurface voids can nucleate. On the other hand, if the material is ductile, where the crack propagation rate is slow, the wear rate will be dictated by the rate of crack propagation. In their study, it is assumed that for voids to nucleate, the only criterion to be satisfied is that the interfacial stress between the matrix and the inclusion should exceed the interfacial strength. This assumption is a reasonable one for inclusions with particle size larger than 1 micron. In the next chapter, we will discuss the energy criterion for void nucleation, which is important for inclusions with smaller particle sizes. In later chapters, analysis and experiments are conducted to investigate the benefits of reducing the size of the inclusion to improve the mechanical as well as the wear resistant properties of inclusion filled materials.

C. FRICTION AND WEAR OF POLYMERS AND COMPOSITES

In the investigation of the friction and wear properties of polymers and its composites, it is important not to overlook the special characteristics of polymeric materials. Some of the important properties that have to be considered are:

(a) The macromolecular structure of a polymeric material is entirely different from the crystalline structure of metallic materials. Within the different types of polymers, their structure can also be very different. There are linear crystalline polymers, crystalline polymers with side

branches, polymers with different crystallinity, linear amorphous polymers, and crosslinked polymers. These different molecular structures are responsible for the vastly different properties of different types of polymers. Therefore, when discussing friction and wear properties in relation to the materials properties, it is important that these differences in molecular structure are recognized, and care should be exercized when trying to adopt theories developed on one particular class of polymers to other classes of polymers.

(b) The response of polymers to mechanical load is not restricted to elastic or plastic behavior. Their response can be visco-elastic, which is time dependent. This visco-elastic behavior can be very pronounced in certain temperature ranges and strain rate, depending on the type of polymer. Under such circumstances, it may be inappropriate to apply theories that are developed based on elastic and plastic assumptions.

(c) Thermal properties of polymers are also important considerations. Polymers in general, have low melting and transition temperatures. Unfortunately, most of these temperatures are in the range of 80°C to 150°C, which is commonly encountered in sliding contacts. Furthermore, polymers usually have low thermal conductivity and high heat capacity. The compounding effect of these properties will be that high temperature can develop at the sliding surface. Consequently, the properties of the material at the surface can be significantly different from those of the bulk of the material. Also, due to the high surface temperature, there is the possibility for some chemical reaction or degradation to take place.

In the following sections, we will discuss the friction and wear properties of polymer based materials in two major categories, the un-

filled basic polymers and polymer based composite materials filled with either particulate or fibrous fillers.

(1) UNFILLED POLYMERS

The history of synthetic polymers is a relatively short one, and it is only no more than thirty years ago that tribologists found their interest in polymers. Their interest then was not so much in the wear properties of polymers but in the extremely low friction coefficient demonstrated by one particular type of polymer; Polytetraflouroethylene (PTFE). At that time, PTFE and polymers in general were looked upon more as solid lubricants than materials that can be used in load carrying structural parts. This concept is illustrated by the idea of incorporating PTFE in the surface of a porous metal such as sintered copper. During the fifties, extensive research efforts were devoted to the frictional properties of different polymers. There are still very few practical applications that would stimulate interests in the investigation of their wear properties. Early investigations are conducted based on the adhesion theory. The study by Shooter and Tabor [13] as well as by Rabinowicz and Shooter [14] show that material transfer from plastic to metals as well as from metal to plastics are observed as described in the adhesion model. Their studies also suggest that the friction coefficient is primarily determined by the ratio of the shear strength to the effective yield pressure of the plastic. Makinson and Tabor [15] observed that under low speed and moderate temperature, the PTFE transferred to a glass substrate as a very thin, highly oriented film. The film was measured by interference techniques to be 10 to 40 nm thick, and from diffraction studies the molecular chains were shown to be oriented in the sliding direction. Similar findings were found

on other linear crystalline polymers such as high density polyethylene (HDPE), but not on glassy amorphous polymers, where lumpy loose particles were generally observed. Pooley and Tabor [16] show that among the group of polymers they investigated, polymers such as PTFE and HDPE that have smooth molecular profile with little or non bulky side groups, the static friction is high ($\mu \gtrsim 0.2$), followed by very low kinetic friction ($\mu < 0.1$). If the molecular structure is changed by introducing an appreciable number of bulky side groups (e.g., tetrafluoroethylene-haxafluoropropylene (TFE-HFP) copolymer, polychlorotrifluoroethylene (PCTFE), or low density polyethylene (LDPE)), the kinetic friction remains the same as the static value. The friction and material transfer resembles that of polypropylene (PP) and amorphous polymers such as polymethylmethacrylate (PMMA) and polystyrene (PS). These observations suggest that the low friction characteristics of PTFE and HDPE under certain sliding conditions, results from the successful development of a highly oriented coherent transfer film on the sliding counterface, and low friction is developed because of the material will then be sliding on this transferred film which has smooth molecular profile.

The observation of thin transfer film from some linear crystalline polymers leads to the investigation of the role of transfer film in wear. Most investigations emphasize on the mechanisms of the transfer film formation. Tanaka *et al* [17] found that the amount of PTFE film transfer is related to the size of the crystalites, rather than the crystallinity of the material. The transfer film type of wear is only found in a minority group of materials under certain sliding conditions. The majority of the polymers, even PTFE and HDPE when sliding at high speed at low

temperature, do not develop coherent transfer films. The wear particles are more similar to the adhesive wear particles found in metal wear. Therefore, the adhesive wear model can be appropriately applied to most wear cases for unfilled polymers. Adhesion plays an important role in the film transfer mechanism. How steady-state wear proceeds once the transfer film has formed is not well understood. Does a transfer film detach from the sliding counterface because of the low surface energy of the polymer and the strain energy stored in the highly oriented film, and quickly being replaced by a new layer of transfer film? And, if the transfer film is stable and firmly attached to the counterface, what is the mechanism that determines and maintains the thickness of this film? From then on, do wear particles come from the polymer slider or are they first transferred to the transfer film and then come off as loose wear particles? These are just a few of the questions that remain to be investigated in connection to the film transfer phenomenon. However, it should be emphasized again that in the majority cases of the wear of unfilled polymers, the lumpy type of adhesive wear particles results.

(2) PARTICULATE AND FIBROUS FILLED POLYMER

There are two major types of particulate fillers that are commonly incorporated in polymers for bearing applications. The first type includes that of powder PTFE, graphite, and MoS_2. Their function is to serve as solid lubricants to reduce friction. The second type of particulate filler used are hard metal or mineral fillers, such as bronze and mica. Their function is to provide thermal stability, reduces shrinkage, increase the stiffness and hardness of the material, as well as for reducing cost. One exception is the study by Briscoe, Pogosian and

Tabor [18], where a mixture of lead oxide and copper oxide is added to HDPE to promote and enhance the formation of a stable transfer film, thus avoiding the more severe wear caused by lumpy wear particle transfer. Fibrous fillers such as glass and carbon are used mainly for reinforcing the strength of the polymer matrix, and increasing its load carrying capacity. The fibers can be incorporated in the form of chopped strands, continuous strands, or as woven fabrics.

There are very few studies on the friction and wear properties of particulate filled polymers besides those of the solid lubricant type. Speerschneider and Li [19] studied the effect of the particle shape of aluminum oxide particles in PTFE on its friction and wear properties. They found that spherical Al_2O_3 particles have a greater effect in reducing the wear of PTFE than irregular shaped Al_2O_3 particles. Also, the friction coefficient is maintained the same as the unfilled PTFE with the spherical Al_2O_3 particles, while the irregular shaped Al_2O_3 particles introduce higher friction. For fiber reinforced thermosetting resins, Giltrow and Lancaster [20] found that for high concentrations (> 40%) of chopped carbon fiber filled polymers, the tribological properties are determined mainly by the type of fibers and the nature of the counterface material. Fiber orientation, the type of matrix resin and the presence of a third component are usually of little significance. Sung and Suh [21] investigated the friction and wear properties of continuous fiber filled polymers with different fiber orientations with reference to the sliding direction. They found that both friction coefficient and wear rate are the lowest when fibers are oriented normal to the plane of sliding, higher values are observed for fibers oriented parallel to the direction of sliding. When

fibers are oriented transversely to the sliding direction, the highest wear rate and friction coefficient is developed. Stimulated by the development of the delamination theory of wear, Clerico [22] studied the subsurface features of sliding contacts of chopped glass fiber filled nylon. Her study shows abundant evidence of mechanical damage in the subsurface, such as cracks and broken fibers. A quantitative relation has yet to be developed to relate these observations to the delamination wear model.

When hard particulate and fibrous filled polymers are used in bearing applications, the effect of these hard inclusions on the sliding counterface should not be overlooked. The most noticable effect is the abrasive wear produced on the counterface. If the inclusion size is small compared to the roughness of the counterface, the effect may be beneficial, because the abrasion actually polishes off the rough spots on the counterface and reduces wear that could be introduced by the ploughing action of these rough ridges [23]. On the other hand, if the particles or fibers are large, they will produce a rough surface on the sliding counterface, and increase the wear of the composite by ploughing action, or result in leakages in applications such as sliding valves. Another important concern is in the design of the sliding pairs. The size of the particle or fiber should not exceed the clearance of the design.

Although the adhesive wear model gives a relatively good description of the wear behavior of the unfilled polymer, in engineering practice, the wear factor K is more commonly used to report wear data of both unfilled and filled polymeric materials than the wear coefficient k used in the adhesive wear model. The wear factor K is defined in the following expression:

$$V = K \cdot P \cdot v \cdot t \qquad \text{(II-2)}$$

Where:

V = wear volume

P = normal load

v = sliding speed

t = time

Another parameter that is commonly used in practice to characterize the wear of polymers and composites is the P-V limit [24]. The P-V limit is the highest pressure at which satisfactory continuous operation of a bearing material can be obtained multiplied by the testing speed. The physical interpretation of the wear factor K and the P-V limit has yet to be determined. But the abundance of available information expressed in these parameters makes them an indispensible tool for practical applications.

III. FAILURE MECHANISMS OF INCLUSION FILLED MATERIALS

The failure of an initially flaw-free material proceeds in two distinctive steps; (1) the initiation and nucleation of microcracks or microvoids and (2) the process of fast crack propagation or slow crack (void) growth that leads to catastrophic failure. The first step of the failure process may not be an important process if flaws are initially present in the material and constitute existing microcracks. The material will then fail when criteria for the second stage process - crack propagation and void growth - are met.

In this study, the first stage failure process - microvoid (crack) initiation - is investigated, particularly for a polymeric material with particulate second phase inclusions. The major interest of this study is to investigate the effect of the particle size of the second phase inclusions on the microvoid (crack) nucleation process. In this chapter, mechanisms and criteria that govern the microvoid nucleation process will be reviewed. Discussions regarding the effect of the microstructure and morphology of the material will also be presented. Both the state of stress and the strain energy in a matrix-inclusion system are examined to establish criteria for microvoid nucleation via different proposed mechanisms. Finally, the effect of the inclusion particle size on these different criteria is discussed.

The second stage of the failure process - crack propagation and void growth - will not be elaborated upon in this thesis. Discussion on this topic will be presented and applied towards the interpretation of data

and observations whenever it is appropriate.

A. MICROCRACK AND MICROVOID NUCLEATION IN A CRYSTALLINE SOLID

The first stage of the failure process - microvoid and microcrack initiation - is heavily influenced by the microstructure of the material system and the local state of stress and deformation. Therefore, the process is usually investigated at a microscopic or even atomistic level, depending on the characteristic scale size of the metallurgical or morphological structure that is involved in the mechanism under investigation. Generally speaking, at temperatures below the brittleness-transition temperature T_D, yielding is a prerequisite for fracture. At these temperatures, the fracture stress of a initially flaw-free material is greater than the yield stress σ_y [25]. This has been found to be the case for most materials, which include metals, polymers as well as brittle ionic-bond solids. Therefore, prior to failure, the micro-flaw initiation and nucleation process must have involved some plastic deformation. For wedge type microcrack nucleation in crystalline solids, Zener [26] and Mott [27] were the first to suggest a dislocation model for the microcrack nucleation process, where shear stresses acting on the slip plane squeezes dislocations together. Stroh [28-30] calculated the local tensile stress at the dislocation pile-up and compare it to the theoretical cohesive strength of the material to establish a stress criterion for microcrack nucleation. It should be noted that although the resultant tensile stress is compared with the theoretical cohesive strength to establish the microcrack nucleation criterion, the dislocation pile-up under local inhomogeneous plastic deformation results from the shear stress

alone. The local tensile stress at the nucleation site is not the driving force behind the nucleation mechanism. Dislocations can pile up against grain boundaries, second phase obstacles or sessile dislocations. For each individual case, similar microvoid nucleation criteria can be developed by calculating the local stress state and applying the dislocation model and argument. Some different modes of the microcrack and microvoid nucleation process based on the dislocation model are illustrated in figures III-1 and III-2.

Most analyses based on the dislocation model were made with a single slip line. Friedel [32] argues that one giant pile-up on a single slip plane will never occur, because plastic relaxation of the pile-up stress will begin where the stress exerted by the pile-up group on secondary sources exceeds the elastic limit and dislocations will be generated from these other slip planes. This implies that many pile-up groups must be formed on different slip planes, and this is in agreement with experimental observations that microscopic features such as slip bands and grain boundary sliding, rather than a single slip line, are observed along with the process of microcrack and microvoid nucleation. Averback [33] has made this modification in his analysis of extending the dislocation model into the larger microscopic region, and calculated the critical slip band width for microcrack nucleation.

B. THE EFFECT OF MATERIAL MICROSTRUCTURE ON THE MICROVOID NUCLEATION PROCESS

On the microscopic level, wedge type microcracks are commonly ob-

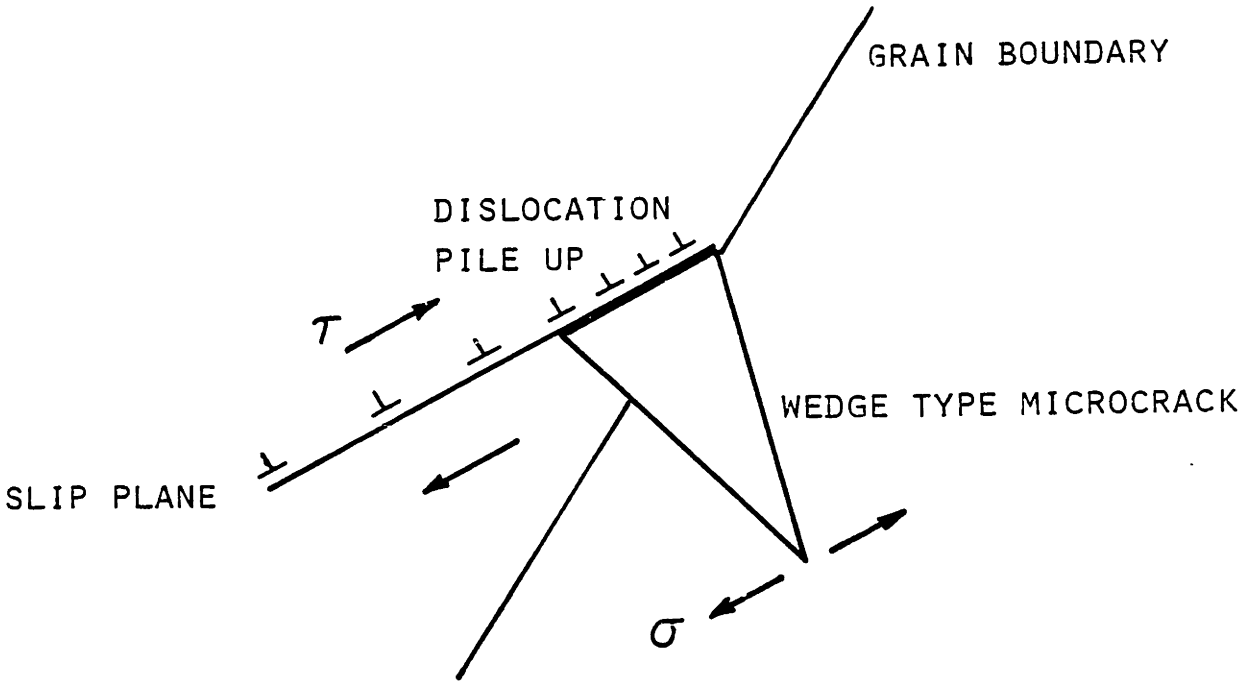

Figure III-1 Microcrack nucleation at the tip of a pile up group of edge dislocation at grain boundary. (reference 25)

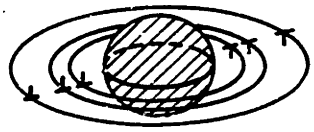

(a) Piled-up loops around particle

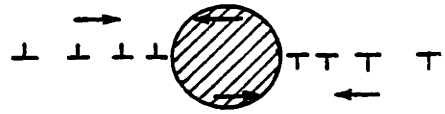

(b) Equilibrium between pile up stress and image force

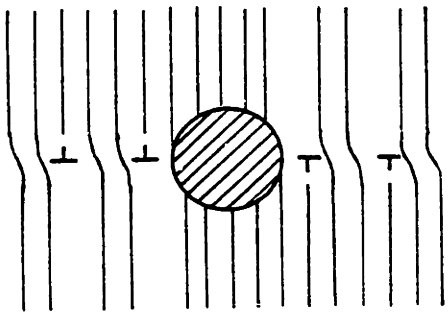

(c) Leading loop pushed into boundary

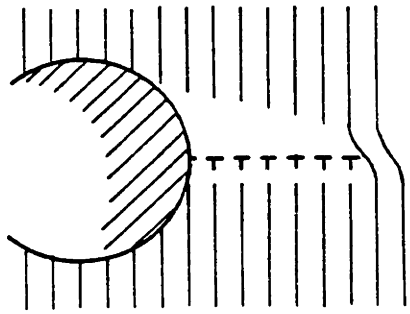

(d) Cavity formation

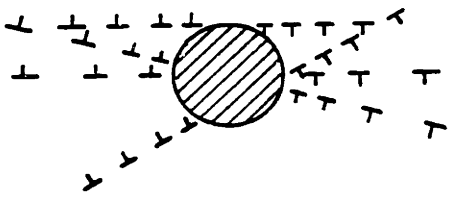

(e) Actual pile ups

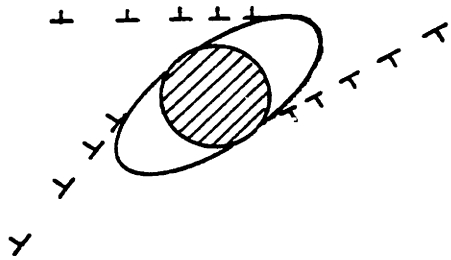

(f) Void growth

Figure III-2 Dislocation model of microvoid nucleation around inclusions. (reference 31)

served to initiate at grain boundaries, especially at triple points and at precipitates and impurities segregated at grain boundaries [34]. Cavitation type of microvoids are usually found at higher temperatures and lower stresses than those for wedge type microcracks initiation [35]. Microvoids were not found in single crystals or polycrystalline solids produced from recrystallizing from a single crystal and are always found to be associated with particles presented at grain boundaries [36]. Grain boundary sliding is the major cause of the microvoid nucleation [37, 38], as illustrated in figure III-3. Earlier, Orowan [39] has also addressed the same problem with the dislocation model, with a single slip line intersecting the particle.

Besides the fact that inclusions in a material are usually the preferrential sites for microcracks and microvoid nucleation, their particle shape, size and distribution all exhibit some influence on the nucleation process. Microvoid nucleation is mainly found around spherical inclusions, while oblong shape inclusions usually initiate wedge type microcracks [40].

(1) EFFECT OF INCLUSION SIZE

Experimental investigations have shown that void nucleation initiates first at large inclusion at relatively small strain [41-43]. Gurland and Plateau [44] use a simple energy argument to justify this observation. By comparing the elastic energy stored around in inclusion to the surface energy created when a microvoid is formed, the criterion for the microvoid formation is:

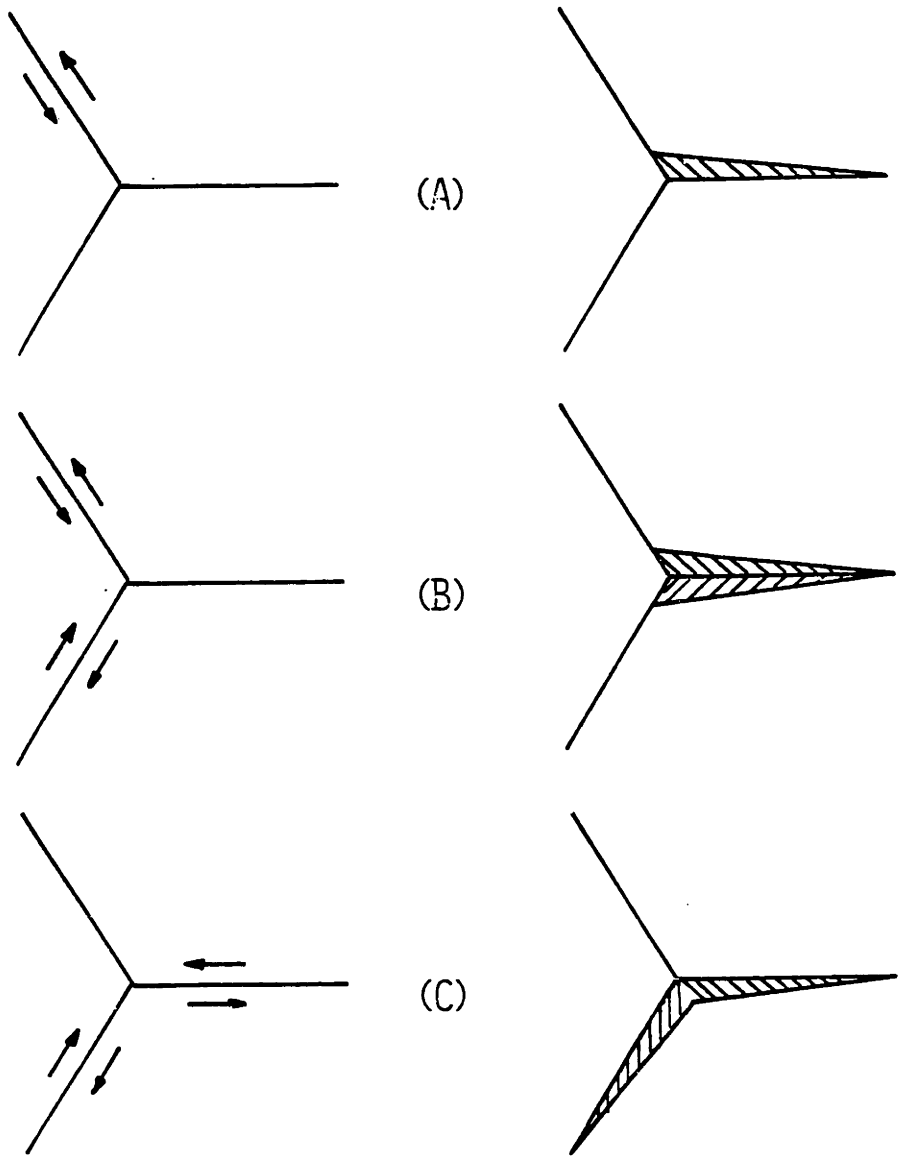

Figure III-3 Schematics of three different types of microcrack initiation at triple points of grain boundaries due to grain boundary sliding. (reference 38)

$$\frac{(k\sigma)^2}{E} d^3 \geq \gamma\, d^2$$

$$\therefore \sigma_{crit} = \frac{1}{k} \left(\frac{E\gamma}{d}\right)^{\frac{1}{2}} \qquad \text{(III-1)}$$

Where:

k = average stress concentration factor

d = inclusion size

γ = surface energy

The critical stress for void formation is shown to be inversely proporational to the particle size. Ashby [45] objected to this kind of energy argument, if consistancy with the dislocation theories is to be maintained. Because the release of the elastic energy to form cavitated interface will require the whole array of dislocation loops around the inclusion to collapse into the interface. In practice, most of the loops are immobilized by intersections with each other and with glide dislocations. These interactions will not permit this type of collapsing mechanism to facilitate. On the other hand, Ashby, in his analysis, relates the interfacial stress to the number of dislocation loops around the inclusion and found that the stress increases linearly with inclusion size. This argument, which is based on the dislocation model, also explains the observation of preferrential void nucleation around large inclusions.

The particle size effect on micro-flaw initiation can also be examined in yet another manner [25]. When the nucleation criterion is based on an energy consideration or on a stress criterion where the ideal cohesive

strength τ_i is related to surface work by:

$$\tau_i \propto \left(\frac{E\gamma}{d}\right)^{1/2} \qquad \text{(III-2)}$$

All such criteria will be implicitly dependent on the term surface work γ. Referring to figure III-4, for a particle with small thickness t, a major part of the nucleated microcrack will be extended in the softer matrix where the surface work γ is high. For thicker particles, most of the microvoids will be confined in the brittle particle with much lower surface work. The size of the microcrack nucleated in the brittle particle may even be long enough to facilitate a Griffith crack propagation. The length ℓ of the particle also has an effect on the microcrack nucleation. If ℓ is short, dislocations in the pile-up may be able to activate sources above or below the particle and relieve the pile-up stress. Therefore, microvoids are mostly nucleated at large inclusions.

Another particle size dependent factor related to the nucleation mechanism is the slip distance L. The slip distance L is related to the inter-particle spacing. The longer the slip distance, the larger is the number of dislocation loops that can be supplied to the pile-up front. At the same inclusion concentration, smaller particles will have shorter inter-particle spacings and thus result in shorter slip distance in the matrix. The pile-up stress will be lower because a smaller number of dislocations are available for the pile-up.

(2) EFFECT OF INCLUSION CONCENTRATION AND DISTRIBUTION

The immediate effect of changing the concentration and the distribution of inclusions in the matrix phase is in the changing of the inter-

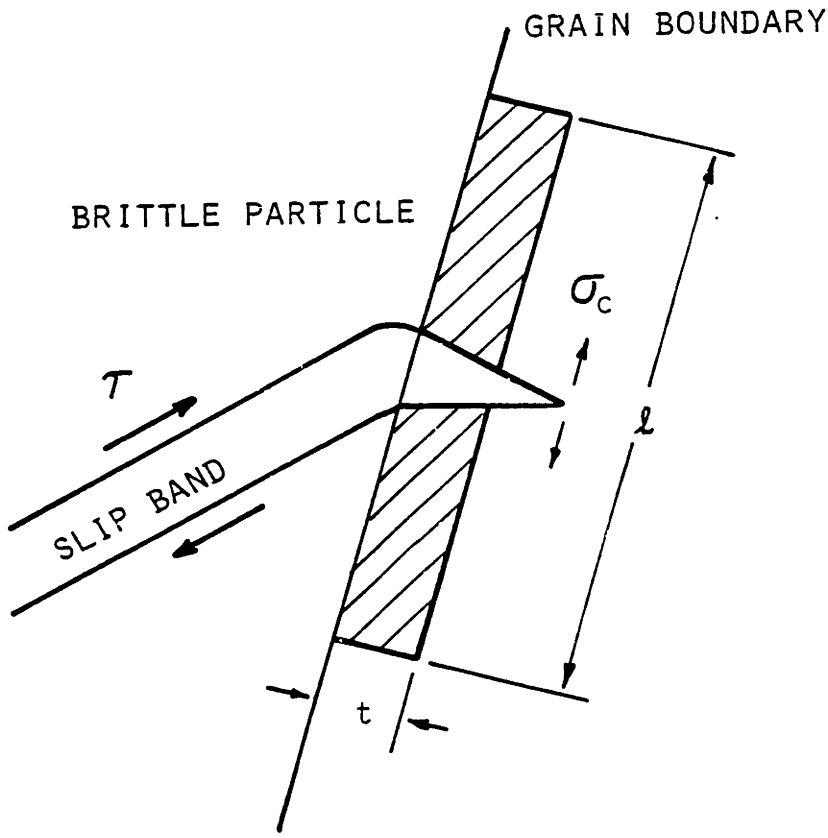

Figure III-4 Transgranular microcrack initiation associated with oblong shape brittle second-phase particle. (reference 25)

particle spacing of the inclusions. Each inclusion in the material establishes a stress field around itself either due to externally applied load or internal stresses. The effect of this stress field is usually not felt beyond a distance of several inclusion sizes. When the inter-particle distance diminishes as the inclusion concentration increases, the stress fields around neighboring inclusions will have a chance to interact with each other. This usually results in an amplification of the stress level, because neighboring inclusions usually has similar surrounding stress fields. Matsuo, Wang and Kwei [46] studied the craze initiation stress and strain in a polystyrene material embedded with two rubber balls. Their use of a simple linear elastic superposition principle on the adjacent stress fields gives reasonably good results when compared to experimental data. A more rigorous analysis of the elastic interaction of two spherical cavities in an infinite media is given by Sternberg and Sadowsky [47]. Discussions of the stress interactions of adjacent inclusions with plastic relaxation in the matrix phase is deferred to in the last section of this chapter.

When considering the energy of the system when the elastic field around one inclusion is felt by a neighboring inclusion, the total energy no longer consists of only the elastic energy of the two individual fields, but will also have to include the interaction energy between these two includions. Detailed discussions regarding the interaction energy among stress fields can be referred to Ëshelby [48, 49].

C. VOID NUCLEATION IN AN INCLUSION FILLED POLYMERIC MATERIAL

The different theories on the mechanisms and criteria for microvoid

nucleation reviewed in the previous sections were developed for crystalline solids, and mainly for metallic systems. To adopt these theories to a polymeric material, it is necessary to first justify their applicability because of the inherent differences between polymeric and crystalline metallic materials.

Two basic approaches are utilized by the various theories presented in the last section. One of them is the continuum approach, and the other one involves some kind of discrete mechanisms, among which the dislocation model is applied extensively. On the continuum level, there is no limitation on the kind of material to which it can be applied, as long as the constitutive relations of the material is known, whether it be elastic, plastic, or visco-elastic. However, the physical scale size of the system on which the model is applied must be taken into consideration. There is a scale size limit below which the continuum arguments will depart from physical reality or even become invalid without elaborate modifications. For a typical metallic system, this limiting scale size is usually associated with some metallurgical parameters, such as grain size and slip band width. For a crystalline polymer, it will be that of the size of the crystallites. In amorphous polymers, the continuum approach may be applied down to the molecular size range, or it will be limited by the size of any inhomogeneity presented in the material.

Theories based on the dislocation model may not be directly applicable to polymer materials, simply because such model is not well established for polymers. Li and Gilman [50] proposed a deformation theory for polymeric materials based on a disclination model. Bowden and Raha [51] also approached the problem using a direct analogy to the dislocation

model. However, these models have not been widely accepted. Another discrete mechanism associated with the deformation of glassy polymers was proposed by Argon [52, 53]. In this model, the deformation process is modeled as a stress biased thermally activated process, involving the rotation of small molecular segments between a pair of double kinks in a long molecular chain. The rotation changes the molecular configuration from an initially random orientation into a direction parallel to the principle tensile extension. Theory based on this model has been shown in good accord with experimental results on the temperature dependence of the plastic shear resistance of a large group of glassy polymers with widely different molecular structure [54].

The continuum approach has the scale size limit below which it cannot be applied without overlooking the effect of material structural parameters, whereas the dislocation or other discrete models have the weakness of over simplification or idealization in constructing the models. However, the two approaches are not conflicting theories. They should be used to complement each other and help to shed more insight into the problem.

In our particular problem of investigating microvoid nucleation in a particulate filled polymeric material, and considering the small particle size filler used in our investigation, we have chosen amorphous glassy polymers as the matrix material. This will enable us to apply the continuum approach appropriately. In determining the criteria for the microvoid nucleation process, we try to avoid using overly simplified arguments such as equation III-1. This is particularly important in our attempt to derive a quantitative estimate of the critical inclusion size for the microvoid nucleation process. Therefore, an important part of our continuum

analysis is to determine the stress and strain field as well as the energy state in an inclusion-matrix two phase system.

D. THE INCLUSION AND INHOMOGENEITY PROBLEM

There are two types of mechanics problems which are of particular interest when discussing the interaction of a finite region in a matrix with its surroundings. As illustrated in figure III-5, first, there is the size and shape misfit inclusion problem, which can be represented by internal stresses resulting from phase transformations, such as martensitic transformation, twinning, etc. Alternatively, if the specific region has a different thermal expansion coefficient from that of the matrix phase, a size misfit problem results when the material experiences a temperature change. The second type of problem occurs when the specific region is made of a material which has different elastic properties from those of the matrix. In this case, the two phases will respond differently when subjected to an applied stress, but they are constrained to have matched boundary conditions at their interface. This is called the modulus misfit inhomogeneity problem.

Some of these problems can be solved in the classical manner as boundary value problems [55-59]. Most treatments of this type deal with special cases such as rigid inclusions or cavities of cylindrical or spherical shape. The solution by Edwards[59] is probably the most general, where elastic inclusions of spheroidal shape is considered. The analysis adopted in this investigation is based on a model developed by Eshelby [60, 61]. His unorthodox approach provides more physical insight into the problem along with the following advantages. First, it avoids the tedious

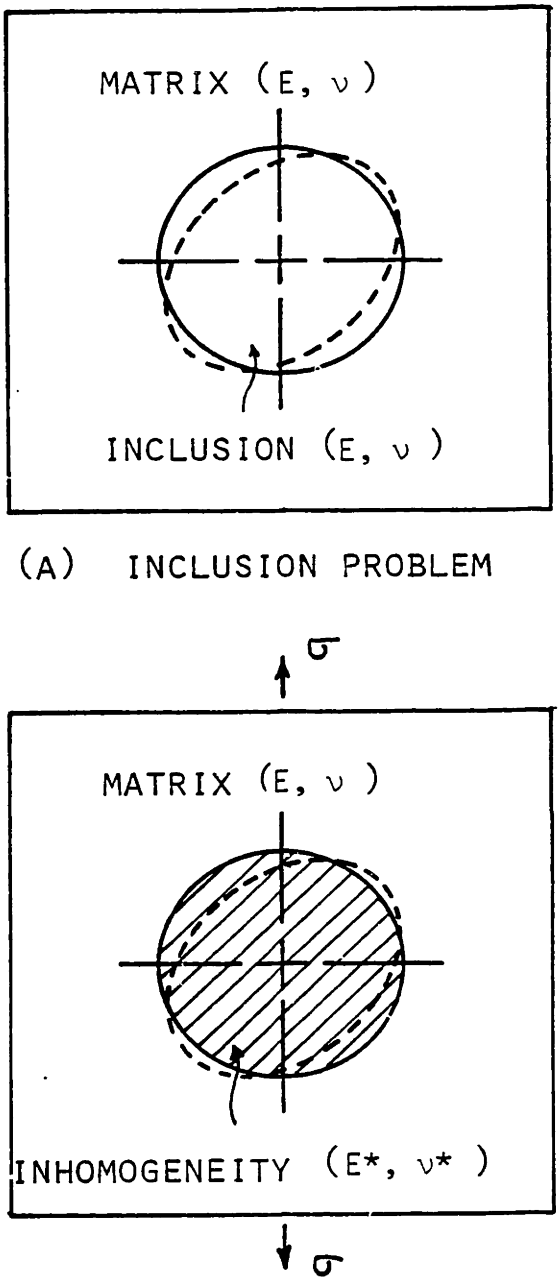

Figure III-5 (a) Size and shape misfit inclusion problem and (b) modulus misfit inhomogeneity problem.

processes of solving the boundary value problem and guessing appropriate stress functions. Secondly, answers are provided for most questions of physical and engineering interest which only require knowledge of the simple elastic field within the inclusion or the inhomogeneity. Thirdly, for our particular problem of void nucleation at stress concentrated poles on the matrix-inclusion interface, the cavitated state can be easily evaluated by a simple transformation process. This problem would be difficult if not impossible to solve by the conventional approach. In this section, we will be devoted mainly to an explanation of the principles used in applying Eshelby's approach to our problem. The detailed mathematical deriviation is given in Appendix A.

(1) ESHELBY'S MODEL

The procedure of solving the size and shape misfit inclusion problem is posed as a hypothetical question as illustrated in figure III-6. A certain region bounded by surface S in a homogeneous matrix undergoes some kind of transformation which changes its size or shape. What will be the resulting elastic state in the system? Eshelby approaches this problem by first cutting out this region before the transformation takes place, as shown in step (b). In the next step (c), he allows this cutout region to go through the transformation without the constraint of the matrix. This stress free transformation strain is denoted as e^T_{ij} with reference to the ground state in (a). Following in step (d), surface traction $-p^T_{ij}$ is applied to the transformed inclusion to restore it back to the original size and shape. Step (e) involves fitting the inclusion back into the original cutout cavity, while still maintaining the surface traction $-p^T_{ij}$. In the last step (f), the surface traction $-p^T_{ij}$ is removed from the

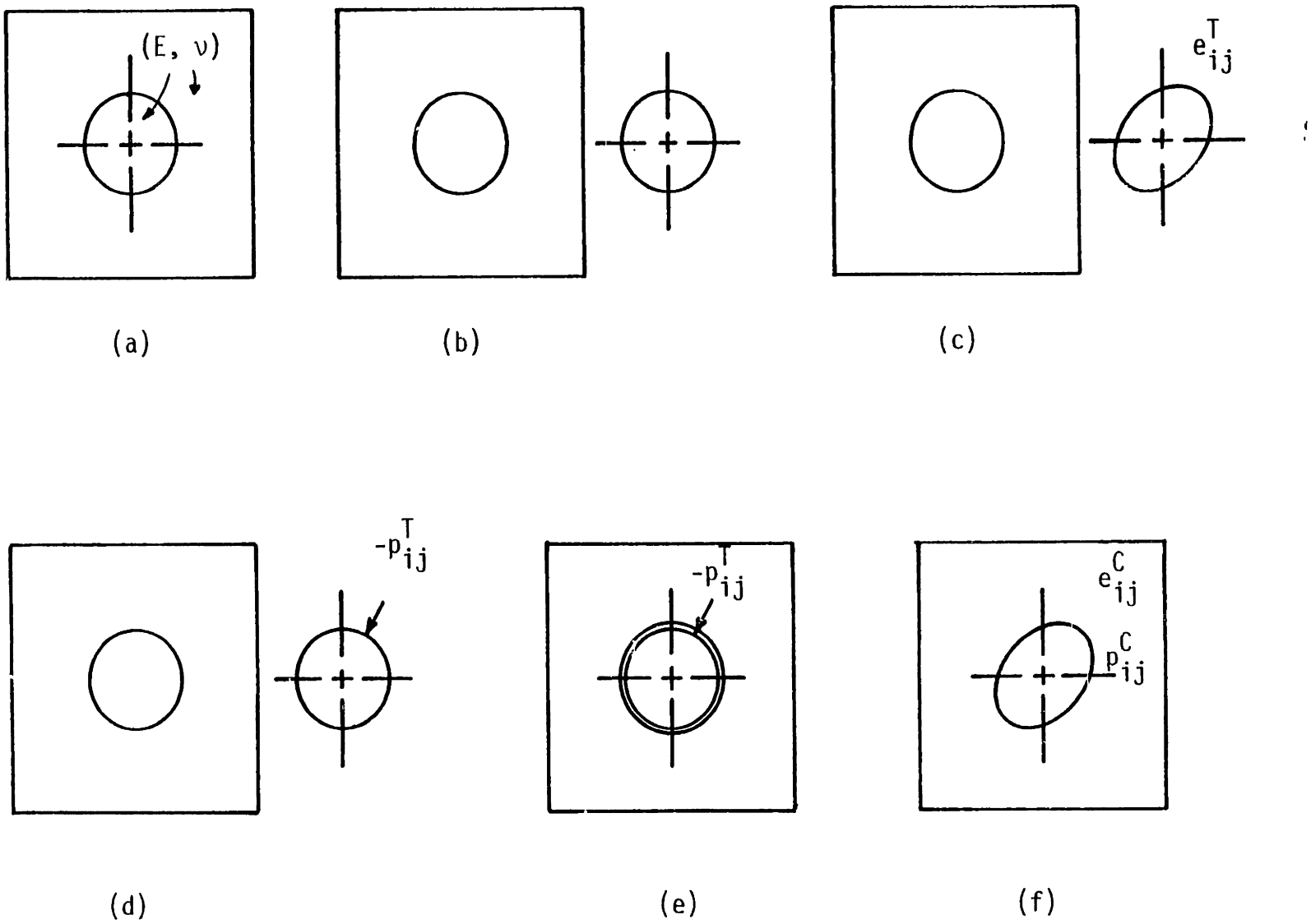

Figure III-6 Eshelby's approach to the inclusion problem.

inclusion by applying a traction $+p^T_{ij}$ at the inclusion-matrix interface on both the inclusion and the matrix. A final constrained state of e^C_{ij} and p^C_{ij} results in the matrix and the inclusion. This constrained state is exactly the same as the one the inclusion would adopt if it went through the transformation process under the constraint of its surroundings without experiencing the cutting and rewelding processes. In the inclusion problem described above, it is usually the stress-free transformation strain e^T_{ij} is known. The problem is solved if a relation between the final constrained state and the known transformation strain is established. In section (1) of Appendix A, this relation is derived in an explicit form for an ellipsoidal inclusion and is presented as the $S_{ijk\ell}$ tensor,

$$e^C_{ij} = S_{ijk\ell} e^T_{k\ell} \qquad \text{(III-3)}$$

From Appendix A, for the special case of a spherical inclusion, the relation takes an even simpler form. Expressed in terms of the scalar and the deviatoric components,

$$\begin{aligned} e^C &= \alpha e^T \\ {}'e^C_{ij} &= \beta\, {}'e^T_{ij} \end{aligned} \qquad \text{(III-4)}$$

Where:

$$\alpha = \frac{1}{3}\frac{(1+\nu)}{(1-\nu)}$$

$$\beta = \frac{2}{15}\frac{(4-5\nu)}{(1-\nu)} \qquad \text{(III-5)}$$

The modulus misfit inhomogeneity problem is illustrated in figure III-7. The inhomogeneity has different elastic constants (E^*, ν^*) from those of the matrix (E, ν). The problem is to determine the elastic state in both the inhomogeneity and the matrix when subjected to applied load. The first step (a), is to cut out the inhomogeneity from the matrix. This is followed by step (b), replacing the inhomogeneity with an equivalent inclusion made of the same material as the matrix phase. In step (c), before putting the equivalent inclusion back into the cavity, allow it to go through a stress free transformation e^T_{ij} with reference to the original shape of the inhomogeneity. This e^T_{ij} is chosen such that when after it is put back into the cavity and rewelded with the matrix, it will result in the same constrained state e^C_{ij} and p^C_{ij} as the original inhomogeneity when subjected to an applied field e^A_{ij} or p^A_{ij}. The remaining steps (d) through (f), are exactly the same as described in the inclusion problem. Thus, the relation between the constrained state and the transformation state (equation III-3 and III-4), is exactly the same for both cases. With replacement of the inhomogeneity with the equivalent inclusion, the problem is simplified to that of dealing with only one material. However, in the inhomogeneity problem, the transformation state e^T_{ij} and p^T_{ij} is unknown. In order to solve the problem, further relations must be established between the unknown transformation state

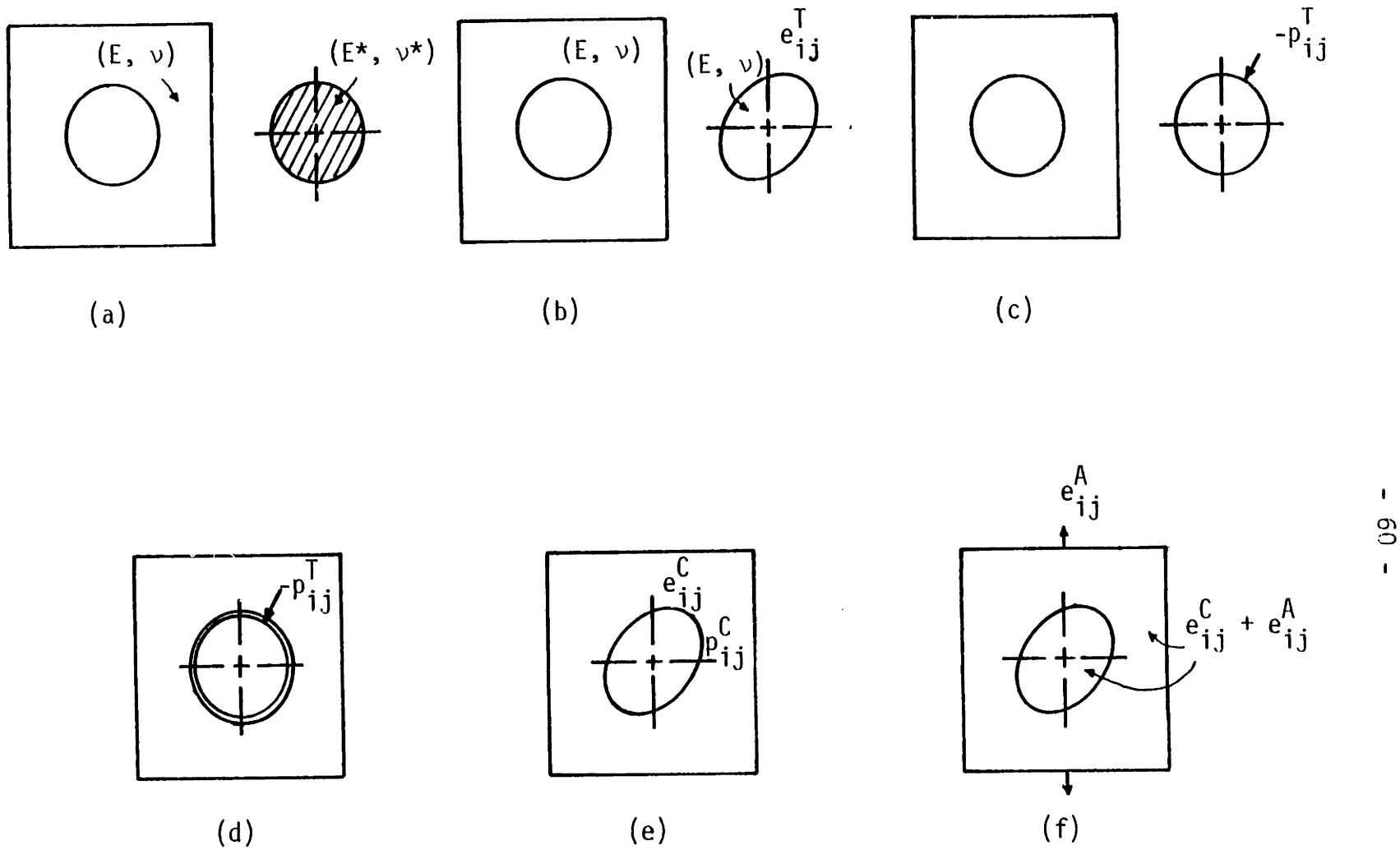

Figure III-7 Eshelby's approach to the inhomogeneity problem.

and that of the known applied field, e^A_{ij} or p^A_{ij}. This relationship is derived in section (2) of Appendix A. For the special case of a spherical inhomogeneity, the relation is expressed explicitly as,

$$\begin{aligned} e^T &= Ce^A \\ {}'e^T_{ij} &= D'e^A_{ij} \end{aligned} \qquad \text{(III-6)}$$

Where:

$$\begin{aligned} C &= \frac{B - B^*}{\alpha(B^* - B) + B} \\ D &= \frac{\mu - \mu^*}{\beta(\mu^* - \mu) + \mu} \end{aligned} \qquad \text{(III-7)}$$

B and μ are the bulk modulus and the shear modulus respectively. The final constrained state e^C_{ij} and p^C_{ij} can be related to the known applied field e^A_{ij} or p^A_{ij} by combining equations III-4 and III-6.

(2) ELASTIC STATE BEFORE VOID NUCLEATION

From the model described above, the strain in both the inclusion and the matrix is found to be e^C_{ij}. The stresses in the matrix are related to the strain by,

$$\begin{aligned} p^M &= 3Be^C \\ {}'p^M_{ij} &= 2\mu'e^C_{ij} \end{aligned} \qquad \text{(III-8)}$$

or

$$p^M_{ij} = \lambda e^C \delta_{ij} + 2\mu e^C_{ij}$$

However, in determining the stresses in the inclusion, it should be noticed that the transformation strain e^T_{ij} is obtained through a stress-free process. The inclusion is later restored to its original shape by applying a surface traction $-p^T_{ij}$ before it is inserted back into the cavity. Therefore, the stresses in the inclusion are,

$$p^I = p^C - p^T$$

$$'p^I_{ij} = 'p^C_{ij} - 'p^T_{ij} \qquad \text{(III-9)}$$

or

$$p^I_{ij} = \lambda(e^C - e^T)\delta_{ij} + 2\mu(e^C_{ij} - e^T_{ij})$$

The strain energy in the inclusion can be found from the stress p^I_{ij} and the strain associated with p^I_{ij} by Hook's law, i.e., $(e^C_{ij} - e^T_{ij})$. Therefore, the strain energy in the inclusion is,

$$E^I = \frac{1}{2}\int_V p^I_{ij}(e^C_{ij} - e^T_{ij})dv \qquad \text{(III-10)}$$

The integral is taken over the volume of the inclusion. As for the matrix, it can be considered to be subjected to a surface traction p^C_{ij} at the matrix-inclusion interface. Therefore, the strain energy in the matrix is,

However, in determining the stresses in the inclusion, it should be noticed that the transformation strain e^T_{ij} is obtained through a stress-free process. The inclusion is later restored to its original shape by applying a surface traction $-p^T_{ij}$ before it is inserted back into the cavity. Therefore, the stresses in the inclusion are,

$$p^I = p^C - p^T$$

$$'p^I_{ij} = 'p^C_{ij} - 'p^T_{ij} \qquad \text{(III-9)}$$

or

$$p^I_{ij} = \lambda(e^C - e^T)\delta_{ij} + 2\mu(e^C_{ij} - e^T_{ij})$$

The strain energy in the inclusion can be found from the stress p^I_{ij} and the strain associated with p^I_{ij} by Hook's law, i.e., $(e^C_{ij} - e^T_{ij})$. Therefore, the strain energy in the inclusion is,

$$E^I = \frac{1}{2}\int_V p^I_{ij}(e^C_{ij} - e^T_{ij})dv \qquad \text{(III-10)}$$

The integral is taken over the volume of the inclusion. As for the matrix, it can be considered to be subjected to a surface traction p^C_{ij} at the matrix-inclusion interface. Therefore, the strain energy in the matrix is,

$$E^M = -\frac{1}{2}\int_S p_{ij}^C u_i^C dS_j \qquad \text{(III-11)}$$

The surface integral is taken over the entire matrix-inclusion interface S. The minus sign appears because the surface normal is in the opposite direction as defined (positive when oriented outward from the surface of the inclusion). Because the surface traction is continuous across the interface, equation III-11 can be replaced by,

$$E^M = -\frac{1}{2}\int_S p_{ij}^I u_i^C dS_j \qquad \text{(III-12)}$$

By applying Gauss' theorem to transform the surface integral to a volume integral enclosed by S, which is also the volume of the inclusion, the strain energy in the matrix is found to be,

$$E^M = -\frac{1}{2}\int_V p_{ij}^I e_{ij}^C dv \qquad \text{(III-13)}$$

Combining equations III-10 and III-13, the total strain energy of the system is,

$$\begin{aligned} E^S &= E^I + E^M \\ &= \frac{1}{2}\int_V p_{ij}^I (e_{ij}^C - e_{ij}^T)\, dv - \frac{1}{2}\int_V p_{ij}^I e_{ij}^C dv \qquad \text{(III-14)} \\ &= -\frac{1}{2}\int_V p_{ij}^I e_{ij}^T dv \end{aligned}$$

It should be noticed that this result requires no knowledge of the elastic state in the surrounding matrix. Only the stress in the inclusion and the transformation state must be known.

In the inhomogeneity problem, an external field is applied to the system. This applied field must be superimposed on the constrained field in both the matrix and the inclusion. Therefore, the strain in both the matrix and the inclusion is $(e^C_{ij} + e^A_{ij})$. The stresses in the matrix are,

$$p^M = 3B\,(e^C + e^A)$$

$$'p^M_{ij} = 2\mu('e^C_{ij} + 'e^A_{ij}) \qquad \text{(III-15)}$$

or

$$p^M_{ij} = \lambda(e^C + e^A)\delta_{ij} + 2\mu(e^C_{ij} + e^A_{ij})$$

The stresses in the inhomogeneity are,

$$p^I = p^C + p^A - p^T$$

$$'p^I_{ij} = 'p^C_{ij} + 'p^A_{ij} - 'p^T_{ij} \qquad \text{(III-16)}$$

or

$$p^I_{ij} = \lambda(e^C + e^A - e^T)\delta_{ij} + 2\mu(e^C_{ij} + e^A_{ij} - e^T_{ij})$$

The total strain energy has exactly the same general form as that of the inclusion problem (equation III-14),

$$E^S = -\frac{1}{2}\int_V p_{ij}^I e_{ij}^T dv \qquad \text{(III-17)}$$

but the p_{ij}^I here will be that of equation III-16 instead of the p_{ij}^I in equation III-9.

One important result obtained from both the classical method [55-59] and the Eshelby's approach [60,61] is the following. For an ellipsoidal inclusion, if the distance applied field is uniform, the elastic field in the ellipsoidal inclusion is also uniform. This finding greatly simplifies both the evaluation of the above equations, and the determination of the elastic state after void nucleation occurs.

(3) ELASTIC STATE AFTER VOID NUCLEATION

Once a microvoid nucleates around an inclusion or inhomogeneity, the elastic field in the system will be different from that which was present prior to the void nucleation. If cavitation occurs at some location on the matrix-inclusion interface, the normal stress on the cavitated surface should be zero. This is the condition that has to be satisfied for finding the cavitated state. Tanaka, Mori and Nakamura [62] addressed this problem by changing the elastic constant of the inclusion in the cavitated direction to zero to evaluate the elastic state after cavitation. Although this approach satisfies the required boundary condition, we consider it to be physically unrealistic. Before presenting our analysis, we will first define a problem to illustrate our approach. For the case of uniaxial tension applied in the 11 direction to a hard inclusion filled material,

the analysis of stress concentration in Appendix A shows that high radial stress concentrations at the matrix-inclusion interface is confined in a narrow region of ± 15° at the 11 poles. We will simply assume that caviatation will first occur at the 11poles. Thus, the condition to be satisfied is that normal stress at the 11 pole interfaces should be zero.

The first step of our approach is to determine the inclusion stress p^I_{ij} at the 11 pole just prior to cavitation when responding to an applied field e^A_{ij} or p^A_{ij}. This result is described in the previous section. The next step is to suggest that the cavitation process can be represented by some kind of inclusion transformation process. The effect of this cavitation transformation (denoted by the superscript T' and C') is to produce a normal stress in the 11 direction. This normal stress will cancel the p^I_{ij} developed before cavitation. Stresses in the inclusion after this cavitation transformation will be,

$$\begin{aligned} p^{I_o}_{ij} &= (p^C_{ij} + p^A_{ij} - p^T_{ij}) + (p^{C'}_{ij} - p^{T'}_{ij}) \\ &= p^I_{ij} + (p^{C'}_{ij} - p^{T'}_{ij}) \end{aligned} \qquad \text{(III-18)}$$

The first term on the right hand side is the inclusion stress before cavitation. The second term is the contribution of the cavitation transformation. Expressed in scalar and deviatoric components,

$$p^{I_o} = p^I + (p^{C'} - p^{T'})$$

$$'p^{I_o}_{ij} = 'p^I_{ij} + ('p^C_{ij} - 'p^T_{ij}) \qquad \text{(III-19)}$$

For our special case of a spherical inclusion, application of equation III-4 results in,

$$p^{I_o} = p^I + (\alpha - 1)p^{T'}$$

$$'p^{I_o}_{ij} = 'p^I_{ij} + (\beta - 1)'p^{T'}_{ij} \qquad \text{(III-20)}$$

Because the elastic state inside the inclusion is uniform, the normal stresses at the 11 poles $(p^{I_o}_{11})_{11 \text{ pole}}$ can be determined from the above equations with i = j = 1.

$$p^{I_o}_{11} = 'p^{I_o}_{11} + \frac{1}{3} p^{I_o}$$

$$= 'p^I_{11} + (\beta - 1)'p^{T'}_{11} + \frac{1}{3} p^I + \frac{(\alpha - 1)}{3} p^{T'}$$

$$= p^I_{11} + (\beta - 1)'p^{T'}_{11} + \frac{(\alpha - 1)}{3} p^{T'} \qquad \text{(III-21)}$$

For cavitation at the 11 poles, $(p^{I_o}_{11})_{11 \text{ pole}} = 0$. Therefore,

$$\frac{(\alpha - 1)}{3} p^{T'} + (\beta - 1)'p^{T'}_{11} = -p^T_{11} \qquad \text{(III-22)}$$

The cavitation transformation process is performed to cancel only the normal stress p^I_{11} at the 11 pole. This requires that $p^{T'}_{11} \neq 0$. All other $p^{T'}_{ij}$ are assumed to be zero. Thus, equation III-22 becomes,

$$\frac{(\alpha - 1)}{3} p^{T'}_{11} + (\beta - 1)\left(p^{T'}_{11} - \frac{1}{3} p^{T'}_{11}\right) = -p^I_{11}$$

i.e.,

$$p_{11}^{T'} = \frac{-3}{[(\alpha - 1) + 2(\beta - 1)]} p_{11}^{I} \qquad \text{(III-23)}$$

$p_{11}^{T'}$ is the cavitation transformation stress required to satisfy the cavitation condition, and is expressed here in terms of the inclusion stress before cavitation p_{11}^{I}, which has already been evaluated.

After $p_{11}^{T'}$ is found, the elastic state associated with the cavitation transformation can be evaluated in the same manner as described in the inclusion problem. Superposition of this elastic state with the one present before cavitation results in the elastic state of the system after the cavitation process.

The same procedure can be applied to soft inclusions, and to inclusion shapes other than spheres. The process involves the determination of the maximum stress concentration site on the interface, evaluate the normal stress at that location, and apply the above analysis. The resulting cavitation transformation stress $p_{ij}^{T'}$ will have a more complex form than the one derived in our simple example.

E. CRITERIA FOR MICROVOID NUCLEATION

(1) STRENGTH CRITERION

The microvoid nucleation process involves the separation of materials. In the inclusion filled material, the separation will take place at the matrix-inclusion interface if the bonding is weak. If strong bonding exists, the separation may take place in either the matrix or the inclu-

sion, whichever is the weaker material. At the atomistic level, the initiation of the separation process can be viewed as a process of overcoming the short-range attractive forces between adjacent atoms or molecules. Such attractive force are know as the cohesive or adhesive strength. One criterion for void nucleation is that the local stresses reaches the level of the cohesive strength of the material. This is generally referred to as the strength criterion. Geometrically speaking, the creation of voids involves the normal displacement of the separated surfaces. It is very unlikely that the initial separation will be that of creating an equial-axial cavity. Therefore, it is usually appropriate to examine only one of the maximum principle normal stress in tension $(\sigma_{kk})_{max}$ and compare it to the ideal cohesive strength τ_i. The strength criterion for void nucleation can be stated as,

$$(\sigma_{kk})_{max} \geq \tau_i \qquad \text{(III-24)}$$

The stress criterion is strictly a local criterion. When applied to an inclusion filled material, the criterion itself bears no relationship to the size or shape of the inclusion. The shape of the inclusion will have to be considered in order to find the location of $(\sigma_{kk})_{max}$ and the magnitude of the applied stress $(\sigma_{ij})_A$ to produce this $(\sigma_{kk})_{max}$. However, the analysis is still independent of the inclusion size.

In an inclusion filled material, the maximum tensile stress is usually the normal stress at some location on the matrix-inclusion interface. The location and magnitude of the stress concentration can be obtained from continuum mechanics analyses. The elastic solutions for the stress

concentration on a spherical inclusion under uniaxial tension and pure shear are shown in figures A-3 and A-4 in Appendix A. Once the stress concentration factor K is found, the stress criterion can be expressed in terms of the applied stresses,

$$(\sigma_{ij})_A \geq \frac{1}{K} \tau_i \qquad \text{(III-25)}$$

Materials may demonstrate plastic or anelastic behavior once the yield strength is exceeded. In the simple case of an elastic-perfectly plastic material, the maximum stress concentration is limited by the flow stress of the material $Y(\bar{e}^p)$.

The interfacial stress concentration in a rigid cylinderical inclusion filled elastic-plastic material were studied by Huang [63] as well as by Orr and Brown [64]. Their studies also include materials with different strain-hardening characteristics. Rhee and McClintock [65] show that for strain-hardening materials, the strain concentration around several different geometric shapes in an inhomogeneous deformation fields are generally bounded by two limiting idealization of the plastic behavior of the material: a nonhardening rigid-plastic behavior and a linear hardening behavior with zero yield stress. Argon [66, 67] summarized these different studies along with his own analysis. He concluded that the interfacial stress σ_{rr} at the surface of a cylinderical inclusion after yielding is bounded by,

$$\frac{3}{2} k \leq \sigma_{rr} - \sigma_T \leq 2k \qquad \text{(III-26)}$$

Where k is the flow stress in shear and σ_T is the hydrostatic tensile component of the applied stress if the distance field is not pure shear. These limits are very close to each other, and can be approximated by the flow stress in tension $Y(\bar{e}^p)$. Therefore, the interfacial radial stress on the cylindrical inclusion can be taken as,

$$\sigma_{rr} \approx Y(\bar{e}^p) + \sigma_T \qquad \text{(III-27)}$$

Argon [66] also discussed the interfacial stress problem using a punched out cylinder to simulate the dislocation relaxation mechanism. Effects of inclusion concentration on particle interactions were also discussed in the same paper.

Examining the normal separation of materials at the atomistic or molecular level, the severance of bonds between atoms or molecules should be purely elastic. It should not be affected by the plastic relaxation processes such as the macroscopic plastic flow or the microscopic dislocation motions. These plastic relaxation processes play the role of relaxing the stresses in the distant stress field and limiting them to the level of the flow stress of the material. Based on the above arguments, a simple model can be constructed to describe the process of the normal separation of bonds between atoms or molecules as illustrated in figure III-8. Plastic relaxation is excluded from the near field around the separating atoms or molecules. The near field itself is considered to be purely elastic. Thus, from the free body diagram shown, the stresses transmitted to the near field are regulated by the elastic or inelastic response of the distant field to the applied load $(\sigma_{ij})_A$. When the

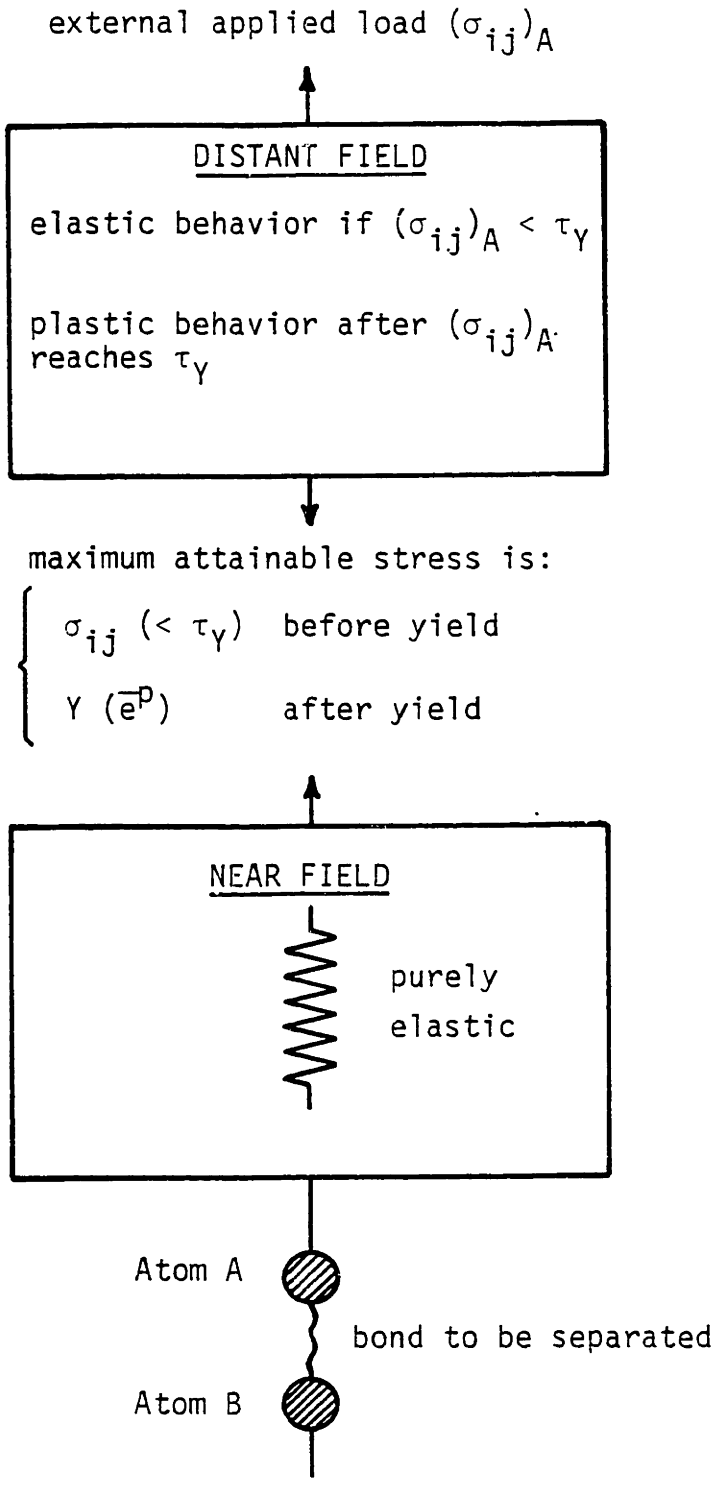

Figure III-8 Model of the separation of bonds between atoms and molecules.

applied load $(\sigma_{ij})_A$ is less than the yield strength, the stress transmitted to the near field is $(\sigma_{ij})_A$. When $(\sigma_{ij})_A$ exceeds the yield strength, the stress transmitted will be the flow stress $Y(\bar{e}^p)$ of the material. The stress at the separating bond will be the same as that of the near field unless it is further amplified by a stress concentration factor K due to any geometric conditions which may exist between the boundary of the near field and the separating bond. Therefore,

$$\text{before yield:} \quad (\sigma_{ij})_A \leq (\sigma_{kk})_{\substack{\text{separating} \\ \text{bond}}} \leq K(\sigma_{ij})_A$$

$$\text{after yield:} \quad Y(\bar{e}^p) \leq (\sigma_{kk})_{\substack{\text{separating} \\ \text{bond}}} \leq KY(\bar{e}^p) \qquad \text{(III-28)}$$

Comparing this with the cohesive strength τ_i, the strength criterion can be stated as:

$$\text{before yield:} \quad (\sigma_{ij})_A \geq \frac{1}{K}\tau_i$$

$$\text{after yield:} \quad Y(\bar{e}^p) \geq \frac{1}{K}\tau_i \qquad \text{(III-29)}$$

This simple model bears some resemblance to the ones commonly used to deal with dislocation problems. In those problems, the near field of the dislocation is usually treated as elastic, and inelastic behavior of the material is used as boundary conditions to the near field.

Theoretical studies and models on the ideal cohesive strength τ_i of

materials can be found in references [68-72]. In the Orowan model [68], the ideal strength is expressed as,

$$\tau_i = \left(\frac{E\gamma}{a_o}\right)^{1/2} \qquad \text{(III-30)}$$

Where:

a_o = equilibrium atomic spacing

γ = surface energy

E = tensile modulus

The ideal cohesive strength of the material is shown to be proportional to the square root of the modulus of the material from the above expression. Experimentally, it is found that for most materials [71, 72],

$$\tau_i \approx \frac{1}{10} \text{ to } \frac{1}{20} E \qquad \text{(III-31)}$$

(2) ENERGY CRITERION

Another aspect of the void nucleation process that has to be considered is the energetics involved in the process. When the inclusion filled material is subjected to an external load, strain energy is stored in the elastic field within and around the inclusion. This strain energy will change as the elastic field changes during void nucleation. The energetics of this process require that the change in strain energy in the matrix-inclusion system should be sufficient to provide for the new surface energy created by the void nucleation process. This is expressed as,

$$(E^S)_{before} - (E^S)_{after} \geq \Delta\gamma \cdot A \qquad \text{(III-32)}$$

A is the surface area of the nucleated void and, $\Delta\gamma$ is the surface energy change during void nucleation. If the void nucleates at the matrix-inclusion interface,

$$\Delta\gamma = \gamma_{M-I} - (\gamma_M + \gamma_I)$$

where γ_M, γ_I are the surface energies of the matrix and the inclusion respectively, and γ_{M-I} is the interfacial energy of the matrix and the inclusion. γ_{M-I} can be estimated by the Dupre equation as a first order approximation,

$$\gamma_{M-I} \approx |\gamma_M - \gamma_I| \qquad \text{(III-33)}$$

The strain energies before and after void nucleation were derived in the previous section (equations III-14 and III-17). These equations indicate that the strain energy change is associated with the volume of the system. The final form of the strain energy is expressed as an integration over the volume of the inclusion. This volume is proportional to the cube of the inclusion size. The surface energy change is associated with the area A of the nucleated void, which is proportional to the square of the inclusion size. It is apparent that the energy criterion for void nucleation (equation III-32) is inclusion size dependent.

Figure III-9 shows schematically both the strength and the energy

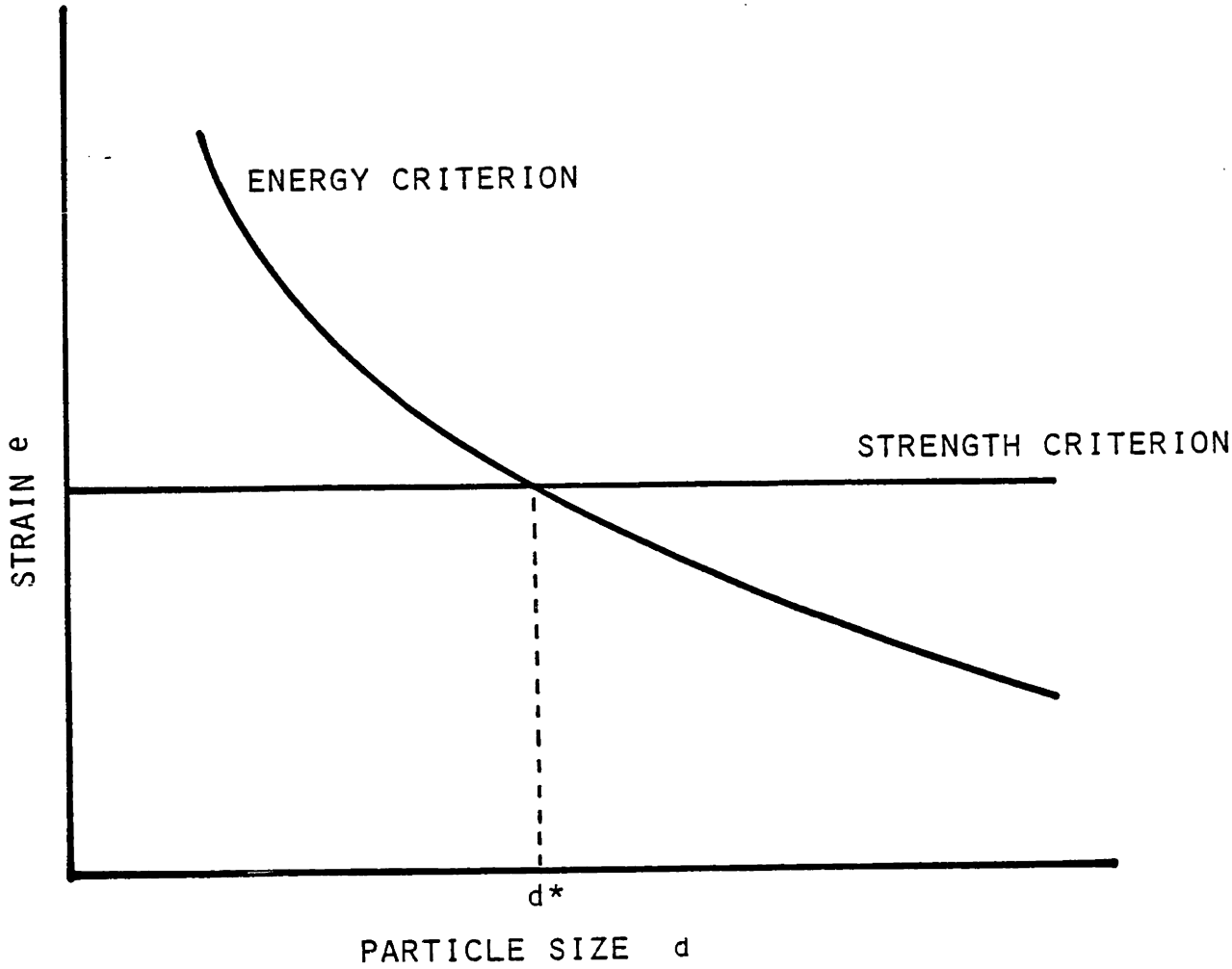

Figure III-9 Schematics of the energy and stress criterion for void nucleation

criteria expressed in units of applied elastic strain as a function of the inclusion size. For inclusion sizes larger than d*, the energy criterion is always satisfied whenever the strength criterion is reached. However, for inclusion sizes smaller than d*, satisfying the strength criterion does not necessarily guarantee the satisfaction of the energy requirement. Therefore, it may be argued that void nucleation will not be an energetically favorable process in this range of inclusion sizes.

The energy and the strength criteria are only necessary conditions for void nucleation. Neither of them has been proved to be a sufficient condition for voids to nucleate. The purpose of this study is to investigate the validity of the inclusion size dependency of the energy criterion. The experimental investigation is presented in Chapter IV. If the inclusion size dependent energy criterion is found to be valid, attempts will be made to exploit this fact by replacing the particulate fillers in a material where void nucleation is the major cause for failure with smaller particle size fillers. In figure III-10, the strength and the energy criteria are plotted using properties of typical glassy polymers and inorganic filler. Elastic propteries of some polymers and silica filler are shown in Table III-1. The filler particle shape is assumed to be spherical. The critical particle size d* is found to be in the order of 0.3 micron (3000 Å). Appendix D describes a method of preparing particulate dispersions of this dimension or smaller in a polymeric matrix material. Wear studies were conducted on these materials as well as on materials with large particle size fillers. The purpose of these tests is to determine if void nucleation contributes to the wear of such materials and to see if it can be remedied by the reduc-

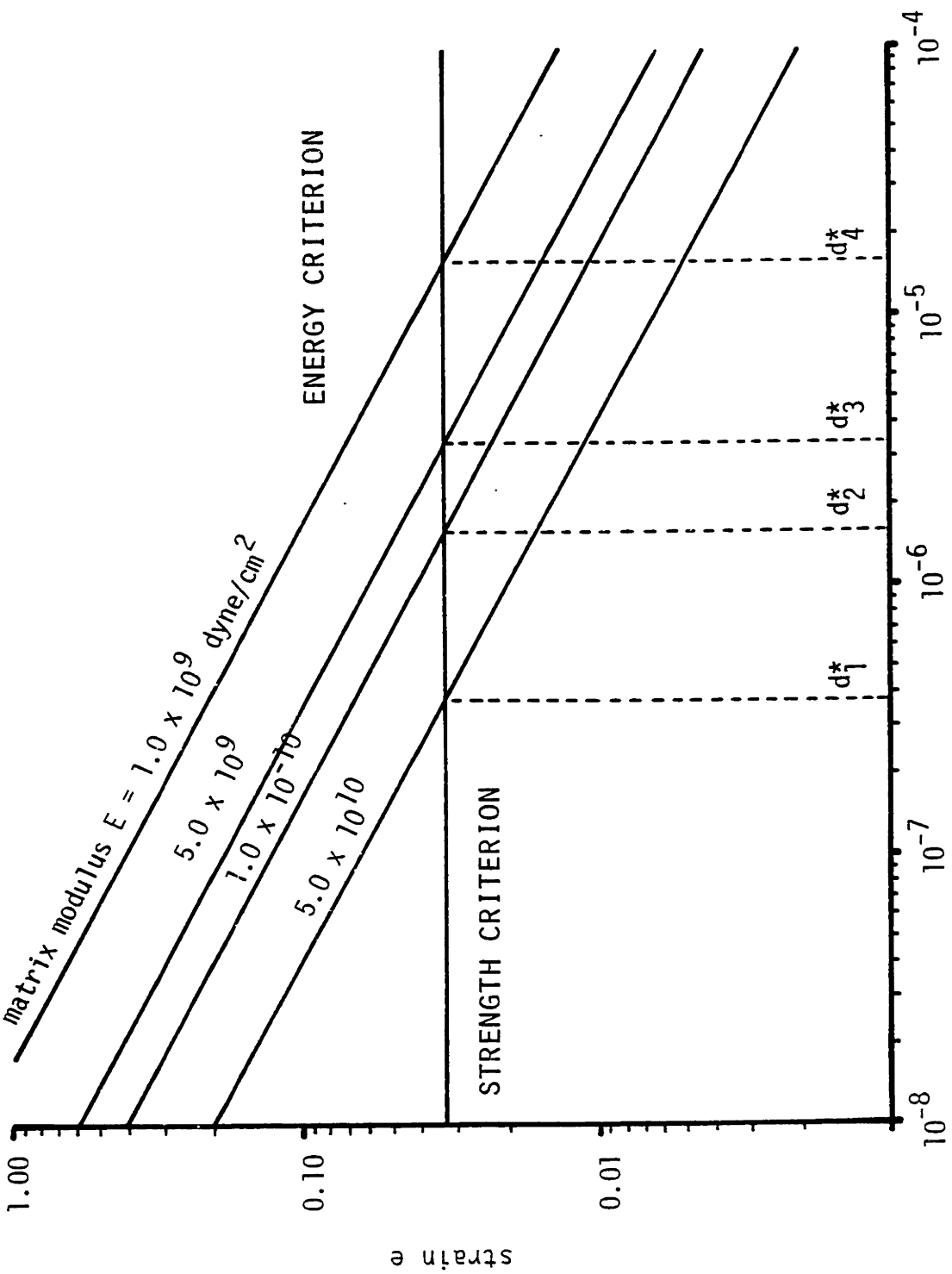

Figure III-10 Energy and stress criterion for void nucleation in polymers with different modulus.

	Tensile Modulus E	
	10^5 psi	10^{10} dyne/cm^2
PMMA	3.8 - 4.5	2.6 - 3.1
Epoxy	3.5 - 5.0	2.4 - 3.4
Polycarbonate	3.7 - 3.8	2.5 - 2.6
Polyester (thermosetting)	3.0 - 6.4	2.1 - 4.4
Polystyrene	3.2 - 4.6	2.2 - 3.2
Silica	110	70

	Poisson's Ratio
Polymers	0.33
Silica	0.14

	Surface Energy (erg/cm^2)
Polymers	400*
Silica	300

*Estimated from the breaking of C-C bonds, not from surface tension measurements.

Table III-1 Properties of some polymers and silica filler used in the calculation of energy criterion for void nucleation.

tion of the particle size of the filler material. Results from the wear investigation are given in Chapter V.

IV. EXPERIMENTAL INVESTIGATION OF THE VOID NUCLEATION PROCESS

The energy and strength criteria for microvoid nucleation around inclusions in a material were discussed in Chapter III. It was found that for a typical glassy polymer and inorganic filler system, the critical particle size below which the energy criterion may not be satisfied even if the strength criterion is exceeded, is below that of 3000 Å. The analysis also indicates that the further the particle size decreases below this critical dimension, the more difficult it is to satisfy the energy criterion. In Appendix E, methods for dispersing fumed silica with primary aggregate size in the range of 500 to 1000 Å in an epoxy resin were described. It is very difficult to experimentally verify the energy criterion for void nucleation in materials containing very small particles. In this chapter, a method for verifying the particle size dependent energy criterion using a large scale model is described.

In Chapter III, the analyses of the inclusion and inhomogeneity problem show that the strain energy density stored in a material is related to the modulus of the material. For the same amount of applied strain, the strain energy density is lower for materials with lower stiffness. Therefore, a larger volume of material is required to provide for the surface energy created in the cavitation process. Since the cavitation process takes place around the inclusions, a larger inclusion will be needed for void nucleation in low modulus materials. Therefore, if the modulus of the epoxy matrix material can be reduced significantly, we will be able to simulate the void nucleation process using a large inclusion in the size range that can be easily investigated with simple microscopy

techniques.

The model system used in this investigation was a glass bead filled epoxy. The epoxy material is the same as the one used in the fine particulate dispersion experiment described in Appendix E. Glass beads of three different particle sizes, 20, 50 and 100 μm in diameter, are obtained from Cataphote Division, Ferro Corporation. Initially, 10% by weight of the glass beads were mixed in the resin. However, the concentration of the glass beads in the final cast samples is much lower than the initial 10%, due to particle settling during the curing process.

In order to observe void nucleation in this glass bead filled model material, the stiffness of the matrix is reduced by testing the material at an elevated temperature. The modulus-temperature relation of the epoxy material is shown in figure IV -1. With this information, the energy and stress criteria for different matrix stiffiness (as a function of test temperature) are recalculated and shown in figure IV -2.

A. DETERMINATION OF THE CRACK ARREST TEMPERATURE

Before a multiple number of voids can nucleate in the material, crack propagation may intervene with the stable void nucleation process. A crack can propagate from a previously formed microvoid or microcrack, or, from any pre-existing flaw in the material. The prevention of crack propagation is dependent on the material's ability to deform plastically so as to blunt the crack front and relieve the stresses at the crack tip. In order to observe evidence of void nucleation, it is necessary to test the material to a strain where stable void nucleation occurs before the material fails by crack propagation. This can be done by conducting tests

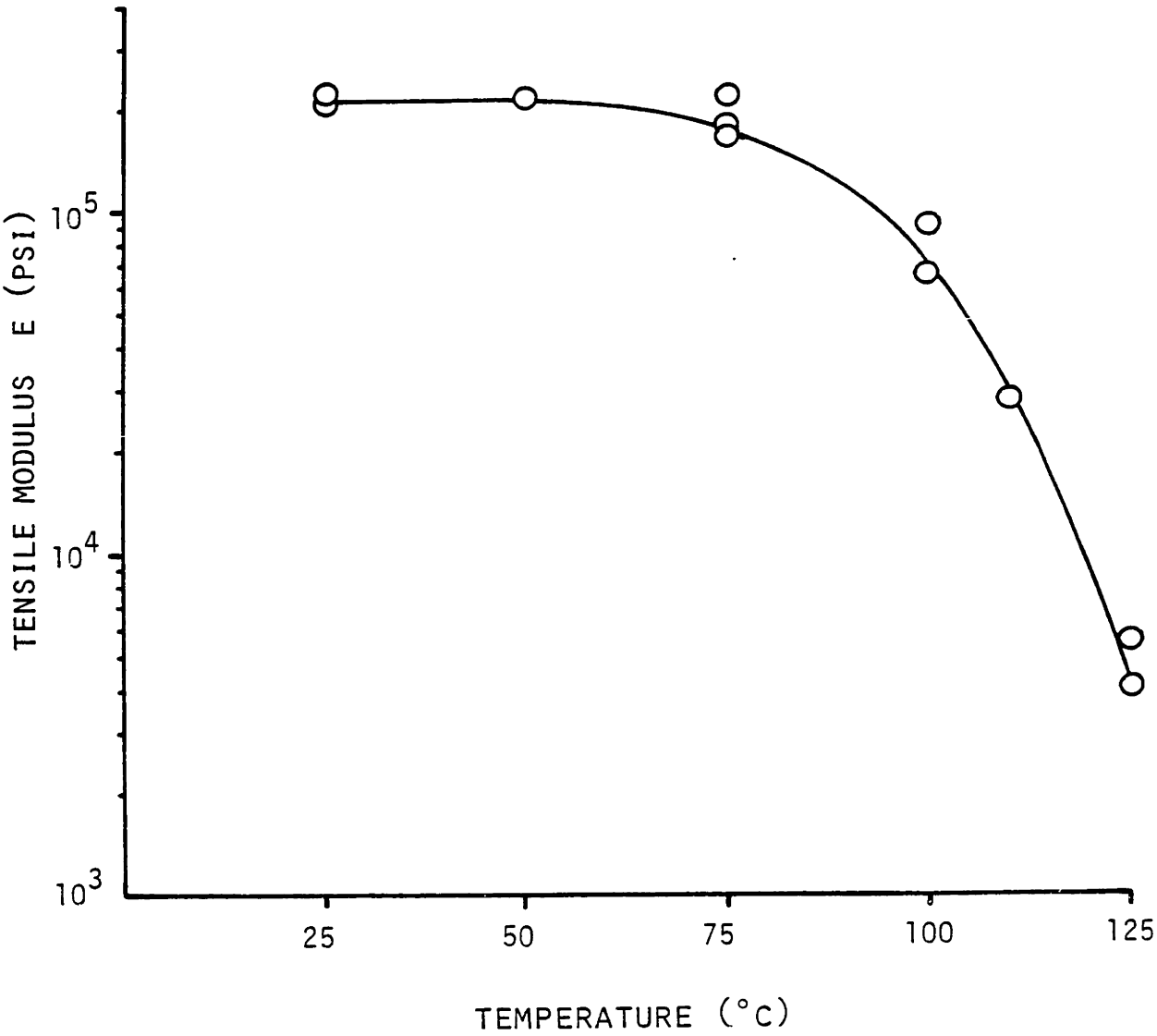

Figure IV-1 Tensile modulus of epoxy at different temperatures.

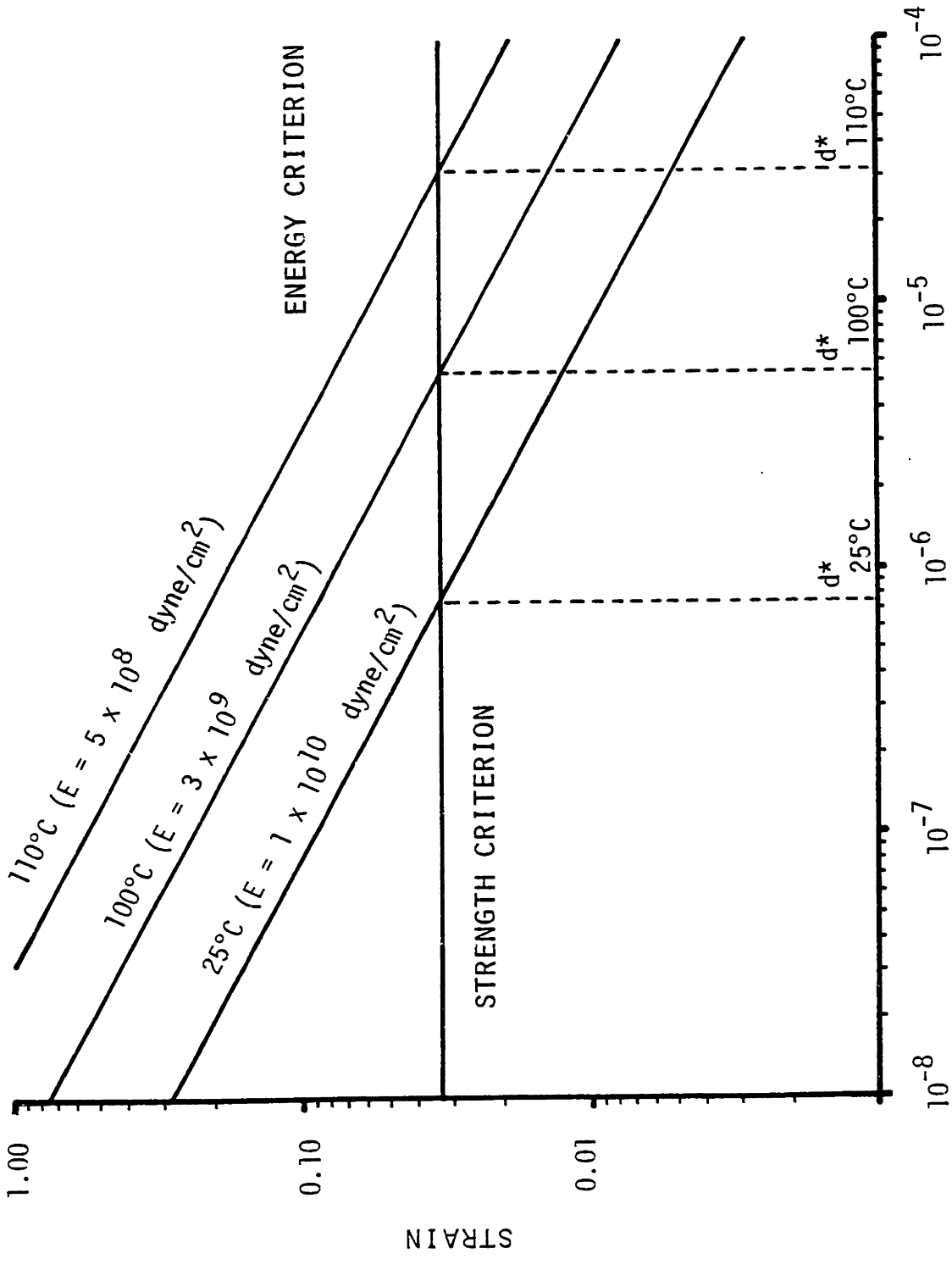

Figure IV -2 Energy and strength criterion for void nulceation in epoxy at different temperature.

at temperatures above the crack arrest temperature of the material. Crack arrest temperature can be determined by conduting a series of uniaxial tensile tests at increasing test temperatures above ambient. The lowest temperature at which stable void nucleation can be detected is the crack arrest temperature. In our experiment, all samples were tested to failure at a strain rate of 0.1 inch/min, and then sectioned in directions transverse ($\perp$) and parallel (//) to the tensile axis. These sectioned samples were then polished and examined under an optical microscope. Shiny rings such as those shown in figure IV-3 were found on the transverse sections of samples tested at temperature above 95°C. By adjusting the focal distance of the objective lens on the microscope, it was found that these rings existed beneath the polished surface of the transparent epoxy. No rings were found on the parallel section of any sample tested at any temperature. From figure IV -4 and referring to the stress concentration analysis in Appendix A, these microscophy findings can be interpreted as follows. Cavitation around the glass beads begins at locations near the two poles in the tensile direction. Therefore, when examining transverse sections with incident light, the cavitated poles serve as reflecting planes for light that penetrates into the material. This causes the cavitated poles to appear as rings in the micrographs. On the parallel sections, the cavitated surface will appear as lines, since lines do not reflect light as well as planes, they are not observed on the micrographs. Optical micrographs of the polished cross section of samples tested at different temperatures and scanning electron micrographs on the fractured surface of these samples are documented in Appendix B. Evidence of void nucleation as well as growth were found on the SEM fractographs at tem-

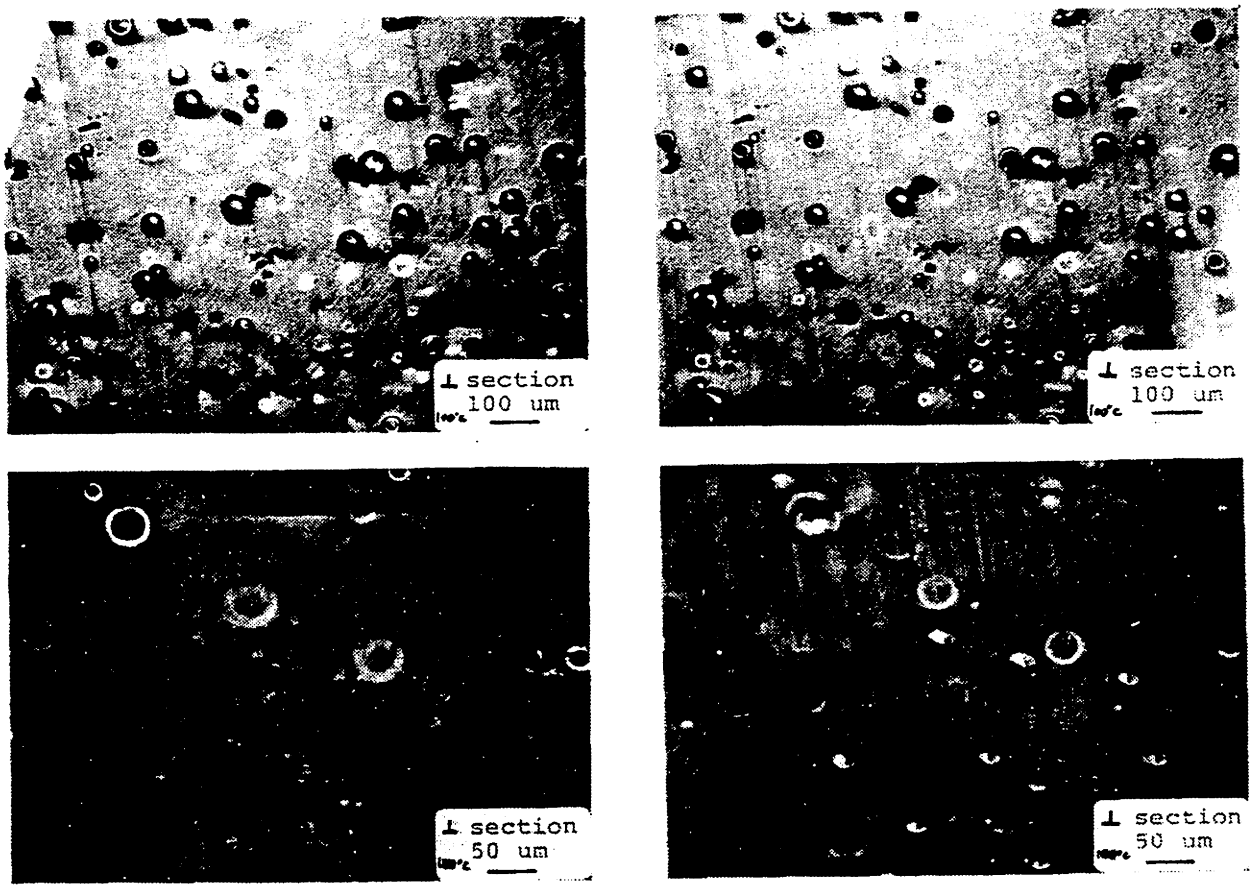

L: focus on polished surface R: focus beneath polished surface

Figure IV-3 Optical micrograph of polished transverse (⊥) cross section of tensile test sample. Rings indicate cavitation around glass bead fillers in the material.

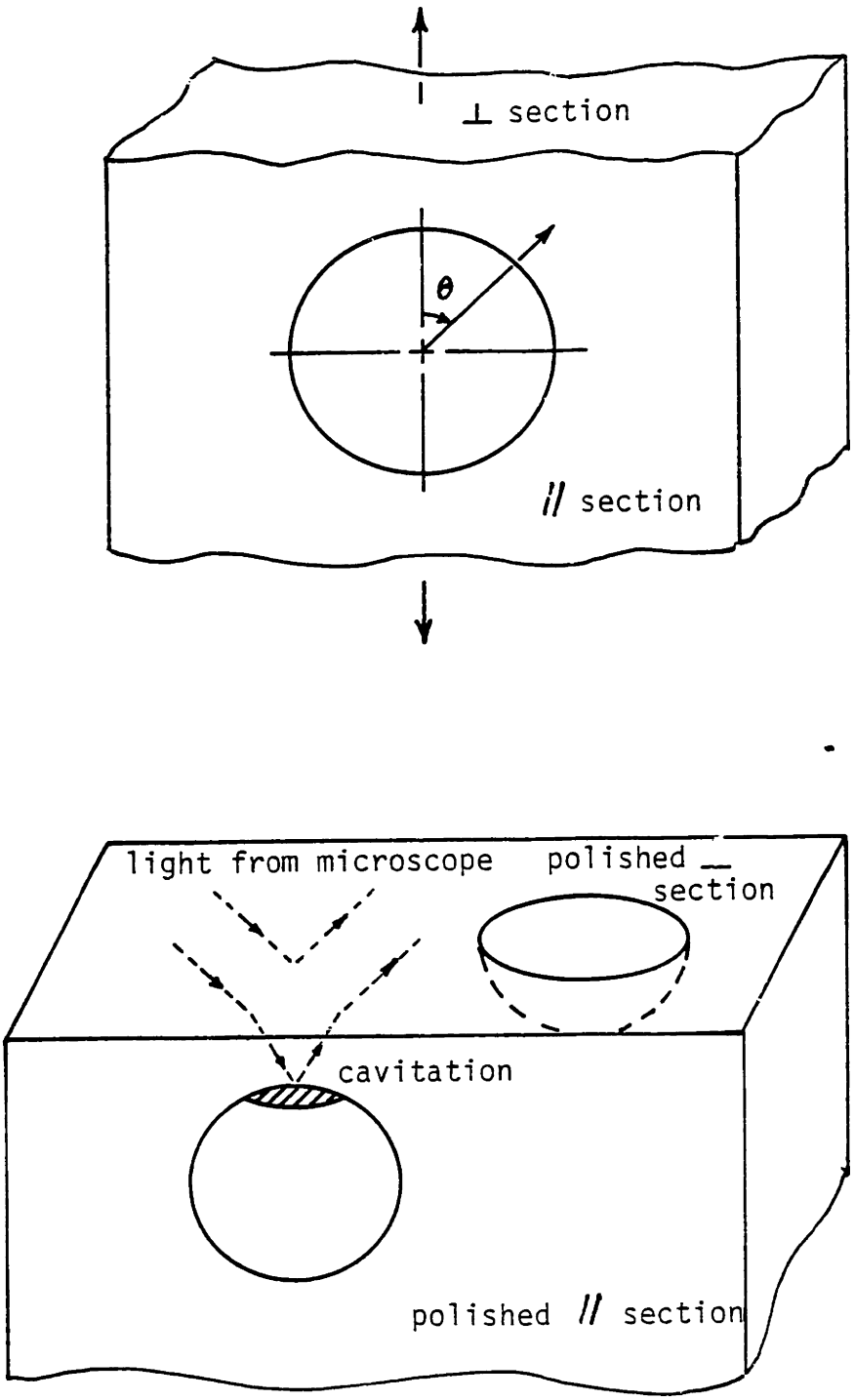

Figure IV -4 Observation of void formation in tensile test samples.

peratures above 100°C. The crack arrest temperature is determined to be about 95°C from this study.

B. VERIFICATION OF THE ENERGY CRITERION

After determining the crack arrest temperature above which stable void nucleation can occur before cleavage fracture, tests were performed by pulling samples to different amounts of strain above this temperature, and observe for evidence of void nucleation. Uniaxial tensile tests were conducted at two temperatures, 100°C and 110°C at a strain rate of 0.1 inch/min. After each test, the sample was sectioned and examined in the same manner as described in the preceding section. In this test, the minimum amount of strain to initiate void nucleation for a particular particle size was determined. This critical strain was determined by comparing the population and the size of the rings found on samples stretched to different magnitudes of strain. Rings generated during the initial stage of the cavitation process should be smaller than those which have already experienced some growth.

Typical load-extension curve for epoxy at 100°C and 110°C are shown in figure IV-5. After yielding, the material continued to deform plastically with some degree of strain hardening. In these tests, the load was released from the sample after the desired amount of total strain e_t was reached. The sample recovered the elastic part of the strain e_e and was left with the plastic strain e_p. In the energy consideration, the strain energy stored in the system is only associated with the elastic strain e_e. The rest of the work done on the system during stretching is dissipated through plastic deformation. Therefore, in estimating the strain

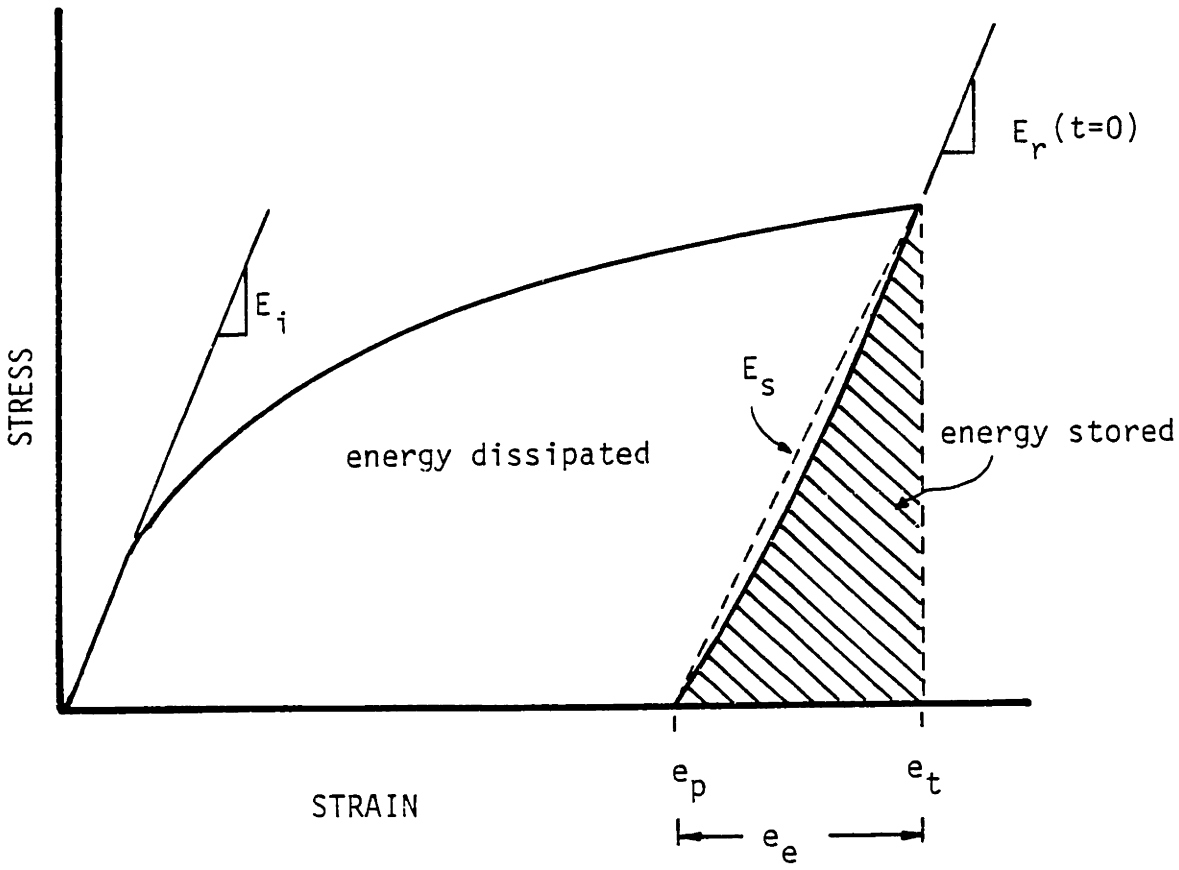

Figure IV -5 Typical stress-strain curve of epoxy above 100°C.

energy before and after the cavitation process, the relaxation modulus E_r (t=0) or the secant modulus E_s should be used in the calculation, whichever gives better approximation to the shaded area in figure VI-5. E_r(t=0) is comparable to the initial modulus unless it is affected by changes in microstructure during elongation.

For materials that deform plastically after yield, the strength criterion for the initiation of material separation is given by equation III-29,

$$KY(\bar{e}^p) \geq \tau_i \qquad (IV-1)$$

The left hand side of the above equation represents the local stress state at the separation site. For an inclusion filled material, where cavitation occurs around the inclusions, it is appropriate to choose the maximum stress concentration factor around the inclusion to be the K factor in the above equation. From Appendix A, the maximum stress concentration near the poles of a rigid inclusion under tension is about 2.3. This value can be lower if the inclusion is elastic. Referring to the elastic-plastic analysis discussed in Section E of ChapterIII, we will assume the local stress state at the poles of the inclusions to be about $2Y(\bar{e}^p)$. Table IV-1 shows the flow stress $Y(\bar{e}^p)$ of the epoxy material at different temperatures. It is shown to be proportional to the modulus over a range of temperatures. The right hand side of equation IV-1 is the ideal strength τ_i of the material, τ_i is also proportional to the modulus of the material as discussed in Chapter II, Section B. Therefore, as the modulus changes with temperature, both the flow stress $Y(\bar{e}^p)$ and the ideal

Temperature	$Y(\bar{e}^p)$ at 6.8% strain (10^3 psi)	Modulus E (10^5 psi)	$Y(\bar{e}^p)_{6.8\%}/E$ (%)
90°C	5.54	1.55	3.56
95°C	4.58	1.44	3.18
100°C	2.70	1.30	2.07
105°C	1.30	0.77	1.70
110°C	0.55	0.45	1.22

Table IV-1 Flow stress and modulus of epoxy at different temperatures.

strength of the material τ_i will change accordingly. If the strength criterion in equation IV -1 is normalized with respect to the modulus of the material, it appears that the stress criterion should be relatively independent of the modulus at different test temperatures,

$$K \left[\frac{Y(\bar{e}^p)}{E} \right] \geq \left[\frac{\tau_i}{E} \right] \qquad (IV-2)$$

From figure IV-5, the term $Y(\bar{e}^p)/E$ is equivalent to the elastic strain e_e. The strength criterion can now be expressed as,

$$e_e \geq \frac{1}{K} \left[\frac{\tau_i}{E} \right] \qquad (IV-3)$$

From Chapter III, Section E, τ_i/E is typically equals to 1/15. This value will be used in our discussion of the strength criterion.

The experimental findings are shown in figure IV -6 through IV-11. In these figures, the recovered elastic strain e_e is plotted against the applied total strain e_t. Data points that are represented by open circles indicate that cavitation is observed for these tests. The minimum strain at which cavitation is observed for the three particle size glass beads at the two test temperatures are plotted in figure IV-12, along with the analytical results of the energy and the stress criterion. The results show that the void nucleation process is inclusion size dependent, which is in agreement with the energy criterion. The discrepancy between the experimental and the analytical results is a constant shift in the log-log

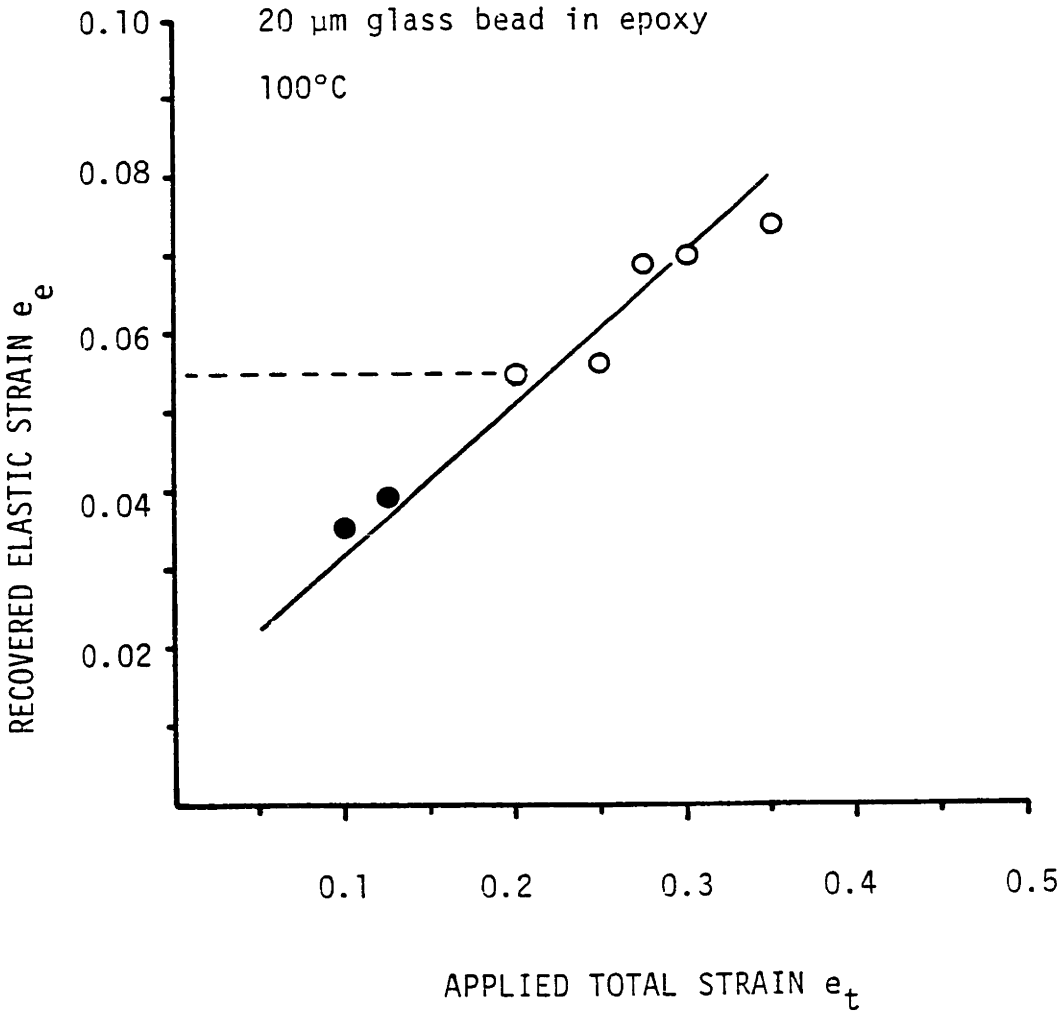

Figure IV -6 Tensile test of 20 μm glass bead filled epoxy at 100°C. Open circle indicates cavitation is observed.

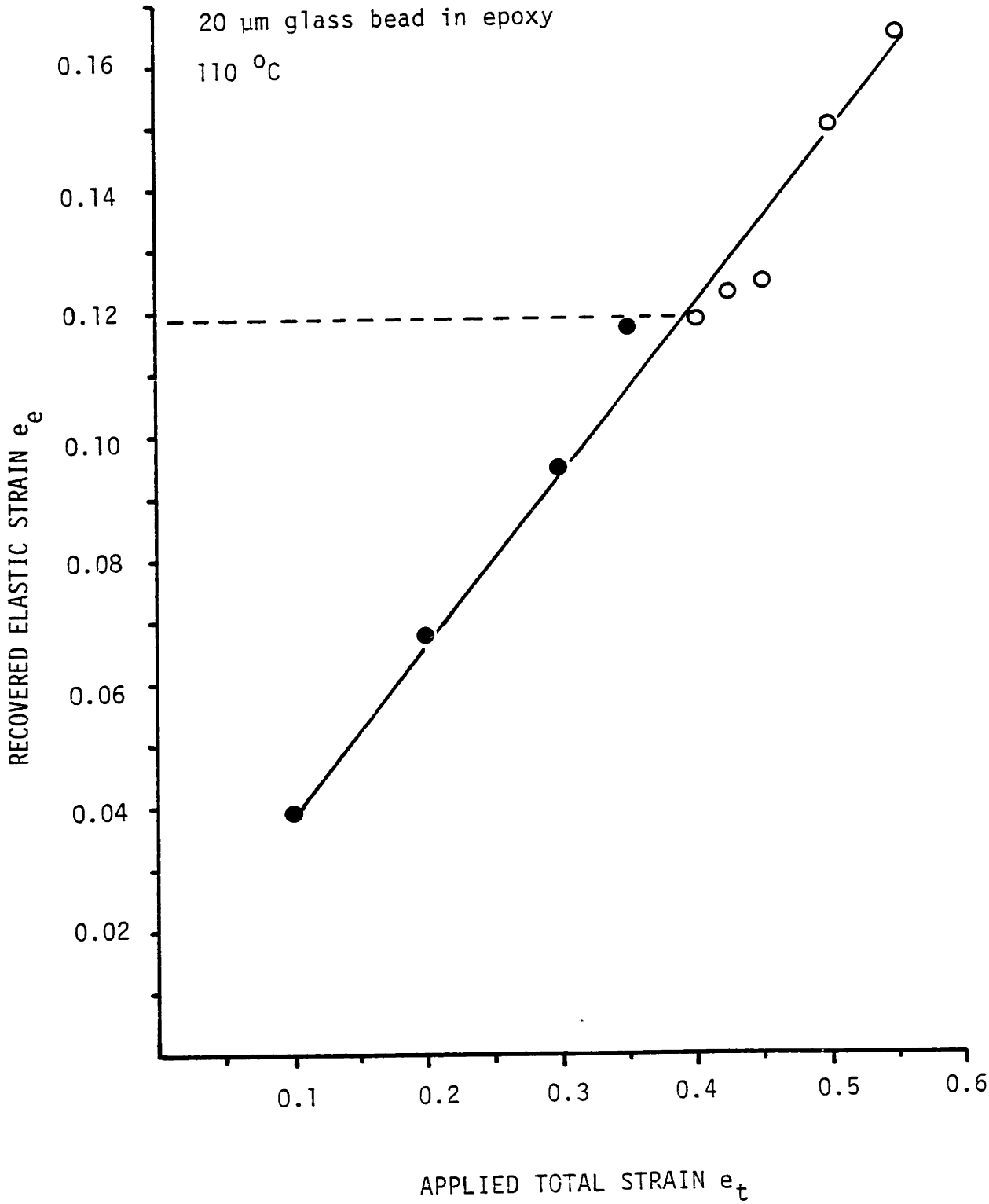

Figure IV-7 Tensile test of 20 μm glass bead filled epoxy at 110°C. Open circle indicates cavitation is observed.

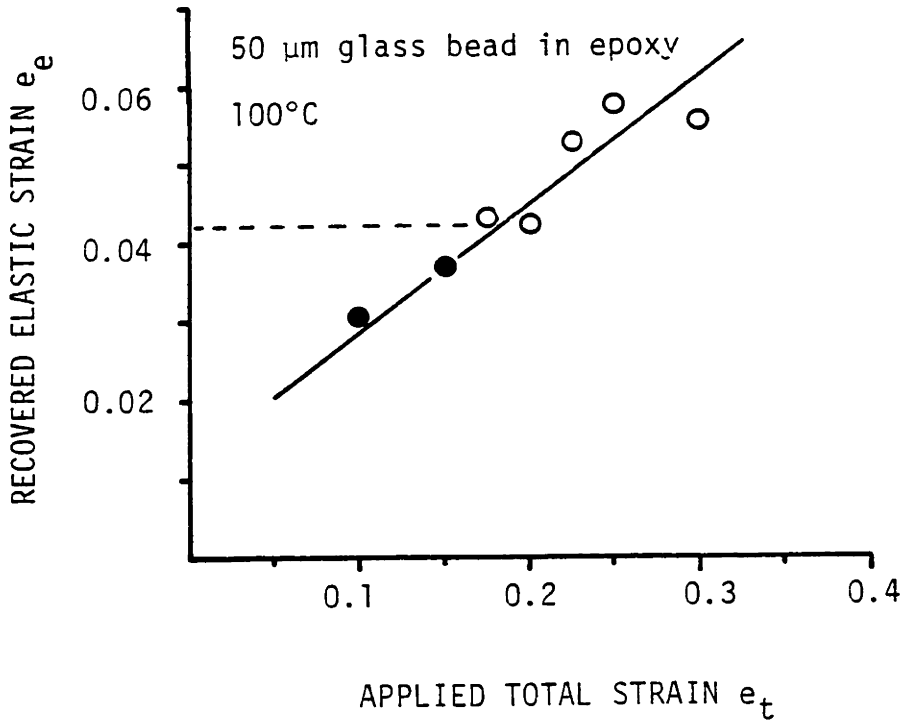

Figure IV-8 Tensile test of 50 μm glass bead filled epoxy at 100°C. Open circle indicates cavitation is observed.

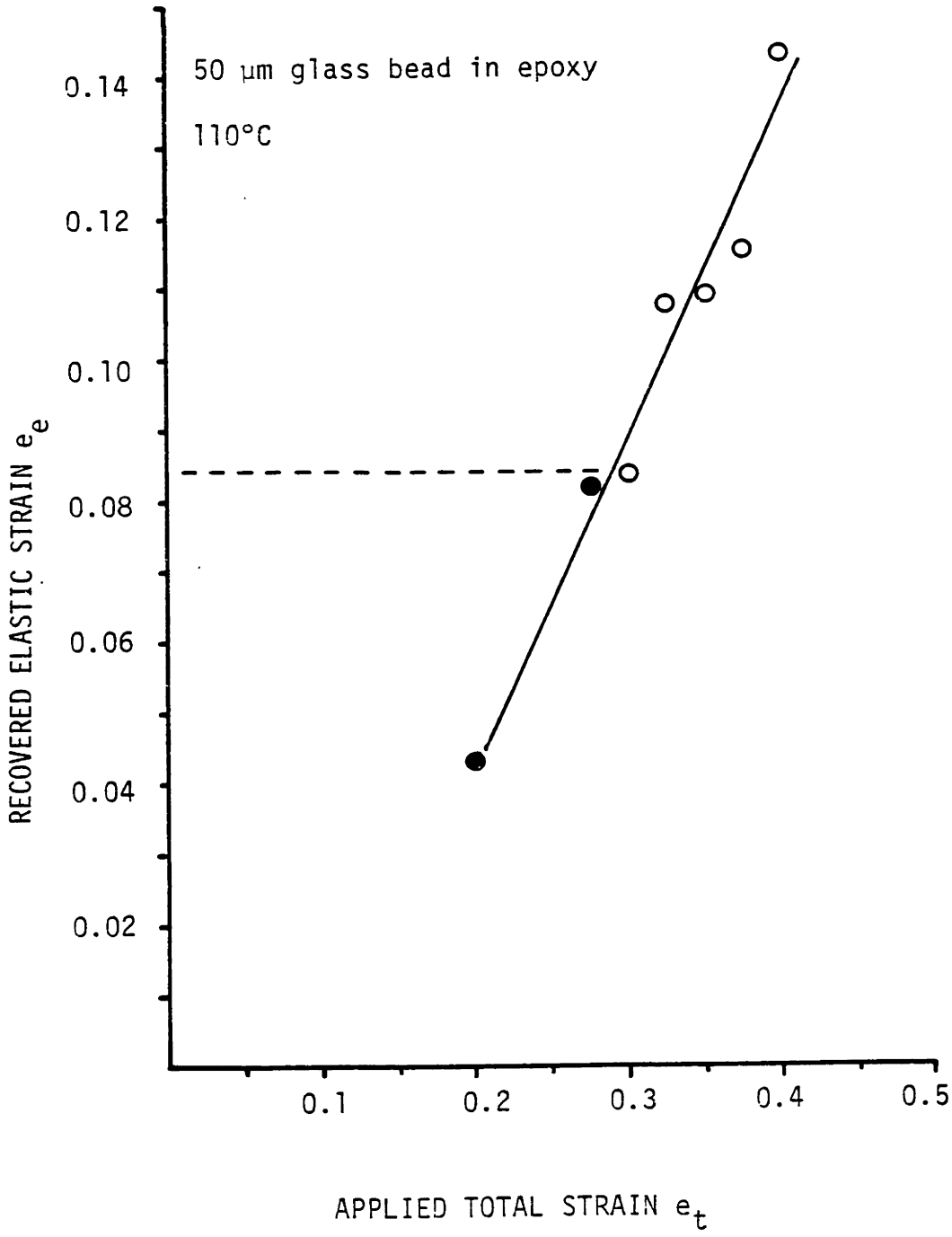

Figure IV-9 Tensile test of 50 μm glass bead filled epoxy at 110°C
Open circle indicates cavitation is observed.

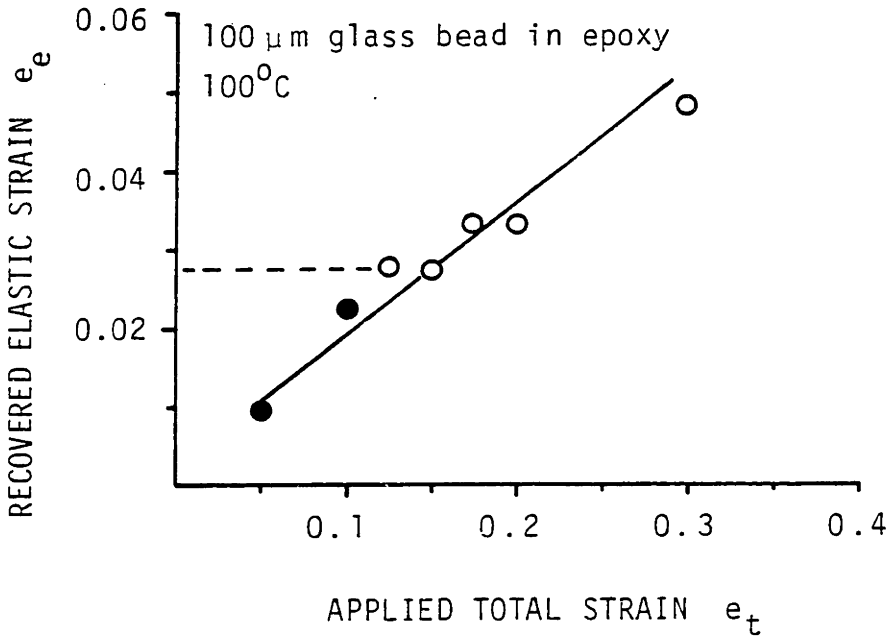

Figure IV-10 Tensile test of 100 μm glass bead filled epoxy at 100°C
Open circle indicates cavitation is observed.

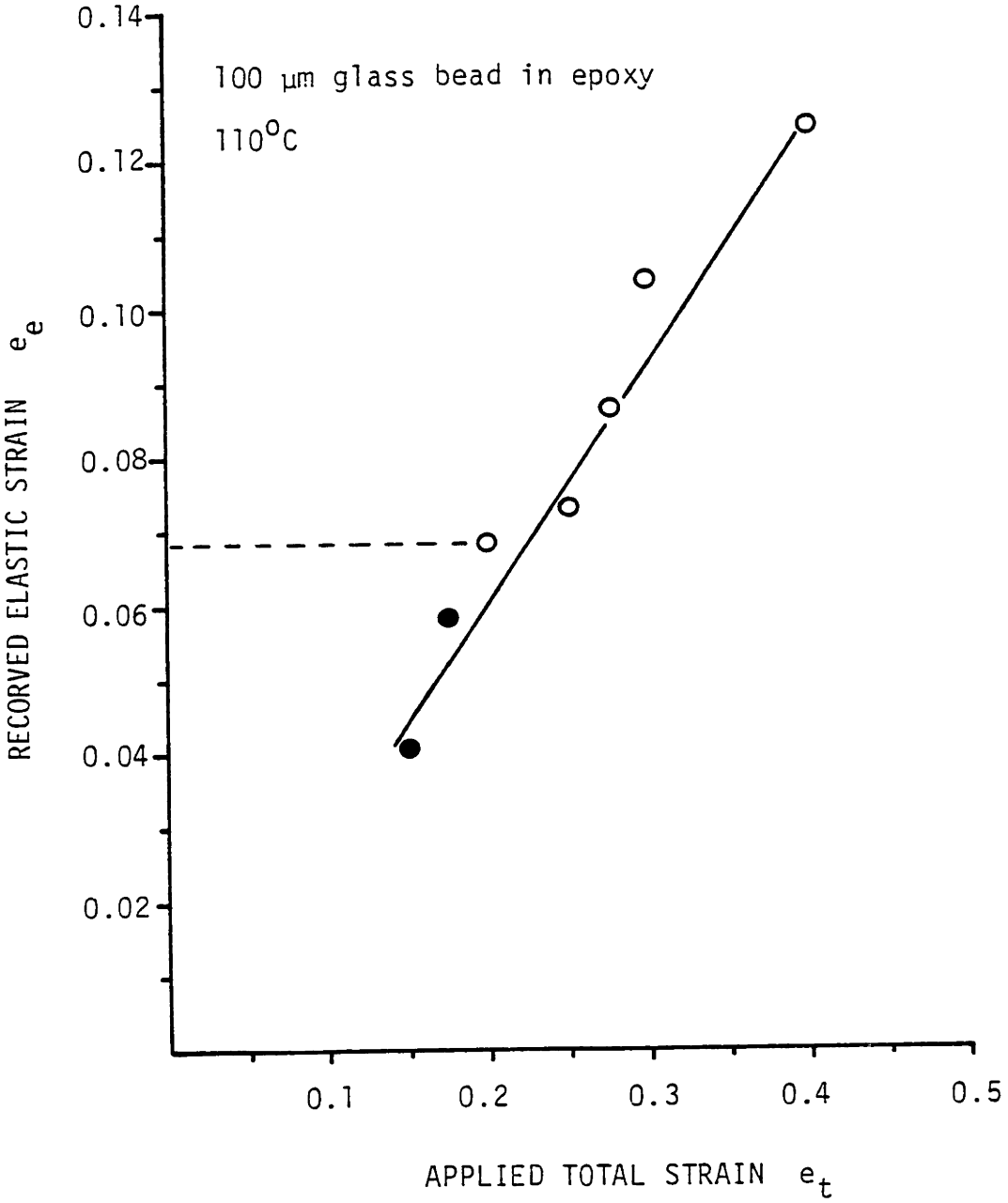

Figure IV-11 Tensile test of 100 μm glass bead filled epoxy at 110°C
Open circle indicates cavitation is observed.

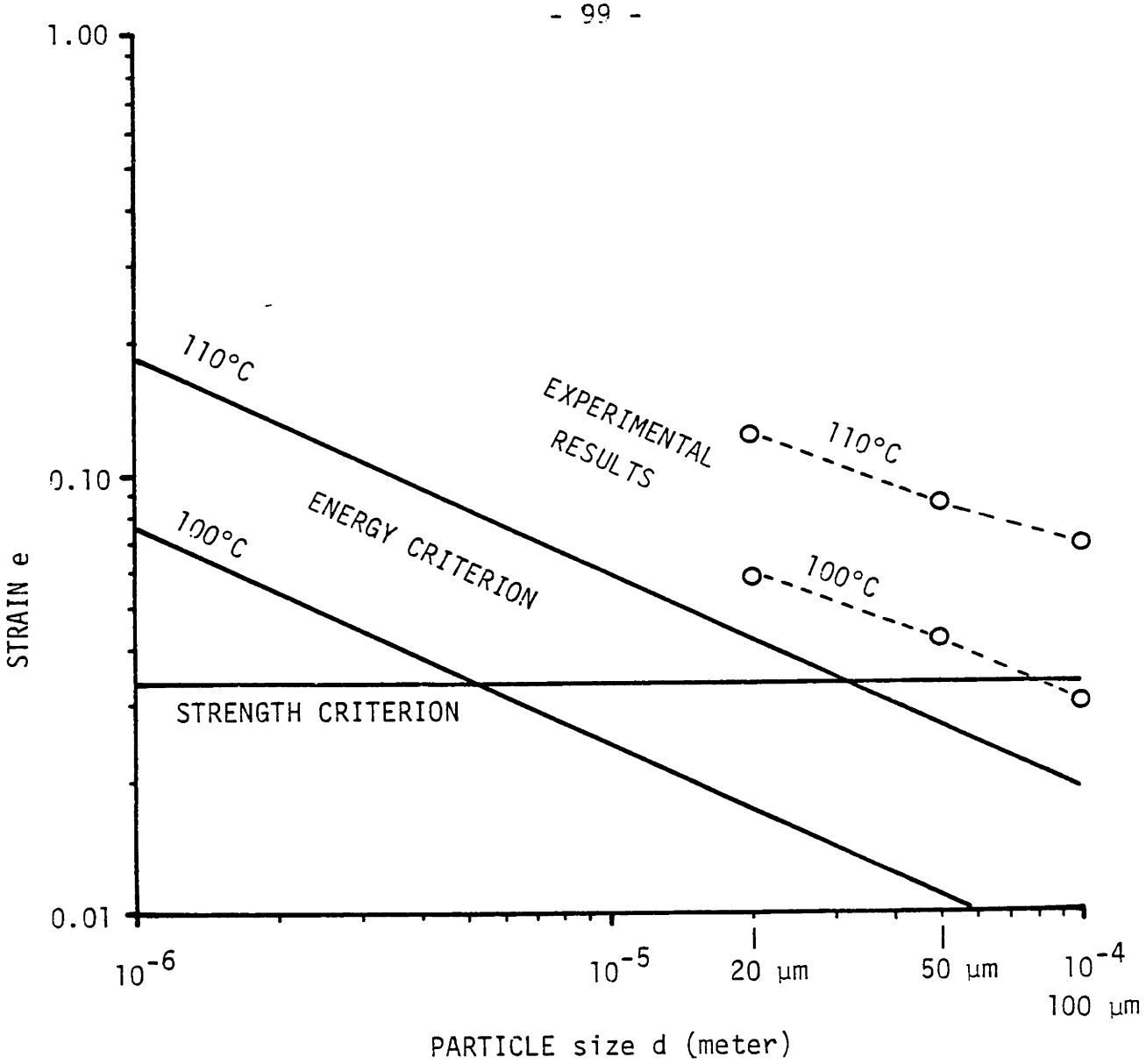

Figure IV-12 Results of analytical and experimental investigation of the criteria for void nucleation in glass bead filled epoxy.

plot presented. This indicates a discrepancy of a constant multiplication factor, which can be attributed to inaccurate data for one or more of the parameters used in the analysis. A significant source of possible error is the data on surface energies. However, inaccurate data on these parameters should not effect the slope of the curves and the difference between results from the two temperatures. In this regard, the experimental results strongly support the accuracy of our analysis.

Optical micrographs of the samples tested in the above investigation are documented in Appendix C. Readers should direct particular attention towards comparing the populations of rings evident in the low magnification micrographs of different samples.

V. FRICTION AND WEAR INVESTIGATION

The following are some of the issues associated with friction and wear which should be investigated. (1) Does microvoid nucleation contribute to the wear of particulate filled polymeric materials? (2) Under what conditions does microvoid nucleation become the controlling wear mechanism? How can these conditions be correlated with results from other investigations, such as the uniaxial tensile test described in Chapter IV. (3) Under conditions where microvoid nucleation is an important wear mechanism, can wear resistance of the material be improved by reducing the filler particle size?

Wear studies were conducted on three materials: (1) The unfilled epoxy, which was used as a reference material. (2) The fumed silica filled epoxy as described in Appendix D, which has a filler particle size distribution in the range of 500 to 1000 Å. The sample used in the wear tests have a silica to resin weight ratio of 11%. (3) A crushed silica gel filled epoxy with filler particle size of 3 to 5 microns. A transmission electron micrograph of this material is shown in figure V-1. The crushed silica gel has physical properties which are similar to those of the fumed silica. The crushed silica gel (grade G-100) was obtained from Glidden Pigments, SMC Corporation. Samples used in the wear tests had a silica to resin weight ratio of 9%.

A. WEAR TEST ARRANGEMENT

A plane on cylinder arrangement as shown in figure V-2 was used in the wear tests. Test samples were machined into 2 x 0.5 x 0.25 inch strips.

Figure V-1 TEM micrograph of crushed silica gel filled epoxy.

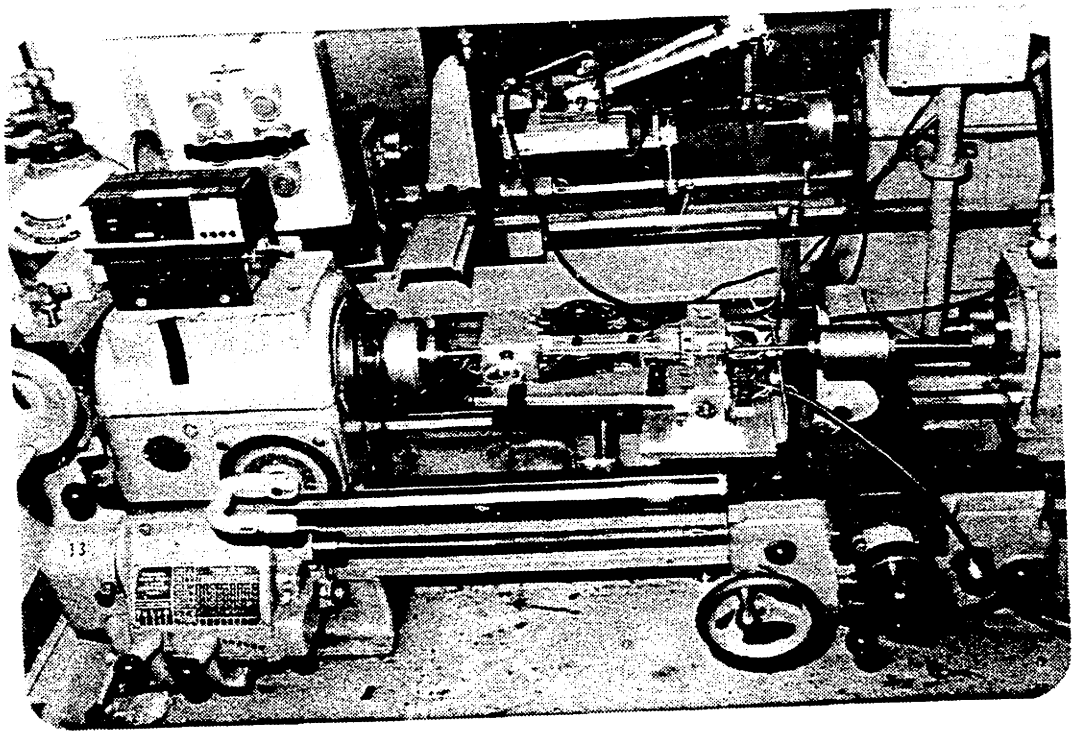

(a) Wear test apparatus modified from an engine lathe

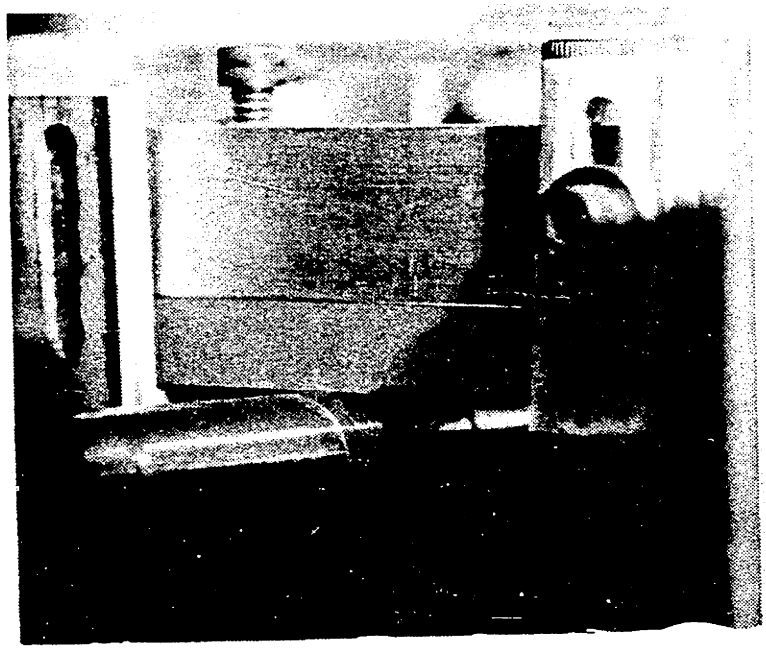

(b) Plane on cylinder test arrangement

Figure V-2 Wear test apparatus.

The sliding surface was as cast without machining. The sliding counterpart was a 0.375 inch diameter rotating cylinder made of AISI 52100 steel. Test loads of 500, 750, and 1000 grams were utilized. Tests were conducted at sliding speeds of 7.48 cm/sec at 150 rpm and 14.96 cm/sec at 300 rpm. The sliding distance for each test was 4.848 kilometers, corresponding to 18 hours at 150 rpm and 9 hours at 300 rpm.

B. TECHNIQUES FOR INVESTIGATING THE ROLE OF VOID NUCLEATION IN WEAR

It is very difficult to obtain direct evidence of void nucleation in a wear study. Therefore, a technique similar to that used in the large scale modeling of the void nucleation process was employed in the wear investigation. Wear tests were conducted at a number of different temperatures. As test temperature increases, the modulus of the matrix material decreases, and the critical particle size for void nucleation is increased to a larger dimension as explained in Chapter IV. If the filler particles are larger than the critical particle size at a lower test temperature , we would expect to observe a decrease in wear as the test temperature is raised above some level where the criticle particle size for void nucleation become greater than that of the filler particle size. On the other hand, if the filler particle size is already below the critical particle size at a low test temperature, increases in test temperature should not produce any significant changes in the wear behavior. If significant changes in wear rate are observed, wear mechanisms other than void nucleation are becoming dominent. The testing of a reference unfilled material along with the particulate filled materials is used to monitor any such changes.

An insulated metal box was placed around both the sample and the rotating steel cylinder, as shown in figure V-3. The temperature in this box was controlled by a series of resistent foils. Tests were conducted at three different chamber temperatures; 21°C, 80°C, and 105°C. However, because of frictional heat generated at the sliding interface, both the average sample temperature near the sliding interface and the flash temperature at the sliding contact will be higher than ambient. As discussed in Chapter II, voids are expected to nucleate at some distance below the sliding surface. Therefore, the average temperature in the sample near the wear surface is more relevant to the void nucleation process than the flash temperature at the sliding contact. The average sample temperature near the wear surface was measured in our tests with a fine gage thermocouple (0.001 inch diameter bead size) imbedded in the sample at about 2 mm from the sliding surface. Temperatures measured at different loads, speeds, and chamber temperature combinations are shown in V-4 and V-5. An analysis of the rise in average and maximum flash temperature at the sliding contact is given in Appendix E.

C. WEAR TEST RESULTS

Both weight loss and the dimensions of the wear tracks were measured after each test. Wear particles and wear tracks were studied under a scanning electron microscope. Wear volume can be calculated from either the weight loss and the density of the material or from the geometric dimensions of the wear track. Wear volume calculations based on weight loss seem to be less reliable than those based on geometric measurements. This is probably because there are usually some wear debris adhered to the

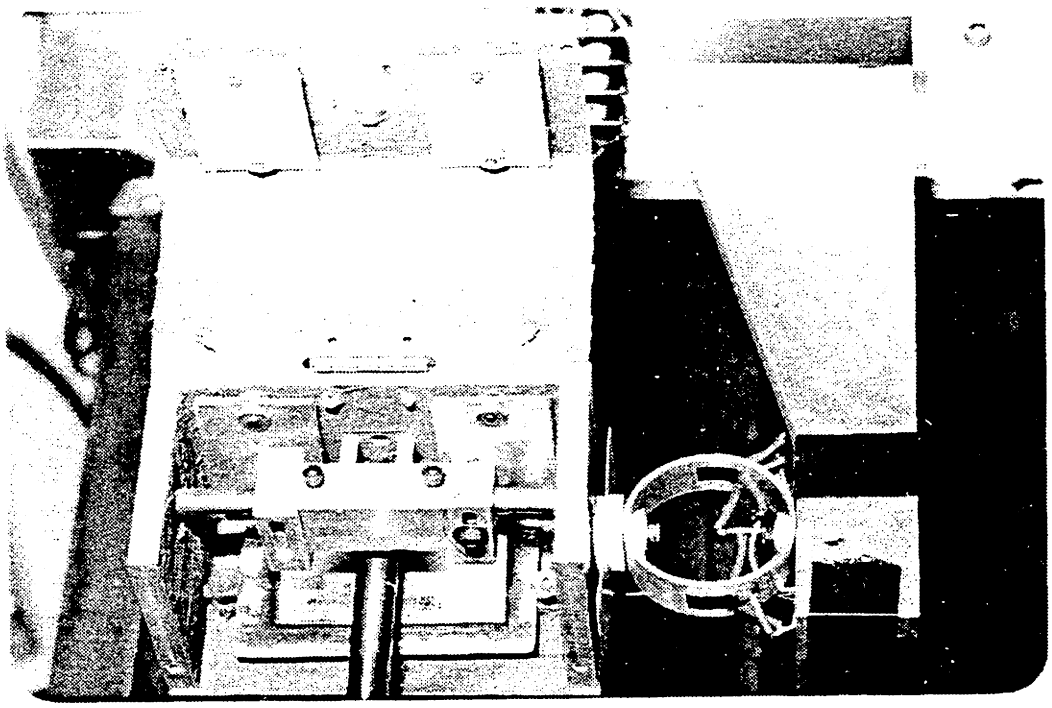

Figure V-3 Environmental chamber for wear tests conducted at elevated temperature. Photo shown with cover opened.

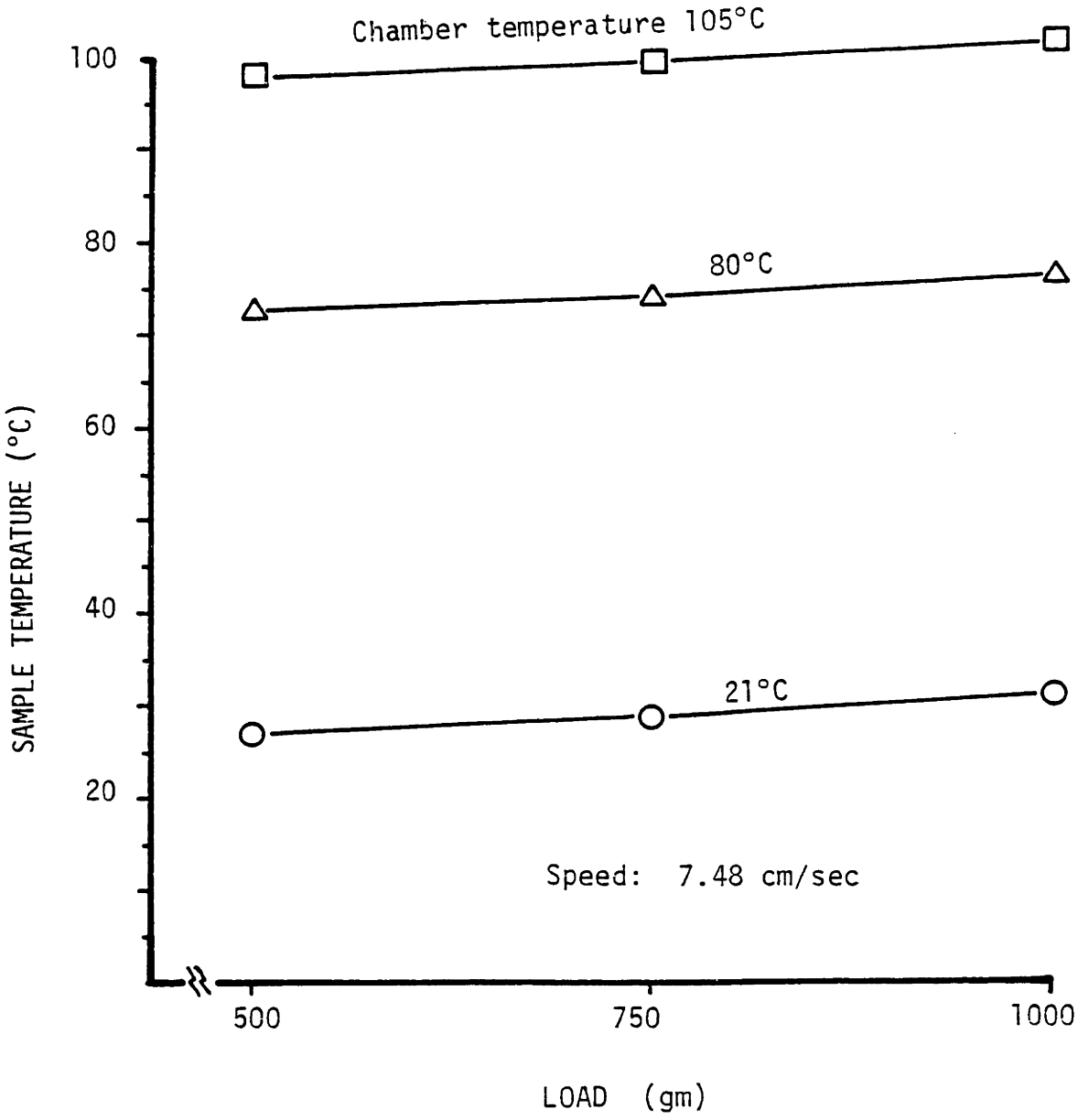

Figure V-4 Sample temperature at a sliding speed of 7.48 cm/sec at different chamber temperatures.

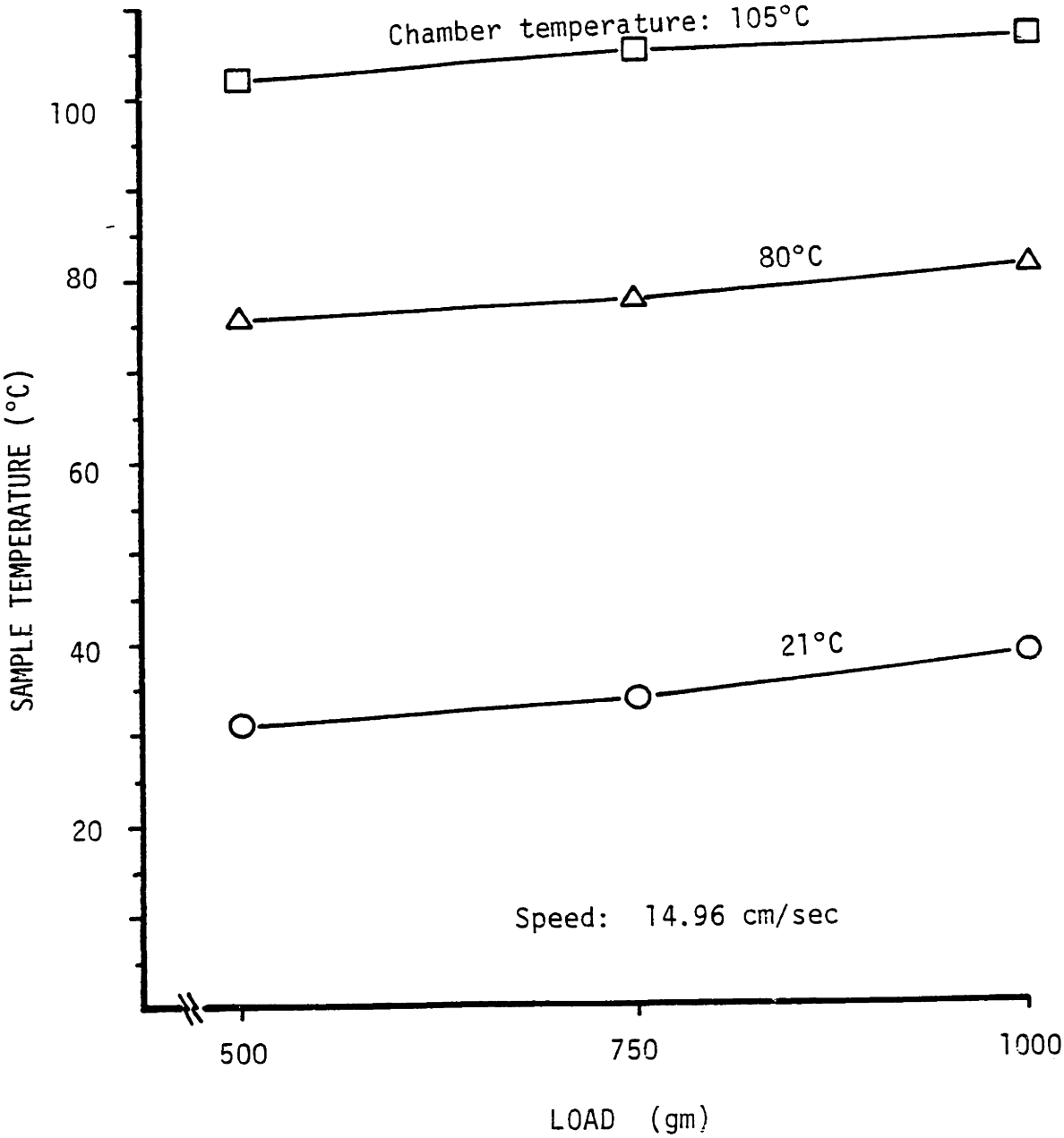

Figure V-5 Sample temperature at a sliding speed of 14.86 cm/sec at different chamber temperatures.

wear track. On samples with clean and smooth wear tracks, the results from the two calculations are very close to each other. Geometric volume loss is used in this thesis to report wear data.

Figures V-6 through V-8 show the wear volume plotted against load at two sliding speeds and three testing temperatures. The same data are replotted in figures V-9 and V-10, where they are plotted against test temperature. The temperatures in the above figures are the environmental temperature in the test chamber. Readers should refer to figures V-4 and V-5 for the sample temperature associated with these chamber temperatures. Wear factors are calculated and tabulated in Table V-1. The differences in wear volume of all samples at all test conditions are within roughly one order of magnitude with each other. Repetitive tests of each data point show discrepancies of less than a factor of 2. Therefore, the general trends of the wear behavior shown in these figures should be fairly reliable, but the quantitative value of each data point is subjected to much greater experimental error.

The reference unfilled and fumed silica filled materials show similar wear characteristics at nearly all test conditions. Differences are found at the two most severe wear conditions at room temperature; 750 g and 1000 g at 300 rpm. These discrepancies could be due to the differences in the load carring capacity of the two materials which start to become apparent only at relatively high loads (> 750 g). The most significant observation is in the data for the large particle filled material, containing crushed silica gel. For this material there is a sharp reduction in wear as the test temperature increases from 21°C to 80°C and 105°C. This reduction in wear is observed for all loads and sliding speeds. This

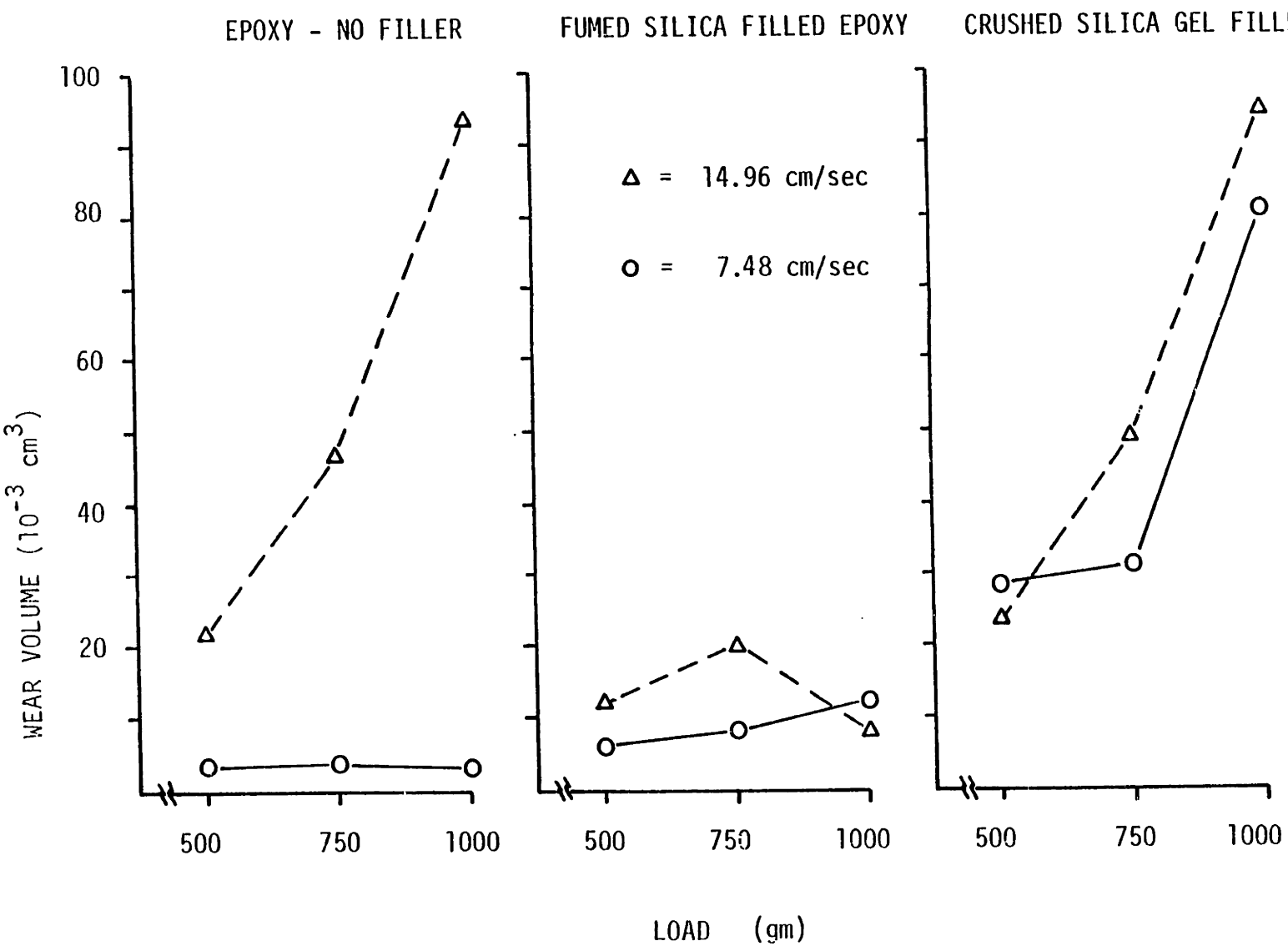

Figure V-6 Wear test results at 21°C chamber temperature.

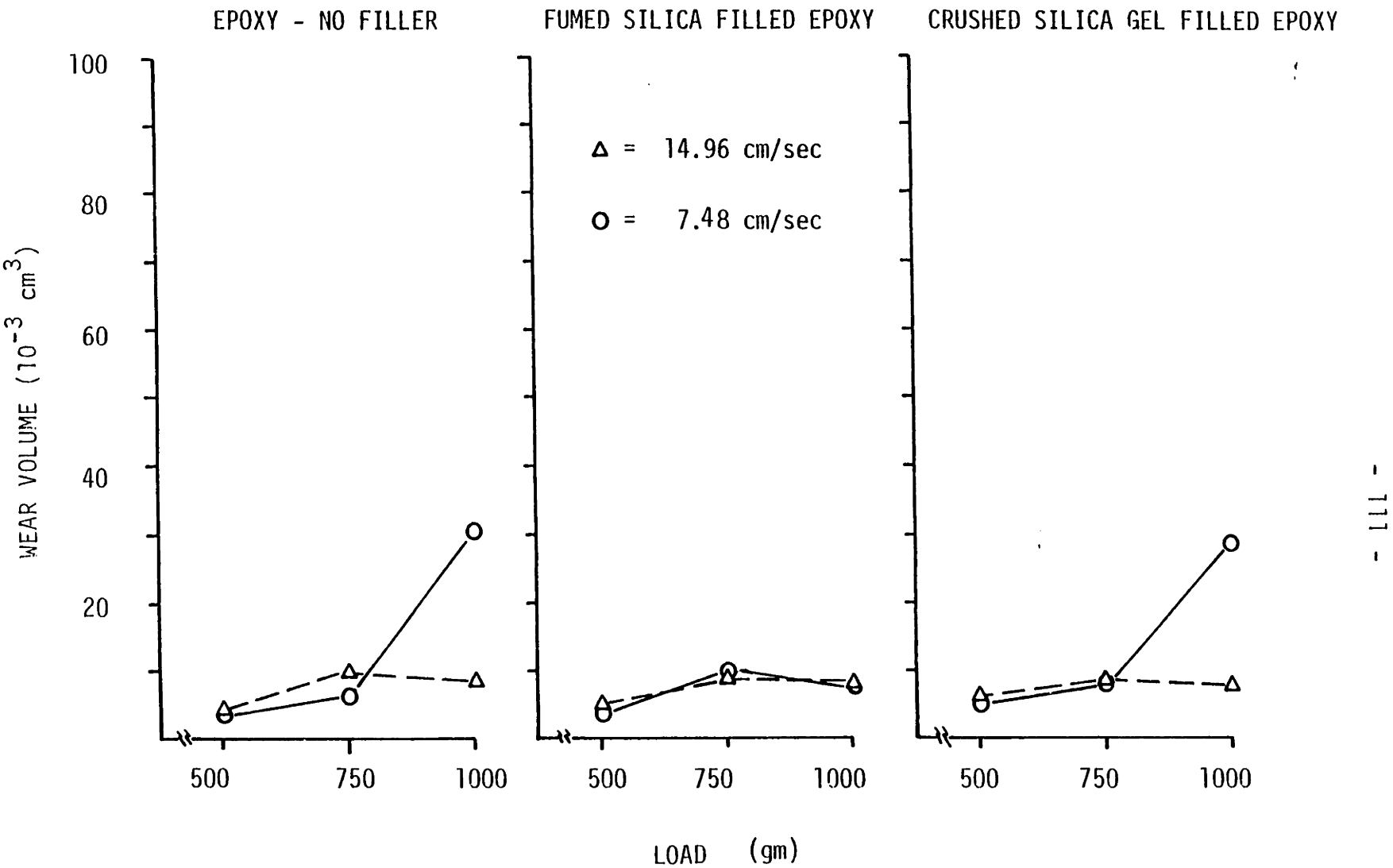

Figure V-7 Wear Test results at 80°C chamber temperature.

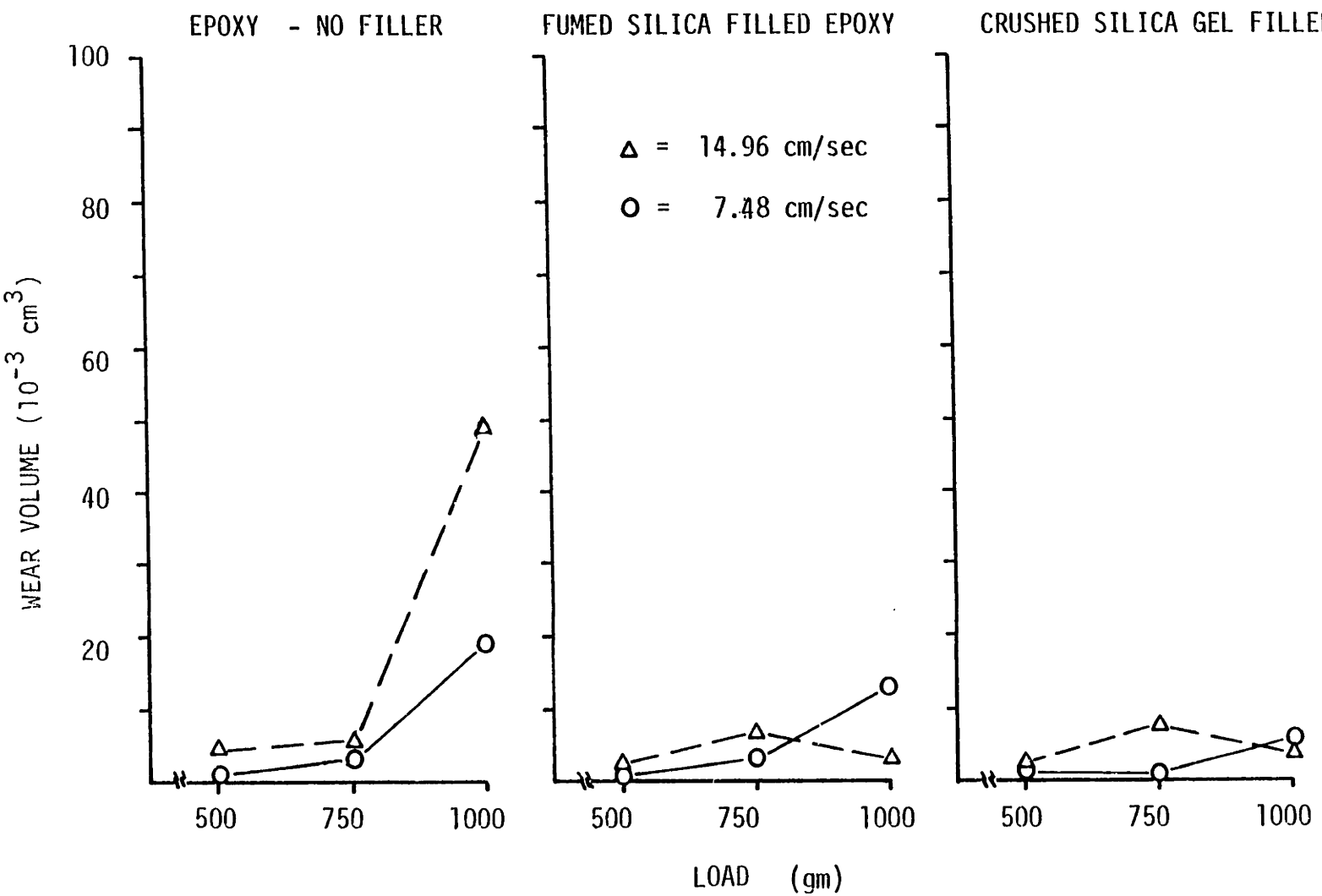

Figure V-8 Weat test results at 105°C chamber temperature

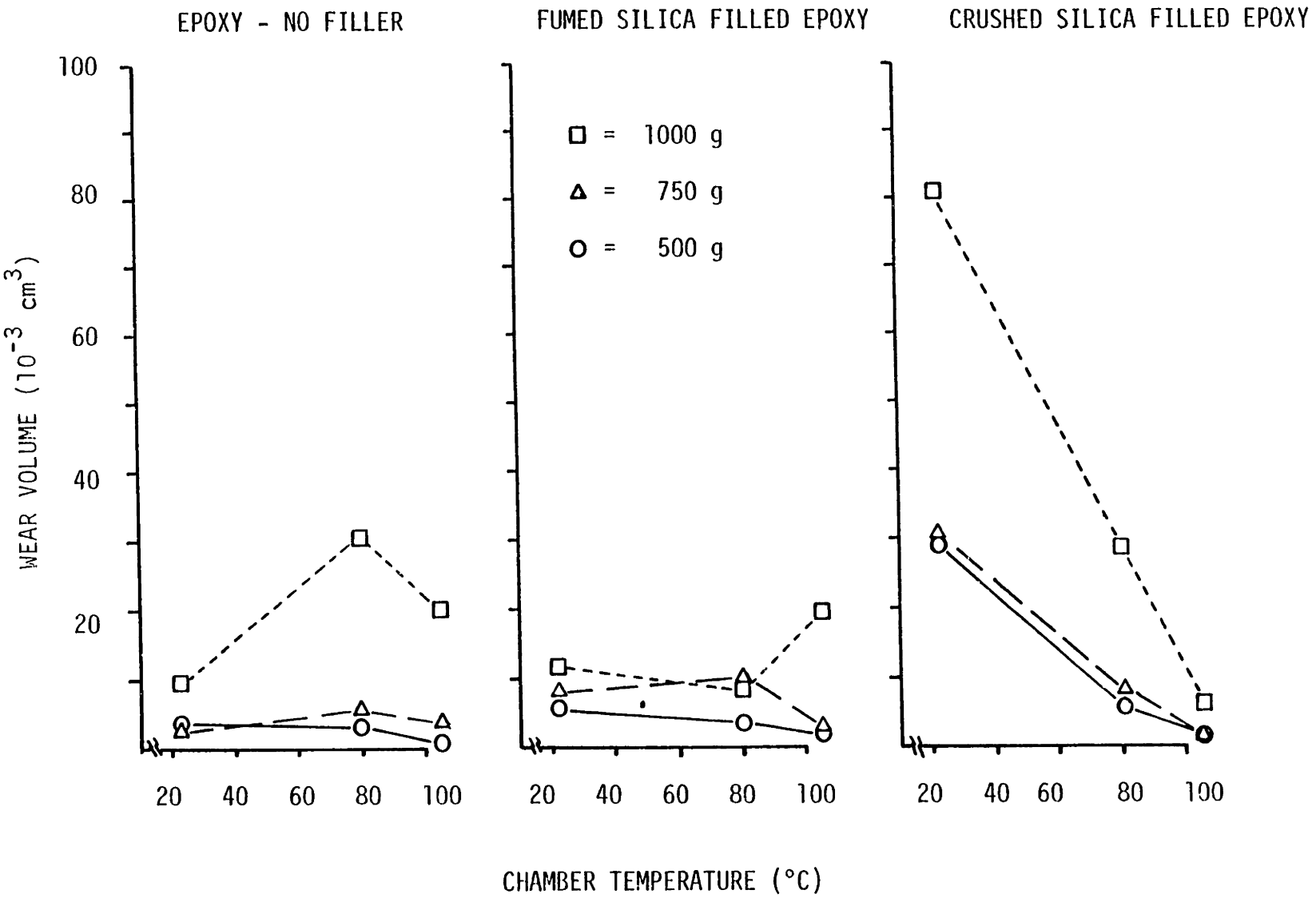

Figure V-9 Wear test results at a sliding speed of 7.48 cm/sec.

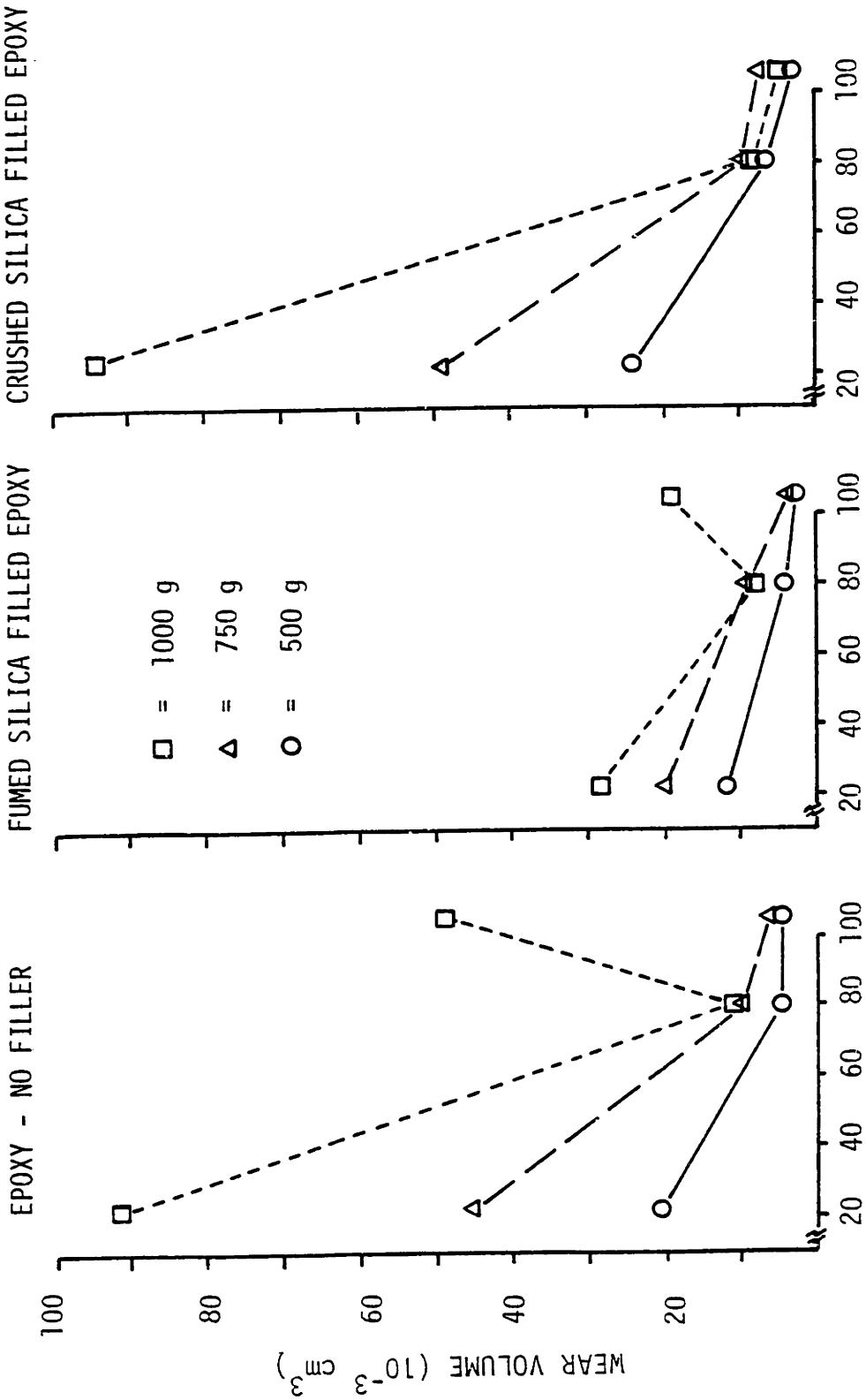

Figure V-10 Wear test results at a sliding speed of 14.96 cm/sec.

Wear Factor K in 10^{-11} $\frac{cm^3}{gm \cdot cm/sec \cdot sec}$ and (10^{-6} $\frac{in^3}{lb \cdot ft/min \cdot hr}$)

		epoxy - no filler			fumed silica filled epoxy			crushed silica gel filled epoxy		
		21°C	80°C	105°C	21°C	80°C	105°C	21°C	80°C	105°C
150 rpm (7.48 cm/sec)	500g	1.46 (3.60)	1.30 (3.19)	0.38 (0.93)	2.53 (6.21)	1.46 (3.59)	0.78 (1.93)	11.84 (29.12)	2.08 (5.11)	0.39 (0.96)
	750g	0.86 (2.12)	1.71 (4.20)	0.91 (2.24)	2.26 (5.55)	2.72 (6.70)	0.85 (2.09)	8.42 (20.71)	2.29 (5.64)	0.25 (0.61)
	1000g	0.65 (1.59)	6.30 (15.51)	3.73 (9.18)	2.64 (6.49)	1.70 (4.19)	2.68 (6.60)	16.72 (41.13)	5.92 (14.56)	1.42 (3.48)
300 rpm (14.96 cm/sec)	500g	8.99 (22.12)	1.65 (4.07)	2.06 (5.07)	5.02 (12.36)	2.06 (5.07)	1.12 (2.75)	9.98 (24.55)	2.57 (6.33)	0.99 (2.45)
	750g	12.87 (31.66)	2.74 (6.74)	1.49 (3.65)	5.57 (13.70)	2.49 (6.13)	1.87 (4.59)	13.60 (33.47)	2.30 (5.66)	2.08 (5.12)
	1000g	19.39 (47.71)	1.71 (4.22)	10.16 (25.00)	1.71 (4.20)	1.70 (4.19)	0.56 (1.38)	19.48 (47.92)	1.57 (3.86)	1.22 (2.99)

Table V-1 Wear factor calculated from wear test results.

behavior was not found in the fine particle size fumed silica filled material.

Before using different wear models to interpret these observations and judge on the merits and demerits of each model, we will first try to relate these observations to the void nucleation mechanism discussed throughout this thesis. From the void nucleation mechanism discussed, we may interpret the wear data as follows; at low test temperature, the epoxy matrix has a high modulus. The calculated critical particle size for void nucleation (3000 Å) is larger than the fumed silica particles (500-1000 Å), but it is significantly smaller than that of the crushed silica gel particles (3-5 microns). If microvoid nucleation is the major cause of wear for inclusion filled materials under our test conditions, it should only contribute significantly to the wear of the crushed silica gel filled material, where its large filler particle size is favorable for microvoids to nucleate. The wear of the fumed silica will be controlled by other mechanisms which do not appear to be particle size dependent. As test temperature increases, the critical particle size for void nucleation also increases. This will have no effect on the fumed silica filled material, since its particle size is below the critical size even at low temperatures. However, the critical particle size will eventually increase with temperature to about or even above the dimension of the crushed silica gel particles. At this stage, void nucleation will cease to be the controlling factor in the wear of this material. These explanations are in accord with the experimental observations. At the highest test temperature of 105°C, all materials have about the same wear rate, which indicates that the void nucleation criterion is no longer satisfied by any of the three materials. The wear of all three

materials is controlled by some other mechanism which is not dependent on the particle size of the filler. The above interpretation does not enable us to conclude definitively that void nucleation is the mechanism responsible for the wear of the crushed silica gel filled material. However, there are no major contradictions between the experimental data and the theory.

Without further supporting evidence to substantiate the void nucleation model, it may be useful to examine other wear theories to see if they correlate more closely with our experimental data. The adhesive wear theory fails to explain the observed decrease in wear rate with increasing test temperature. An increase in test temperature will result in a decrease in the hardness of a material. Therefore, the adhesive wear model predicts an increase in wear with increasing temperature. Also, on an atomistic scale, adhesion is a process that will be enhanced by thermal activation. A higher environmental temperature should promote the establishment of adhesive joints at the sliding contact. This will result in an increase of the probability factor k in the adhesive wear model, and a corresponding higher wear rate. These difficiencies make it inappropriate to apply the adhesive wear model to explain the general wear behavior of all three materials investigated. It is even more difficult in applying it to explain the difference in wear behavior between the crushed silica gel filled material and the fumed silica filled material without further investigation into the adhesive mechanisms of these materials.

Abrasive wear, which is related to the cutting of the surface by hard abrasive particles, will also predict the increase in wear with increase in test temperature. Cutting becomes easier as the material softens,

since the abrasive particles of a given size and sharpness can penatrate more deeply into the surface, and facilitate more chip generation. Sin, Saka and Suh [73] showed very conclusively that abrasive wear is particle size dependent. Abrasive wear is negligible at a particle size below 1 μm. Between 1 μm and 80 μm, there are both extensive plastic deformation and abrasive cutting. For abrasive particles larger than 80 μm, wear is dominated by the cutting mechanism. The particle size of the fumed silica and the crushed silica gel are 500-1000 Å and 3-5 μm respectively. Therefore, it is unlikely that the wear is due to abrasion. Typical wear coefficients for abrasive wear are of the order of 10^{-1}, which is also found to be the case in the abrasive wear of polymers [73]. From equation II-1 and II-2, wear coefficient of our wear test results can be obtained from the wear factor shown in Table V-1. For a room temperature hardness of 20 to 25 kg/mm^2 measured from our samples, the wear coefficients are calculated to be of the order of 10^{-4} to 10^{-5}, which are at least three orders of magnitude smaller than what would result from abrasion. Therefore, it is unlikely that abrasive wear played an important role in our wear study.

Another aspect of the delamination wear is the crack propagation from the nucleated microvoids and microcracks. Jahanmir, Abrahamson and Suh [74] showed that when wear is controlled by crack propagation in an inclusion filled material, the wear rate is inversely proportional to the inter-particle spacing. For the same volume fraction of inclusions in the material, inter-particle spacing is directly proportional to the size of the inclusion. Therefore, if the wear rate was controlled by the crack propagation rate rather than the crack nucleation rate, the wear

rate of the fumed silica filled epoxy is expected to be much greater than the crushed silica gel filled epoxy, since the inter-particle spacing in the former material is 30-100 times closer than in the latter. This prediction contradicts the experimental results. Furthermore, if the crack propagation rate is decreased by the reduction of the matrix stiffness at high test temperatures, decrease in wear should be observed in both materials. However, the wear test results show the reduction in wear with increasing test temperature only in the crushed silica gel filled epoxy. Therefore, it can be reasonably concluded that the wear in our investigation was controlled by crack nucleation rather than crack propagation.

Wear particles and wear tracks were studied using a scanning electron microscope. Very little conclusive information can be drawn from these studies. Wear particle size tends to decrease with decreasing wear rate, regardless of test conditions or the type of material. Typical wear particles are shown in figure V-11. The larger wear particles appear in the form of plates or sheets. Such observations are similar to those reported in delamination wear studies on metals [6]. However, the wear track studies failed to supply any evidence of these wear particles in the early stage of delamination which was observed in highly ductile metals by Jahanmir [6]. In less ductile materials, these early stages of delamination were not observed even in metals. However, the possibility of they being loose wear particles which were trapped in the sliding interface and deformed into the observed plate shape cannot be totally eliminated. Figure V-12 shows a few of the typical wear track surfaces. Some of the wear tracks have a polished smooth surface. Most such surfaces are

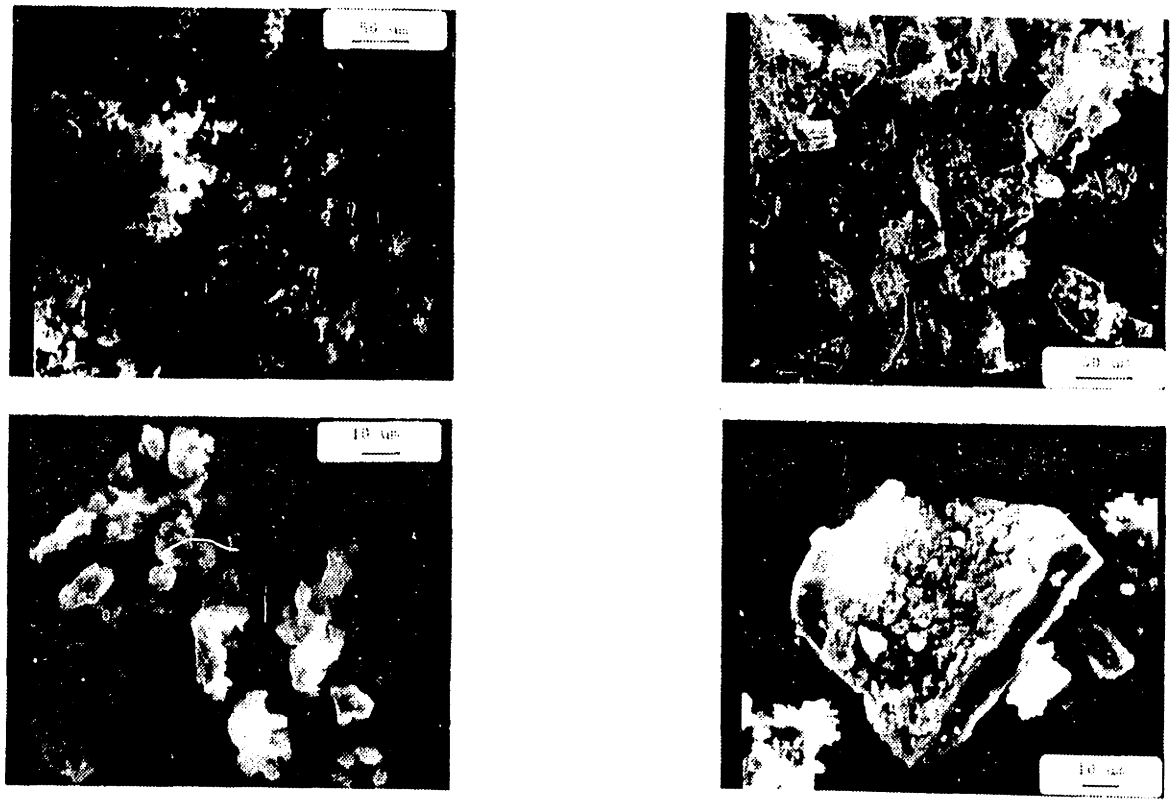

(a) (b)

Figure V-11 Typical wear particles. (a) small symetrical wear particles and (b) large plate or sheet form wear particles.

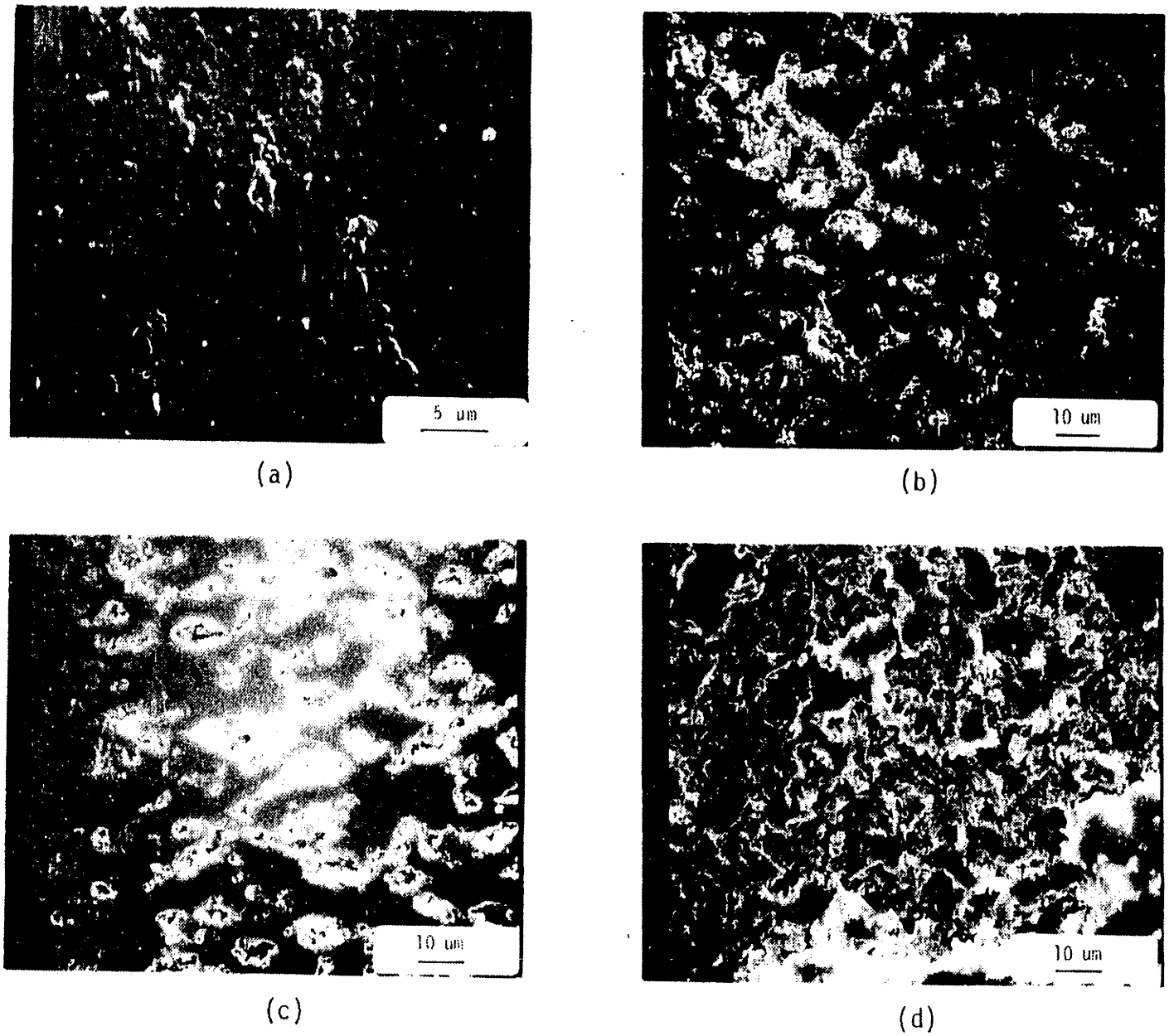

Figure V-12 Typical wear tracks (a) to (d) from smooth to cratered and to rough surfaces.

associate with a low wear rate. Other wear tracks are found to be rough, with closely spaced shallow craters. Micrographs of wear particles and wear tracks for all three materials tested at different conditions are documented in Appendices F and G. Cross sections of the wear tracks were taken in the transverse and parallel directions relative to the sliding direction. The samples were polished and examined under optical and electron microscopes. There are little substential evidence of subsurface cracks on these samples. The sectioning and polishing technique may not be suitable for polymer samples, for it may destroy microscopic features on the samples.

D. FRICTION COEFFICIENT MEASUREMENT

Friction coefficients were measured using strain gages during the wear test. The average steady state friction coefficients are shown in figure V-13 through V-15. That the friction coefficient decreases with load is a commonly observed phenomenon with polymeric bearings [75]. For room temperature tests, low friction coefficients of 0.4-0.6 were found to be associated with the high wear rates of the crushed silica gel filled material and at the two most severe test conditions for the unfilled material. High friction coefficients in the range of 0.8-0.9 are associated with the low wear rate of the unfilled and fumed silica filled material. In test conducted at higher temperatures, where all three materials show similar wear rates, the friction coefficients are in the range of 0.5-0.6 for all three materials.

Rabinowicz [76], Suh et al [77] show that, in most materials, the wear coefficient increases exponentially with the friction coefficient. The reasons for this phenomenon can be explained by the delamination theory of wear. As the coefficient of friction increases, plastic deformation

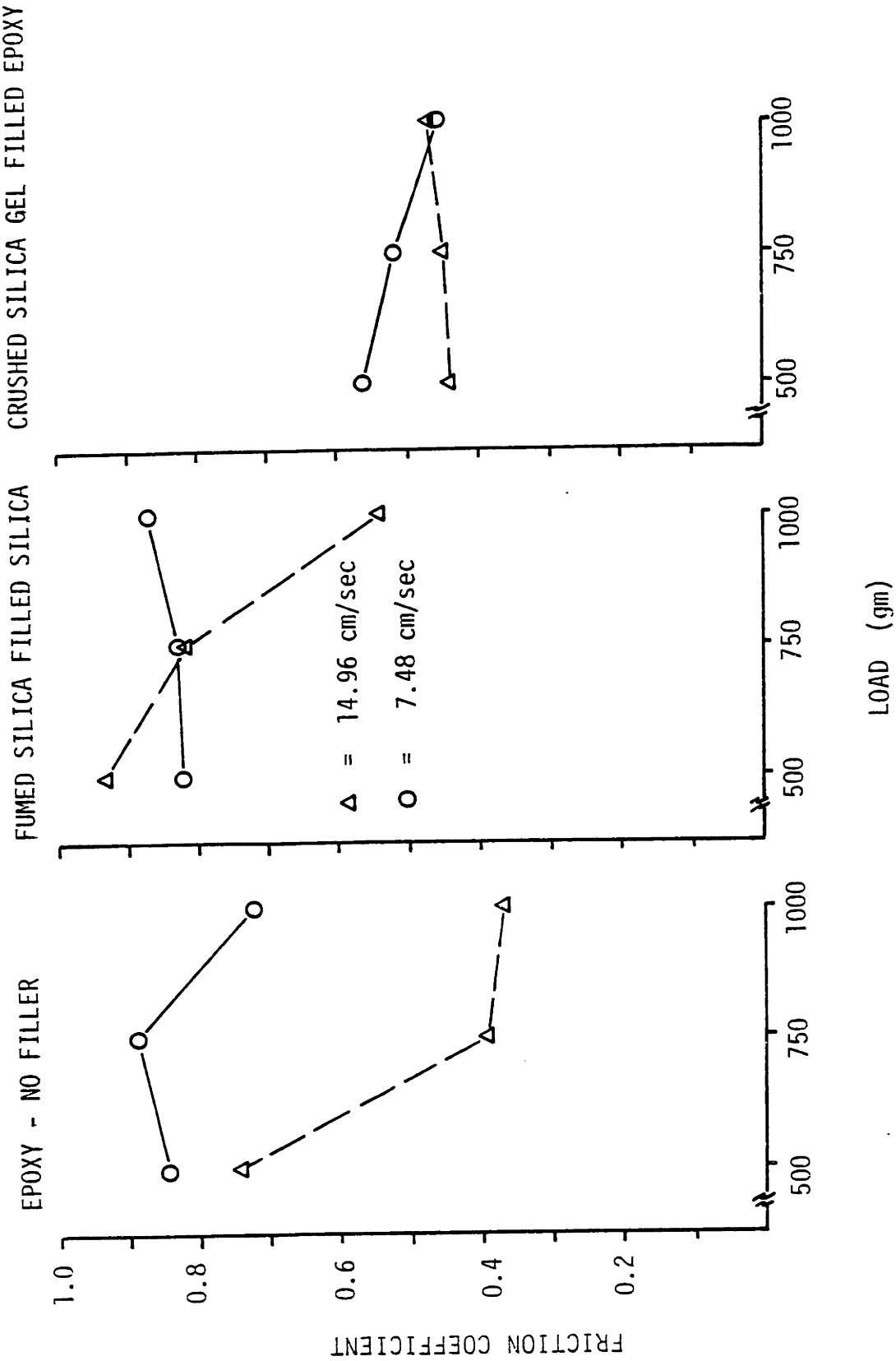

Figure V-13 Friction coefficient at 21°C chamber temperature.

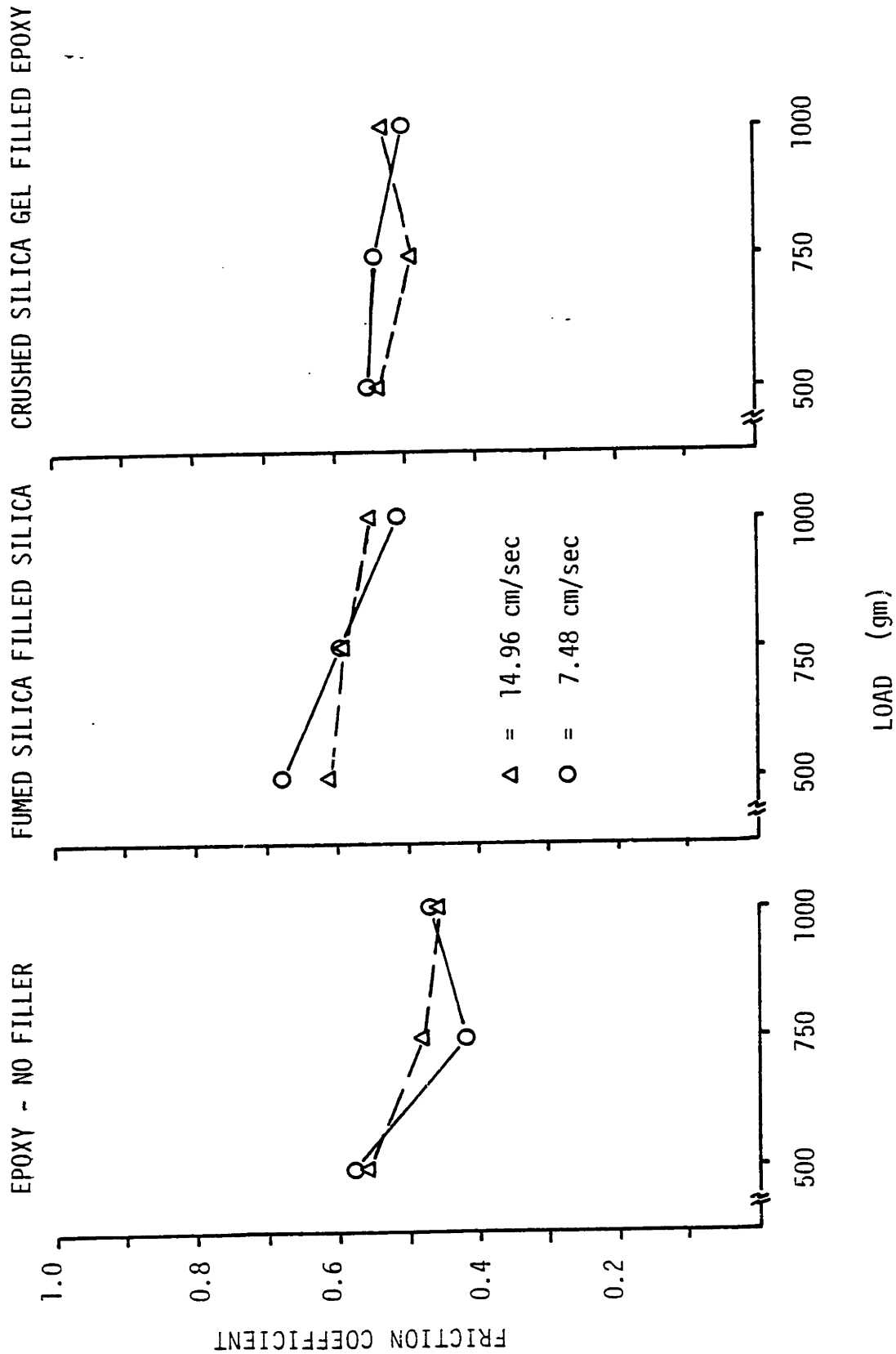

Figure V-14 Friction coefficient at 80°C chamber temperature.

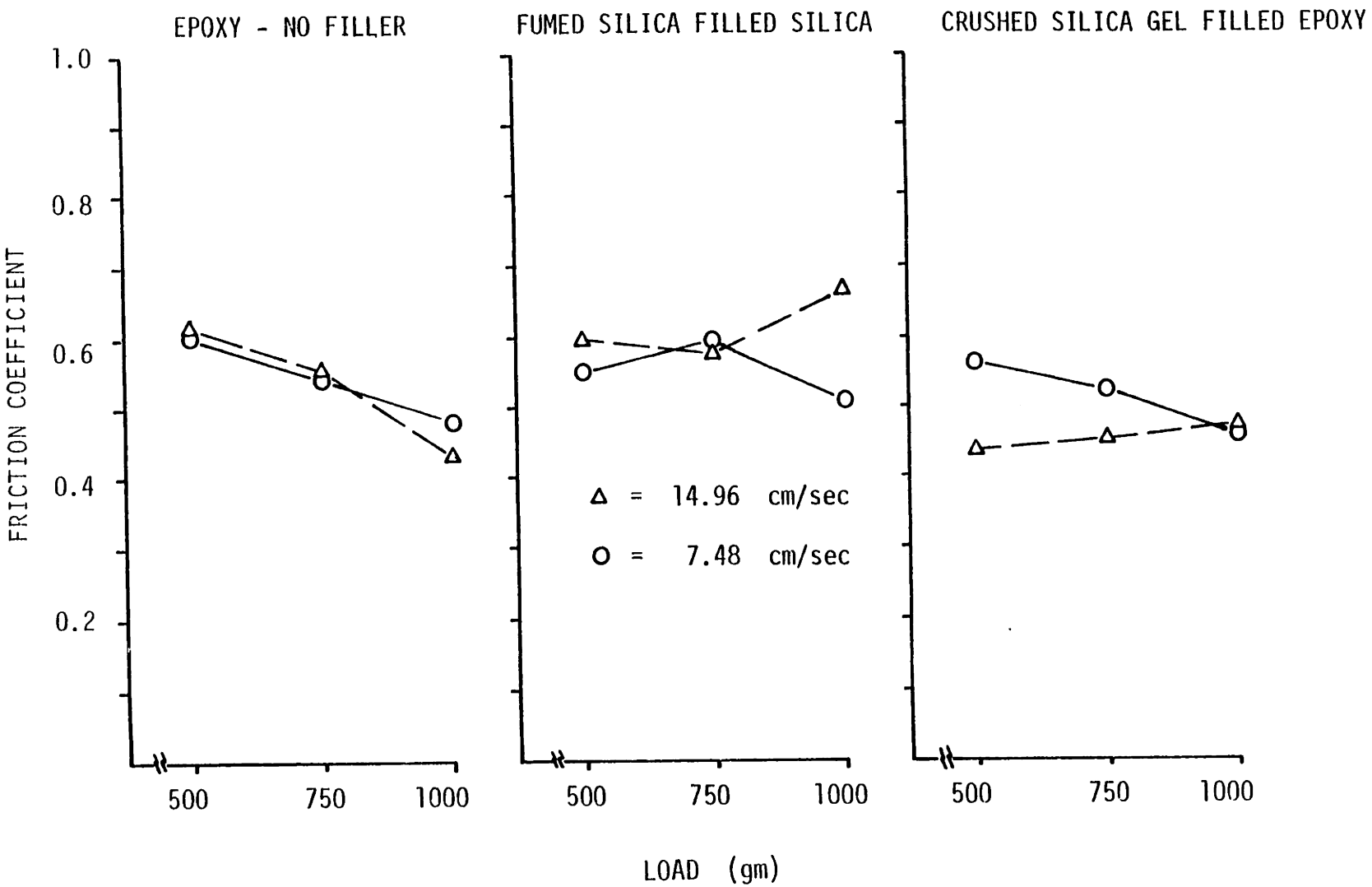

Figure V-15 Friction coefficient at 105°C chamber temperature.

increases with the number of loading cycles, which accelerates the crack nucleation rate. As point out by Fleming and Suh [78], the increase in friction coefficient also increases the stress intensity factor at the crack tip, and increases the crack growth rate per cycle of loading, when the asperity of the opposite surface passes over the surface of the specimen. These two mechanisms which depend sensitively on the tangential traction at the surface increase the wear rate with increasing friction coefficient. The wear data and the friction coefficients are plotted together in figures V-16 through V-18. These figures do not show strong dependency of the wear rate on the friction coefficient. This is probably due to the fact that the wear in our investigation was controlled mainly by the void nucleation process as discussed in the preceding section, and did not experience the more commonly observed complete delamination wear process (i.e., plastic deformation, crack nucleation, and crack propagation).

In our room temperature wear tests, it is observed that high friction coefficients are associated with lower wear and produce smooth wear tracks, and vice versa. A plausible explanation might be that when the delamination wear due to the subsurface damage process was so slow, that the surface of the specimen and the slider conformed with each other, resulting in high friction coefficients due to the large real area of contact from these well conformed mating surfaces. As the wear due to subsurface damage increases, the interface becomes rough and the real area of contact decreases, and result in a reduction of the friction force.

The followings are some studies that may be worth pursuing in future investigations. (i) Polymers, especially glassy polymers, does not have easily identifiable microstructures such as the grain boundaries in metals,

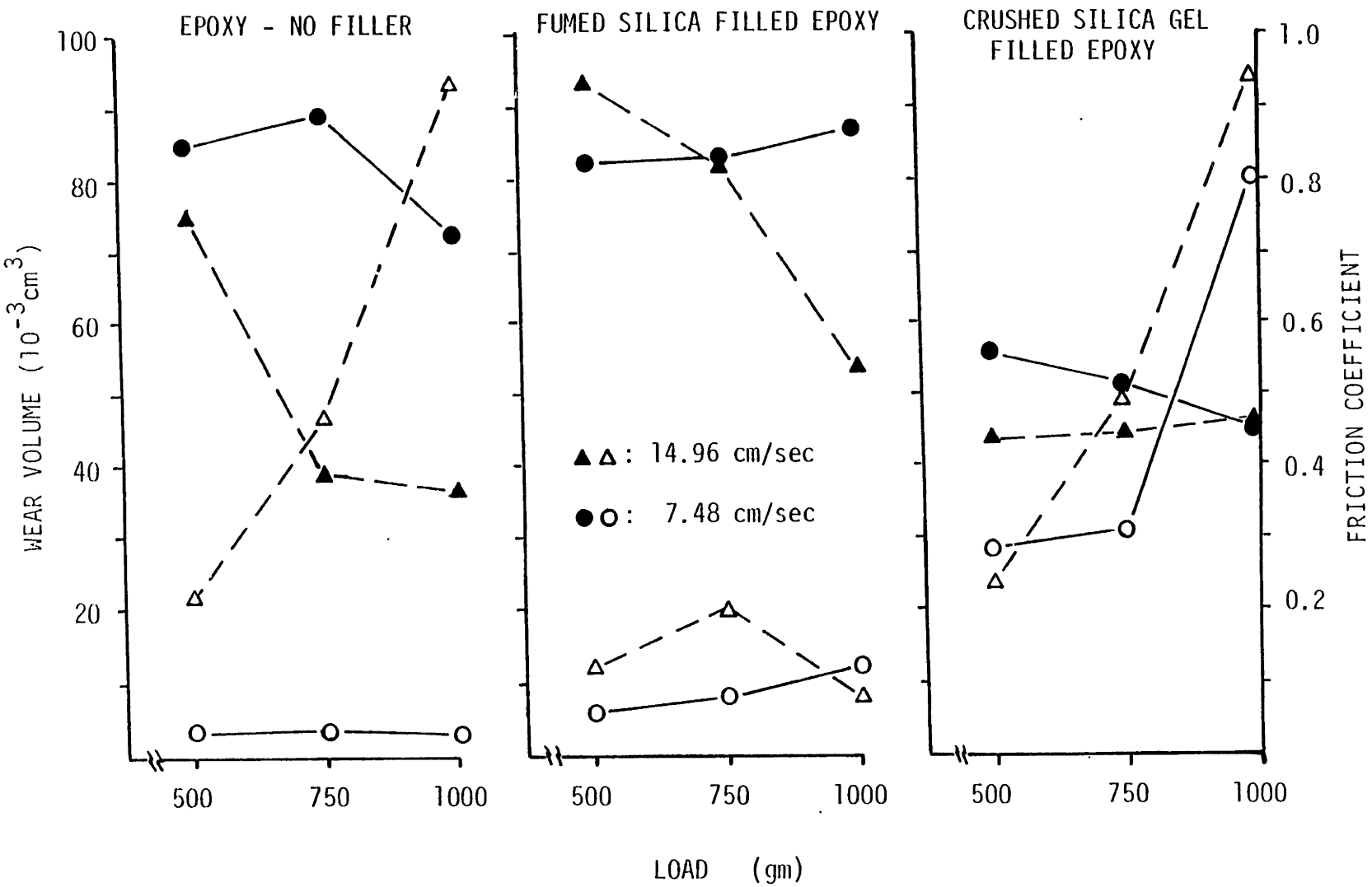

Figure V-16 Comparison of wear and friction coefficient data at 21°C chamber temperature open symbols: wear data, solid symbols: friction coefficients.

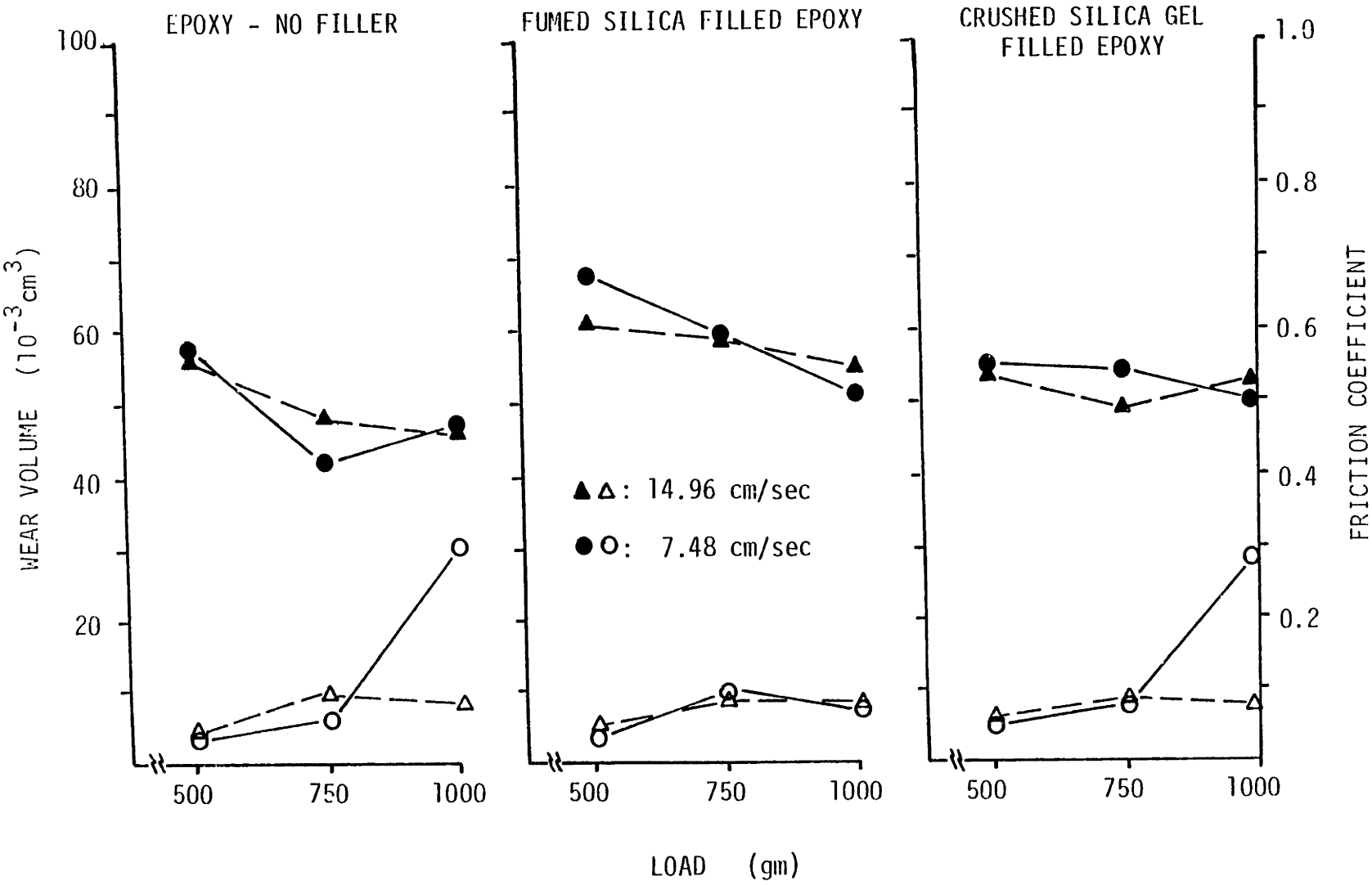

Figure V-17 Comparison of wear and friction coefficient data at 80°C chamber temperature
open symbols: wear data, solid symbols: friction coefficients.

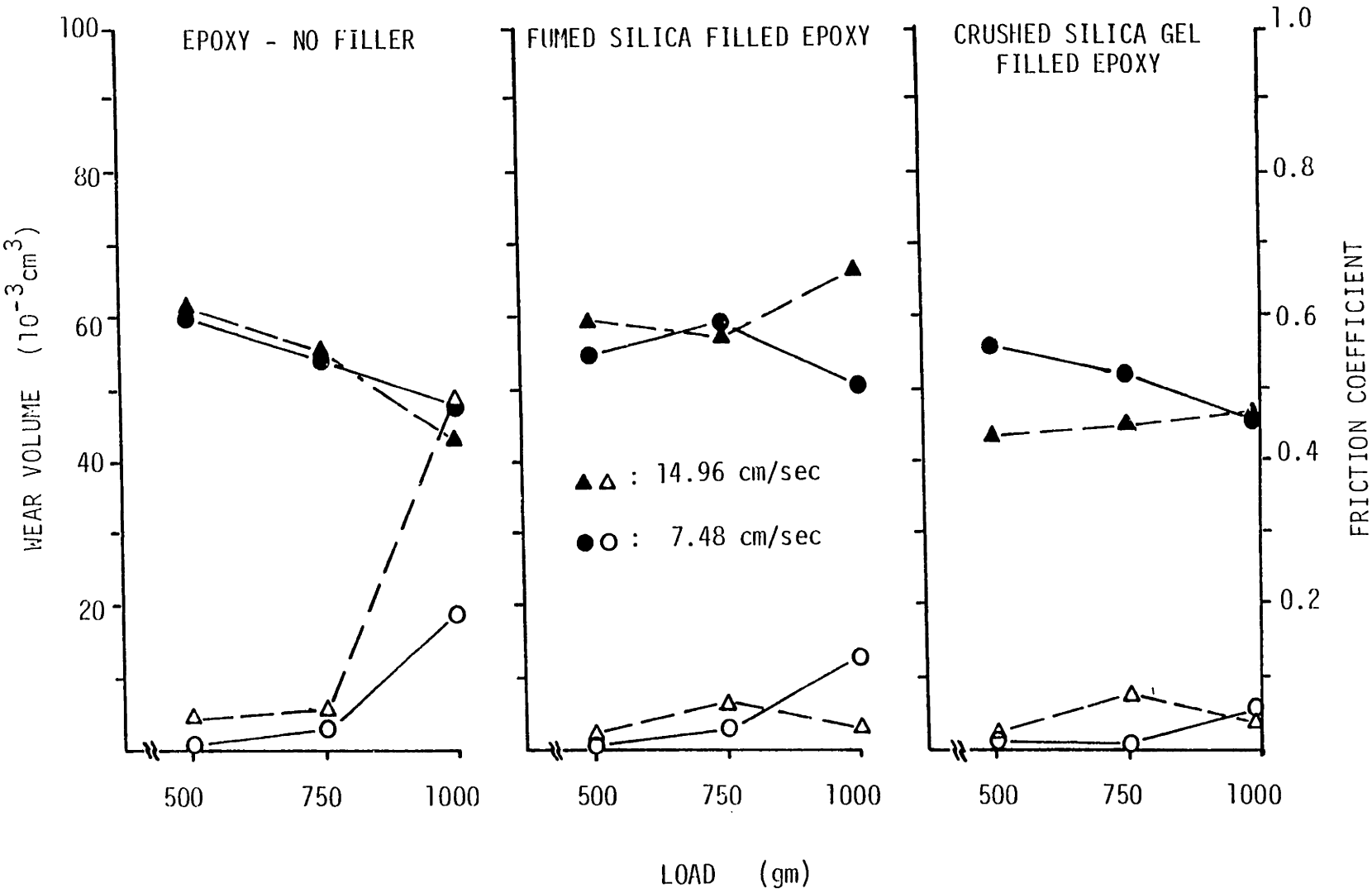

Figure V-18 Comparison of wear and friction coefficient data at 105°C chamber temperature open symbols: wear data, solid symbols: friction coefficients.

which can be used as references to identify subsurface deformation.-- Also, polymer samples are easily susceptible to artifacts introduced in standard microscope sample preparation methods, such as sectioning and polishing. Therefore, more refined sample preparation methods need to be developed in order to acquire direct evidence of subsurface deformation and fracture features. (ii) The role of fillers in a polymeric material can be very different from the inclusions in a metalic material. For example, in metal systems, the hardening effects due to the presence of second phase inclusions are mainly caused by metallurgical transformations as well as entangled dislocation motions. These hardening effects are strongly influenced by heat treatment processes as well as mechanical deformation, and to a lesser degree by the concentration of the second phase inclusions. The increase in hardness in polymers by the addition of fillers is an increase in the average bulk hardness. The addition of fillers does not increase the hardness of the polymer matrix material. The increase in the average bulk hardness is only a function of the filler concentration. Therefore, the parameter "hardness" in most existing wear theories needs to be re-examined carefully when they are applied to the study of polymer composite materials.

VI. CONCLUSIONS

(1) The analytical study on the criterion of void nucleation around second phase inclusions in a ductile material showed that void nucleation follows the energy criterion and is dependent on the size of the inclusions. This finding is confirmed experimentally using a large scale modeling technique, which enabled a direct observation of void nucleation at different magnitudes of applied strain.

(2) The analysis show that the critical inclusion size for void nucleation can be as large as 5 to 10 microns in low modulus polymeric materials, such as polyethylene and polypropylene. Particulate fillers with particle size slightly smaller than this dimension are easily obtained. Therefore, the control of the void nucleation in these materials can easily be achieved. On the other hand, the critical inclusion size is about 1000 to 3000 Å for polymers with high elastic moduli, such as epoxy and most thermosetting polymers. Enormous difficulty is encountered in preparing particle dispersions with filler particles of this dimension. For these materials, pre-existing flaws are difficult to elimenate by standard commercial techniques and consequently, crack propagation is usually the more prevailing failure mode. Under such conditions, the control of crack propagation is a more critical problem than the void nucleation problem.

(3) Based on the energy criterion, the analysis of the void nucleation process showed that the void nucleation consumes only part of the strain energy stored in the matrix-inclusion system. The system still

retains an appreciable amount of strain energy after void nucleation. Energy analyses which assume that all the strain energy stored in the pre-cavitation state goes into the void nucleation process could be erroneous. Therefore, the determination of the energy state after void nucleation is an important part of the energy analysis.

(4) The misfit in moduli between the matrix and the inclusion has an important effect on both the strain energy stored in the system as well as the stress concentration at the matrix-inclusion interface. The modulus misfit effect should be taken into consideration in the design of composite systems.

(5) The results from the wear study were examined in terms of different wear theories. There is strong evidence that adhesive and abrasive wear are not the controlling wear mechanisms in our were experiment. Although the complete process of delamination wear (i.e., plastic deformation, void nucleation and crack propagation) was not observed, the wear is dominated by the microvoid nucleation aspect of the delamination wear, when large particles were used. This is not surprising because the test conditions were designed to favor this type of wear, in order to investigate the particle size effect on the void nucleation aspect of the delamination wear. Experimental results show that the void nucleation aspect of the delamination wear is dependent on the particle size of the fillers in the material. The use of smaller particulate fillers has the effect of reducing wear, when void nucleation is the controlling wear mechanism.

REFERENCES

1. Bowden, F.P. and Tabor, D., The Friction and Lubrication of Solids, Part I and II, Oxford U. Press (1950, 1954, 1964).

2. Rabinowicz, E., Friction and Wear of Materials, Wiley (1965).

3. Archard, J.F., "Contact and Rubbing of Flat Surfaces," J. Appl. Phys., 24, p. 981 (1953).

4. Rabinowicz, E., "Influence of Surface Energy on Friction and Wear Phenomenon," J. Appl. Phys., 32, p. 1440 (1961).

5. Rabinowicz, E., "The Determination of the Compatibility of Metals Through Static Friction Tests," Trans. ASLE, 14, p. 198 (1971).

6. Jahanmir, S., A Fundamental Study on the Delamination Theory of Wear, Ph.D. Thesis, M.I.T. (1976).

7. Suh, N.P., "The Delamination Theory of Wear," Wear, 25, p. 111 (1973).

8. Suh, N.P., *et al*, The Delamination Theory of Wear, Elesevier (1977).

9. Smith, J.O. and Liu, C.K., "Stresses due to Tangential and Normal Loads on an Elastic Solid with Application to Some Contact Stress Problems," J. Appl. Mech., June, p. 157 (1953).

10. Poritsky, H., "Stresses and Deformations of Cylinderical Bodies in Contact with Application to Contacts of Gears and Locomotive Wheels," J. Appl. Mech., June, p. 191 (1950).

11. Suh, N.P. and Jahanmir, S., "Mechanics of Subsurface Void Nucleation in Delamination Wear," Wear, 44, p. 17 (1977).

12. Marwin, J.E. and Johnson, K.L., "An Analysis of Plastic Deformation in Rolling Contact," Proc. Instn. Mech. Engrs., 177, p. 676 (1963).

13. Shooter, K.V. and Tabor, D., "The Frictional Properties of Plastics," Proc. Phys. Soc., London, B-65, p. 661 (1952).

14. Rabinowicz, E. and Shooter, K.V., "The Transfer of Metal to Plastics During Sliding," Proc. Phys. Soc., London, B-65, p. 671 (1952).

15. Makinson, K.R. and Tabor, D., "The Friction and Transfer of Polytetrafluorethylene," Proc. Roy. Soc., A-281, p. 49 (1964).

16. Pooley, C.M. and Tabor, D., "Friction and Molecular Structure: The Behavior of Some Thermoplastics," Proc. Roy. Soc., A-329, p. 251 (1972).

17. Tanaka, K., Uchiyama, Y., and Toyobka, S., "The Mechanism of Wear of Polytetrafluorethylene," Wear, 23, p. 153 (1973).

18. Briscoe, B.J., Pogosian, A.K., Tabor, D., "The Friction and Wear of High Density Polythene: The Action of Lead Oxide and Copper Oxide Filler," Wear, 27, p. 19 (1974).

19. Speerschneider, C.J. and Li, C.H., "The Role of Filler Geometrical Shape in Wear and Friction of Filled PTFE," Wear, 5, p. 362 (1962).

20. Giltrow, J.P. and Lancaster, J.K., "The Role of the Counterface in the Friction and Wear of Carbon Fibre Reinforced Thermosetting Resins," Wear, 16, p. 359 (1970).

21. Sung, N.H. and Suh, N.P., "Friction and Wear of Fiber Reinforced Polymeric Composites," Proc. 38th Annl. Tech. Conf., SPE, p. 311 (1977).

22. Clerico, M., "Sliding Wear of Polymeric Composites," Wear, 53, p. 279 (1979).

23. Lancaster, J.K., "Polymer-based Bearing Materials, The Role of Filler and Fibre Reinforcement," Tribology, Dec., p. 249 (1972).

24. Lewis, R.B., "Wear of Plastics - Evaluation for Engineering Applications," ASME paper, 63-WA-325 (1963).

25. Tetelman, A.S. and McEvily, Jr., A.J., Fracture of Structural Materials, Wiley (1967).

26. Zener, C., "The Micromechanism of Fracture," in Fracturing of Metals, ASM, Metal Park, Ohio (1948).

27. Mott, N.F., "Dislocations, Plastic Flow and Creep," Proc. Roy. Soc., A-220, p. 1 (1953).

28. Stroh, A.N., "The Formation of Cracks as a Result of Plastic Flow," Proc. Roy. Soc., A-223, p. 404 (1954).

29. Stroh, A.N., "The Formation of Cracks in Plastic Flow, II," Proc. Roy. Soc., A-232, p. 548 (1955).

30. Stroh, A.N., "A Theory of the Fracture of Metals," Advances in Phys., 6, p. 418 (1957).

31. Brock, D., "The Role of Inclusions in Ductile Fracture and Fracture Toughness," Eng. Fracture Mech., 5, p. 55 (1973).

32. Friedel, J., Dislocations, Pergamon Press, Oxford (1964).

33. Averbach, B.L., "Micro and Macro Crack Formation," Int. J. Frac. Mech., 2, p. 272 (1966).

34. McMahon, C.J. and Cohen, M., "Initiation of Cleavage in Polycrystalline Iron," Acta Met., 13, p. 591 (1965).

35. Greenwood, J.W., Miller, D.R., and Suiter, J.W., "Intergranular Cavitation in Stressed Metals," Acta Met., 2, p. 250 (1954).

36. Boettner, R.C. and Robertson, W.D., "A Study of the Growth of Voids in Copper During the Creep Process by Measurement of the Accompanying Change in Density," Trans. AIME, 221, p. 613 (1961).

37. Harris, J.E., "Nucleation of Creep Cavities in Magnesium," Trans AIME, 233, p. 1509 (1965).

38. Chang, H.C. and Grant, N.J., "Mechanism of Intercrystalline Fracture," Trans. AIME, 206, p. 544 (1956).

39. Orowan, E., "Dislocations in Metals," Trans. AIME, p. 190 (1954).

40. Johnston, T.L., Stokes, R.J., and Li, C.H., "The Fracture Behavior of Silver Chloride-Alumni," Trans. AIME, 221, p. 792 (1961).

41. Cox, T.B. and Low, Jr., J.R., "An Investigation of the Plastic Fracture of AISI 4340 and 18 Nickel-200 Grade Maraging Steels," Met. Trans., 5, p. 1457 (1974).

42. Puttick, K.E., "Ductile Fracture in Metals," Phil. Maz., ser. 8, 4, p. 964 (1959).

43. Palmer, I.G. and Smith, G.C., "Fracture of Internally Oxidized Copper Alloys," Proc. 2nd Bolton Landing Conf. on Oxide Dispersion Strengthening, Gordon & Breach, p. 253 (1968).

44. Gurland, J. and Plateau, J., "The Mechanism of Ductile Rupture of Metals Containing Inclusions," Trans. ASM, 56, p. 442 (1963).

45. Ashby, M.F., "Work Hardening of Dispersion-Hardened Crystals," Phil. Mag., 14, p. 1157 (1966).

46. Matsuo, M., Wang, T.T., and Kwei, T.K., "Crazing of Polystyrene Containing Two Rubber Balls: A Model for ABS Plastics," J. Polym. Sci., A-2, 10, p. 1085 (1972).

47. Sternberg, E. and Sadowsky, M.A., "On the Axisymmetric Problem of the Theory of Elasticity for an Infinite Region Containing Two Spherical Cavities," J. Appl. Mech., 19, p. 19 (1952).

48. Eshelby, J.D., "The Elastic Interaction of Point Defects," Acta. Met., 3, p. 487 (1955).

49. Eshelby, J.D., "The Continuum Theory of Lattice Defects," Solid State Phys., 3, p. 79 (1956).

50. Li, J.M.C. and Gilman, J.J., "Disclination Loops in Polymers, " J. Appl. Phys., 41, p. 4248 (1970).

51. Bowden, P.B. and Raha, S., "A Molecular Model for Yield and Flow in Amorphous Glassy Polymers Making Use of a Dislocation Analogue," Phil. Mag., 29, p. 149 (1974).

52. Argon, A.S., "A Theory for the Low-Temperature Plastic Deformation of Glassy Polymers," Phil. Mag., 28, p. 839 (1973).

53. Argon, A.S., "Physical Basis of Distortional and Dilational Plastic Flow in Glassy Polymers," J. Macromol. Sci - Phys., B-8, p. 573 (1973).

54. Argon, A.S. and Bessonov, M.I., "Plastic Flow in Glassy Polymers," Polym. Eng. Sci., 17, p. 174 (1977).

55. Goodier, J.N., "Concentration of Stress Around Spherical and Cylindrical Inclusions and Flaws," Trans. ASME, 55, p. 39 (1933).

56. Southwell, R.V. and Gough, H.J., "On the Concentration of Stress in the Neighborhood of a Small Spherical Flow; and on the Properties of Fatigue Fracture in Statistically Isotropic Materials," Phil. Mag., p. 71 (1926).

57. Sadowsky, M.A. and Sternberg, E., "Stress Concentration Around on Ellipsoidal Cavity and Infinite Body Under Arbitrary Plane Stress Perpendicular to the Axis of Revolution of Cavity," J. Appl. Mech., Trans. ASME, 69, p. A191 (1947).

58. Sadowsky, M.A. and Sternberg, E., "Stress Concentration Around a Triaxial Ellipsoidal Cavity," J. Appl. Mech., 16, p. 149 (1949).

59. Edwards, R.H., "Stress Concentrations Around Spheroidal Inclusions and Cavities," J. Appl. Mech., 18, p. 19 (1951).

60. Eshelby, J.D., "The Determination of the Elastic Field of an Ellipsoidal Inclusion, and Related Problems," Proc. Roy. Soc., A-242, p. 376 (1957).

61. Eshelby, J.D., "The Elastic Field Outside an Ellipsoidal Inclusion," Proc. Roy. Soc., A-252, p. 561 (1959).

62. Tanaka, K., Mori, T., and Nakamura, T., "Cavity Formation at the Interface of a Spherical Inclusion in a Plastically Deformed Matrix," Phil. Mag., 21, p. 267 (1970).

63. Haung, W.C., "Theoretical Study of Stress Concentrations at Circular Holes and Inclusions in Strain Hardening Materials," Int. J. Solids Structures, 8, p. 149 (1972).

64. Orr, J. and Brown, D.K., "Elasto-Plastic Solution for a Cylindrical Inclusion in Plane Strain," Eng. Fracture Mech., 6, p. 261 (1974).

65. Rhee, S.S. and McClintock, F.A., "On the Effects of Strain Hardening on Strain Concentrations," Proc. 4th Ntl. Cong. Appl. Mech., ASME, N.Y., 2, p. 1007 (1962).

66. Argon, A.S., Im, J., and Safogla, R., "Cavity Formation From Inclusions in Ductile Fracture," Meta. Trans., 6A, p. 825 (1975).

67. Argon, A.S., "Formation of Cavities from Non-deformable Second-Phase Particles in Low Temperature Ductile Fracture," J. Eng. Mat. Tech., Trans. ASME, p. 60 (1976).

68. Orowan, E., "Fracture and Strength of Solid," Repts. Prog. Phys., p. 185 (1949).

69. Gilman, J.J., in Fracture, Averback, B.L. *et al* eds., M.I.T., Wiley, N.Y., p. 193 (1959).

70. Gilman, J.J. Strength of Ceramic Crystals, Amer. Ceramic Soc. Conf., N.Y., April (1972).

71. Tyson, W.R., "Theoretical Strength of Perfect Crystals," Phil. Mag., 14, p. 925 (1966).

72. Kelly, A., Tyson, W.R., and Cottrell, A.H., "Ductile and Brittle Crystals," Phil. Mag., 15, p. 567 (1967).

73. Sin, H., Saka, N. and Suh, N.P., "Abrasive Wear and the Girit Size Effect," Wear, 55, p. 163 (1979).

74. Jahanmir, S., Abrahamson, E.P., and Suh, N.P., "The Effect of Second Phase Particles on the Sliding Wear of Metals," Proc. 3rd. North American Metalworking Research Conf., Soc. Mfg. Eng. (1975).

75. Suh, N.P. and Turner, A.P.L., Elements of the Mechanical Behavior of Solids, McGraw-Hill (1975).

76. Rabinowicz, E., "The dependence of the adhesive wear coefficient on the surface energy of adhesion," Wear of Materials, The Intl. Conf. on Wear of Materials, ASME, p. 36 (1977).

77. Suh, N.P., Sin, H., Tohkai, M., and Saka, N., "Surface Topography and Functional Requirements for Dry Sliding Surfaces," to be

published in ann. CIRP, 1980.

78. Fleming, J.R. and Suh, N.P., "Mechanics of Crack Propagation in Delamination Wear," Wear, 44, p. 39 (1977).

Appendix A

DERIVIATION OF FORMULARS USED IN APPLYING ESHELBY'S METHOD TO THE INCLUSION AND INHOMOGENEITY PROBLEM

Before deriving the equations, some useful-elastic relations are listed here for reference. Displacement u_i, strain e_{ij} and stress p_{ij} are related by,

$$e_{ij} = \frac{1}{2}(u_{i,j} + u_{j,i})$$

$$p_{ij} = \lambda e_{mm}\delta_{ij} + 2\mu e_{ij} \qquad \text{(A-1)}$$

Where λ is the Lamé constant and μ is the shear modulus. These relations are sometimes more convenient to manipulate when they are expressed in scalar and deviatoric components,

$$p = p_{mm}$$

$$'p_{ij} = p_{ij} - \frac{1}{3}\delta_{ij}p \qquad \text{(A-2)}$$

and

$$e = e_{mm}$$

$$'e_{ij} = e_{ij} - \frac{1}{3}\delta_{ij}e \qquad \text{(A-3)}$$

The stress strain relationship becomes,

$$p = 3Be$$

$$'p_{ij} = 2\mu\,'e_{ij} \qquad \text{(A-4)}$$

Where B is the bulk modulus. B and μ are related to the tensile modulus E and Poisson's ratio ν by,

$$B = \lambda + \frac{2}{3}\mu = \frac{E}{3(1-2\nu)} \qquad (A-5)$$

$$\mu = \frac{E}{2(1+\nu)}$$

(1) RELATION BETWEEN THE CONSTRAINED FIELD AND THE TRANSFORMATION FIELD:

In Eshelby's analysis of the inclusion and the inhomogeneity problem (Chapter III, Section D), the relation between the final constrained state and the transformation state must be found in order to solve the problem. This relation can be determined by examining the last two steps of the cutting and rewelding process performed on the inclusion and the inhomogeneity (figure III-6 and figure III-7). The free body diagrams of the inclusion and the matrix are reproduced in figure A-1. When the transformed inclusion is inserted back into the matrix, the matrix is still free of stress. The inclusion has a surface traction $-p^T_{ij}$ applied on its surface. After the insertion is completed, the surface traction on the inclusion $-p^T_{ij}$ is removed by applying another surface traction $+p^T_{ij}$ on both the inclusion and the matrix, and result in the final constrained state. Therefore the solution of the constrained state for either the matrix or the inclusion is exactly that of solving the problem of an elastic body subjected to a load distributed over its surface S. The solution of the displacement $\bar{u}$ at any point $\bar{r}$ due to a point load F_1 in the X_1 direction applied at $\bar{r}'$ in an elastic media can be found in

Love [A-1],

$$u_1 = -\frac{(\lambda+\mu)}{8\pi\mu(\lambda+2\mu)} F_1 \frac{\partial^2(r-r')}{\partial x_1^2} + \frac{1}{4\pi\mu(r-r')} F_1$$

$$u_2 = -\frac{(\lambda+\mu)}{8\pi\mu(\lambda+2\mu)} F_1 \frac{\partial^2(r-r')}{\partial x_1 \partial x_2} \qquad \text{(A-6)}$$

$$u_3 = -\frac{(\lambda+\mu)}{8\pi\mu(\lambda+2\mu)} F_1 \frac{\partial^2(r-r')}{\partial x_1 \partial x_3}$$

Equation A-1 can be generalized to include forces in the x_2 and x_3 directions,

$$u_j = \frac{1}{4\pi\mu(r-r')} F_j - \frac{\lambda+\mu}{8\pi\mu(\lambda+2\mu)} F_\ell \frac{\partial^2(r-r')}{\partial x_\ell \partial x_j} \qquad \text{(A-7)}$$

In our case, u_j is the displacement in the constrained state u_j^C. The Load F_j is the surface traction $p_{jk}^T dS_k$. Next, we integrate over the surface S where p_{jk}^T is applies, and transform to an integral over the volume of the inclusion. Notice that $\partial|r-r'|/\partial x_i = -\partial|r-r'|/\partial x_i'$. Equation A-7 becomes,

$$u_j^C = \int_S \left[\frac{1}{4\pi\mu} \frac{p_{jk}^T dS_k}{(r-r')} - \frac{\lambda+\mu}{8\pi\mu(\lambda+2\mu)} p_{\ell k}^T \frac{\partial^2(r-r')}{\partial x_\ell \partial x_j} dS_k\right]$$

$$= -\int_V \frac{1}{4\pi\mu} p_{jk}^T \frac{\delta}{\delta x_k}\left(\frac{1}{r-r'}\right)dv + \int_V \frac{\lambda+\mu}{8\pi\mu(\lambda+2\mu)} p_{\ell k}^T \frac{\partial^3}{\partial x_\ell \partial x_j \partial x_k}(r-r')dv$$

$$= \frac{-1}{4\pi\mu} P^T_{jk} \phi_{,k} + \frac{\lambda+\mu}{8\pi\mu(\lambda+2\mu)} P^T_{\ell k} \psi_{,\ell jk} \qquad \text{(A-8)}$$

where:

$$\phi = \int_v \frac{1}{(r-r')} \, dv \qquad \text{is the Newtonian potential}$$

$$\psi = \int_v (r-r') \, dv \qquad \text{is the bihamonic potential} \qquad \text{(A-9)}$$

apply the relations:

$$\lambda = B - \frac{2}{3}\mu = \frac{E}{3(1-2\nu)} - \frac{2}{3}\mu$$

$$\mu = \frac{E}{2(1+\nu)}$$

equation A-8 becomes,

$$u^C_j = \frac{-1}{4\pi\mu} P^T_{jk} \phi_{,k} + \frac{1}{16\pi\mu(1-\nu)} P^T_{\ell k} \psi_{,\ell jk} \qquad \text{(A-10)}$$

The strain is related to the displacement by:

$$e^C_{ij} = \frac{1}{2}(u^C_{i,j} + u^C_{j,i})$$

$$= \frac{1}{2}\left[\frac{-1}{4\pi\mu}(P^T_{ik}\phi_{,kj} + P^T_{jk}\phi_{,ki}) + \frac{1}{16\pi\mu(1-\nu)} P^T_{\ell k}(\psi_{,\ell ikj} + \psi_{,\ell jki})\right]$$

(A-11)

For a particular inclusion shape, if only the geometric functions $\phi_{,ij}$ and $\psi_{,ijk\ell}$ can be evaluated, and further apply the stress-strain relation to the transformation stress p^T_{ij} in equation A-11. The relation between the constrained strain e^C_{ij} to the transformed strain e^T_{ij} will be established. $\phi_{,ij}$ and $\psi_{,ijk\ell}$ can be evaluated for a general ellipsoidal shape inclusion, and the relation between e^C_{ij} and e^T_{ij} is expressed as:

$$e^C_{ij} = S_{ijk\ell} e^T_{k\ell} \qquad \text{(A-12)}$$

The explicit form of the $S_{ijk\ell}$ tensor for an ellipsoidal inclusion is given by Chow [A-2, A-3]. An even more specialized case, the spherical inclusion, which is relevant to our investigation, is presented here.

For a spherical inclusion,

$$S_{ijk\ell} = \frac{1}{3}(\alpha-\beta)\delta_{ij}\delta_{k\ell} + \frac{1}{2}\beta(\delta_{ik}\delta_{j\ell} + \delta_{i\ell}\delta_{jk}) \qquad \text{(A-13)}$$

Where:

$$\left\{ \begin{array}{l} \alpha = \dfrac{(1+\nu)}{3(1-\nu)} \\ \beta = \dfrac{2}{15}\dfrac{(4-5\nu)}{(1-\nu)} \end{array} \right. \qquad \text{(A-14)}$$

and δ_{ij} is the Kronecker delta. Therefore,

$$S_{mmmm} = \frac{(7-5\nu)}{15(1-\nu)}$$

$$S_{mmnn} = \frac{(5\nu-1)}{15(1-\nu)}$$

$$\{ \quad S_{mnmn} = \frac{(4-5\nu)}{15(1-\nu)} \qquad \text{(A-15)}$$

$$S_{mnnm} = \frac{(4-5\nu)}{15(1-\nu)}$$

and all other components of $S_{ijk\ell}$ are zeros.

Equation A-12 takes a simple explicit form when expressed in the scalar and deviatonic terms.

$$e^C = \left[\frac{1}{3}\frac{(1+\nu)}{(1-\nu)}\right] e^T = \alpha e^T$$

$$'e^C_{ij} = \left[\frac{2}{15}\frac{(4-5\nu)}{(1-\nu)}\right] e^T_{ij} = \beta' e^T_{ij} \qquad \text{(A-16)}$$

Equation A-16 is the transformation relation between the constrained state and the transformation state for a spherical inclusion.

(2) RELATION BETWEEN THE TRANSFORMATION FIELD AND THE APPLIED FIELD:

Knowledge of the relation between the constrained and transformation states is not sufficient for solving the inhomogeneity problem. We also need to know the relation between the transformation and the applied fields. To establish the latter relation. We observed that if the inhomogeneity had not been subjected to the cutting, replacement, transformation and rewelding process, then the stresses in the inclusion would

have been,

$$p^I = 3B^*(e^C + e^A)$$

$$'p^I_{ij} = 2\mu^*('e^C_{ij} + 'e^A_{ij}) \qquad \text{(A-17)}$$

Where B^* and μ^* are the bulk modulus and the shear mudulus of the inhomogeneity. In applying Eshelby's method, the inhomogeneity is replaced by an equivalent inclusion made of the same material as the matrix phase. In this case, the stresses in the inclusion becomes

$$p^I = 3B(e^C + e^A - e^T)$$

$$'p^I_{ij} = 2\mu('e^C_{ij} + 'e^A_{ij} - 'e^T_{ij}) \qquad \text{(A-18)}$$

Where B and μ are the bulk and shear modulus of the matrix. These two expressions (equations A-17 and A-18) for the inclusion stresses should be equivalent. Therefore,

$$B^*(e^C + e^A) = B(e^C + e^A - e^T) \qquad \text{(A-19a)}$$

$$\mu^*('e^C_{ij} + 'e^A_{ij}) = \mu\,('e^C_{ij} + 'e^A_{ij} - 'e^T_{ij}) \qquad \text{(A-19b)}$$

For the deviatoric components $'e_{ij}$, only the second equation has to be satisfied. By replacing $'e^C_{ij}$ with $'e^T_{ij}$ through equation A-12 we obtained

for a general ellipsoidal inclusion:

$$'e_{ij}^{T} = \frac{\mu - \mu^*}{2S_{1212}(\mu^* - \mu) + \mu} \; 'e_{ij}^{A} \qquad \text{(A-20)}$$

in the special case of a sphere, where $\beta = 2S_{1212}$ (from equations A-14 and A-15),

$$'e_{ij}^{T} = \left[\frac{\mu - \mu^*}{\beta(\mu^* - \mu) + \mu}\right] \; 'e_{ij}^{A} \qquad \text{(A-21)}$$

Both equations A-19a and A-19b have to be applied in order to solve for the scalar component e. When i = j, for example, i = j = 1, and from equation A-3, $'e_{11}$ can be replaced by $'e_{11} = e_{11} - \frac{1}{3} e$, equation A-19b becomes:

$$\mu^*(e_{11}^{C} + e_{11}^{A}) - \frac{1}{3}\mu^*(e^{C} + e^{A}) = \mu(e_{11}^{C} + e_{11}^{A} - e_{11}^{T}) - \frac{1}{3}\mu(e^{C}+e^{A}-e^{T}) \qquad \text{(A-22)}$$

Applying the relation $B = \lambda + \frac{2}{3}\mu$ from equation A-5, gives,

$$\mu^*(e_{11}^{C} + e_{11}^{A}) + \frac{1}{2}(\lambda^* - B^*)(e^{C} + e^{A}) = \mu(e_{11}^{C} + e_{11}^{A} - e_{11}^{T}) +$$

$$\frac{1}{2}(\lambda - B)(e^{C} + e^{A} - e^{T}) \qquad \text{(A-23)}$$

Substitute equation A-19a in the above relation:

$$2\mu^*(e^C_{11} + e^A_{11}) + \lambda^*(e^C + e^A) = 2\mu(e^C_{11} + e^A_{11} - e^T_{11}) +$$

$$\lambda(e^C + e^A - e^T) \qquad \text{(A-24)}$$

Applying the relation between the constrained state and the transformation state, $e^C_{ij} = S_{ijk\ell}\, e^T_{k\ell}$, the above equation becomes:

$$2\mu^*(S_{11k\ell}e^T_{k\ell} + e^A_{11}) + \lambda^*(S_{jjk\ell}e^T_{k\ell} + e^A)$$

$$= 2\mu(S_{11k\ell}e^T_{k\ell} + e^A_{11} - e^T_{11}) + \lambda(S_{jjk\ell}e^T_{k\ell} + e^A - e^T) \qquad \text{(A-25)}$$

Equation A-25 holds for a general ellipsoidal inclusion geometry. In the following steps, we will solve for the transformation state in the special case of a spherical inclusion by applying the explicit expression for $S_{ijk\ell}$ (equation A-15). First, we define the following terms,

$$\gamma_1 = S_{1111} = S_{2222} = S_{3333} = \frac{7 - 5\nu}{15(1 - \nu)} \qquad \text{(A-26)}$$

$$\gamma_2 = S_{1122} = S_{2233} = S_{3311} = S_{2211} = S_{3322} = S_{1133}$$

$$= \frac{5\nu - 1}{15(1 - \nu)}$$

Substituting into equation A-25 gives,

(A-27)

$$2\mu^*(\gamma_1 e_{11}^T + \gamma_2 e_{22}^T + \gamma_2 e_{33}^T + e_{11}^A) + \lambda^*[(\gamma_1 + 2\gamma_2)e^T + e^A]$$

$$= 2\mu(\gamma_1^T e_{11}^T + \gamma_2 e_{22}^T + \gamma_2 e_{33}^T + e_{11}^A - e^T) + \lambda[(\gamma_1 + 2\gamma_2)e^T + e^A - e^T]$$

The above relation can be derived in a similar fashion for the 22, and 33 components. Summing up these three equations for the three component directions yields,

$$3(\lambda^* - \lambda)\ (\gamma_1 + 2\gamma_2)\ e^T + 3\lambda e^T + 2\mu e^T + 2(\mu^* - \mu)\ (\gamma_1 + 2\gamma_2)e^T$$

$$= 3(\lambda - \lambda^*)\ e^A + 2(\mu - \mu^*)\ e^A$$

$$\left\{(\gamma_1 + 2\gamma_2)\ [(\lambda^* - \lambda) + \frac{2}{3}\ (\mu^* - \mu)] + (\lambda + \frac{2}{3}\ \mu)\right\}\ e^T$$

$$= [(\lambda - \lambda^*) + \frac{2}{3}\ (\mu - \mu^*)]\ e^A \qquad \text{(A-28)}$$

Notice that $B = \lambda + \frac{2}{3}\mu$ and from equations A-26 and A-14,

$$\gamma_1 + 2\gamma_2 = \frac{7 - 5\nu}{15(1 - \nu)} + 2\ \frac{5\nu - 1}{15(1 - \nu)} = \frac{1}{3}\ (\frac{1 + \nu}{1 - \nu}) = \alpha$$

Therefore, equation A-28 becomes,

$$e^T = \left[\frac{B - B^*}{\alpha(B^* - B) + B}\right] e^A \qquad \text{(A-29)}$$

Equations A-21 and A-29 are the relations between the transformation field and the known applied field for a spherical inhomogeneity.

(3) STRESS CONCENTRATION AT THE MATRIX-INCLUSION INTERFACE:

In Eshelby's approach, an elegant method is used to solve the stress concentration problem. The results were presented without deviation in his paper [60, 61]. The method is explained here alone with the deviation for both the general case of an inclusion of arbitrary shape, and the special case of a spherical inclusion.

Equation A-11 shows that the strain in the final constrained state is:

$$e^C_{ij} = \frac{1}{2}\left[\frac{-1}{4\pi\mu}\left(p^T_{ik}\phi_{,kj} + p^T_{jk}\phi_{,ki}\right) + \frac{1}{16\mu\pi(1-\nu)} p^T_{\ell k}\left(\psi_{,\ell ikj} + \psi_{,\ell jki}\right)\right]$$

which involves the ∇^2 of the Newtonian potential ϕ and the $\nabla^2\nabla^2$ of the biohamonic potential ψ, where ϕ and ψ are defined in equation A-9 as,

$$\phi = \int_V \frac{1}{(r - r')} \, dv$$

$$\psi = \int_V (r - r') \, dv$$

The Newtonian potential ϕ satisfies the Poisson's equation:

$$\nabla^2 \phi = -4\pi \tag{A-30}$$

In the following deriviations, the reader is referred to references on the characteristics of potential functions that satisfy the Poisson's equation, such as in Kellogg [A-4]. ∇^2 of functions of this type experiences a jumpof -4π when passing from an exterior point to an interior point through the boundary S. Therefore,

$$(\phi_{,ij})_{out} - (\phi_{,ij})_{in} = 4\pi n_i n_j \tag{A-31}$$

whre n_i, n_j, are direction cosines of the surface normal to the i and j reference axes. The bihamonic potential ψ is related to the Newtonian potential ϕ by,

$$\nabla^2 \psi = 2\phi \tag{A-32}$$

which can be derived from equation A-9. Therefore, $\nabla^2 \psi$ will also satisfy the Poisson's equation,

$$\nabla^2(\nabla^2\psi) = \nabla^2(2\phi) = -8\pi \tag{A-33}$$

and the jump of $\nabla^2(\nabla^2\psi)$ across the boundary will be,

$$(\psi_{,ijk\ell})_{out} - (\psi_{,ijk\ell})_{in} = 8\pi n_i n_j n_k n_\ell \tag{A-34}$$

For normal strain components, where i = j, equation A-11 reduces to:

$$e^C_{ij} = \frac{-1}{4\pi\mu} p^T_{ik}\phi_{,ki} + \frac{1}{16\pi\mu(1-\nu)} p^T_{\ell k}\psi_{,\ell iki} \tag{A-35}$$

Applying equations A-31, A-34 and A-35, the difference between the normal strain across the matrix inclusion boundary is,

$$\Delta e^C_{ii} = (e^C_{ii})_{out} - (e^C_{ii})_{in}$$

$$= \frac{-1}{4\pi\mu} p^T_{ik} \cdot 4\pi n_k n_i + \frac{1}{16\pi\mu(1-\nu)} p^T_{\ell k} \cdot 8\pi n_\ell n_i n_k n_i$$

$$= -\frac{1}{\mu} p^T_{ik}\, n_k n_i + \frac{1}{2\mu(1-\nu)} p^T_{\ell k}\, n_\ell n_i n_k n_i \tag{A-36}$$

For example, equation A-36 can be expressed explicity for the 11 component,

$$\Delta e^C_{11} = \frac{-1}{\mu}(p^T_{11}n_1n_1 + p^T_{12}n_1n_2 + p^T_{13}n_1n_3) + \frac{1}{2\mu(1-\nu)} n_1n_1(p^T_{\ell k}n_\ell n_k) \tag{A-37}$$

Similar results can be derived for the 22 and 33 components. Summing up these three components gives;

$$\Delta e^C = (e^C)_{out} - (e^C)_{in}$$

$$= \frac{-1}{\mu} (p^T_{\ell k} n_\ell n_k) + \frac{1}{2(1-\nu)} (p^T_{\ell k} n_\ell n_k)(n_{11} + n_{22} + n_{33}) \qquad \text{(A-38)}$$

For the directional cosines, $n_{11} + n_{22} + n_{33} = 1$. By changing the $p^T_{\ell k}$ into its scalar and deviatoric components and applying the stress-strain relation in equation A-4, we arrive at the result shown in Eshelby's paper,

$$\Delta e^C = (e^C)_{out} - (e^C)_{in}$$

$$= -\frac{1}{3} \frac{(1+\nu)}{(1-\nu)} e^T - \frac{(1-2\nu)}{(1-\nu)} e^T_{\ell k} n_\ell n_k \qquad \text{(A-39)}$$

For arbitrary i and j, from equations A-11, A-31 and A-34,

$$\Delta e^C_{ij} = (e^C_{ij})_{out} - (e^C_{ij})_{in}$$

$$= \frac{1}{2} \left[\frac{-1}{4\pi\mu} (p^T_{ik} \cdot 4\pi n_k n_j + p^T_{jk} \cdot 4\pi n_i n_k) \right.$$

$$\left. + \frac{1}{16\pi\mu(1-\nu)} p^T_{\ell k} (8\pi n_\ell n_i n_k n_j + 8\pi n_\ell n_j n_k n_i) \right]$$

$$= \frac{1}{2}\left[-\frac{1}{\mu}\left(p^T_{ik}n_k n_j + p^T_{jk}n_i n_k\right) + \frac{1}{\mu(1-\nu)}\,p^T_{\ell k}n_\ell n_i n_k n_j\right] \tag{A-40}$$

Notice that $n_\ell n_k \delta_{\ell k} = 1$, and $n_k n_j \delta_{ik} = n_i n_j$. Then, by changing Δe^C_{ij}, p^T_{ik}, p^T_{jk} and $p^T_{\ell k}$ into their scalar and deviation components, and applying the stress-strain relation in equation A-4, we observe:

$$\Delta' e^C_{ij} = (' e^C_{ij})_{out} - (' e^C_{ij})_{in} \tag{A-41}$$

$$= \frac{1}{1-\nu}\,' e^T_{\ell k}n_\ell n_i n_k n_j - ' e^T_{ik}n_k n_j - ' e^T_{jk}n_i n_k$$

$$+ \frac{(1-2\nu)}{3(1-\nu)}\,e^T n_\ell n_k \delta_{ij} - \frac{1}{3}\,\frac{(1+\nu)}{(1-\nu)}\,e^T\left(n_i n_j - \frac{1}{3}\,\delta_{ij}\right).$$

Equations A-39 and A-41 are results that are presented in Eshelby's paper. The stresses in the constrained state immediately outside the inclusion, $(p^C)_{out}$ and $('p^C)_{out}$, can be obtained by applying the stress-strain relationships to equations A-39 and A-41,

$$\Delta p^C = (p^C)_{out} - (p^C)_{in}$$

$$= -\frac{1}{3}\,\frac{(1+\nu)}{(1-\nu)}\,p^T - \frac{(1+\nu)}{(1-\nu)}\,' p^T_{ij}n_i n_j \tag{A-42}$$

$$\Delta' p^C_{i\ell} = (' p^C_{i\ell})_{out} - (' p^C_{i\ell})_{in}$$

$$= \frac{1}{1-\nu} ' p^T_{jk} n_j n_k n_i n_\ell - ' p^T_{ik} n_k n_\ell - ' p^T_{\ell k} n_k n_i$$

$$+ \frac{(1-2\nu)}{3(1-\nu)} ' p^T_{jk} n_j n_k \delta_{i\ell} - \frac{1}{3} \frac{(1-2\nu)}{(1-\nu)} p^T (n_i n_\ell - \frac{1}{3} \delta_{i\ell}) \quad \text{(A-43)}$$

Notice that the subscripts j and ℓ were switched around when deriving equation A-43 from equation A-41. This is for the convenience of the readers to follow Eshelby's paper in later derived equations. Equations A-42 and A-43 show that $(p^C)_{out}$ and $('p^C)_{out}$ can be found requiring only the knowledge of the elastic field inside the inclusion and of the transformation state. The above equations apply to inclusions of arbitrary shape.

For the special case of a spherical inclusion, the explicit transformation relations in equations A-16, A-21 and A-29 are applied to equations A-42 and A-43. These transformation relations are reproduced below for the benefit of the readers.

$$e^C = \alpha e^T \quad \text{(A-16)}$$

$$' e^C_{ij} = \beta ' e^T_{ij}$$

$$e^T = C e^A \quad \text{(A-29)}$$

$$' e^T_{ij} = D ' e^A_{ij} \quad \text{(A-21)}$$

Where:

$$\alpha = \frac{1}{3}\frac{(1+\nu)}{(1-\nu)}$$

$$\beta = \frac{2}{15}\frac{(4-5\nu)}{(1-\nu)}$$

and

$$C = \frac{B - B^*}{\alpha(B^* - B) + B}$$

$$D = \frac{\mu - \mu^*}{\beta(\mu^* - \mu) + \mu}$$

Equations A-42 and A-43 becomes,

$$\Delta p^C = -\alpha C p^A - \frac{(1+\nu)}{(1-\nu)} D' p^A_{ij} n_i n_j \qquad \text{(A-44)}$$

$$\Delta' p^C_{i\ell} = \frac{1}{(1-\nu)} D' p^A_{jk} n_j n_k n_i n_\ell - D('p^A_{ik} n_k n_\ell + {}'p^A_{\ell k} n_k n_\ell)$$

$$+ \frac{(1-2\nu)}{3(1-\nu)} D' p^A_{jk} n_j n_k \delta_{i\ell} - \frac{(1-2\nu)}{3(1-\nu)} C p^A (n_i n_\ell - \frac{1}{3}\delta_{i\ell}) \qquad \text{(A-45)}$$

The stresses at the boundary of the matrix phase are,

$$(p^M)_{Boundary} = (p^C)_{out} + p^A$$

$$= (p^C)_{in} + \Delta p^C + p^A$$

$$= (\alpha C + 1)p^A + \Delta p^C \qquad \text{(A-46)}$$

$$('p^M_{i\ell})_{Boundary} = ('p^C_{i\ell})_{out} + 'p^A_{i\ell}$$

$$= ('p^C_{i\ell})_{in} + \Delta'p^C_{i\ell} + 'p^A_{i\ell}$$

$$= (\beta D + 1)'p^A_{i\ell} + \Delta'p^C_{i\ell} \qquad \text{(A-47)}$$

Substitute equations A-44 and A-45 for Δp^C and $\Delta' p^C_{i\ell}$ in equations A-46 and A-47 results in,

$$(p^M)_{Boundary} = p^A - \frac{(1 + \nu)}{(1 - \nu)} D'p^A_{ij} n_i n_j \qquad \text{(A-48)}$$

$$('p^M_{i\ell})_{Boundary} = (1 + \beta D)'p^A_{i\ell} + \frac{1}{1 - \nu} D'p^A_{jk} n_j n_k n_i n_\ell$$

$$- D('p^A_{ik} n_k n_\ell + 'p^A_{\ell k} n_k n_i) + \frac{(1 - 2\nu)}{3(1 - \nu)} D'p^A_{jk} n_j n_k \delta_{i\ell}$$

$$- \frac{1}{3} \frac{(1 - 2\nu)}{(1 - \nu)} Cp^A (n_i n_\ell - \frac{1}{3} \delta_{i\ell}) \qquad \text{(A-49)}$$

Equations A-48 and A-49 are the solutions to the stress concentration around a spherical inclusion when subjected to an applied stress field $p^A_{i\ell}$. With reference to the coordinates chosen in figure A-2 for a sphere,

the directional cosins of the surface normal are:

$$n_1 = \sin \phi \cos \theta$$

$$n_2 = \sin \phi \cos \theta$$

$$n_3 = \cos \phi$$

Figure A-3 and A-4 show the resulting stress concentration at the boundary of a spherical inhomogeneity subjected to uniaxial tension and pure shear, respectively.

References

A-1. Love, A.E.H., Mathematical Theory of Elasticity, Dover (1927).

A-2. Chows, T.S., "Elastic Moduli of Filled Polymers: The Effect of Particle Shape," J. Appl. Phys., 48, p. 4072 (1977).

A-3. Chows, T.S., "Effect of Particle Shape at Finite Concentration on the Elastic Moduli of Filled Polymers," J. Polym. Sci., Poly. Phys., 16, p. 959 (1978).

A-4. Kellogg, O.D., Foundations of Potential Theories, Dover (1953).

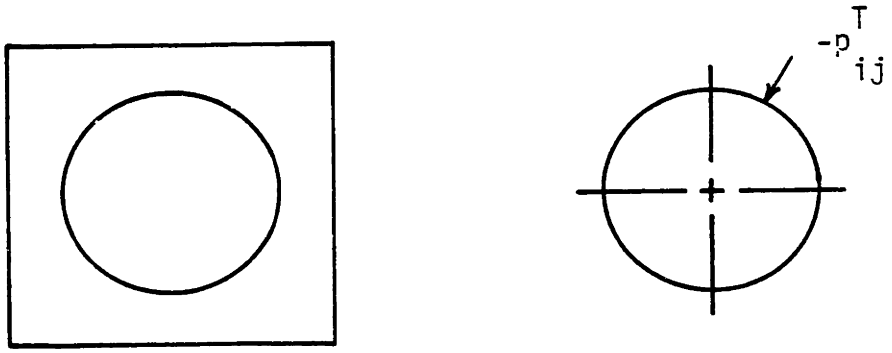

(a) Before insertion of the transformed inclusion

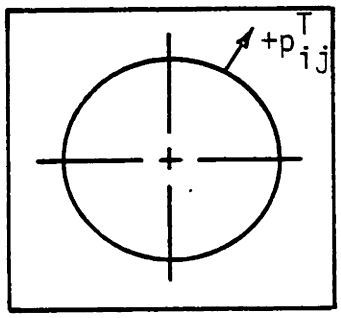

(b) After insertion of the transformed inclusion, apply $+p^T_{ij}$ at the interface to remove $-p^T_{ij}$ from the inclusion

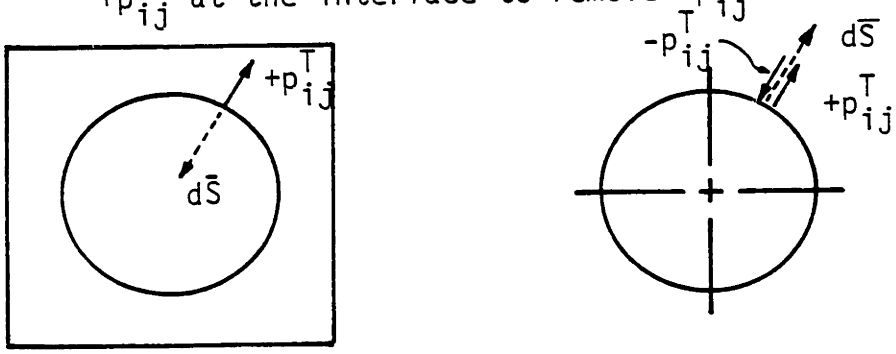

(c) Free body diagram of the matrix and the inclusion in (b)

Figure A-1 Illustration of Eshelby's approach to the inclusion problem. Refer also to figure III-6.

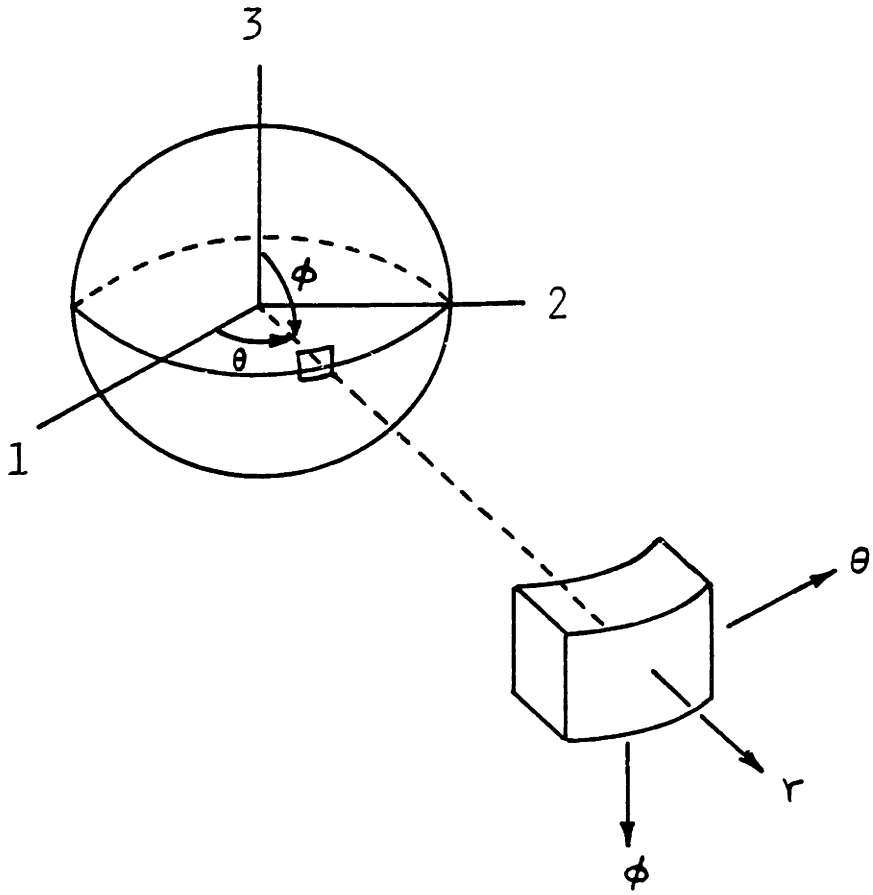

Figure A-2 Coordinate system for a spherical inclusion.

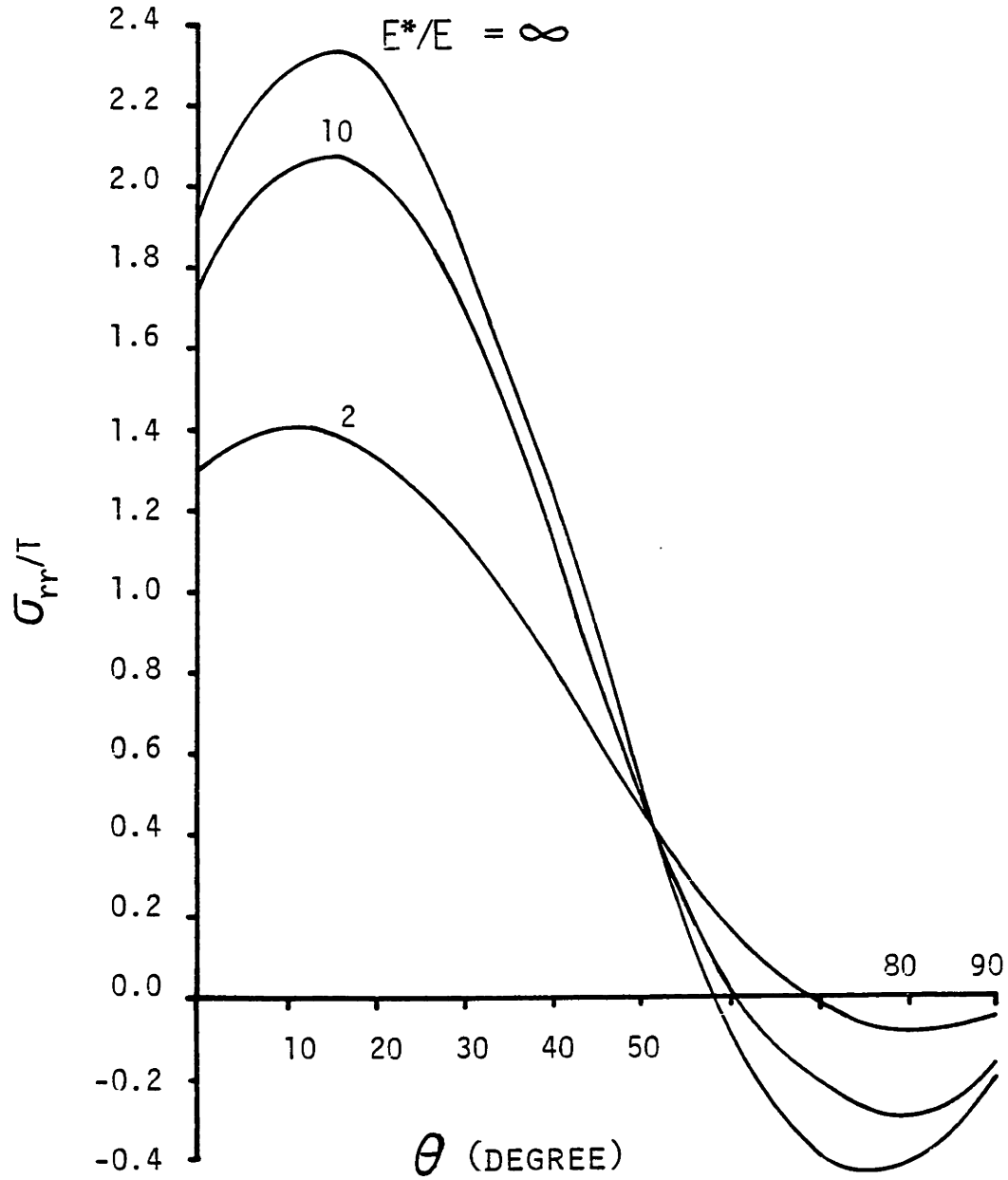

Figure A-3(a) Stress concentration σ_{rr}/T at the surface of a spherical inclusion for $\phi = 90°$, under uniaxial tension $\sigma_{11} = T$.

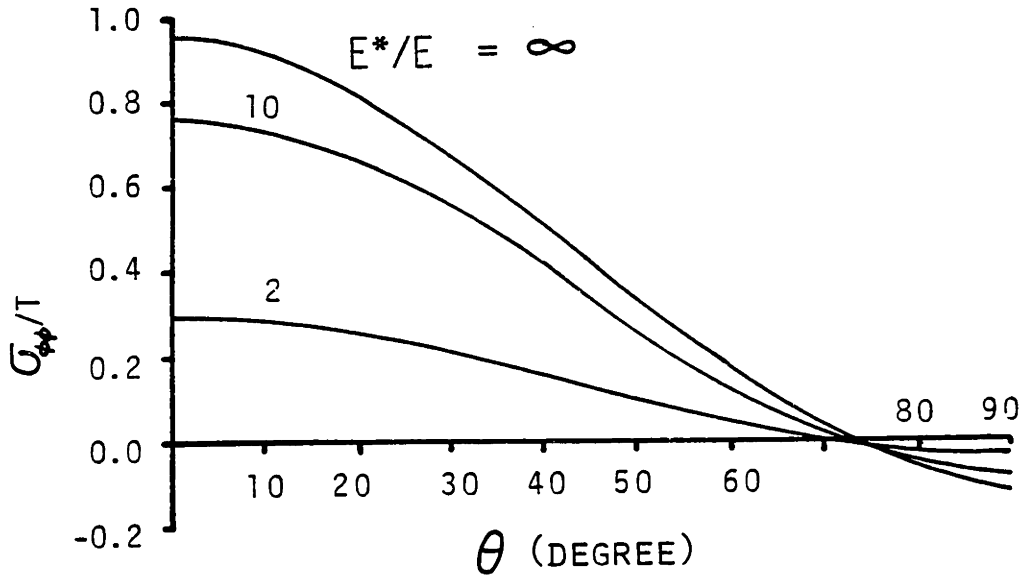

Figure A-3(b) Stress concentration $\sigma_{\phi\phi}/T$ at the surface of a spherical inclusion for $\phi = 90°$, under uniaxial tension $\sigma_{11} = T$.

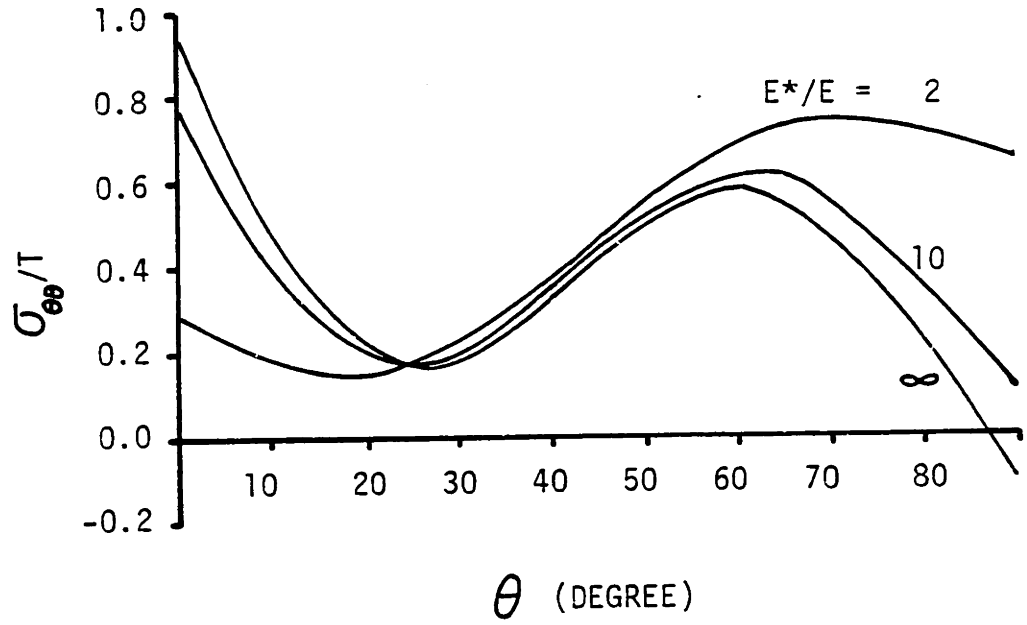

Figure A-3(c) Stress concentration $\sigma_{\theta\theta}/T$ at the surface of a spherical inclusion for $\phi = 90°$, under uniaxial tension $\sigma_{11} = T$.

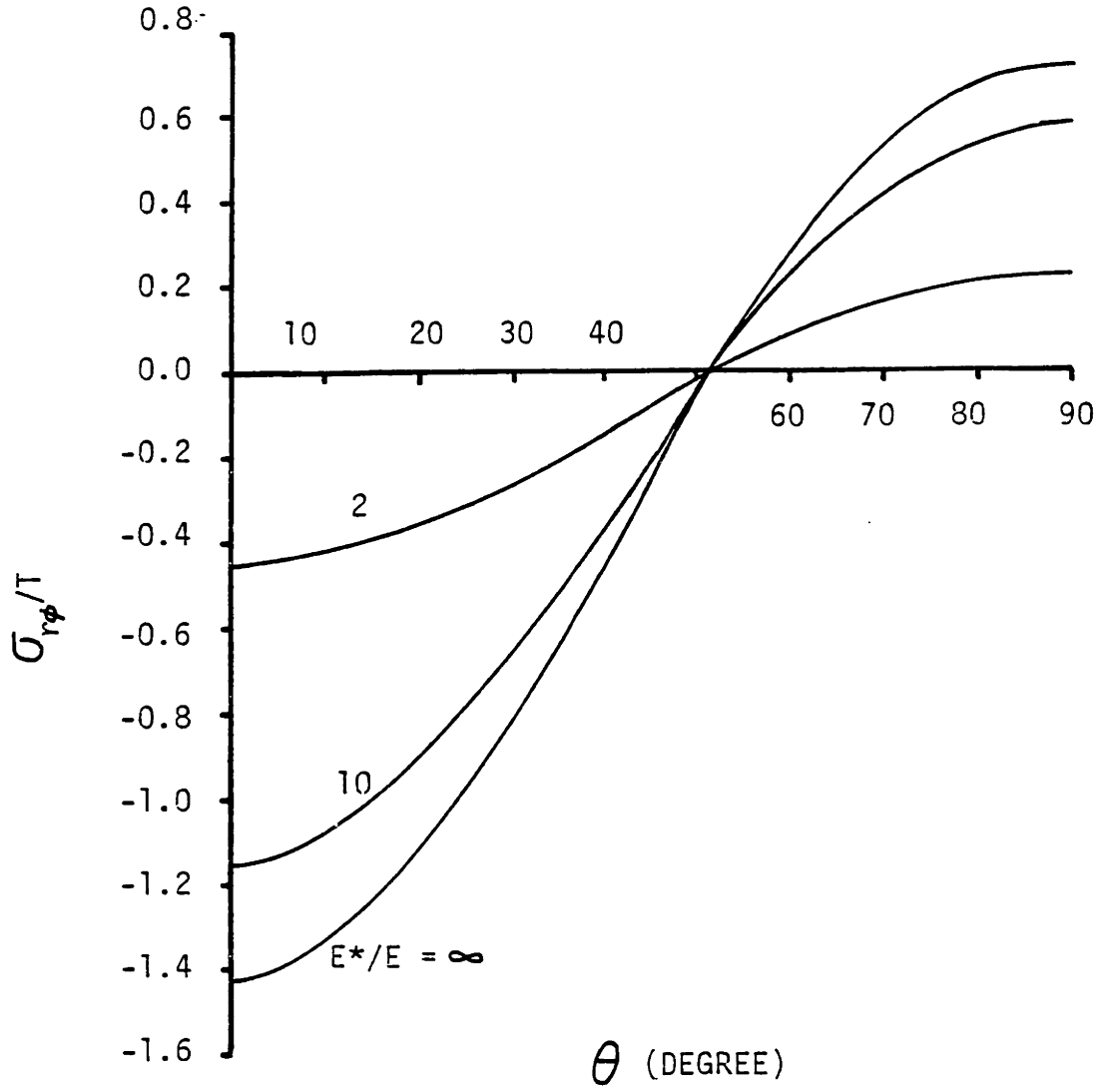

Figure A-3(d) Stress concentration $\sigma_{r\phi}/T$ at the surface of a spherical inclusion for $\phi = 90°$, under uniaxial tension $\sigma_{11} = T$.

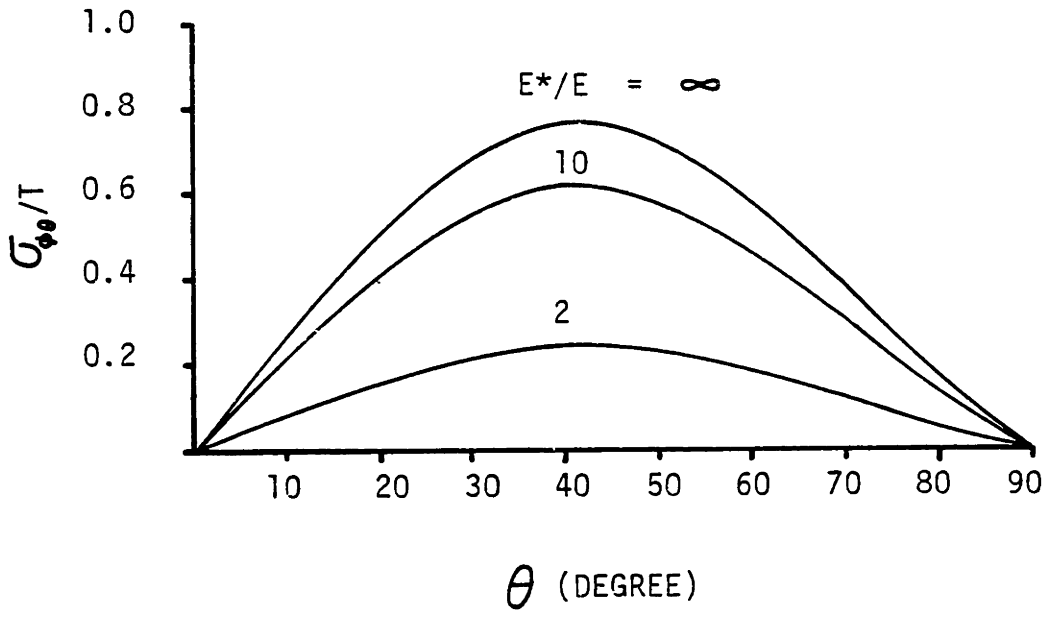

Figure A-3(e) Stress concentration $\sigma_{\phi\theta}/T$ at the surface of a spherical inclusion for $\phi = 90°$, under uniaxial tension $\sigma_{11} = T$.

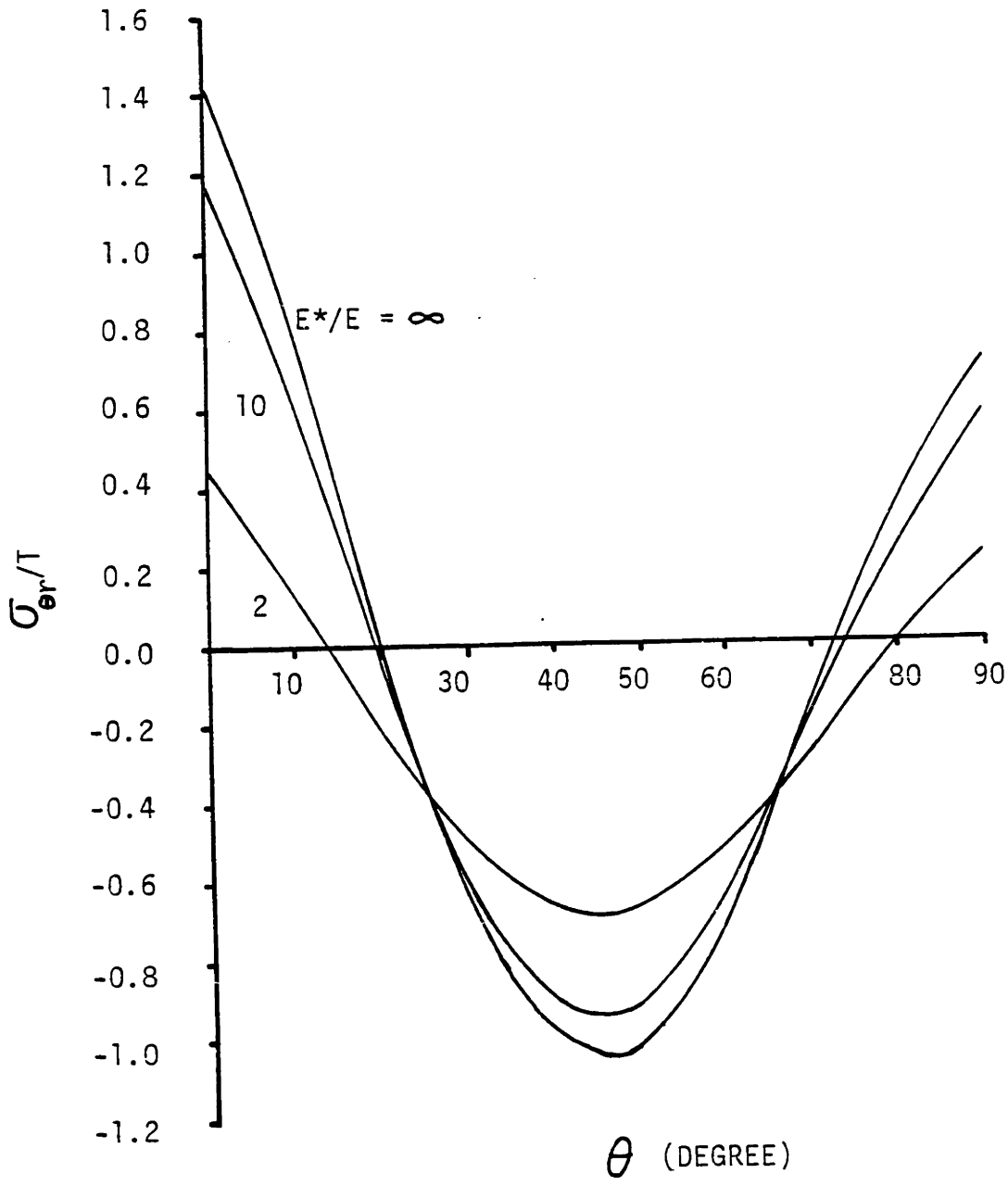

Figure A-3(f) Stress concentration $\sigma_{\theta r}/T$ at the surface of a spherical inclusion for $\phi = 90°$, under uniaxial tension $\sigma_{11} = T$.

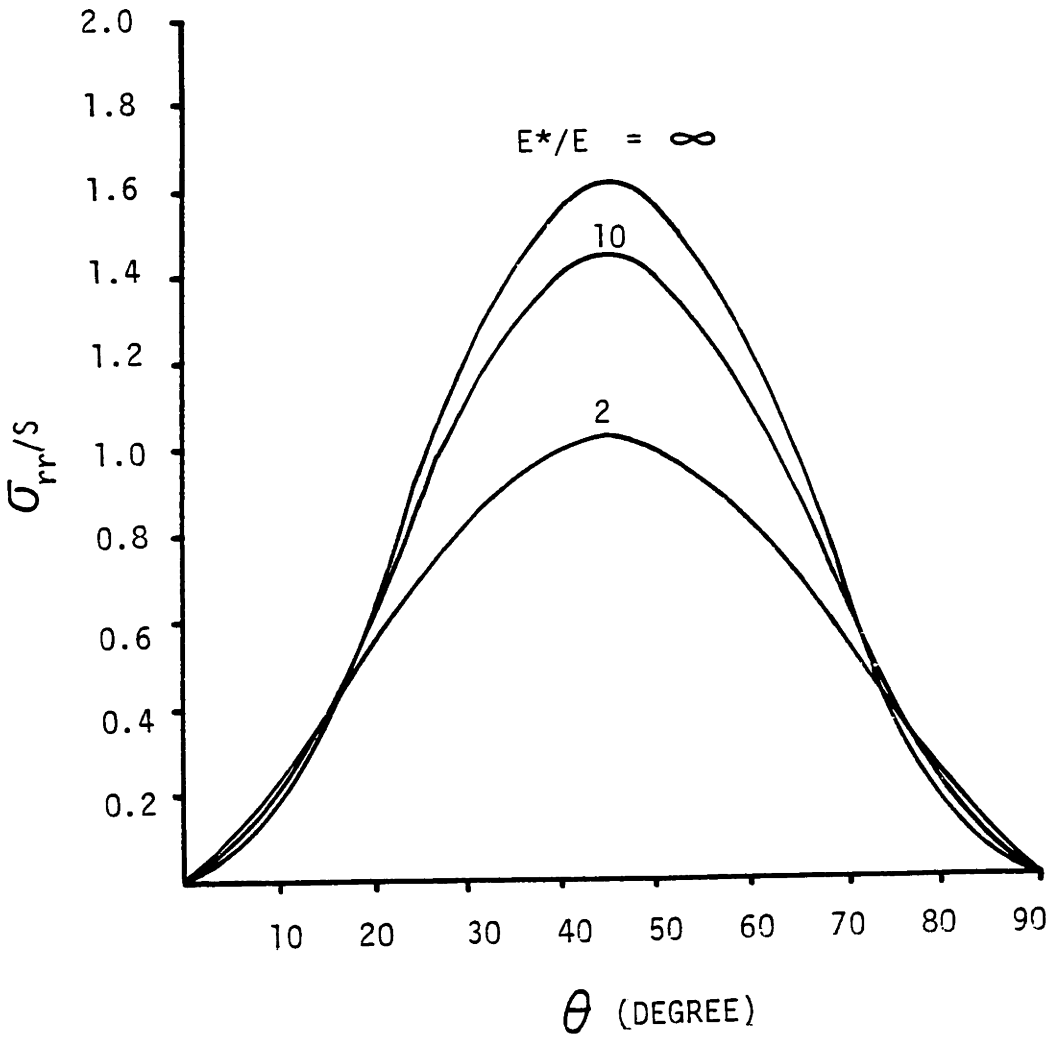

Figure A-4(a) Stress concentration σ_{rr}/S at the surface of a spherical inclusion for $\phi = 90°$, under shear stress $\sigma_{12} = S$.

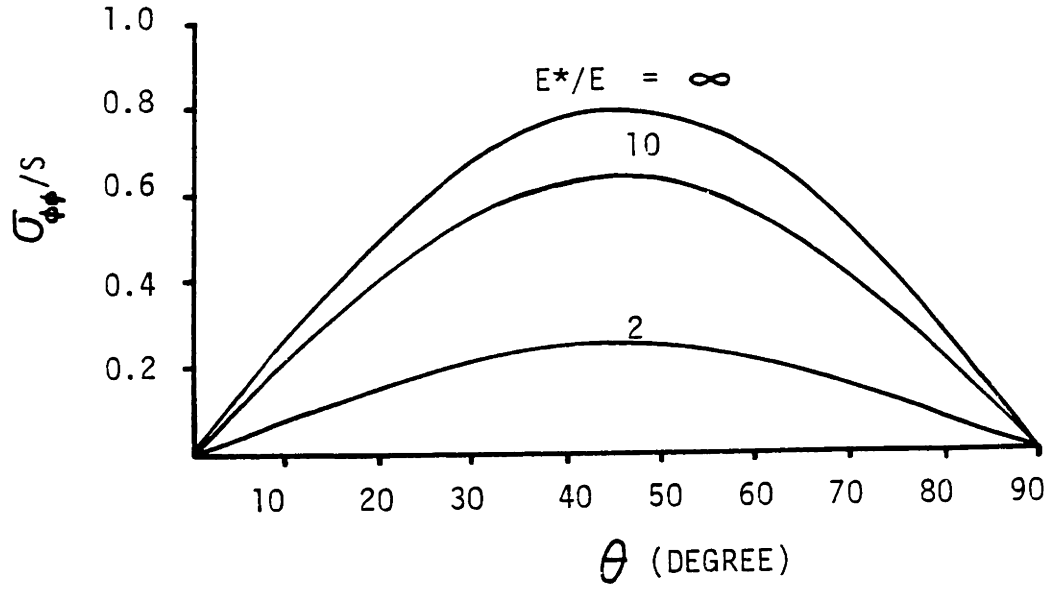

Figure A-4(b) Stress concentration $\sigma_{\phi\phi}/S$ at the surface of a spherical inclusion for $\sigma = 90°$, under shear stress $\sigma_{12} = S$.

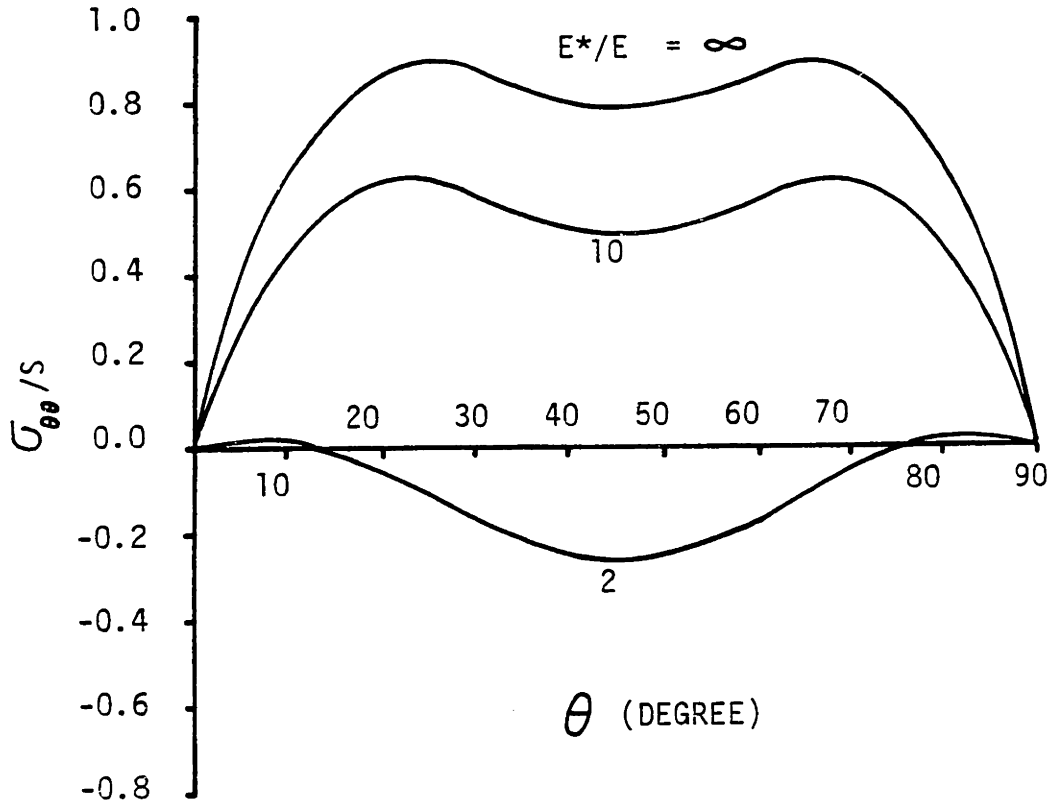

Figure A-4(c) Stress concentration $\sigma_{\theta\theta}/S$ at the surface of a spherical inclusion for $\sigma = 90°$, under shear stress $\sigma_{12} = S$.

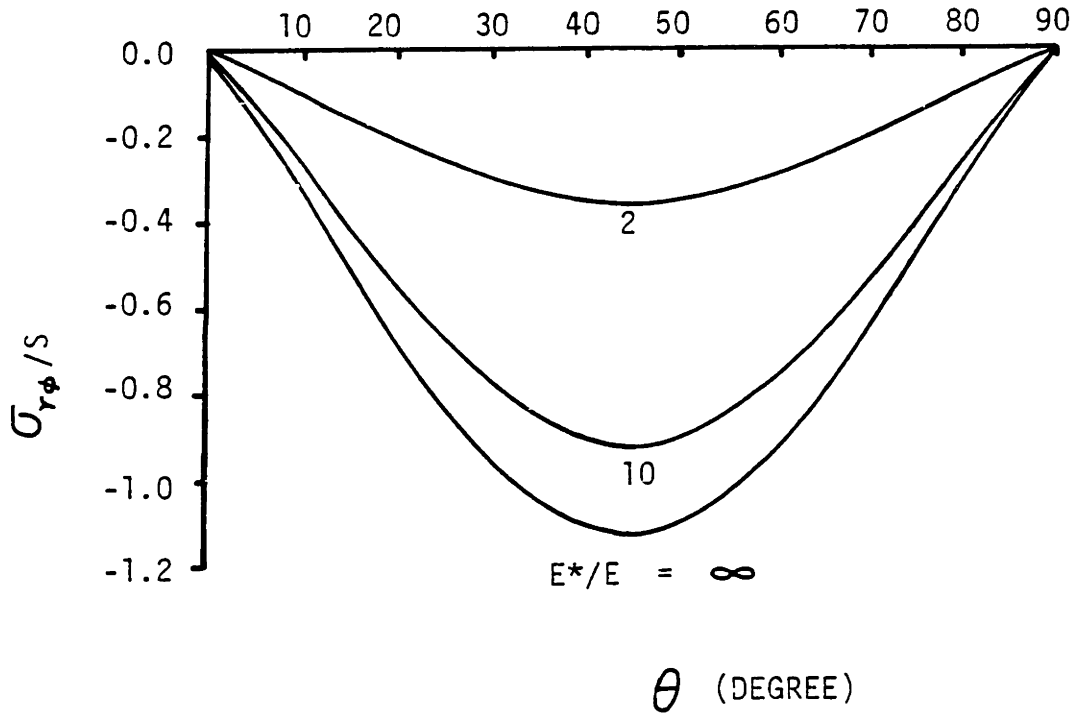

Figure A-4(d) Stress concentration $\sigma_{r\phi}/S$ at the surface of a spherical inclusion for σ = 90°, under shear stress σ_{12} = S.

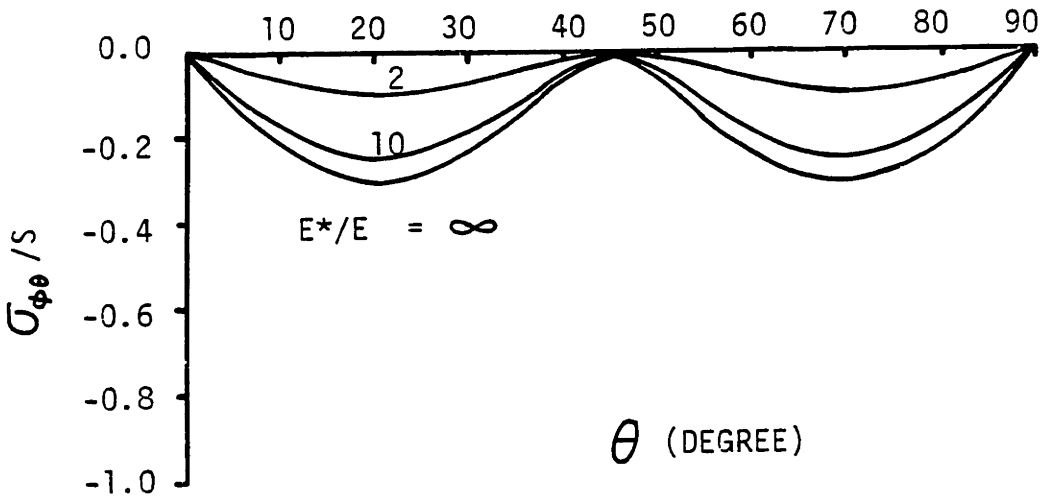

Figure A-4(e) Stress concentration $\sigma_{\phi\theta}/S$ at the surface of a spherical inclusion for $\sigma = 90°$, under shear stress $\sigma_{12} = S$.

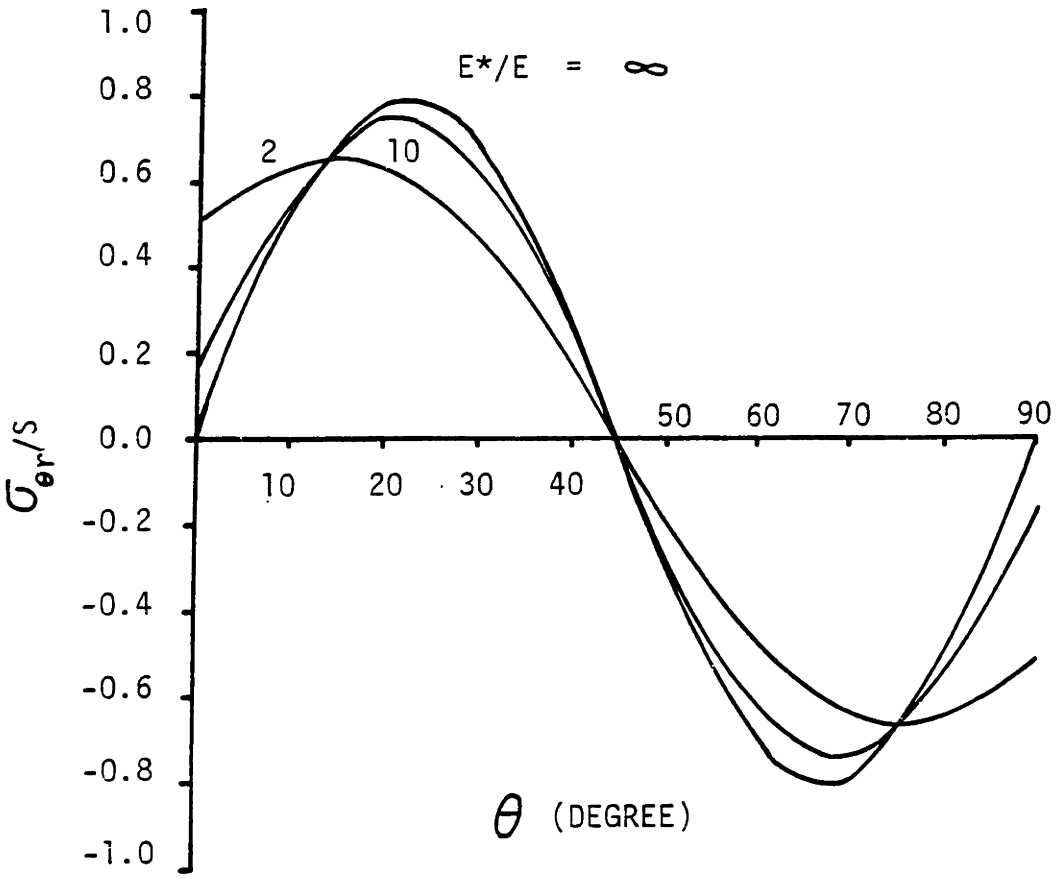

Figure A-4(f) Stress concentration $\sigma_{\theta r}/S$ at the surface of a spherical inclusion for $\sigma = 90°$, under shear stress $\sigma_{12} = S$.

Appendix B

MICROGRAPHS OF SAMPLES USED IN THE DETERMINATION OF THE CRACK ARREST TEMPERATURE

The principle and experimental procedure of determining the crack arrest temperature are described in Chapter VI, Section A. All samples used in this experiment are epoxy filled with 20 μm glass beads. Samples were cut into tensile test specimens with a gage length of 2.2 inches. These specimens were tested to fracture at different temperatures at an elongation rate of 0.1 in/min (7.56×10^{-4}/sec strain rate).

Shown in figure B-1, are optical micrographs of polished transverse ($\perp$) cross sections of the test specimens. The cross sections were cut out from the specimens at about 1 cm to the fractured cross section.

A set of two micrographs of the same magnification were taken from an identical location on the polished sample. The migrograph on the left was taken focusing on the polished surface, the one on the right was taken focusing at some distance below the surface (the epoxy matrix is transparent). Comparing these two micrography, we may conclude that the observed shiny rings, which represents cavitation, come from glass beads beneath the polished surface, and are not due to damage by the sectioning and polishing process. The crack arrest temperature is determined as the lowest test temperature at which numerous rings were found on these micrographs. For this particular low concentration 20 μm glass bead filled epoxy, the crack arrest temperature is found to be about 95°C.

Figure B-2 shows the micrographs taken on the polished parallel ($\parallel$) cross section. Rings were not found on any samples tested at any temp-

perature (for explanation, see Chapter VI, Section A). This finding also confirms that the rings observed on the transverse cross section were indeed features of the cavitation process.

Shown in figure B-3 are the fractured surface of these samples. Cleavage fracture in the matrix phase was found on samples tested at temperatures below 75°C. Above 100°C, significant cavitation and void growth were found around the glass bead fillers.

L: focus on surface R: focus beneath surface

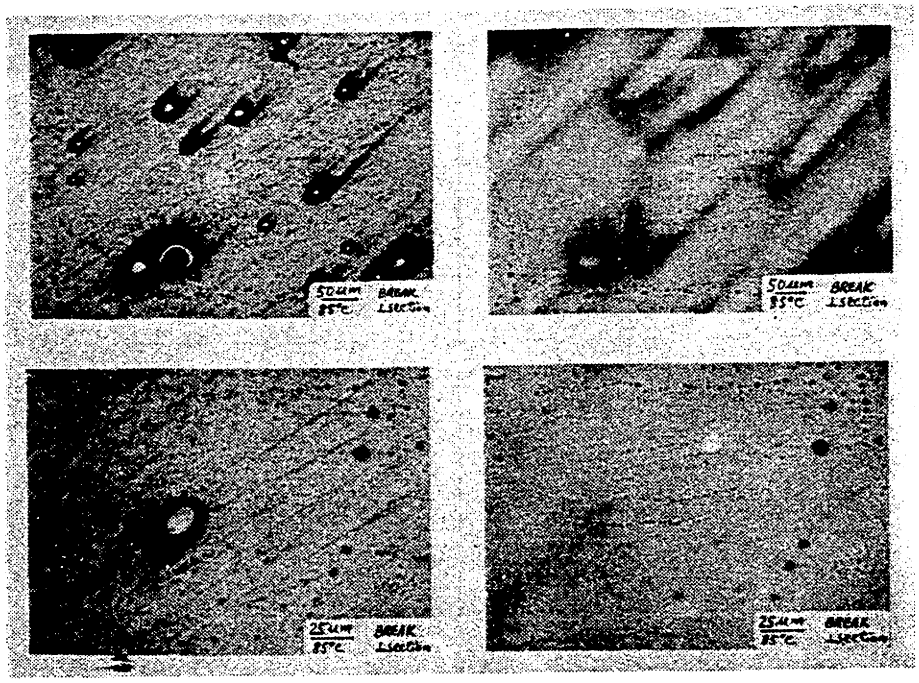

(a) 85°C

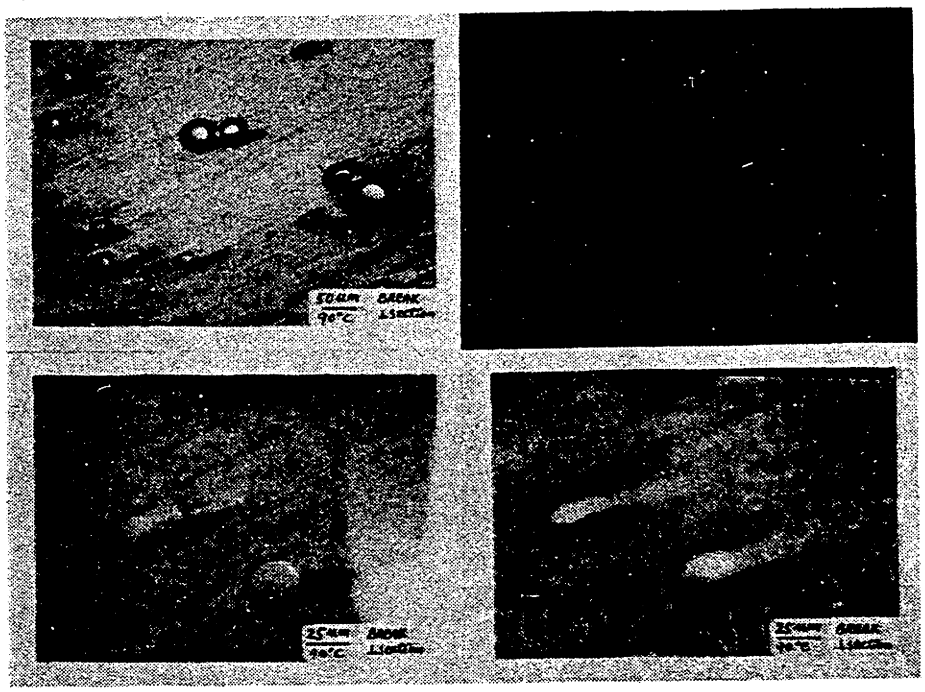

(b) 90°C

Figure B-1 Optical micrograph of polished $\perp$ cross section of 20 μm glass bead filled epoxy. Uniaxial tensile test at different temperatures.

L: focus on surface R: focus beneath surface

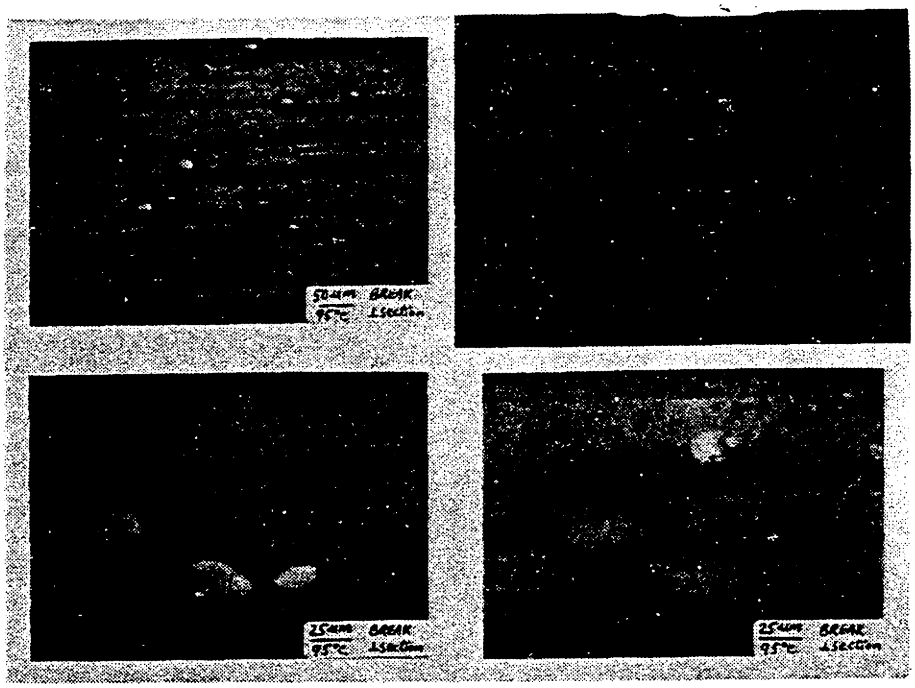

(c) 95°C

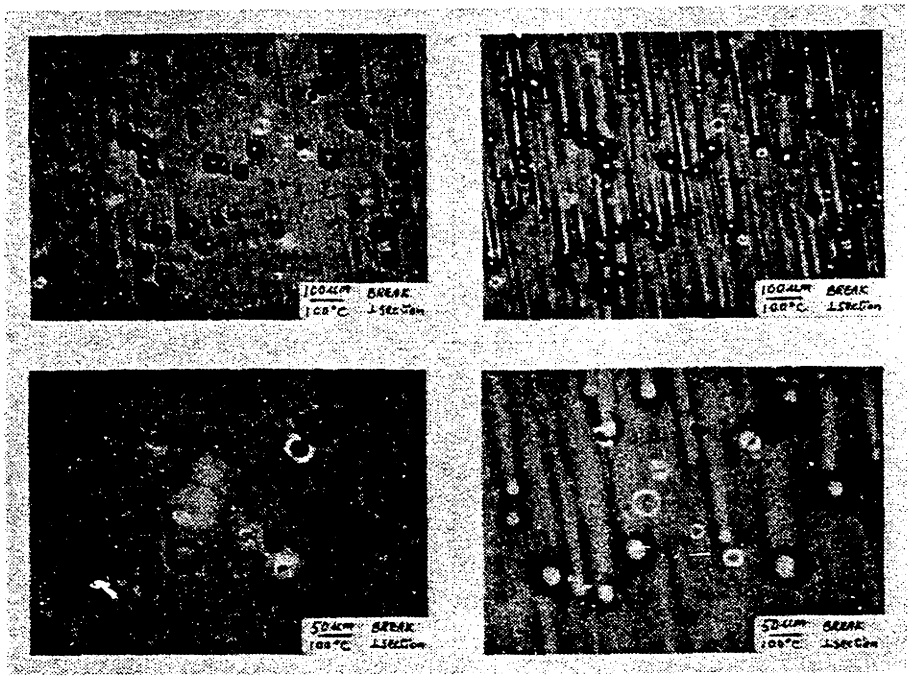

(d) 100°C

Figure B-1 continued

L: focus on surface R: focus beneath surface

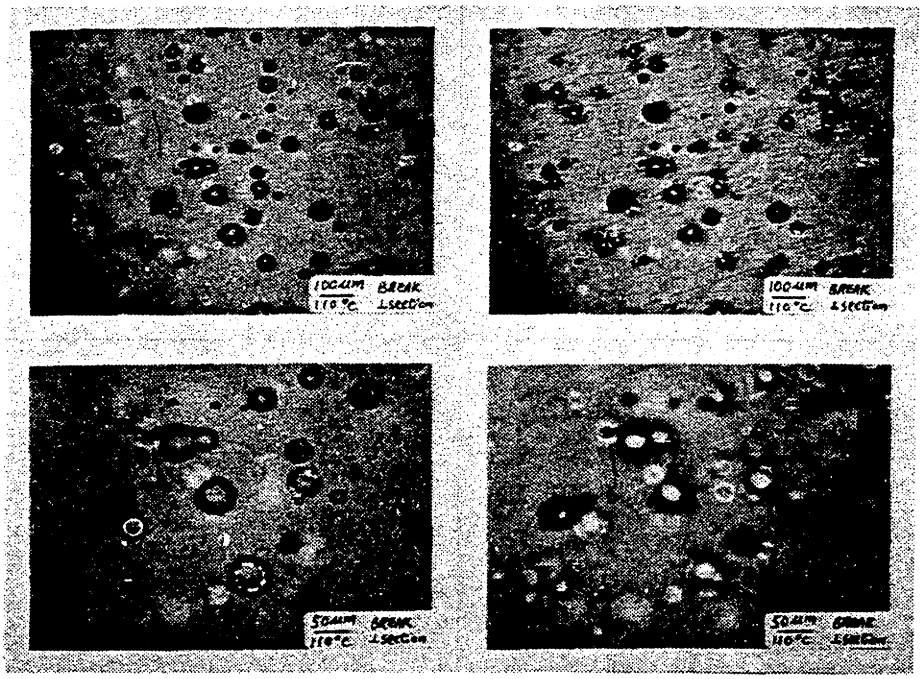

(e) 110°C

Figure B-1 continued

L: focus on surface R: focus beneath surface

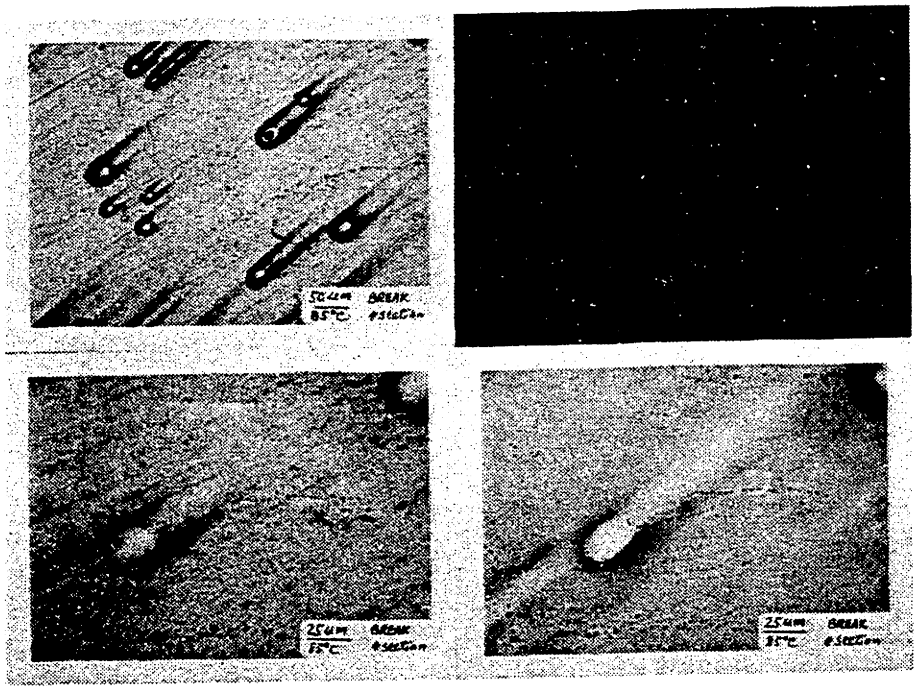

(a) 85°C

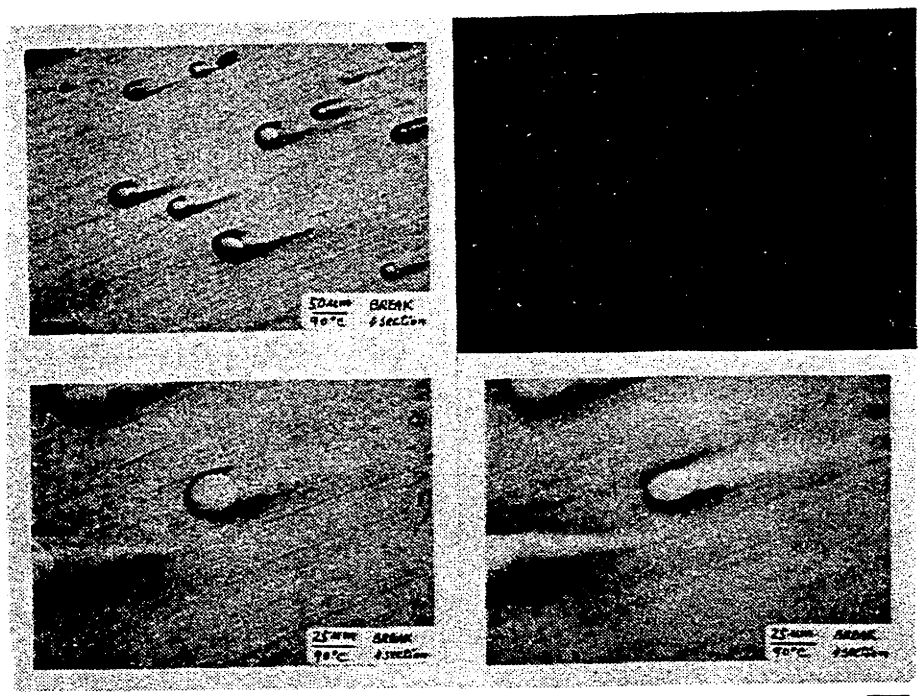

(b) 90°C

Figure B-2 Optical micrograph of polished ⟂ cross section of 20 μm glass bead filled epoxy. Uniaxial tensile test at different temperatures.

L: focus on surface R: focus beneath surface

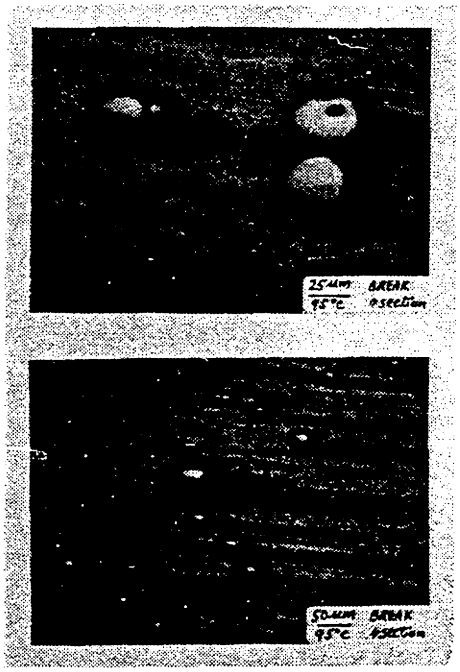

(c) 95°C

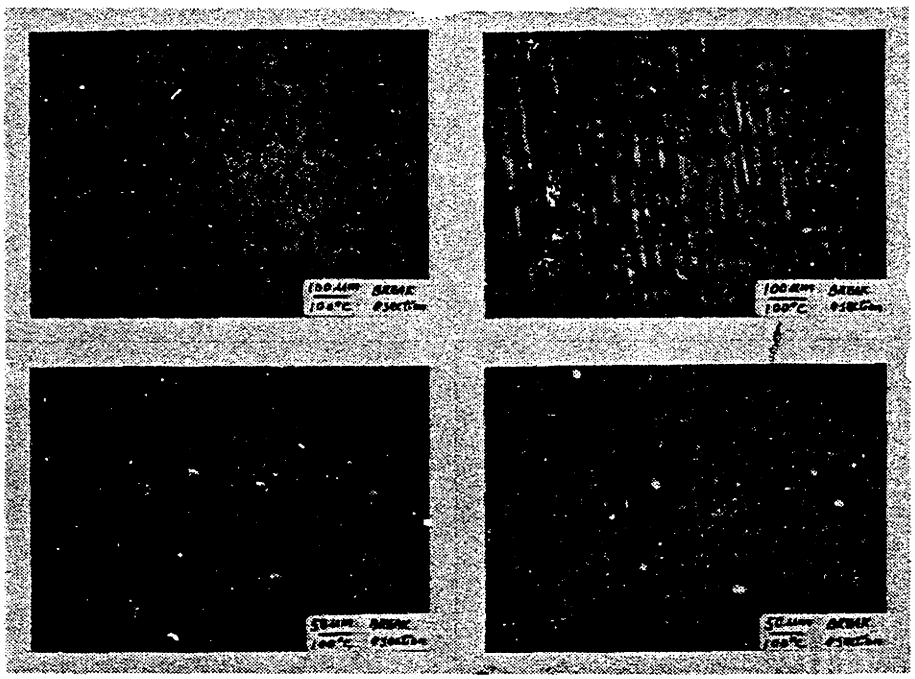

(d) 100°C

Figure B-2 continued

L: focus on surface R: focus beneath surface

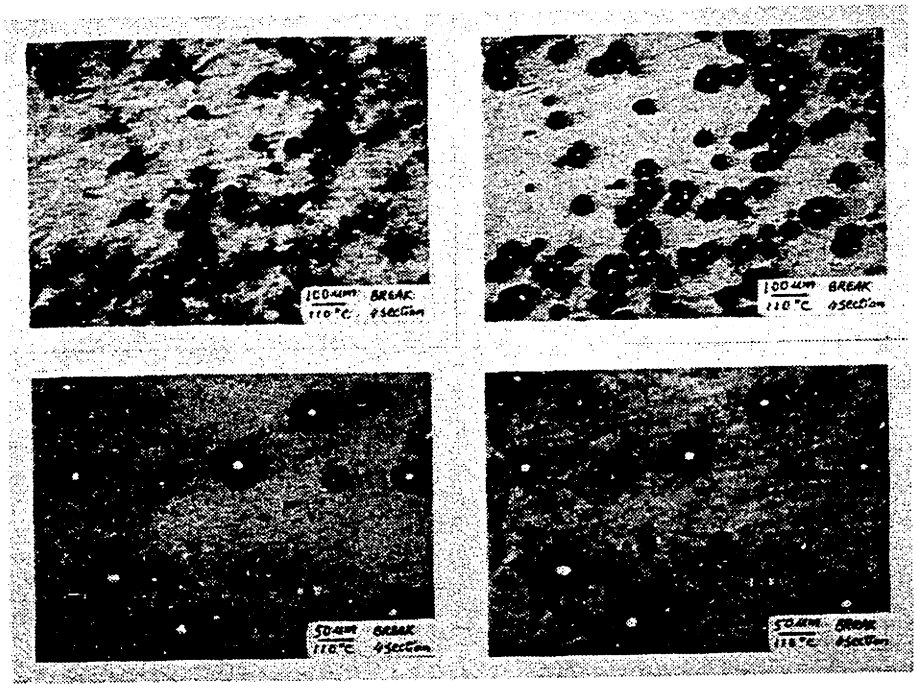

(e) 110°C

Figure B-2 continued

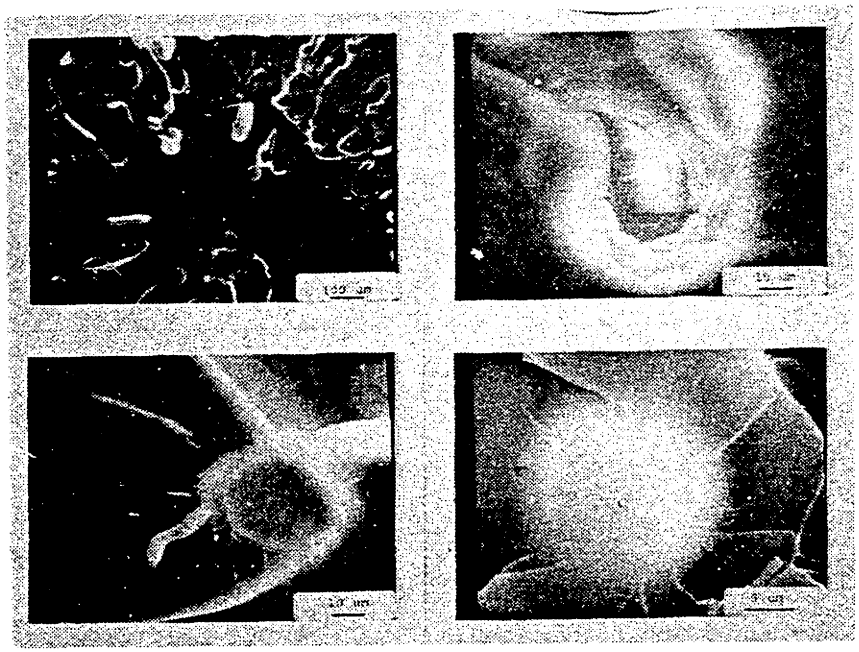

(a) 50°C

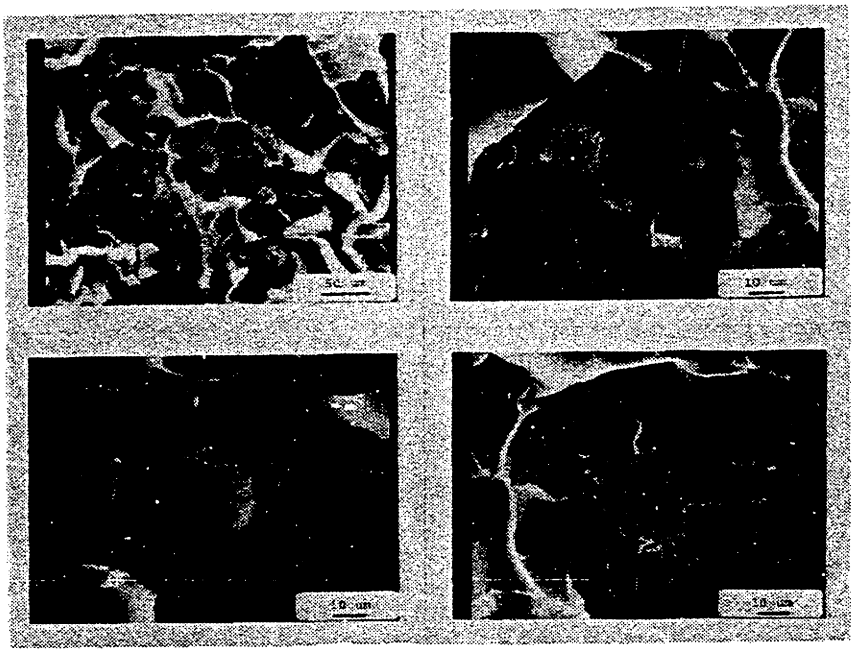

(b) 75°C

Figure B-3 Fracture surface of 20 μm glass bead filled epoxy. Uniaxial tensile test at different temperatures.

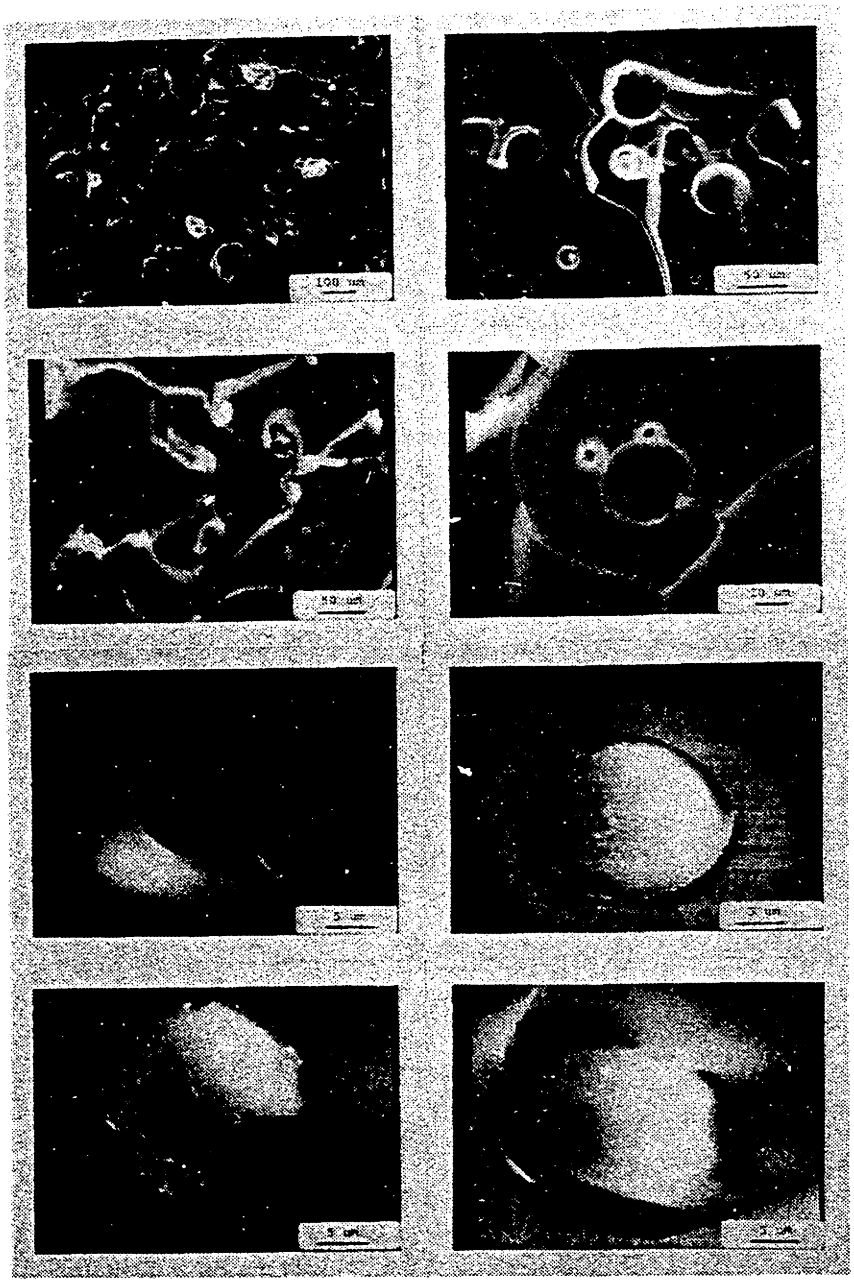

(c) 100°C

Figure B-3 continued

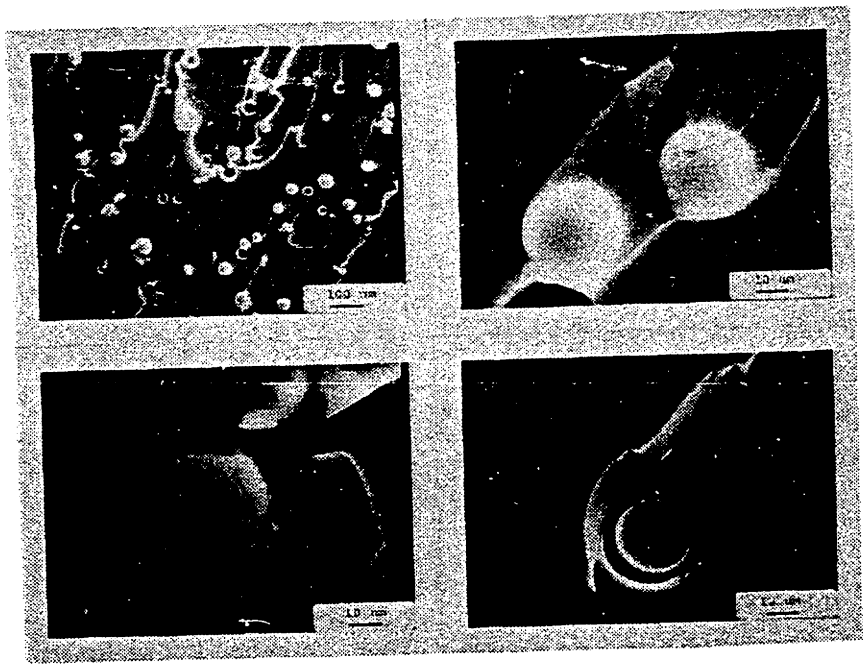

(d) 125°C

Figure B-3 continued

Appendix C

MICROGRAPHS OF SAMPLES USED IN THE DETERMINATION OF THE CRITERION FOR VOID NUCLEATION

The experimental procedure of determining the criterion for void nucleation in an inclusion filled material is described in Chapter IV, Section B. The samples used in the experiment are glass bead filled epoxy. Tensile test specimens of 2.2 inch gage length were tested at an elongation rate of 0.1 in/min (7.56×10^{-4}/sec strain rate). Specimens were pulled to different amount of strain at 100°C and 110°C. Microscopic techniques to observe void nucleation in these specimens are the same as described in Chapter IV and Appendix B. Listed below are micrographs of samples tested in this investigation.

Figure C-1 Transverse ($\perp$) cross section of 20 μm glass bead filled epoxy tested at 100°C

Figure C-2 Parallel ($\parallel$) cross section of 20 μm glass bead filled epoxy tested at 100°C

Figure C-3 Transverse ($\perp$) cross section of 20 μm glass bead filled epoxy tested at 110°C

Figure C-4 Parallel ($\parallel$) cross section of 20 μm glass bead filled epoxy tested at 110°C.

Figure C-5 Transverse ($\perp$) cross section of 50 μm glass bead filled epoxy tested at 100°C

Figure C-6 Parallel ($\parallel$) cross section of 50 μm glass bead filled epoxy tested at 100°C

Figure C-7 Transverse ($\perp$) cross section of 50 μm glass bead filled epoxy tested at 110°C

Figure C-8 Parallel ($\parallel$) cross section of 50 μm glass bead filled epoxy tested at 110°C

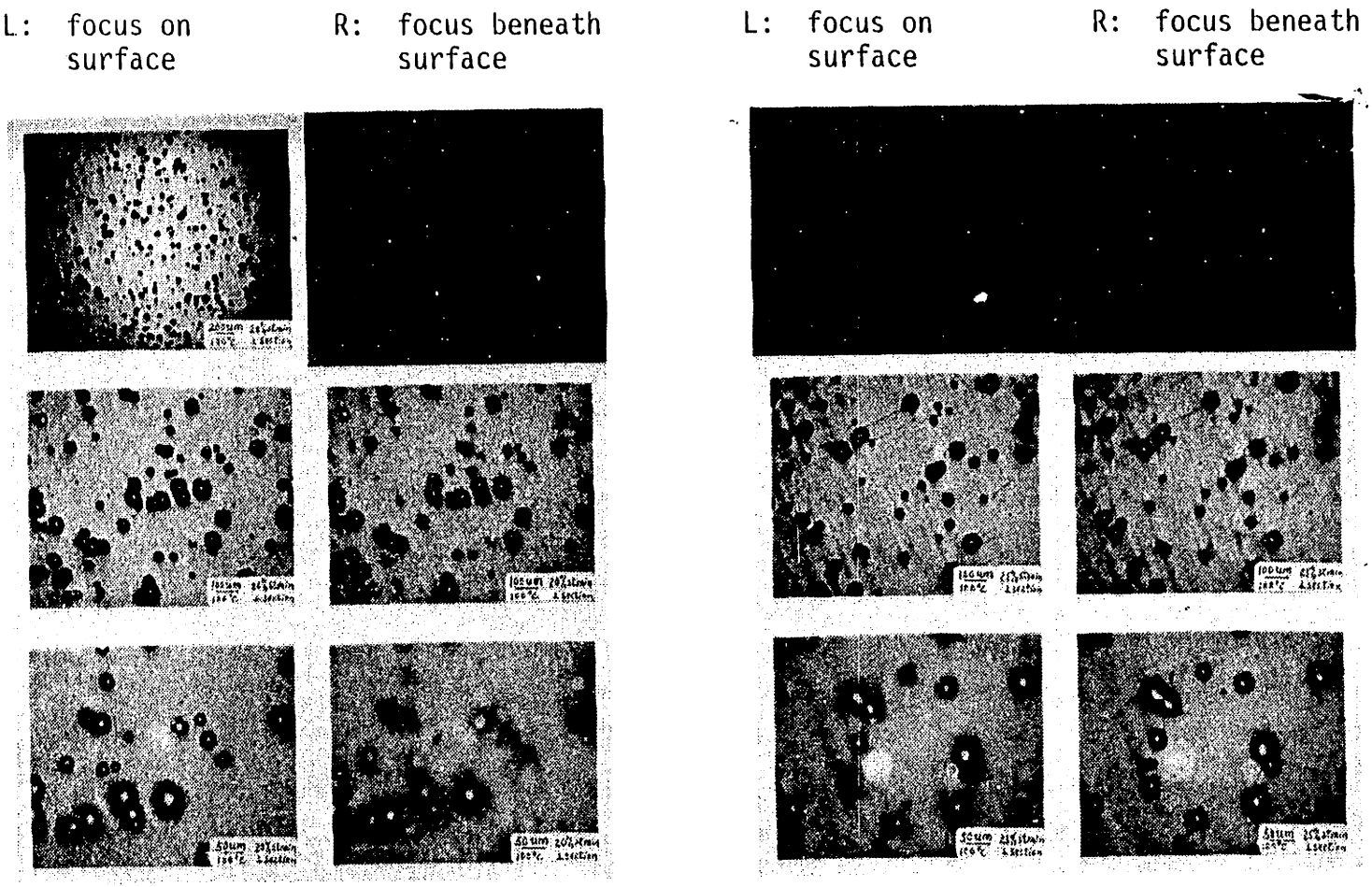

Figure C-1 Optical micrograph of the ⊥ cross section of 20 μm glass bead filled epoxy extended to different amount of strain under uniaxial tension at 100°C.

L: focus on surface R: focus beneath surface

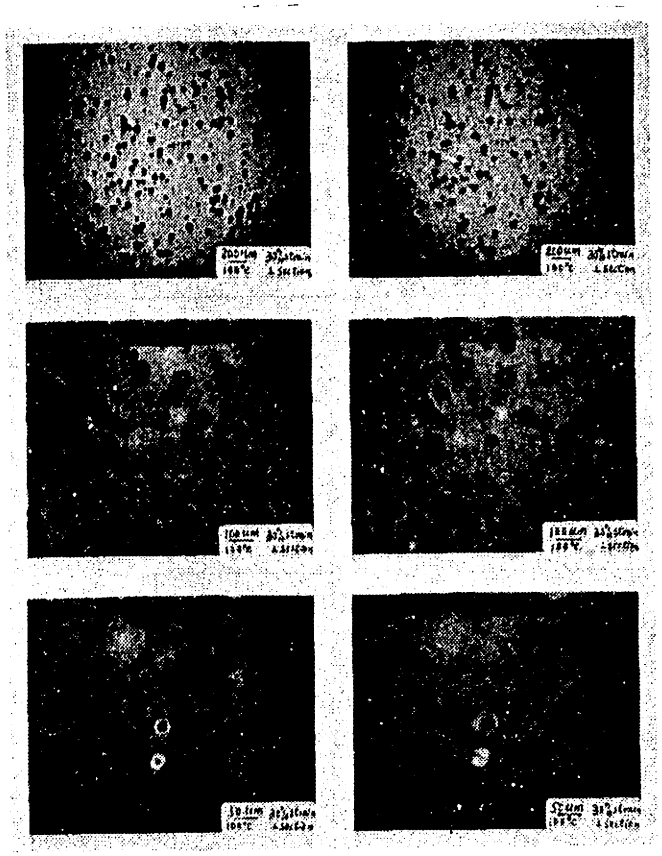

100°C 30% total strain
⊥ cross section

L: focus on surface R: focus beneath surface

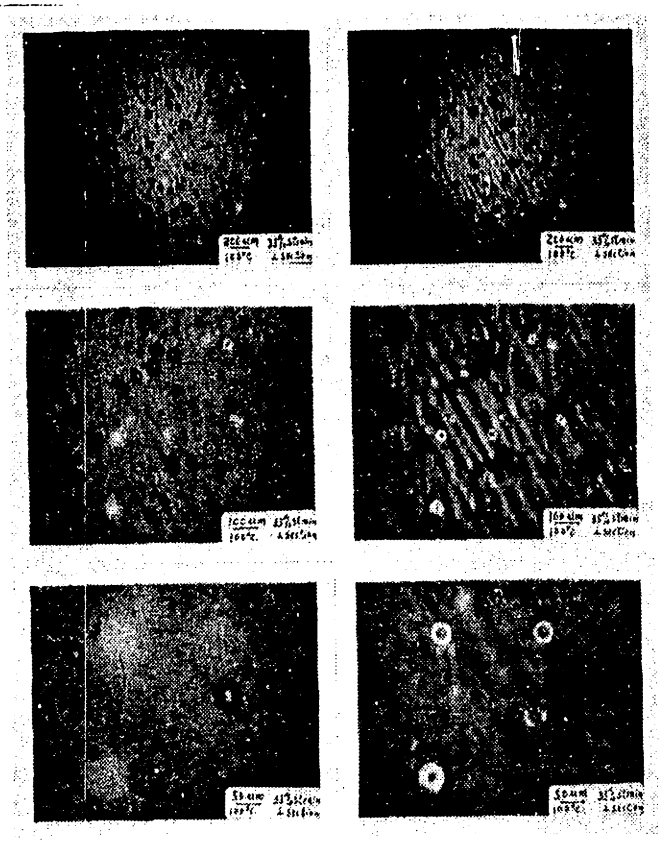

100°C 35% total strain
⊥ cross section

Figure C-1 continued

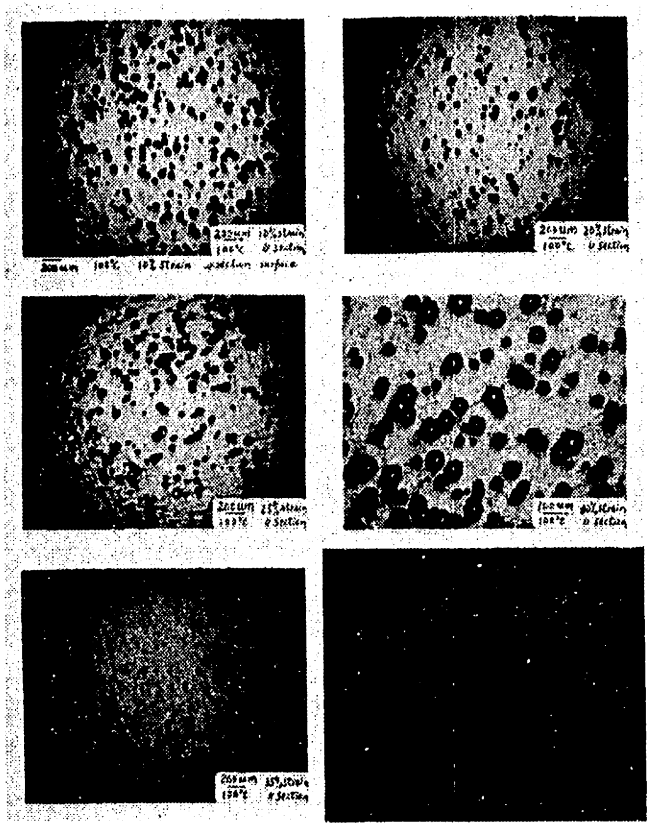

100°C different amount of total strain
|| cross section

Figure C-2 Optical micrograph of the || cross section of 20 μm glass bead filled epoxy extended to different amount of strain under uniaxial tension at 100°C.

L: focus on surface R: focus beneath surface

L: focus on surface R: focus beneath surface

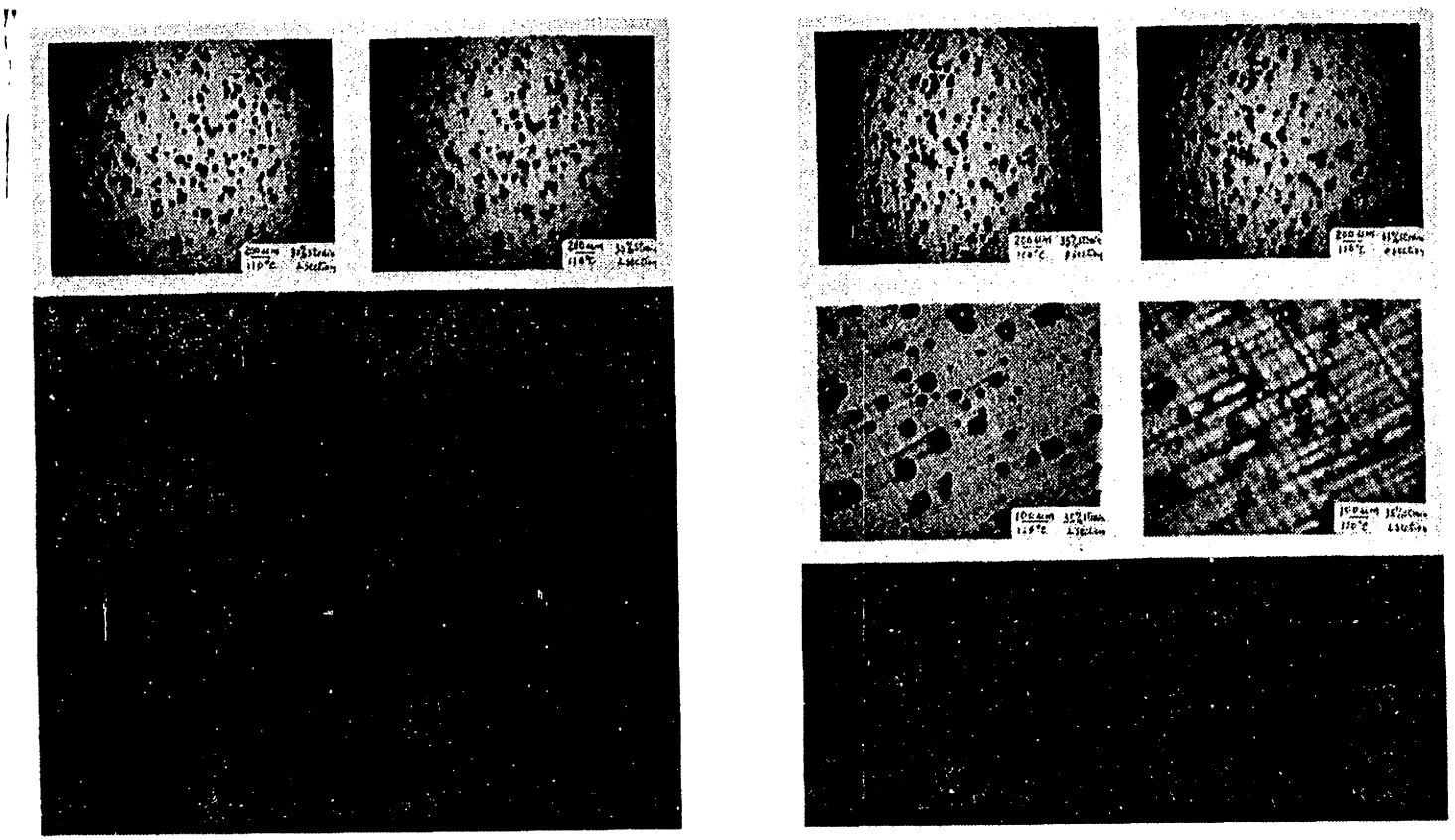

110°C 30% total strain
⊥ cross section

110°C 35% total strain
|| and ⊥ cross section

Figure C-3 Optical micrograph of the ⊥ cross section of 20 μm glass bead filled epoxy extended to di-ferent amount of strain under uniaxial tension at 110°C.

L: focus on surface

R: focus beneath surface

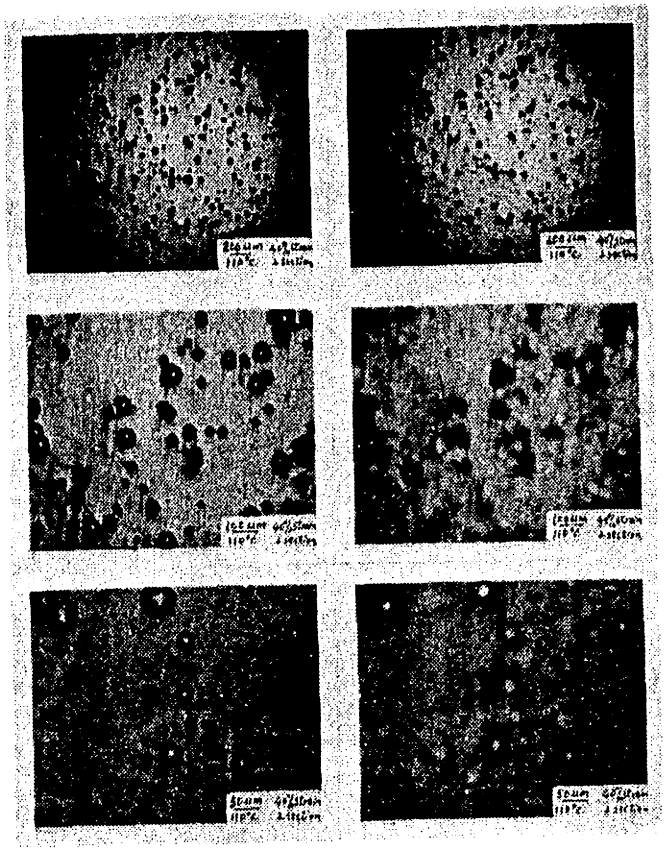

110°C 40% total strain
⊥ cross section

L: focus on surface

R: focus beneath surface

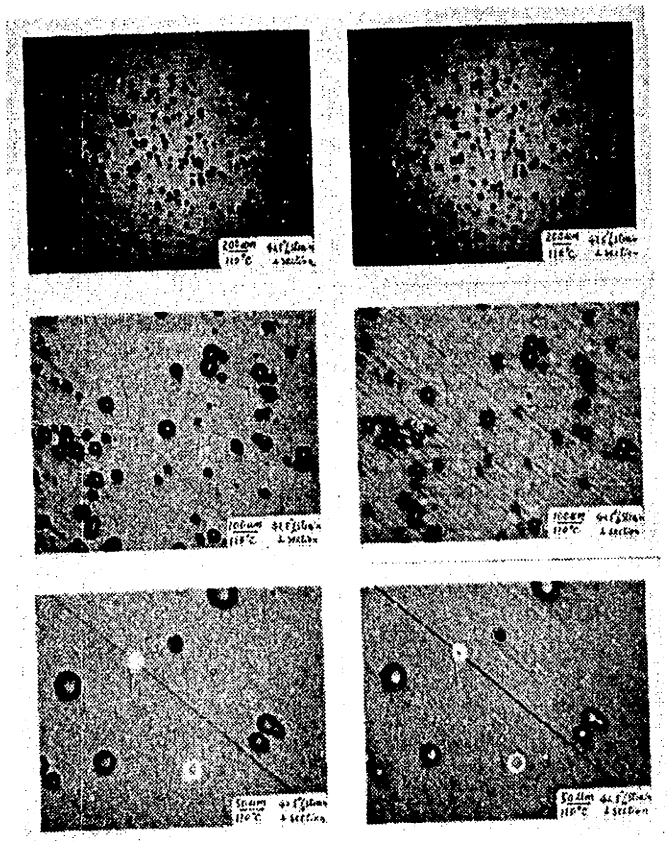

110°C 42.5% total strain
⊥ cross section

Figure C-3 continued

L: focus on surface R: focus beneath surface

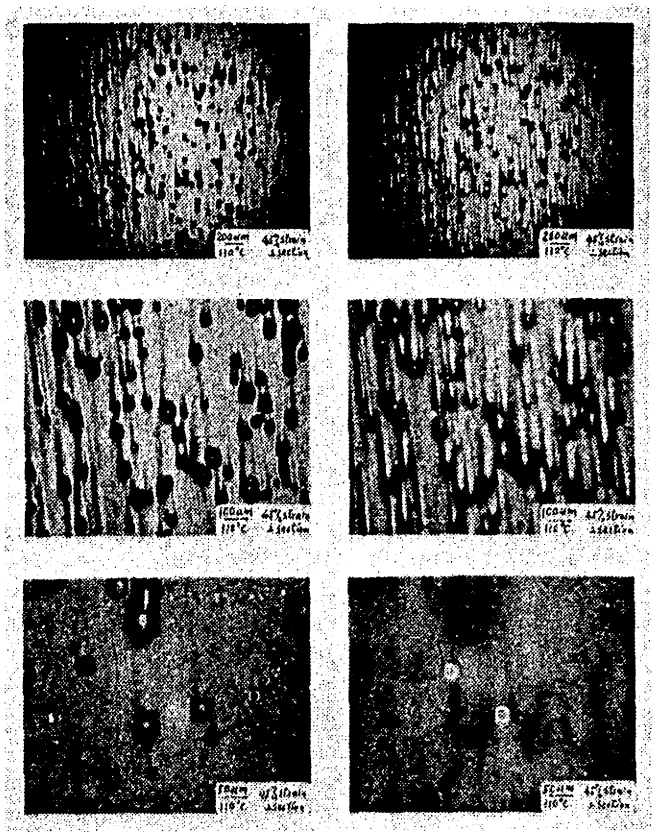

110°C 45 % total strain
⊥ cross section

L: focus on surface R: focus beneath surface

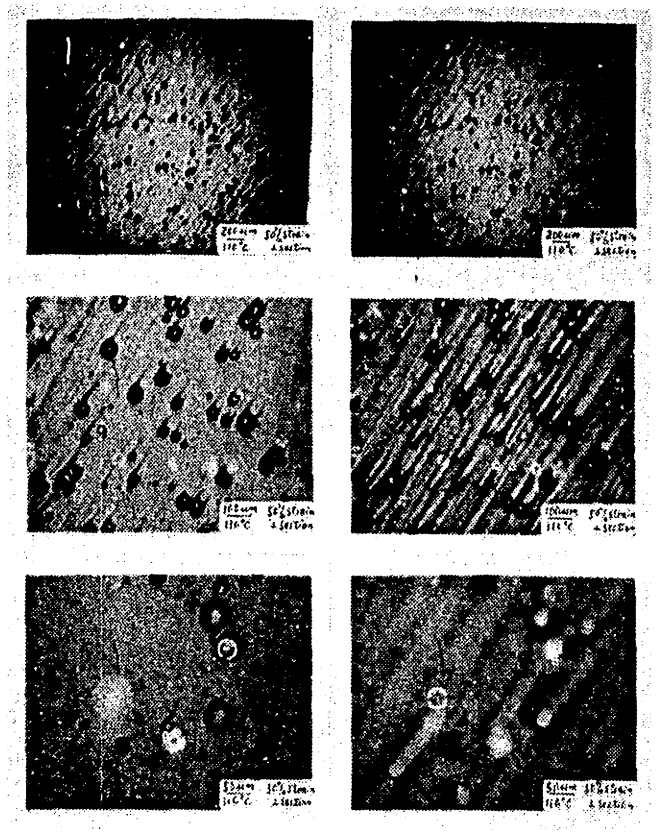

110°C 50% total strain
⊥ cross section

Figure C-3 continued

L: focus on surface

R: focus beneath surface

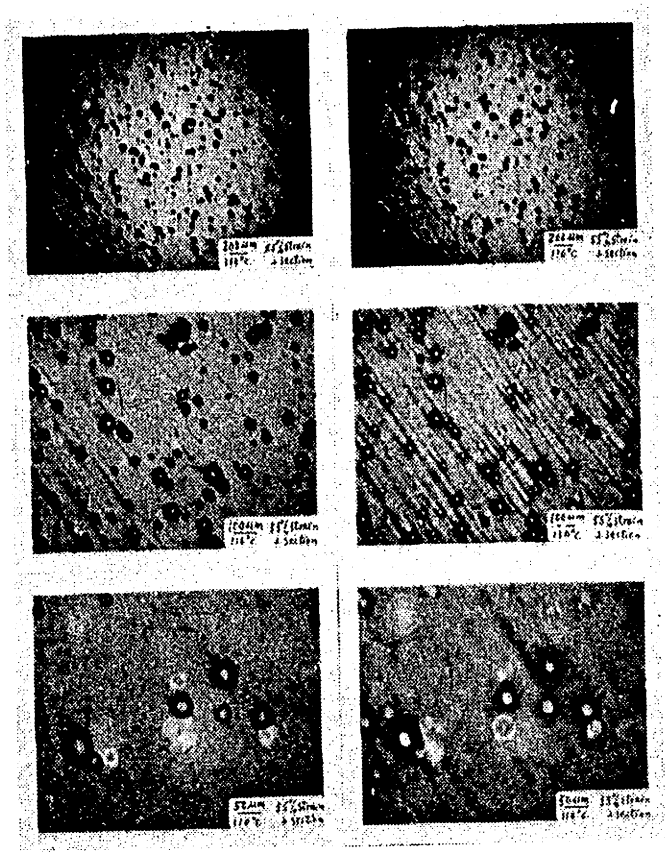

110°C 55% total strain
⊥ cross section

Figure C-3 continued

L: focus on surface R: focus beneath surface

L: focus on surface R: focus beneath surface

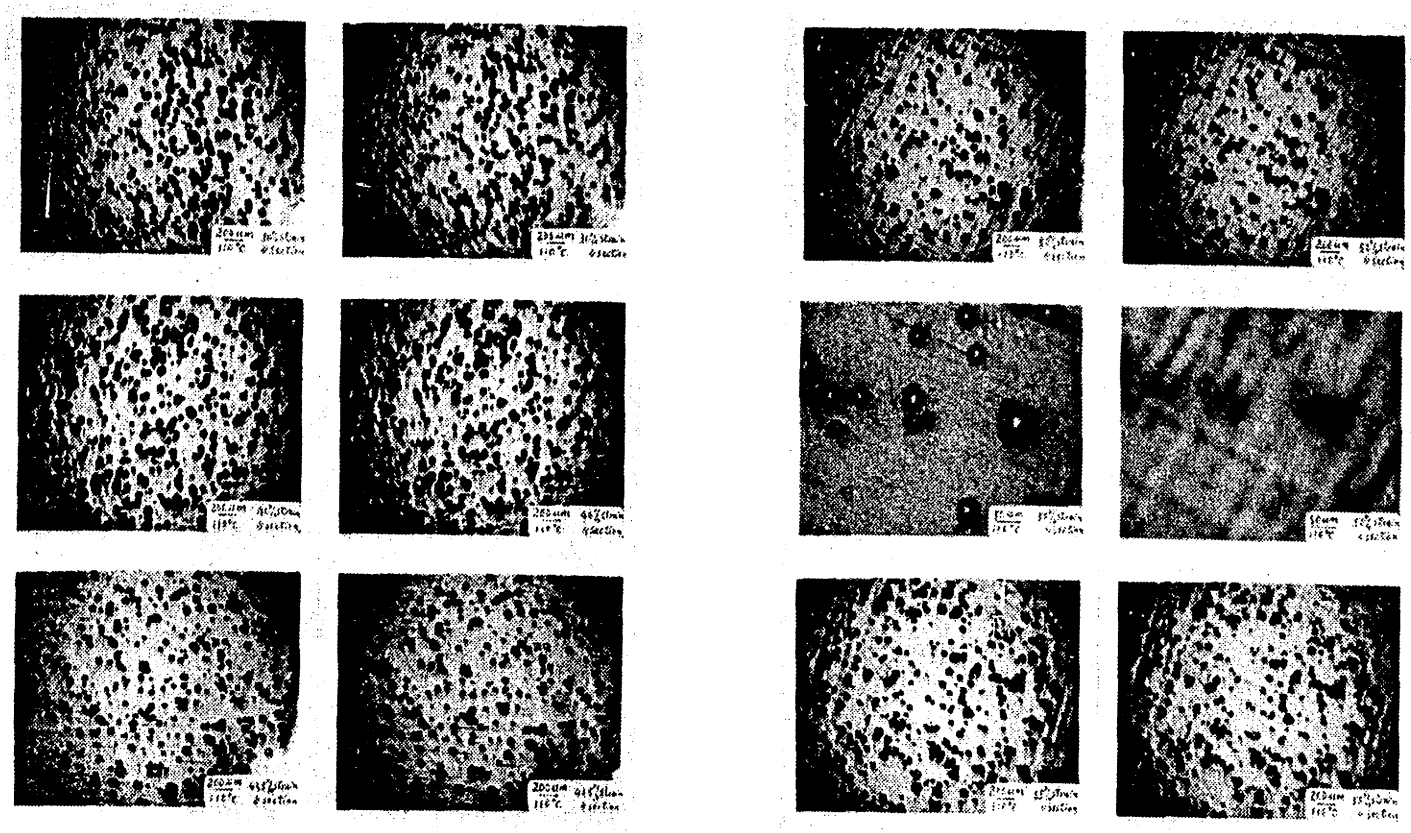

110°C 30-42.5% total strain
|| cross section

110°C 50-55% total strain
|| cross section

Figure C-4 Optical micrograph of the || cross section of 20 μm glass bead filled epoxy extended to different amount of strain under uniaxial tension at 110°C.

L: focus on surface R: focus beneath surface

L: focus on surface R: focus beneath surface

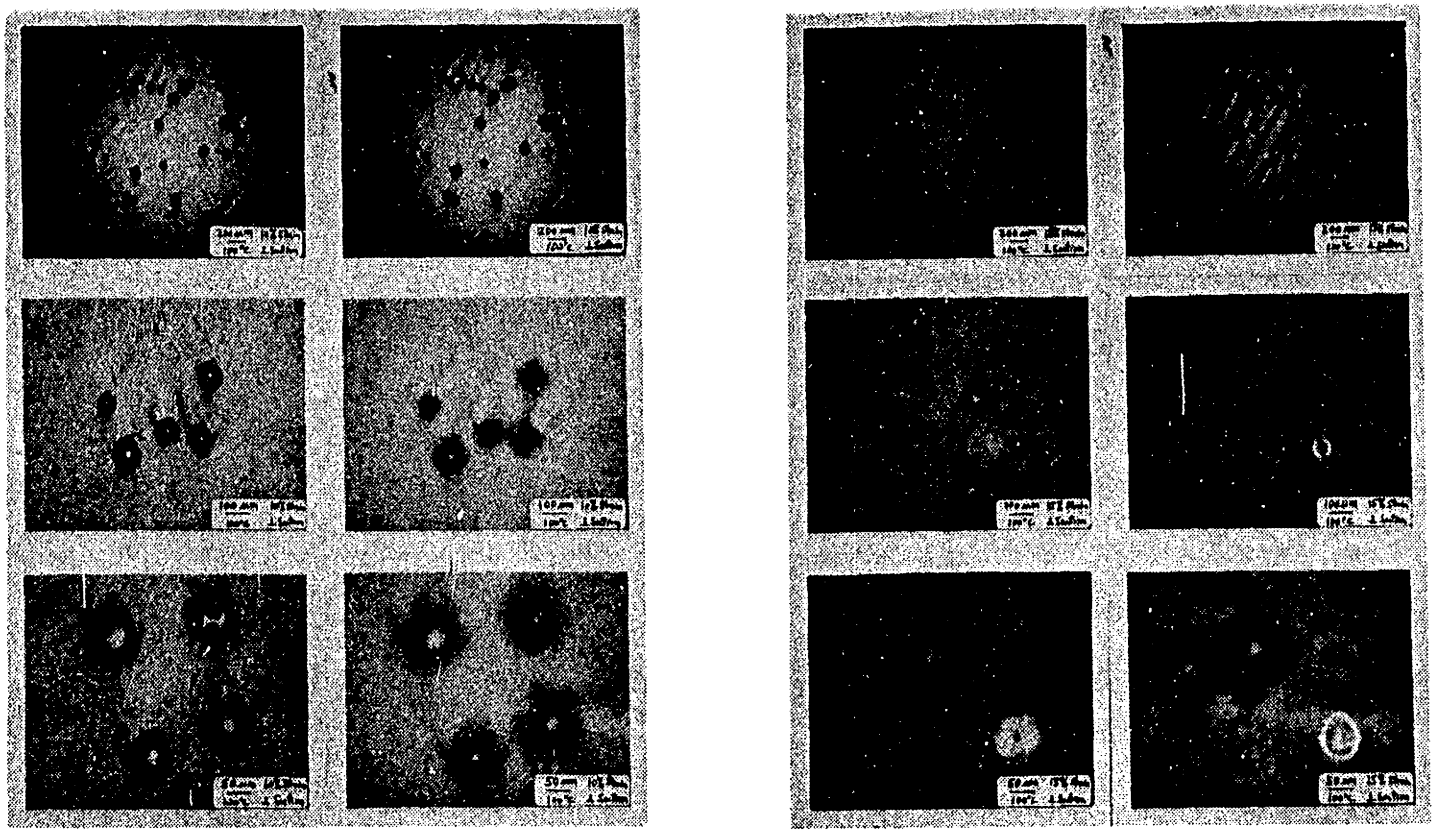

100°C 10% total strain
⊥ cross section

100°C 15% total strain
⊥ cross section

Figure C-5 Optical micrograph of the ⊥ cross section of 50 μm glass bead filled epoxy extended to different amount of strain under uniaxial tension at 100°C.

L: focus on surface

R: focus beneath surface

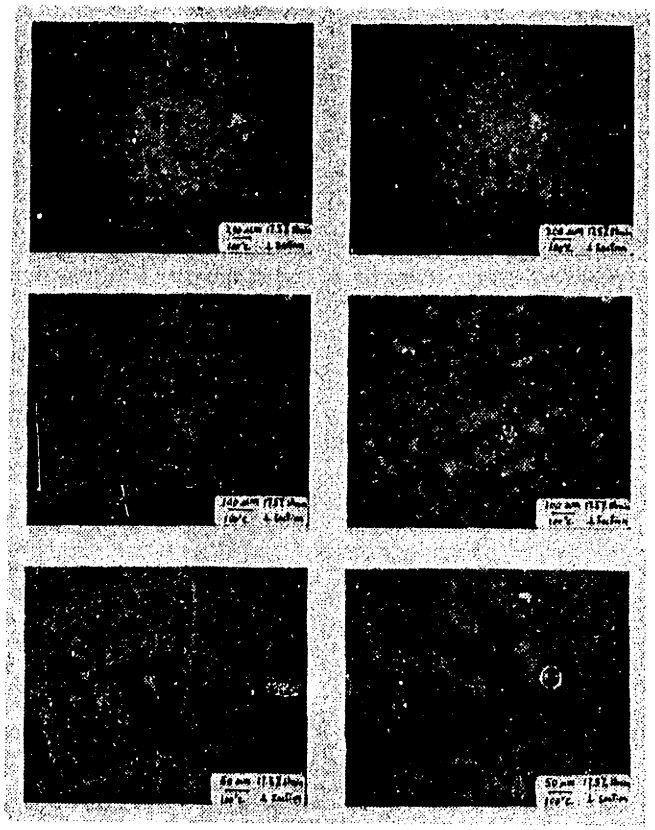

100°C 17.5% total strain
⊥ cross section

L: focus on surface

R: focus beneath surface

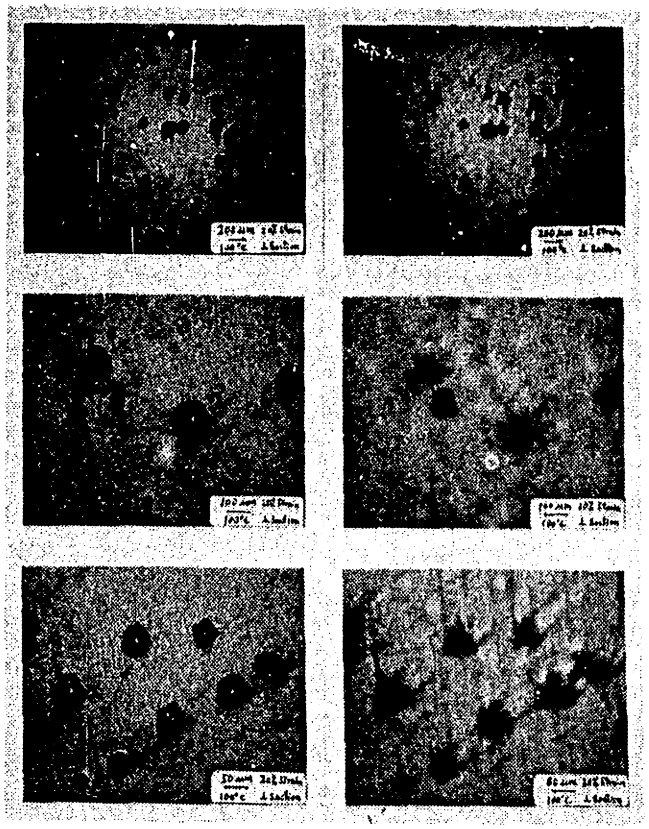

100°C 20% total strain
⊥ cross section

Figure C-5 continued

L: focus on surface R: focus beneath surface

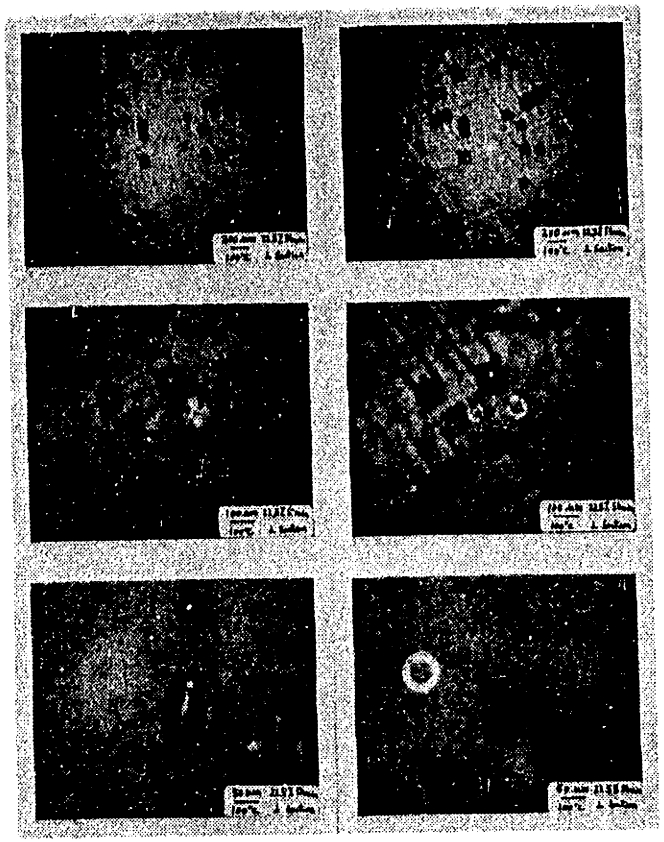

100°C 22.5% total strain
⊥ cross section

L: focus on surface R: focus beneath surface

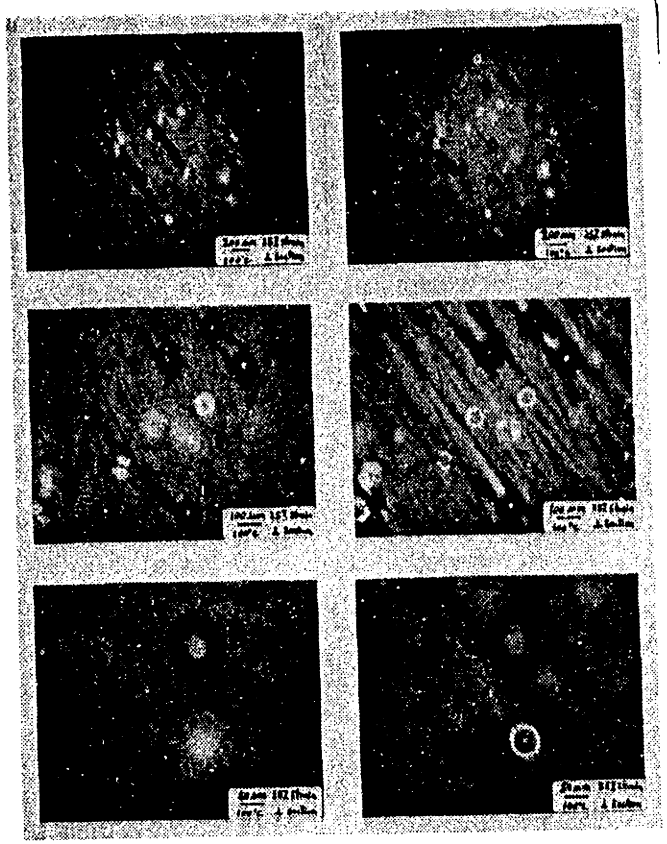

100°C 25% total strain
⊥ cross section

Figure C-5 continued

⊥ cross section

Figure C-5 continued

L: focus on surface

R: focus beneath surface

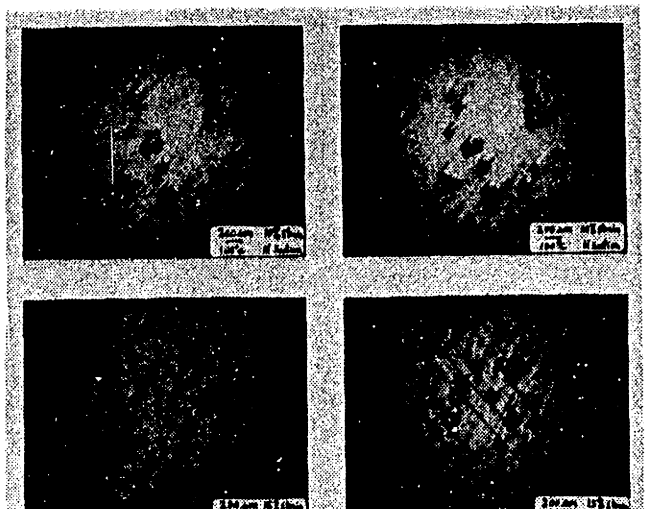

L: focus on surface

R: focus beneath surface

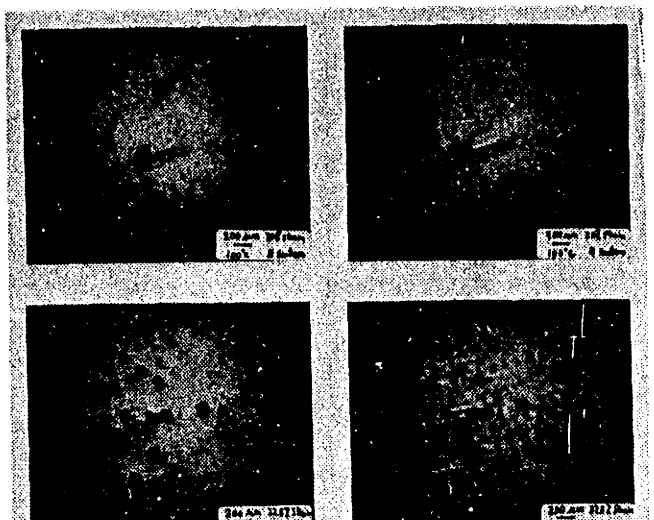

100°C 10-17.5% total strain
|| cross section

100°C 20-22.5% total strain
|| cross section

Figure C-6 Optical micrograph of the || cross section of 50 μm glass bead filled epoxy extended to different amount of strain under uniaxial tension at 100°C.

L: focus on surface

R: focus beneath surface

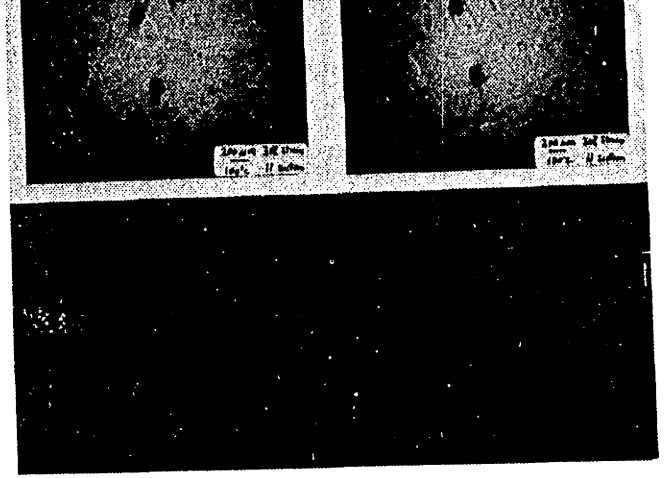

100°C 25-30% total strain
|| cross section

Figure C-6 continued

L: focus on surface R: focus beneath surface L: focus on surface R: focus beneath surface

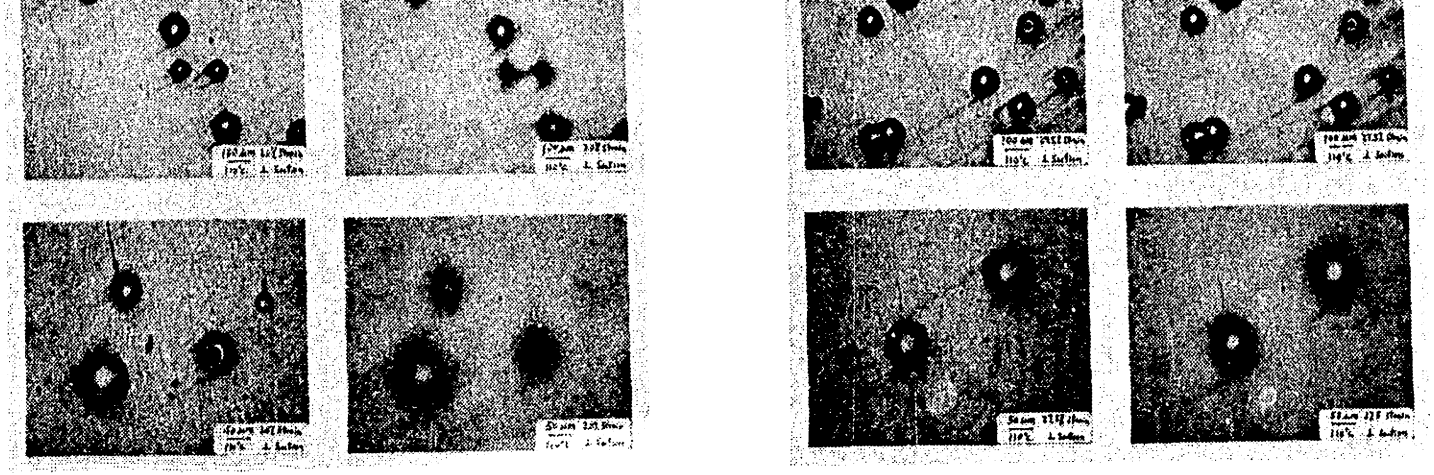

100°C 20% total strain
⊥ cross section

110°C 27.5% total strain
⊥ cross section

Figure C-7 Optical micrograph of the ⊥ cross section of 50 μm glass bead filled epoxy extended to different amount of strain under uniaxial tension at 110°C.

L: focus on surface R: focus beneath surface L: focus on surface R: focus beneath surface

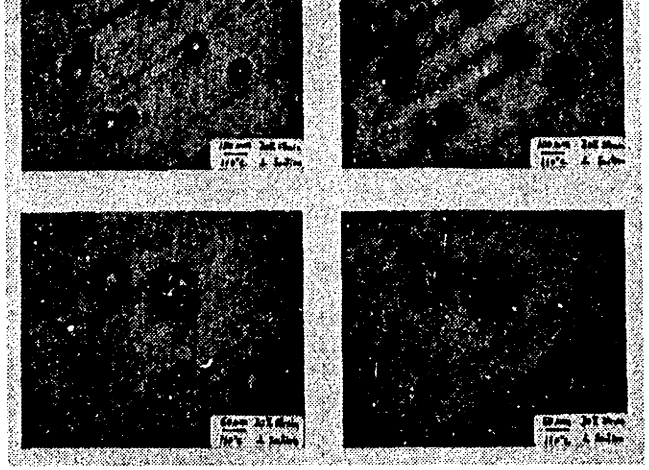

110°C 30% total strain
⊥ cross section

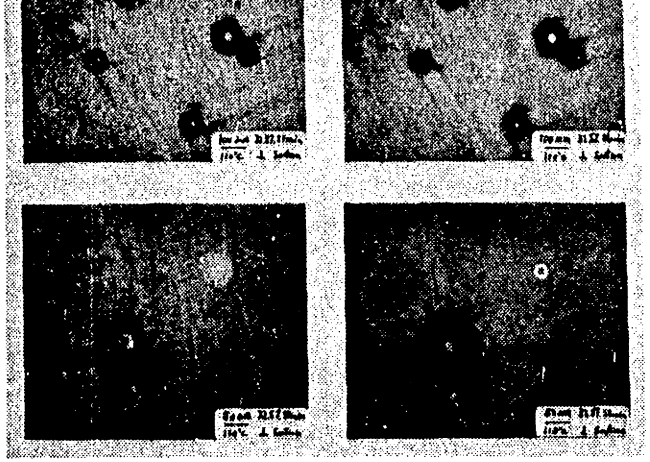

110°C 32.5% total strain
⊥ cross section

Figure C-7 continued

L: focus on surface R: focus beneath surface

L: focus on surface R: focus beneath surface

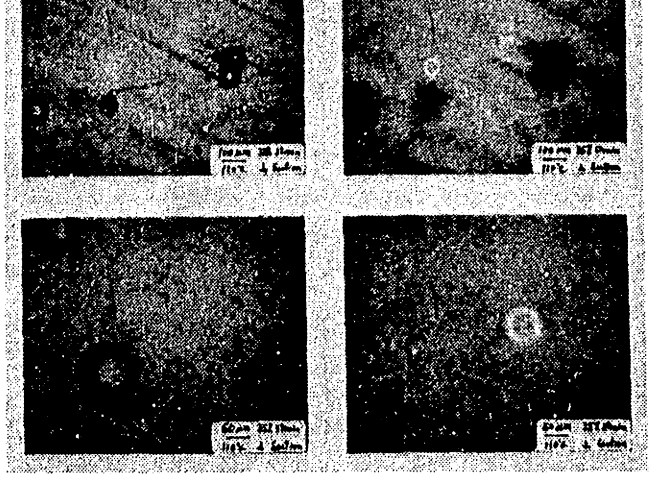

110°C 35% total strain
⊥ cross section

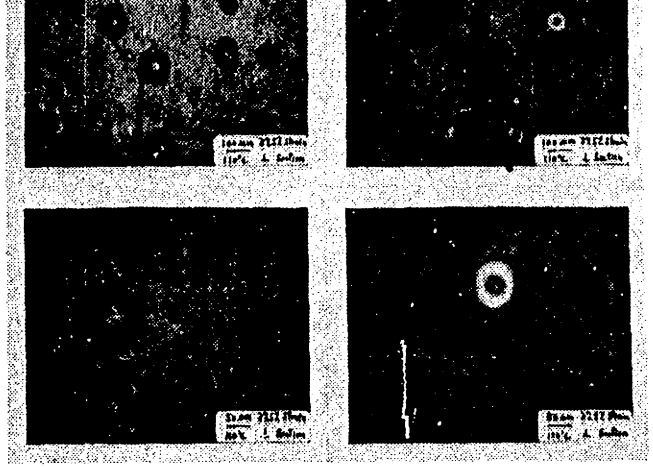

110°C 37.5% total strain
⊥ cross section

Figure C-7 continued

L: focus on surface

R: focus beneath surface

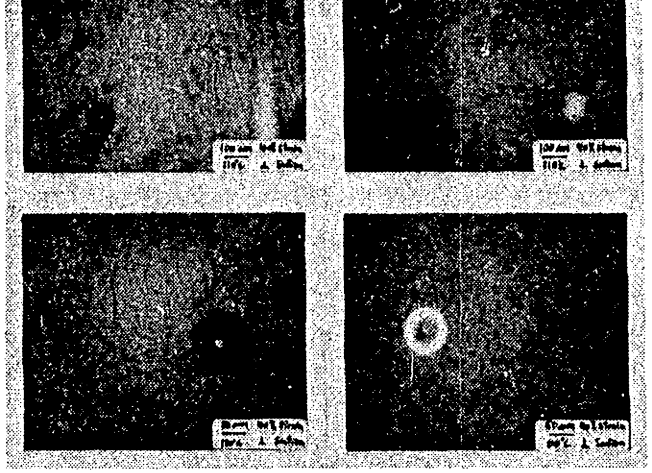

110°C 40% total strain
⊥ cross section

Figure C-7 continued

[redacted]

L: focus on

R: focus beneath

L: focus on

R: focus beneath

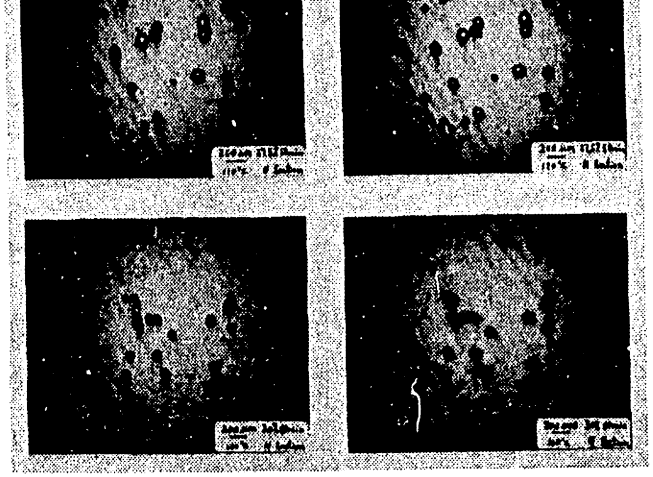

110° 20-30% total strain
|| cross section

110° 32.5-35% total strain
|| cross section

Figure C-8 Optical micrograph of the || cross section of 50 μm glass bead filled epoxy extended to different amount of strain under uniaxial tension at 110°C.

[redacted]

L: focus on surface

R: focus beneath surface

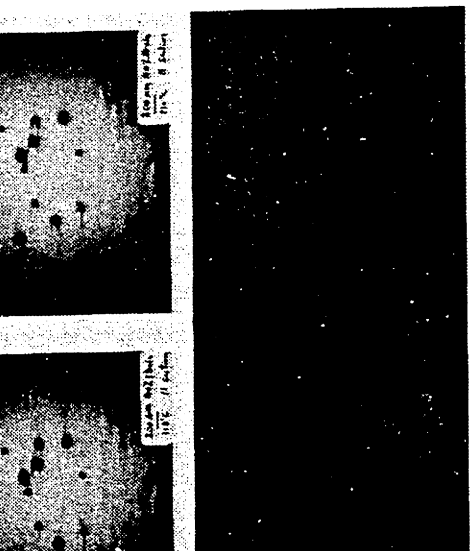

110°C 37.5-40% total strain
|| cross section

Figure C-8 continued

Fumed
particula
below 0.3
EH-5 grad
of this f
the high
are forme
fumed si
seperate
propertie

The
extensiv
racteriz
drogen b
interact
interact
causes f
the pola
liquid m
molecula
cules ma
them to
monofunc

PHISICAL PROPERTIES OF Cab-O-Sil, EH-5 SILICA

Specific Gravity	2.2
Color	White
Silica Content (Ignited Sample)	> 99.8%
Refractive Index	1.46
X-Ray Form	Amorphous
pH (4% in H_2O)	3.5 - 4.2
Surface Area	390 ± 40 m^2/gm
Nominal Particle Size (Calculated from Surface Area, BET Method)	0.007 micron
Ignition loss (1000°C, Moisture-free Basis)	2.5%

Table D-I Physical properties of Cab-O-Sil, EH-5 fumed amorphous silica (from Cabot Corp. Bulletin).

ticle, the rest of the molecule chain extends outward from the particle in to the liquid medium, thus preventing direct particle to particle collision and interaction. In non-polar organic dispersions, as well as in unstable polar liquid dispersions, the system can be stablized by the addition of monofunctional organic molecules, or by applying surface treatment of these molecules to the particles before dispersing in the liquid media.

The above ideas were utilized in the experiment of dispersing fumed silica in liquid polymer resins described in the appendix. Two kinds of polymeric materials were used as the matrix phase; Polymathyl mathacrylate (PMMA) and epoxy. PMMA was used in the initial stage of our investigation. Although a fine silica dispersion was made in the PMMA material, the material failed to be a useful material because of its susceptivity to environmental and stress crazing. However, the dispersion of fumed silica in PMMA is still described here to illustrate and compare the effectiveness of different mixing and dispersion methods in preparing fine particulate dispersions in a non-polar medium. The effectiveness of the polar groups on the polymer molecules in improving the degree of dispersion is illustrated by the SiO_2-epoxy system. The SiO_2-epoxy system is used in the investigation on the mechanical as well as friction and wear properties of fine particulate dispersied polymeric materials.

(1) SiO_2 - PMMA SYSTEM

Silica was dispersed in mathyl mathacrylate monomer before polymeri-

zation. In the initial stage of our experiment, the silica is dispersed through mechanical mixing alone. The mixing process involves propeller mixing, ball milling and ultrasonic disruption. The propeller mixing process was usually carried out for fifteen to thirty minutes. Ball milling was done with 3 mm glass beads in a polyethylene jar and milled for 6 hours to 3 days. The ball milling process was discarded later because it is time consuming and results in only marginal improvement of the degree of dispersion. The most effective mechanical dispersion method is with the ultrasonic disruption. The equipment used is a Heat Systems, Ultrasonic Inc., model W-370 ultrasonic disruptor. The process was conducted at 300 watts output power for 15 minutes for three to five times with intermittent power shut off to cool down the material. With the mechanical mixing alone, the maximum loading of silica is about 8% by weight of the monomer. Beyond this loading limit, the material is no longer a liquid dispersion and become something like wet sand.

After the silica was mechanically mixed into the monomer, the material was filled in test tubes and polymerized in a hot bath. The polymerization was carried out at 40°C in some tests and at 70°C in others. After 24 hours, the polymerization was further carried on to completion by heating at 85°C for at least another 36 hours. The samples were then separated from the test tubes and annealed at near Tg (about 110°C) for at least 48 hours.

Figures D-1 through D-5 are some micrographs which represent the relative effectiveness of dispersion that can be achieved by these different mechanical mixing methods. Shown in figure D-1 is a scanning electron micrograph of a tensile fractured surface of a sample that was

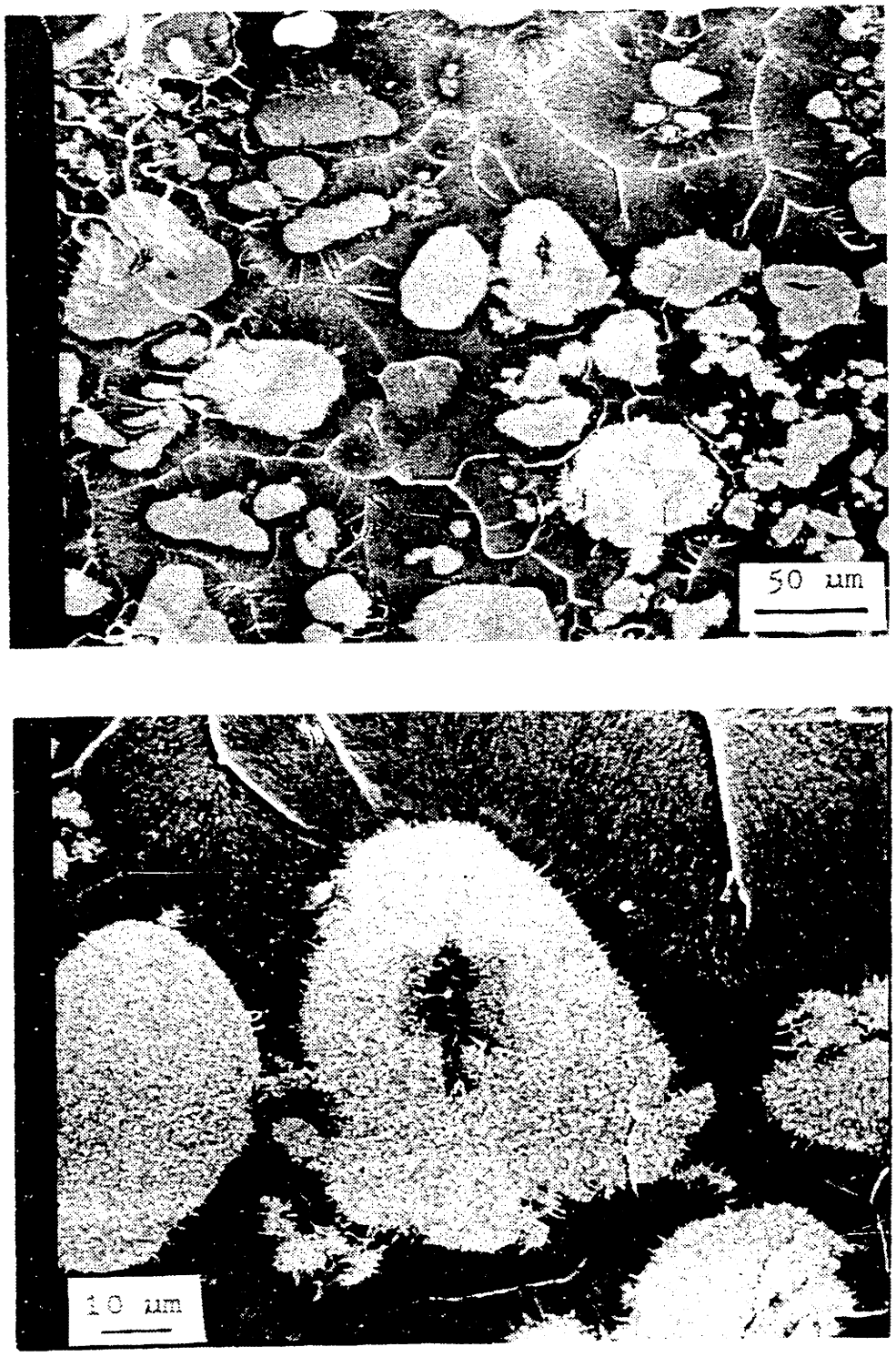

Figure D-1 Fracture section of fumed silica - PMMA material prepared by propeller mixing alone. Silica concentrat is 5% wt.

mixed by propeller mixing. It shows that the silica distribution in the PMMA matrix is not homogeneous. Patches of white areas on the fracture surface arefound to be higher in silica concentration than its surrounding area. This is confirmed by the x-ray image of silicon element from an energy dispersive x-ray analysis (EDAX), as shown in figure D-2. Figures D-3 and D-4 show successive improvement in dispersion by employing ball milling and ultrasonic disruption. These processes break up the high silica concentration area into smaller clumps, but their dimensions are still two to three orders of magnitude greater than desired. Shown in figure D-5 are optical micrographs of polished samples of materials prepared by the different mixing methods, which confirm the findings from fractography studies.

Improvement on the degree of dispersion was achieved by treating the surface of the fumed silica with a monofunctional polar organic liquid. The fumed silica was first dispersed in isopropyl alcohol $(CH_3)_2CHOH$ before mixing into the methyl mathacrylate monomer. Isopropyl alcohol has one C-OH polar group and two short branchings on the same molecule. It is expected that the polar group will be attached to the silica surface, and the two non-polar branches orient outward into the monomer medium.

The silica-alcohol dispersion was prepared by using a blender and the ultrasonic disruptor. The alcohol dispersion is usually made with approximately 1:3 weight ratio of silica to alcohol, determined by density measurement and by measuring the weight change of a fixed amount of dispersion after drying in an oven. The dispersion has a viscosity of 25 centipoise, which is free flowing and easy to mix with other liquids with

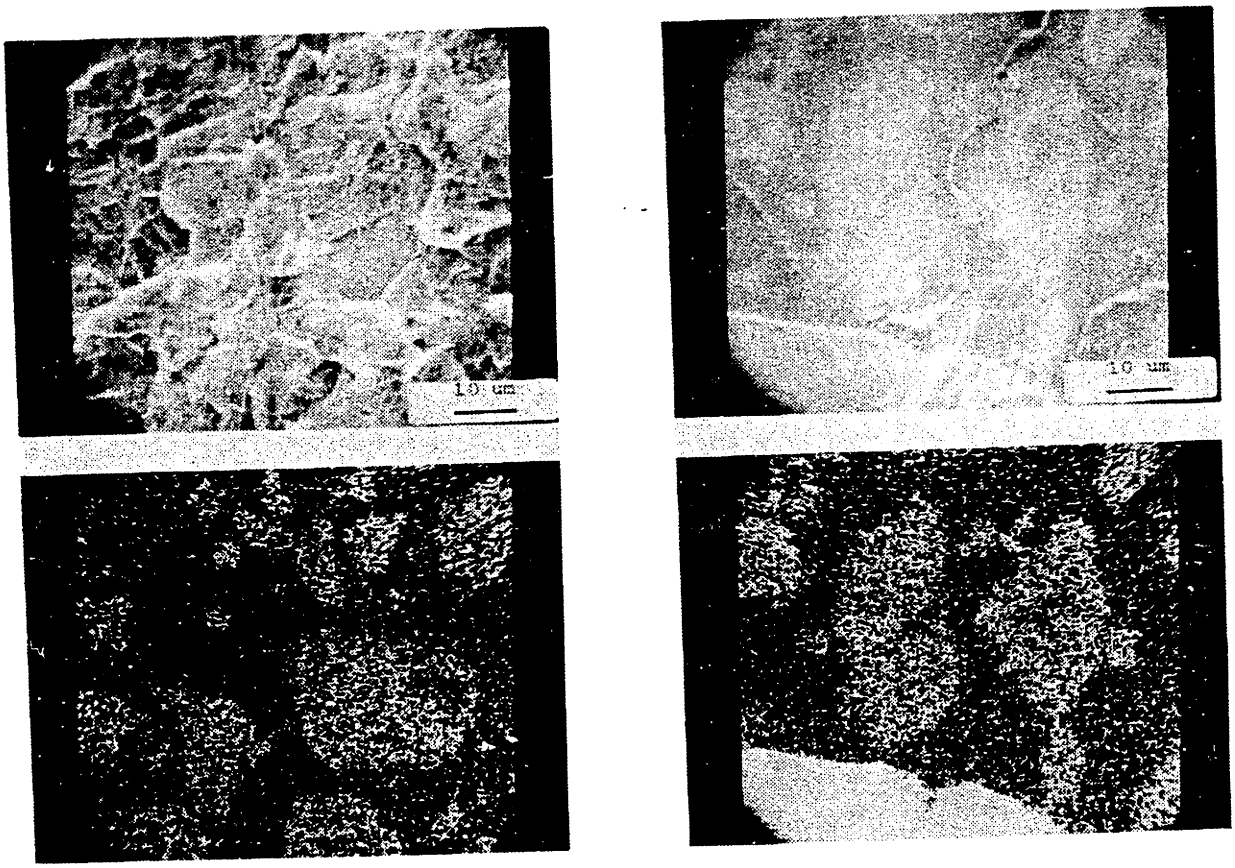

(a) 2% wt SiO_2 (b) 4% wt SiO_2

Figure D -2 Energy dispersive X-ray analysis of the fracture surface of fumed silica - PMMA material prepared by mechanical mixing. On top is SEM micrograph of the surface. At bottom is the X-ray image of the Si element.

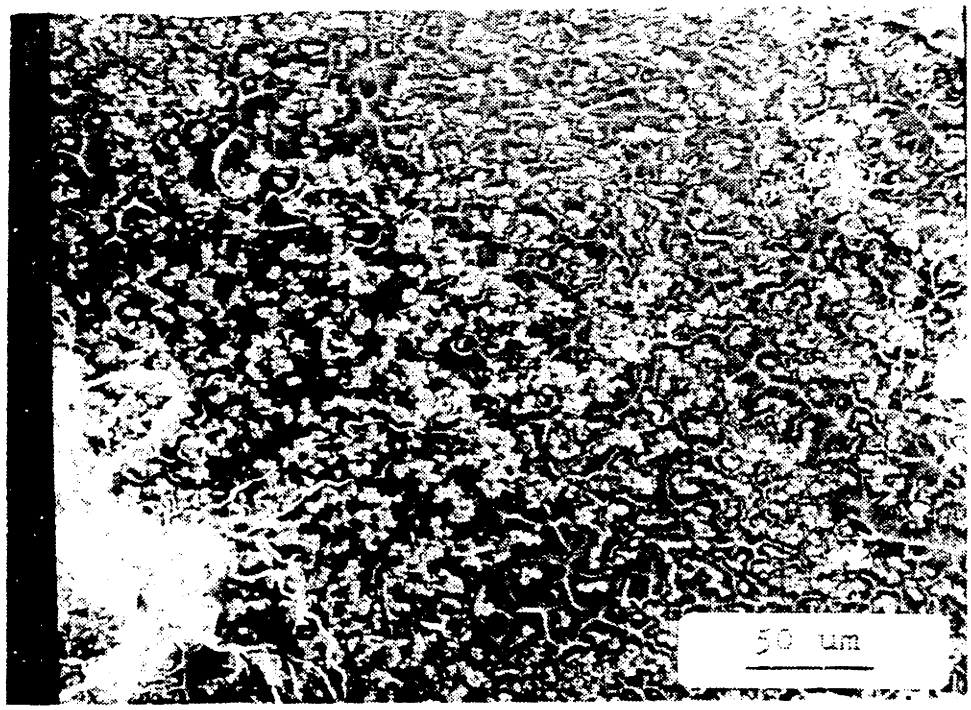

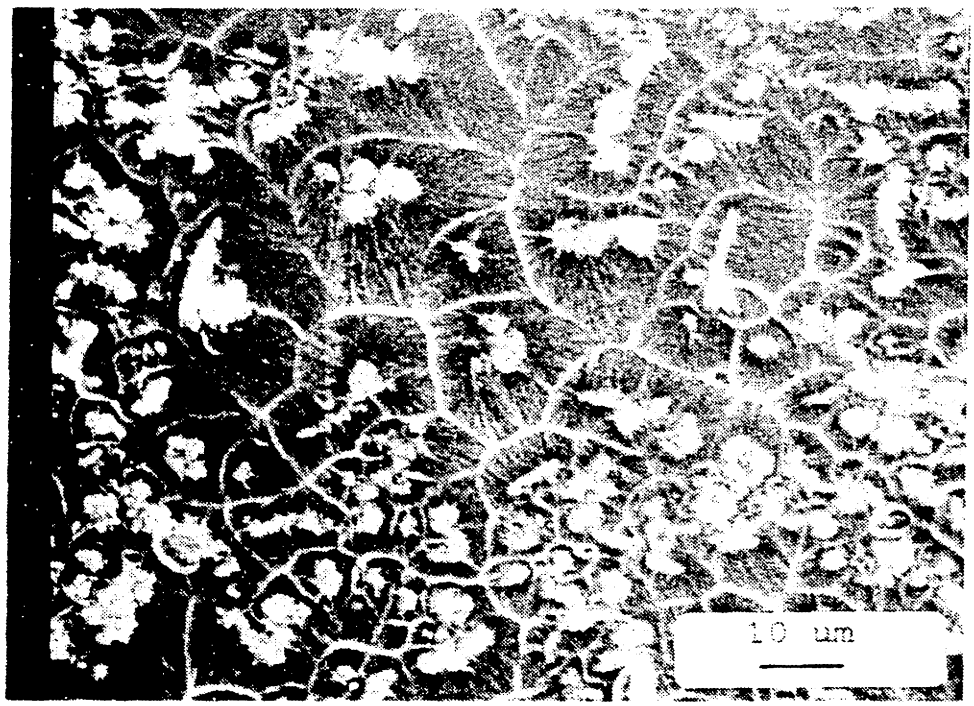

Figure D-3 Fracture cross section of fumed silica - PMMA material prepared by ball milling for 36 hours. Silica concentration is 5% wt.

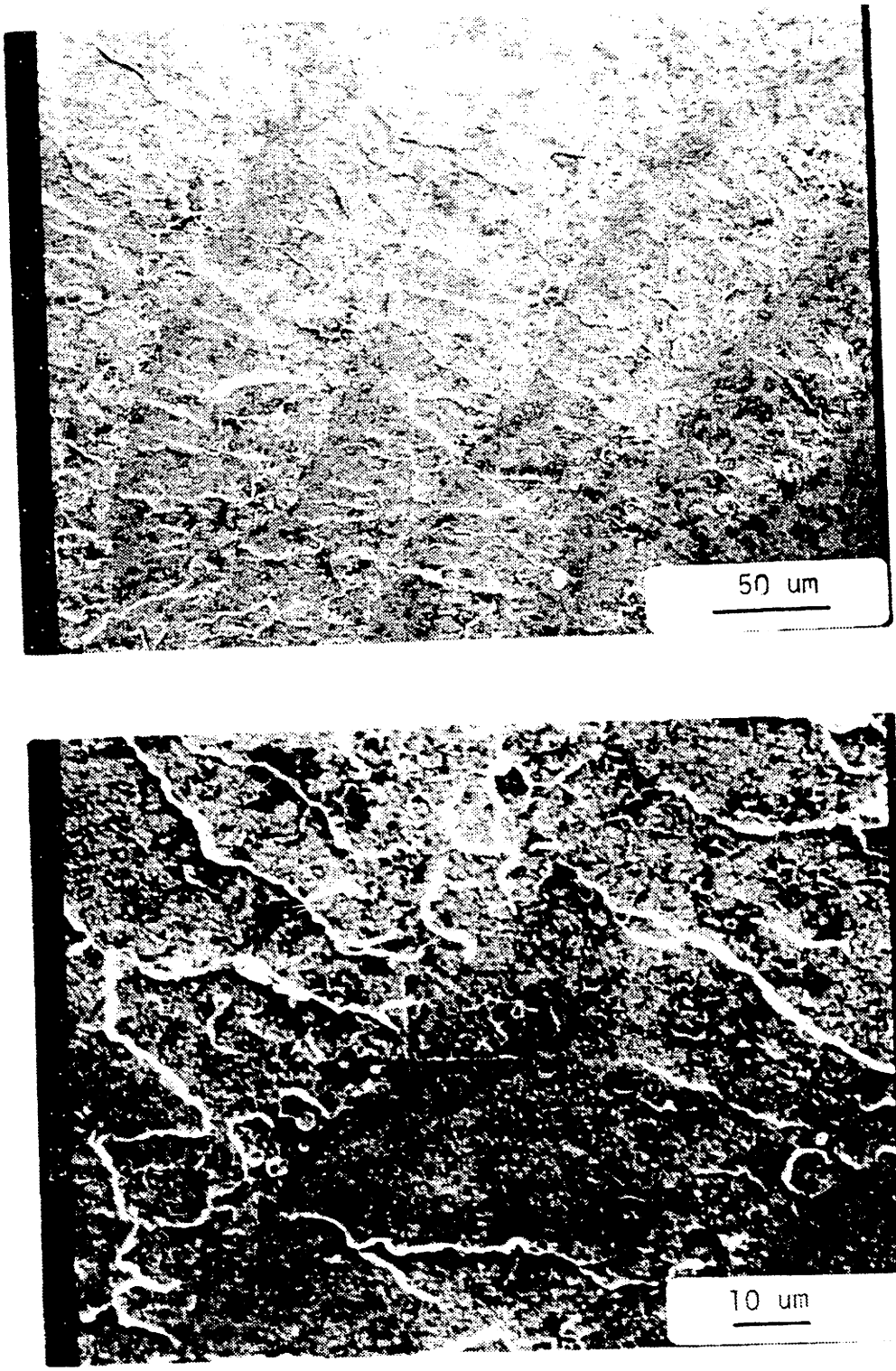

Figure D-4 Fracture cross section of fumed silica - PMMA material prepared by ultrasonic disruption. Silica concentration is 10% wt.

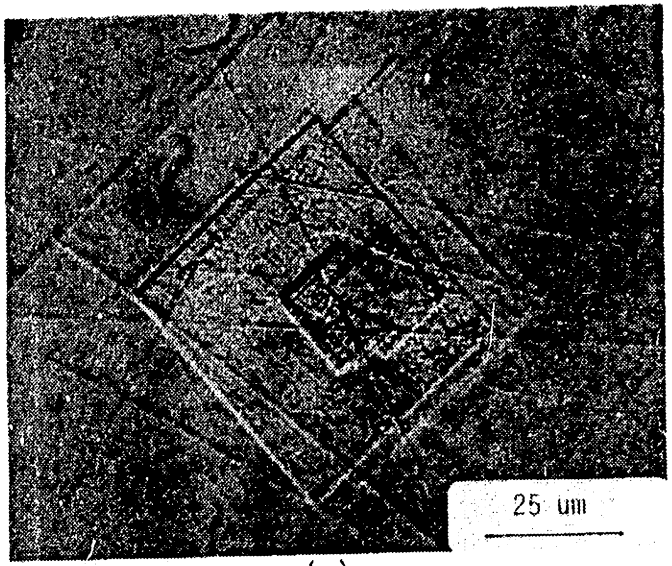

(a)

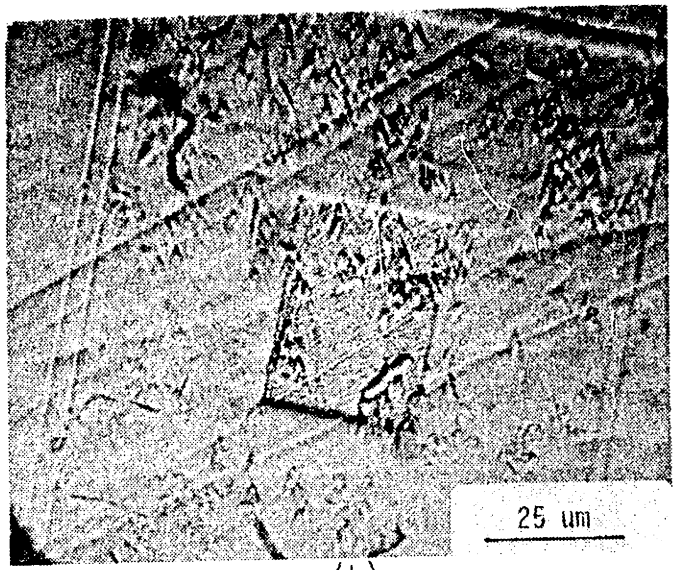

(b)

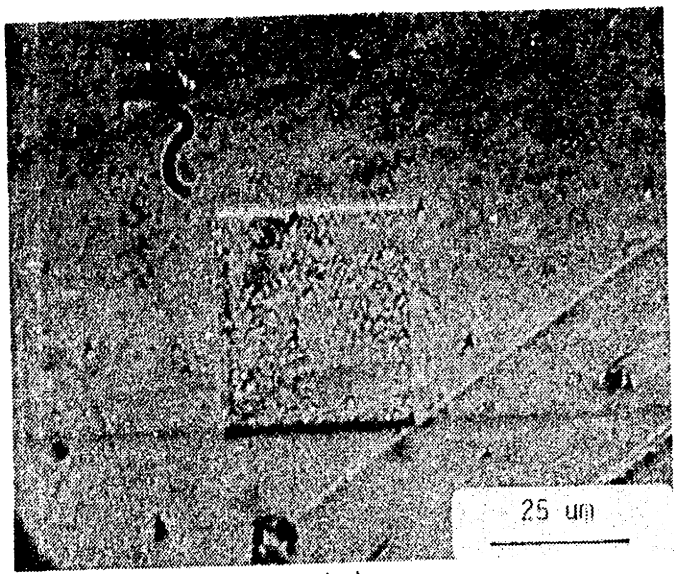

(c)

(a) propeller mixing

(b) ball milling

(c) ultrasonic disruption

Figure D-5 Optical micrographs of fumed silica - PMMA materials prepared by different mechanical methods. Rectangles are etched (burned) marks left after examining. Under scanning electron microscope.

simple mixing equipments. After the silica-alcohol dispersion was mixed into the methyl methacrylate monomer, polymerization was carried out in a hot bath at 75°C. As the molecular weight of PMMA increases, and due to the heat released from the exothermic reaction, the alcohol is driven out from the material. The residual alcohol in the material is later characterized by density measurement to be less than 1% by weight.

Figure D-6 shows the fracture micrograph of the SiO_2-PMMA material that was treated with alcohol. No particulate phase can be found on the surface at the magnification shown. Figure D-7 shows the EDAX analysis of the fracture surface, which also indicates that the silica is uniformly distributed throughout the material. Besides achieving good particle dispersion, the alcohol treatment method also has the advantage of making high silica loading samples. So far, the maximum loading is 20% weight of SiO_2 in PMMA, the silica distribution in the matrix is uniform, and the sample is transparent when examined under visible light, as shown in figure D-8. Some light scattering tyndle effect was observed, which is the optical characteristic of colloidal size particle dispersions. Although the amount of residual alcohol in the material is small, they do effect some of the material properties, especially in stress and environment crazing. Multiple number of crazes were found on some samples when subjected to tensile tests. Also, some of the samples which were never tested shows crazes after several weeks of exposure to the environment. The SiO_2-PMMA system was given up to look for other materials which will tolerate the minute amount of residual alcohol. Nevertheless, it is still presented here to illustrate the important distingtion between the problem of mixing and dispersion, and to demonstrate the effectiveness of

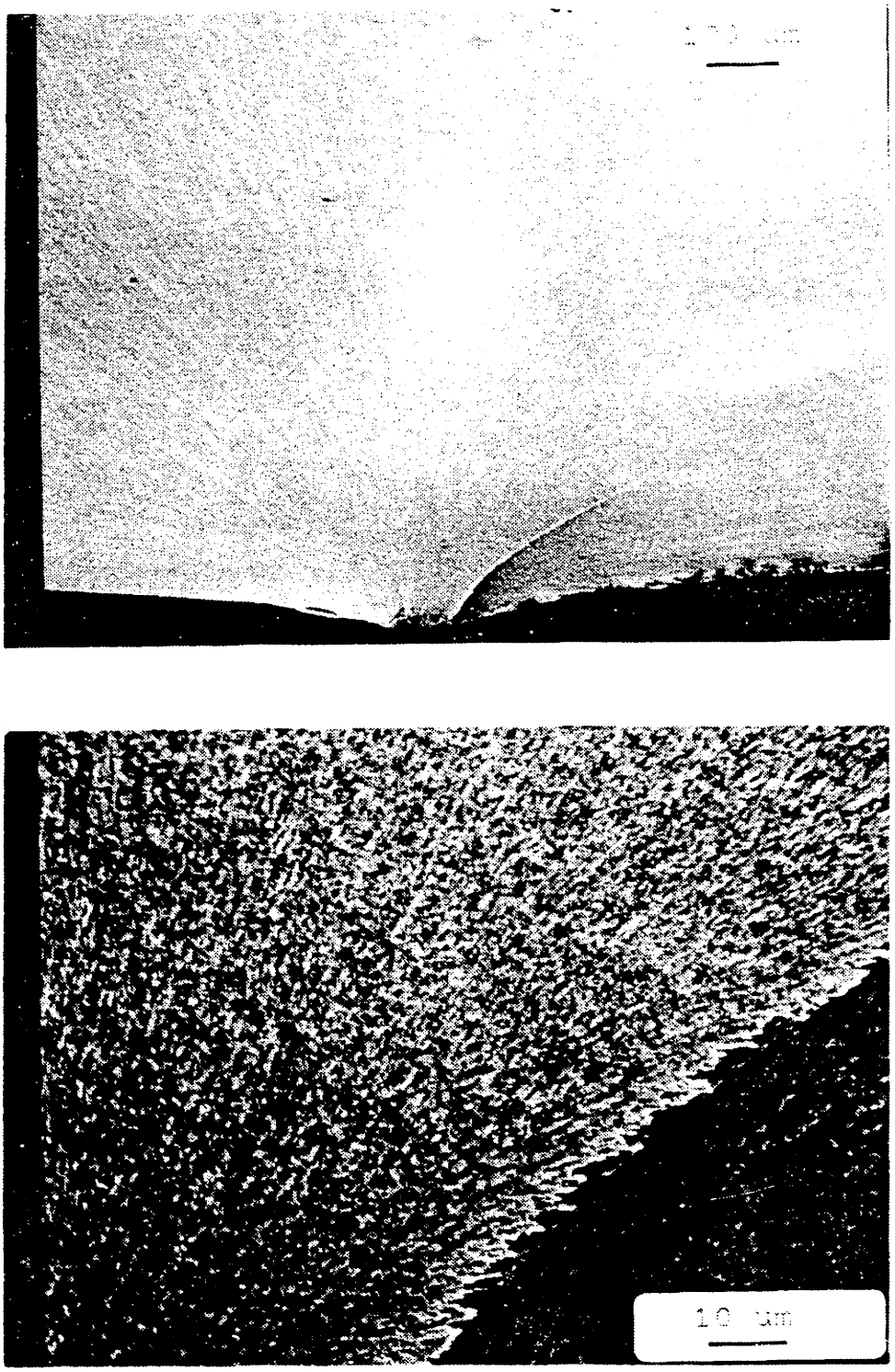

Figure D-6 Fracture cross section of fumed silica - PMMA treated with isopropyl-alcohol. Silica concentration is 11% wt.

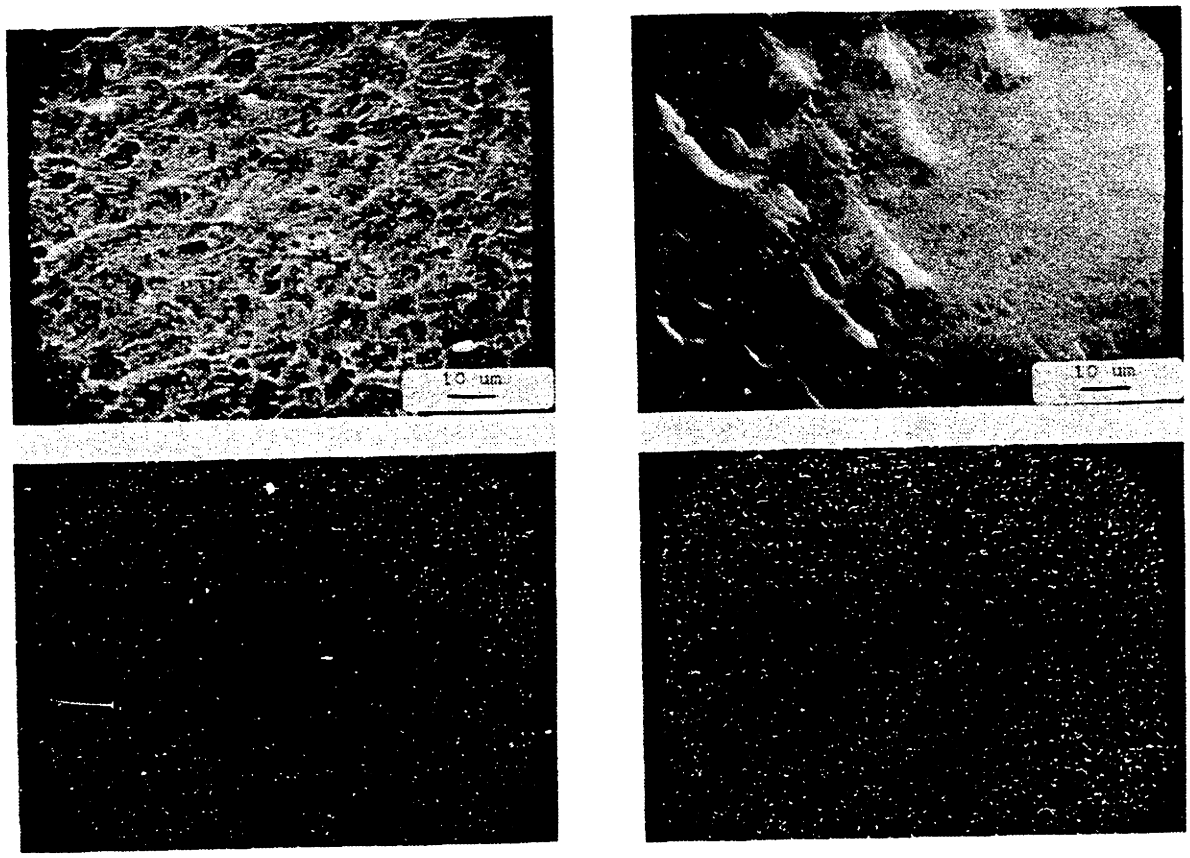

(a) 10% wt SiO_2 (b) 20% wt SiO_2

Figure D-7 Energy dispersive X-ray analysis of the fractured surface of fumed silica - PMMA material treated with isopropyl alcohol. On top is the SEM micrograph of the surface. At bottom is the X-ray image of Si element in the same area.

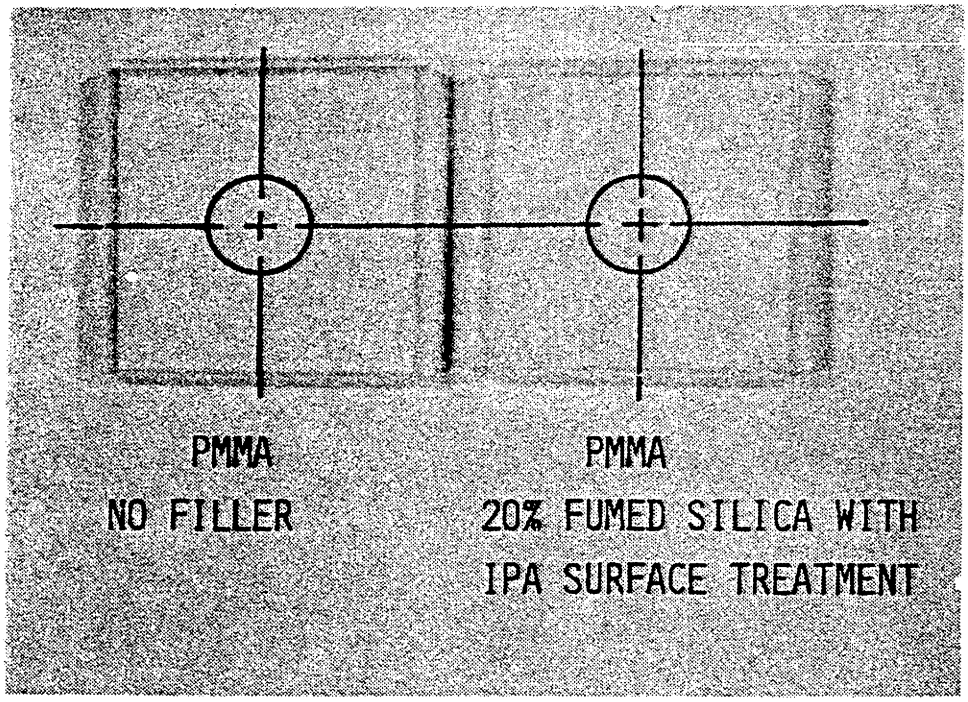

Figure D-8 Isopropyl alcohol treated fumed silica - PMMA material is still transparent even with 20% wt of silica.

the alcohol surface treatment.

(2) SiO_2 - EPOXY SYSTEM

From the experience of the SiO_2-PMMA system, the dispersion provided by alcohol surface treatment is further exploited by choosing a polymer resin that is miscible with alcohol, and its properties are not grossly effected by the presence of minute amount of residual alcohol left in the material after polymerization. In the selection of the polymer resin, it is also considered to choose a material which also has the desired molecular structure to provide the same kind of dispersion effect as the isopropyl alcohol. In the SiO_2-epoxy system, we will demonstrate how the molecular structure of the epoxy effects the degree of dispersion, when no dispersion agent were used. Alcohol was used in most of the later experiments. Besides serving as a dispersion aid along with the chosen epoxy resin, it also serves as a carrier to reduce the viscosity of the mixture, thus enable us to use higher loading of fumed silica in the system.

To choose an epoxy resin that will provide similar dispersion effect as alcohol, we followed the general guideline of selecting an epoxy resin which has a polar group on its molecular structure that will adsorb onto the silica surface. The epoxy chosen is a hydantoin epoxy; Ciba-Geigy XB-2793. Figure D-9 shows the structure of an dimethyl hydantoin moledule, and the charge polarity of the C = O carbonyl group in the structure. The dimethyl hydantoin can be reacted to epichlorohydrin to make an epoxy molecule, as shown in figure D-10. The exact formular of the Ciba-Geigy XB-2793 resin is not revealed by the manufacturer, but it should possess similar characteristics of the resin structure shown in the above figure.

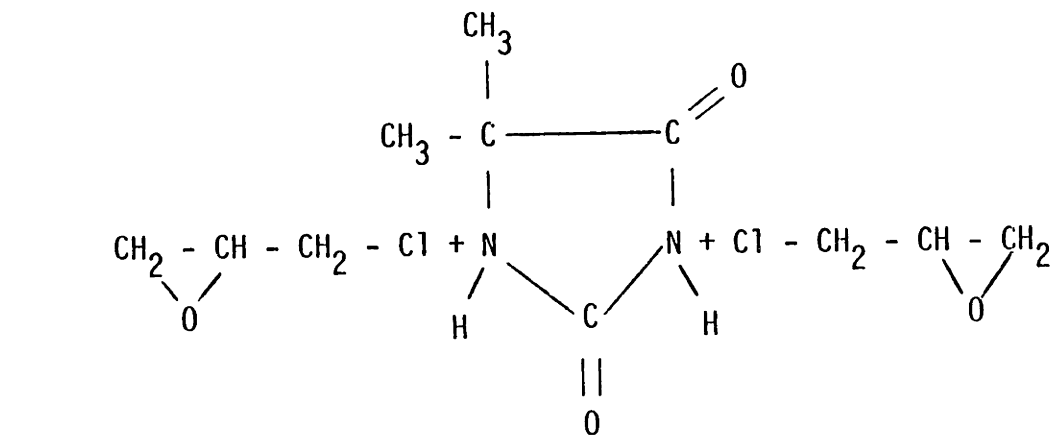

epichlorohydrin dimethyl hydantoin epichlorohydrin

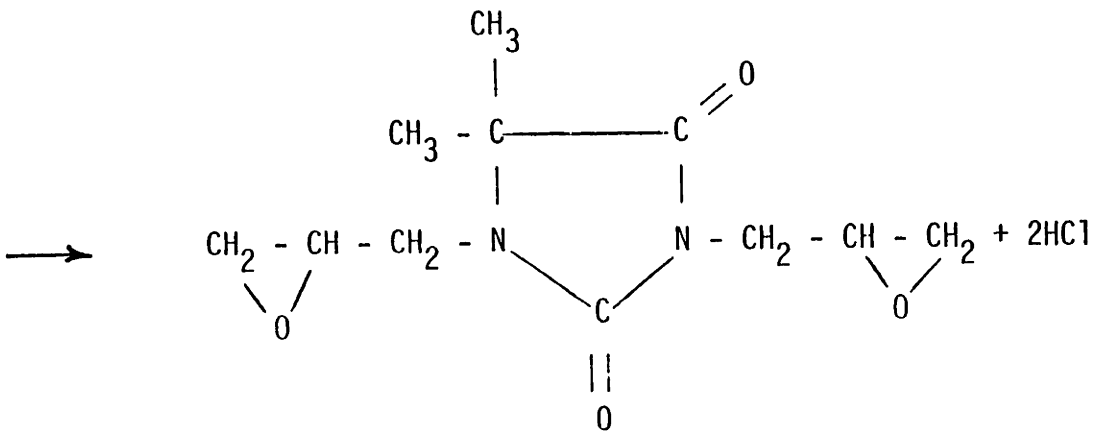

epoxy

Figure D-10 Reaction of a dimethyl hadantoin molecule with epichlorohydrin to form an epoxy molecule

Another epoxy resin; DGEBA (diglycidylether, of bisphenol A), which does not have a strong polar group on its structure was used to compare with the hydantoin epoxy. Molecular structure of DGEBA is shown in figure D-11. The particular type of DGEBA resins used are Shell Epon-828 and 826. The Epon-826 is similar to Epon-828, but with some diluent to lower the viscosity of the resin. To compare the relative dispersion effectiveness of the resins, the fumed silica was mixed in these resins without using alcohol. The mixing was done with a blender and the ultrasonic disruptor. The resins are cured with an anhydride curing agent; Lindride 6K, obtained from Lindau Chemical Inc. The curing was done by pouring the resin mixture in a double aluminum plate mold with a 1/4 inch thick rubber gasket in between to provide for the molding cavity. The curing proceeds in two steps. It was first curet at 85°C for three hours and then changed to 150°C for another 15 hours. Figures D-12 through D-14 are transmission electron micrographs of the fumed silica dispersion in these two different epoxies. Particles in the non-polar DGEBA epoxy resin flocculates together, while particles in the more polar hydantoin epoxy are much well dispersed.

Compared to the mathyl mathacrylate monomer, the epoxy resins have a higher room temperature viscosity at about 2500 centipoise. The effectiveness of the ultrasonic disruptor decreases sharply with increasing media viscosity, because of viscous power dissipation. In order to achieve high silica loading, and for easy removal of air bubbles traped in the material, alcohol was used in most of the experiements. The function of alcohol is twofold; first, it is used as a carrier agent to reduce the viscosity of the mixture while increasing the filler loading, to give the highest

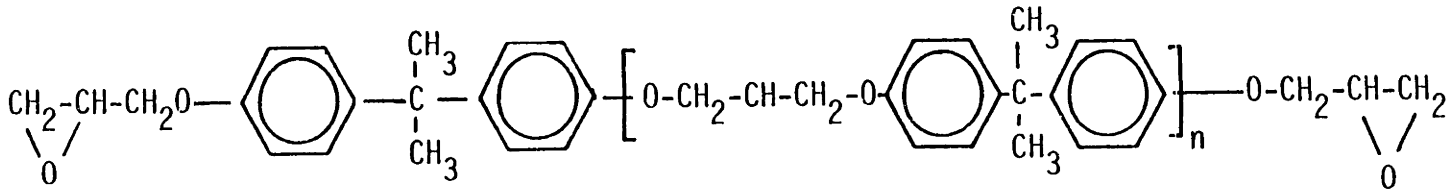

Figure D-11 Structure of DGEBA epoxy.

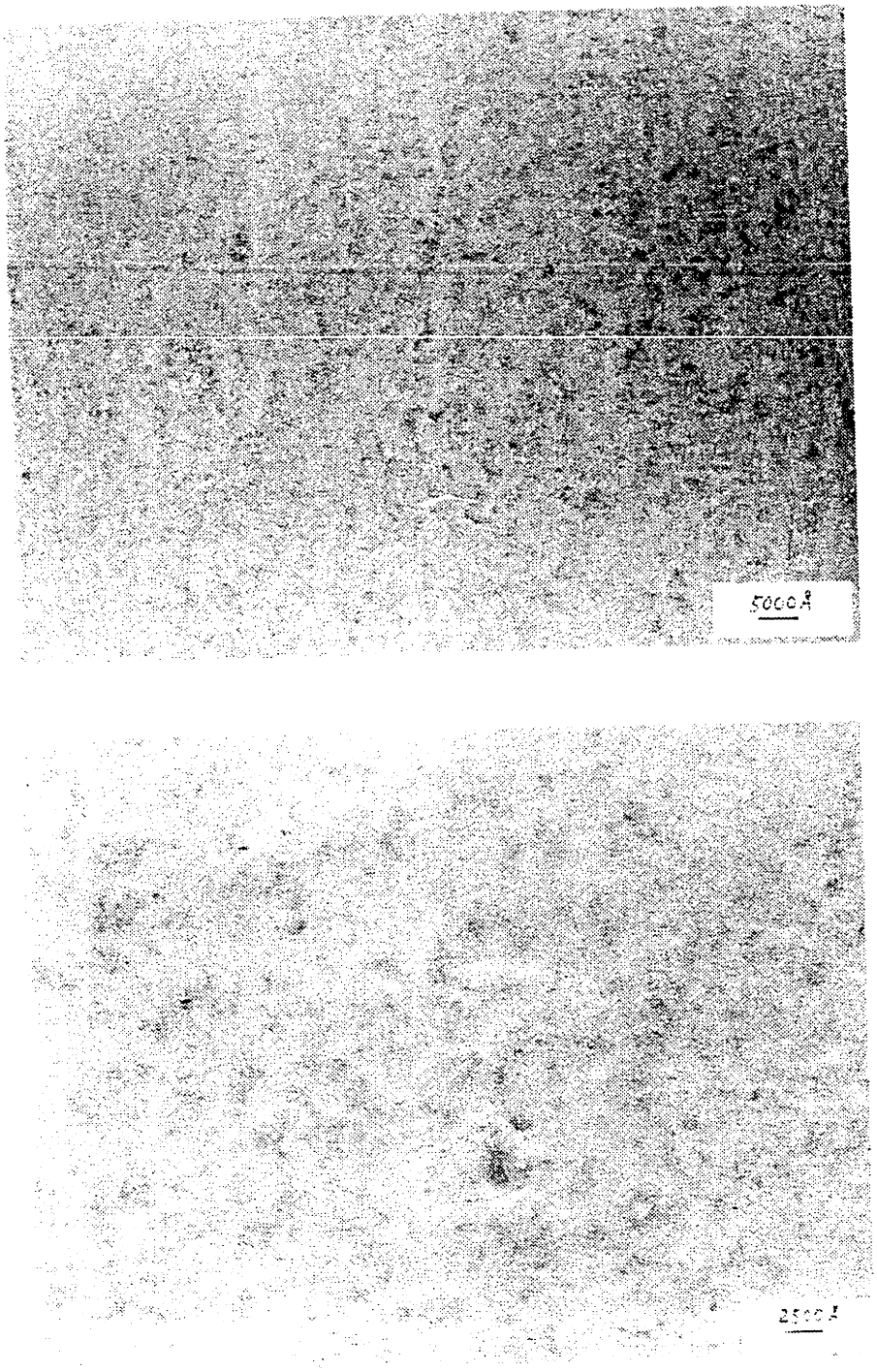

Figure D-12 TEM micrograph of fumed silica in hydantoin epoxy (XB-2793) without isopropyl alcohol treatment. Silica concentration is 5% wt.

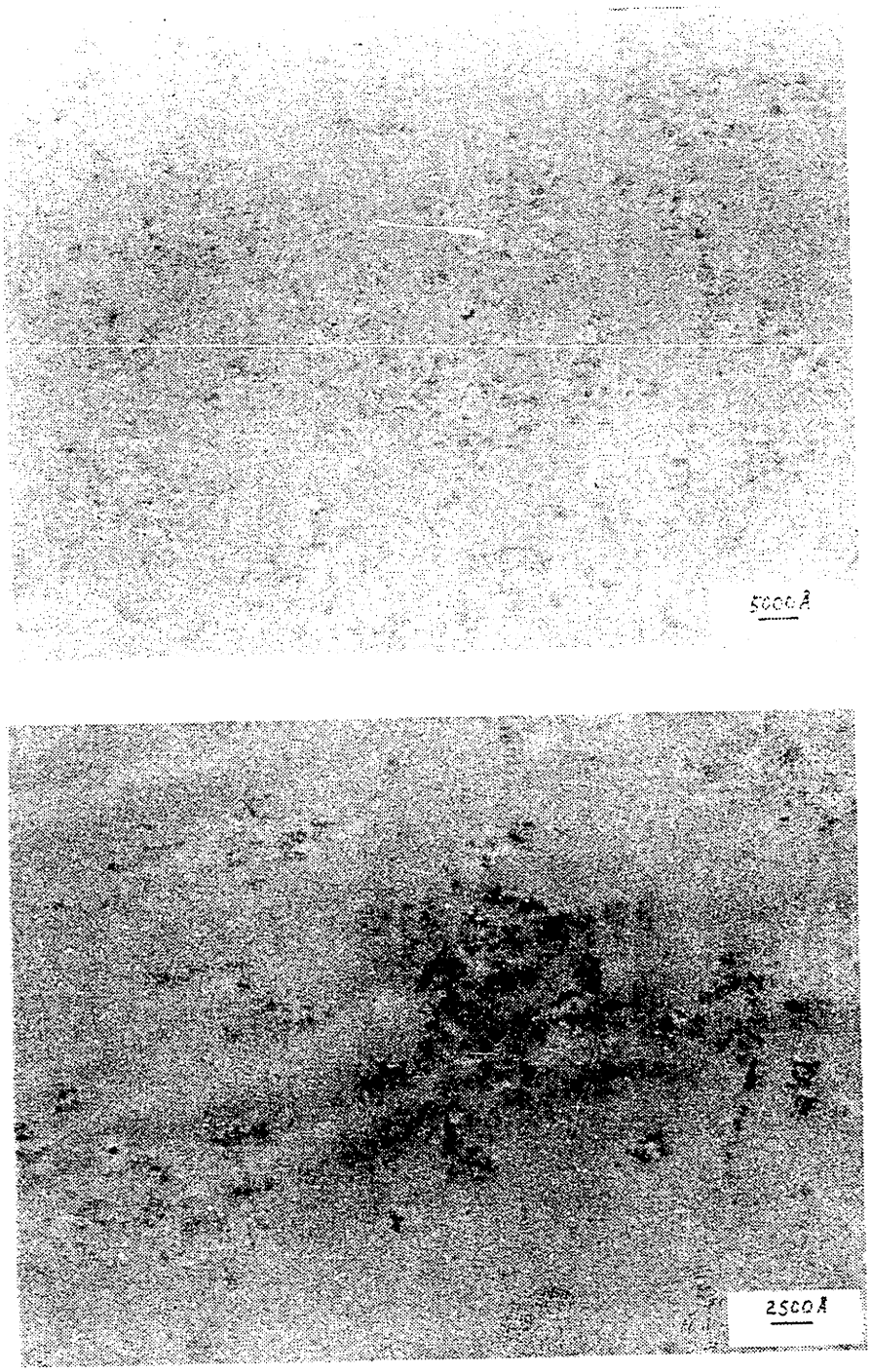

Figure D-13 TEM micrograph of fumed silica in DGEBA epoxy (Epon-828). Silica concentration is 3% wt.

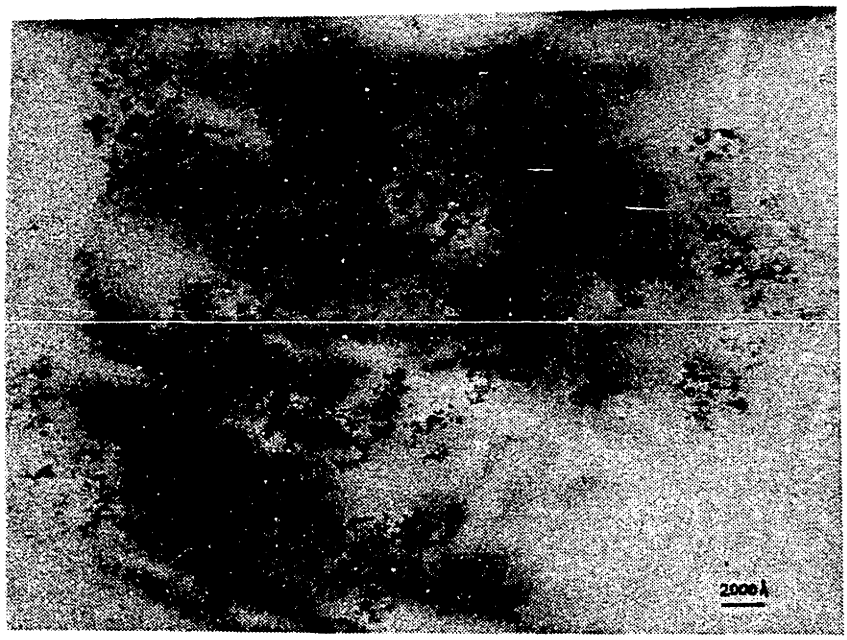

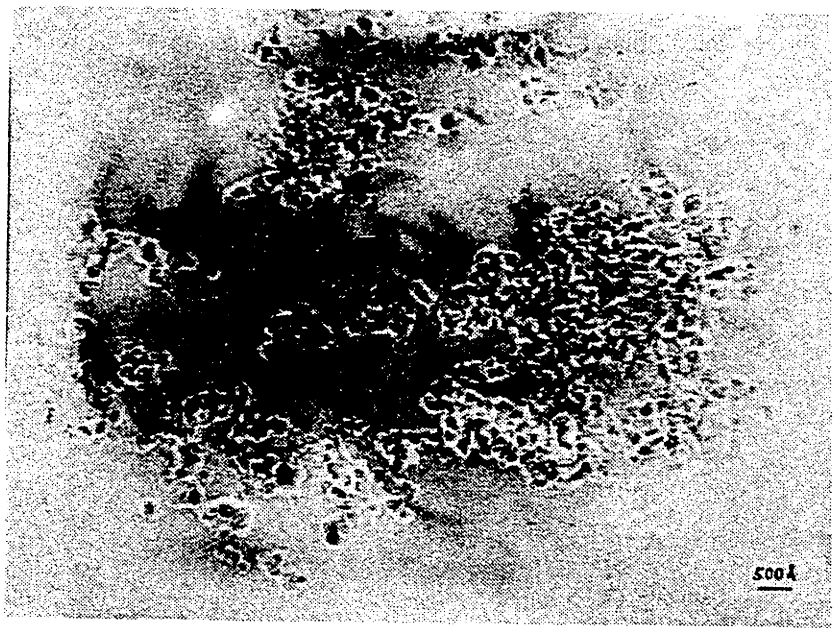

Figure D-14 TEM micrograph of fumed silica in DGEBA epoxy (Epon-826). Silica concentration is 4% wt.

efficiency of the mixing equipment, mainly the ultrasonic disruptor. Secondly, the alcohol may provide further dispersion effect to retard particle flocculation. The process adopted in most of our experiments involves the preparation of a concentrated SiO_2-isopropyl alcohol dispersion; usually at 25% silica to alcohol weight ratio, followed by mixing this concentrated alcohol dispersion in the hydantoin epoxy resin using a blender and the ultrasonic disruptor alternatively for several times. The mixture was then poured in a three neck flask, where stirring and vacuum were applied simultaneously to drive out the alcohol. The material becomes more viscous as the process proceeds. After five hours, the anhydride curing agent was added to the material. The stirring continued for another half an hour to an hour, and vacuum alone was applied for another hour to drive out air bubbles in the material. The material was then casted in aluminum molds with the same process as described previously. The amount of residual alcohol left in the sample is estimated by density measurement to be less than 2% by weight.

The curing agent was found to be critical in maintaining the stability of the dispersion. Because the exact composition of additives and promoters in curing agents is generally not revealed by the manufacturer, the selection was made by a trial and error process. There are two major categories of curing agents for epoxy resins. One type promotes curing by catalytic action. Only a few parts per hundreds of these curing agents are required for curing the epoxy. The other type participates directly in the reaction, and is chemically bounded into the epoxy resin chain. The anhydride curing agent used in our experiment belongs to the second category. In order to achieve high silica loading, the promoter type of

curing agents are preferred. However, of all the promoter type curing agents tested, they resulted in quick gelation as well as resin and particle fall out from the dispersion. Therefore, anhydride curing agent was used in all experiments at a concentration of 45:55 weight ratio of curing agent to epoxy. The silica concentration is effectively diluted in half in the final resin mixture. Starting from a 25% silica-alcohol dispersion, the highest silica loading produced in the final cast sample is about 12% by weight of the resin.

Transmission electron micrographs of the alcohol treated SiO_2-epoxy material are shown in figures D-15 and D-16. The silica particles are shown to be uniformly dispersed in the epoxy matrix. High magnification micrographs reveals that the size of the particulate aggregates are in the range of 500 to 800 angstroms. As shown in figure D-17, the isopropyl alcohol treated fumed silica filled hydantoin epoxy (XB-2793) is relatively transparent when compared to the fumed silica filled DGEBA epoxy (Epon-828) shown in figure D-18, which is also an indication of better dispersion.

Mechanical properties such as tensile modulus, tensile stress and strain at fracture of the fumed silica filled material are characterized and compared with the unfilled material. Samples of the unfilled material with different post-cure history were included in the test. The effect of the residual alohol was also characterized with one batch of the unfilled material. Also, included in the tests are two batches of samples filled with 20 micron size glass beads, which are used to demonstrate the sensitivity of the crack propagation process to the inherent flaw size. The results are shown in figure D-19 through D-21. The properties of the fumed silica filled

material were found to be at least as good as the unfilled material.

Reference

D-1. Iler, R.K., The Colloidal Chemistry of Silica and Silicates, Cornell U. Press, (1955).

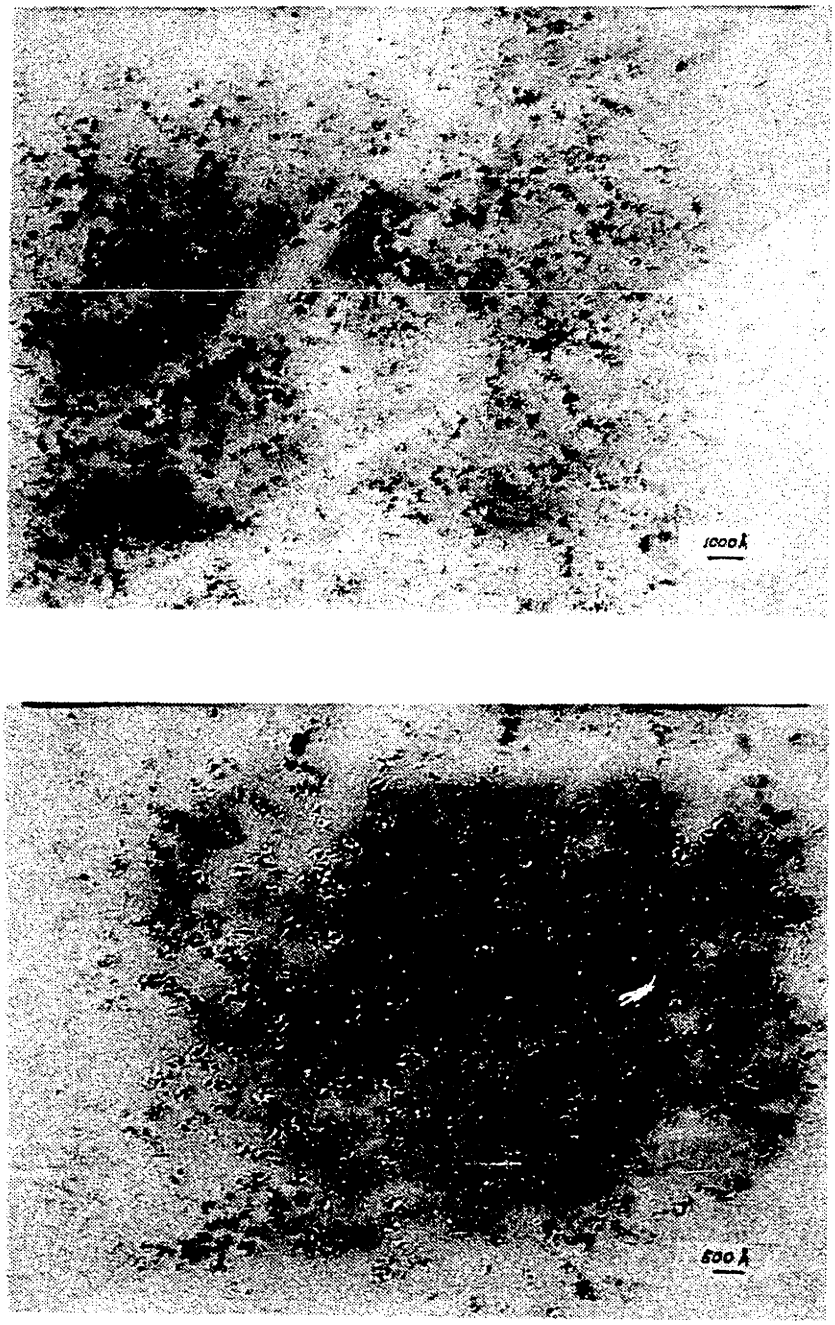

Figure D-15 TEM micrograph of fumed silica in hydantoin epoxy (XB-2793) with isoproyl alcohol treatment. Silica concentration is 10% wt.

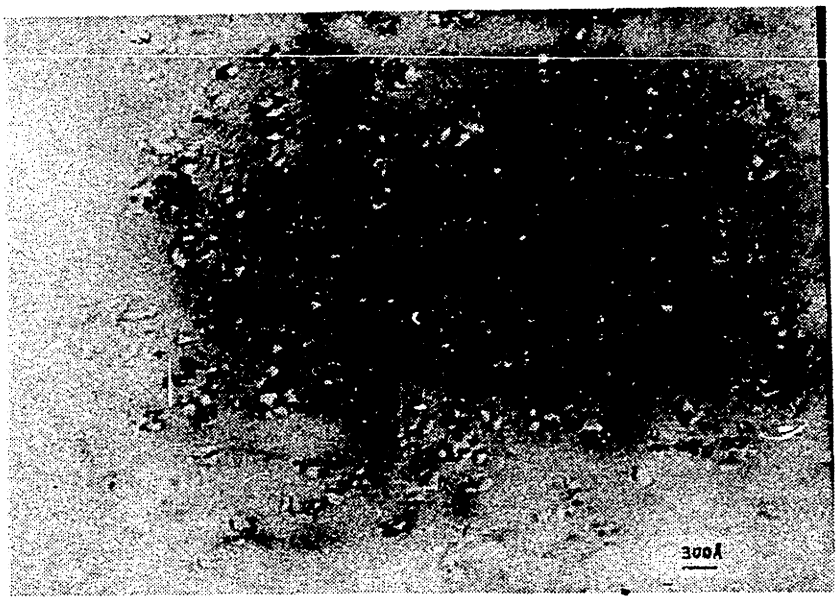

Figure D-15 (continued)

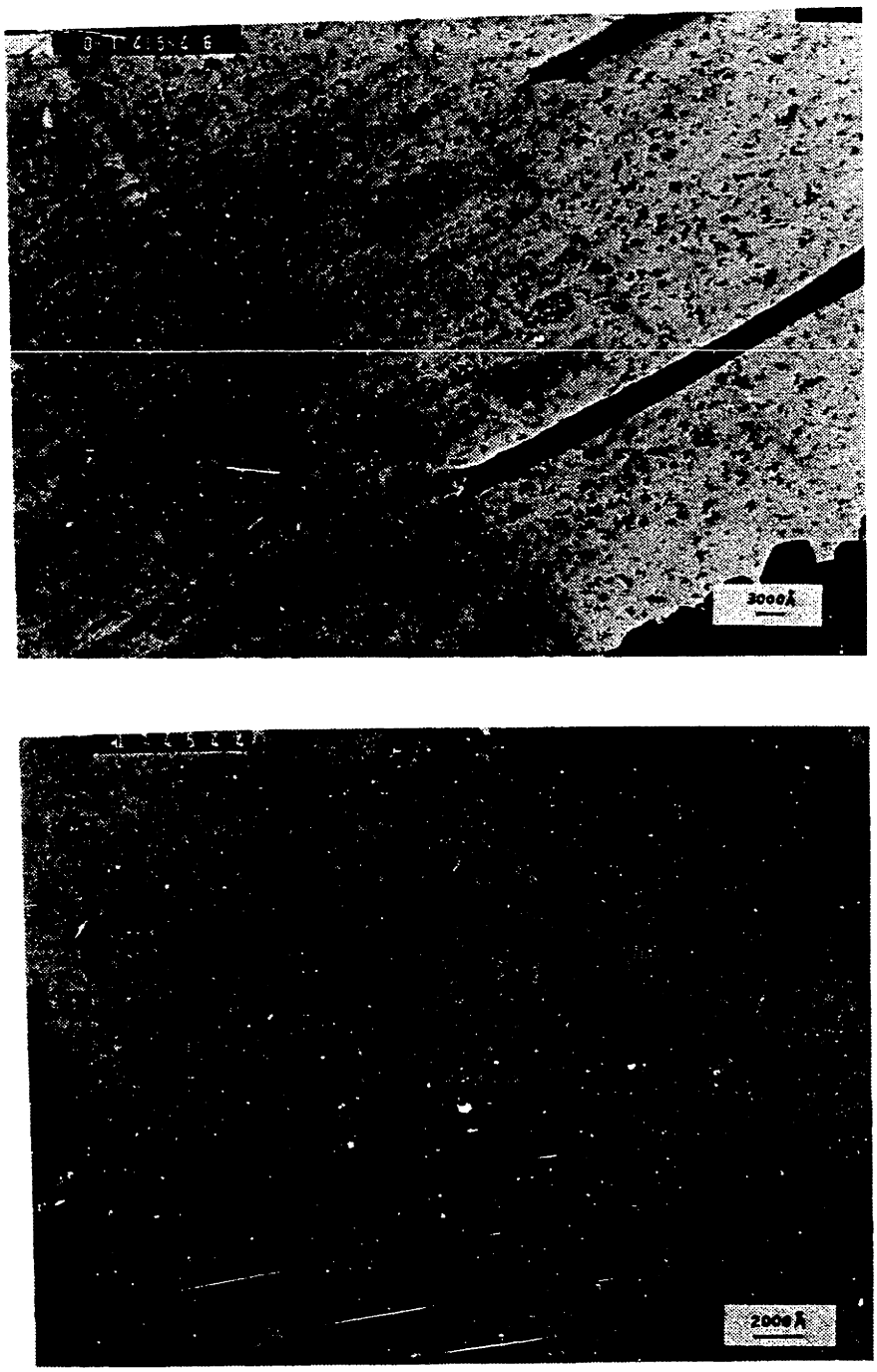

Figure D-16 TEM micrograph of fumed silica in hydantoin epoxy with isopropyl alcohol treatment. Silica concentration is 5% wt.

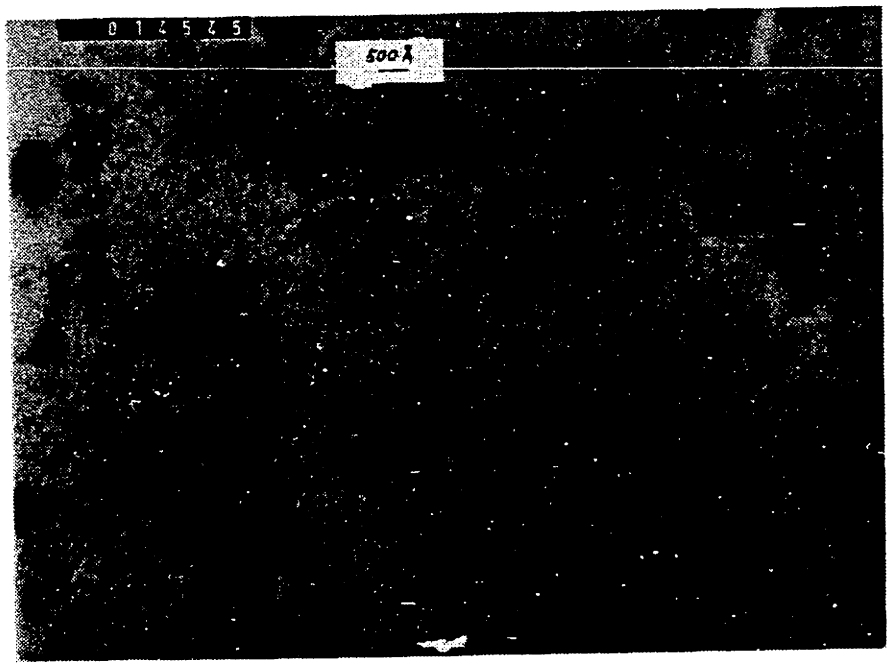

Figure D-16 (continued)

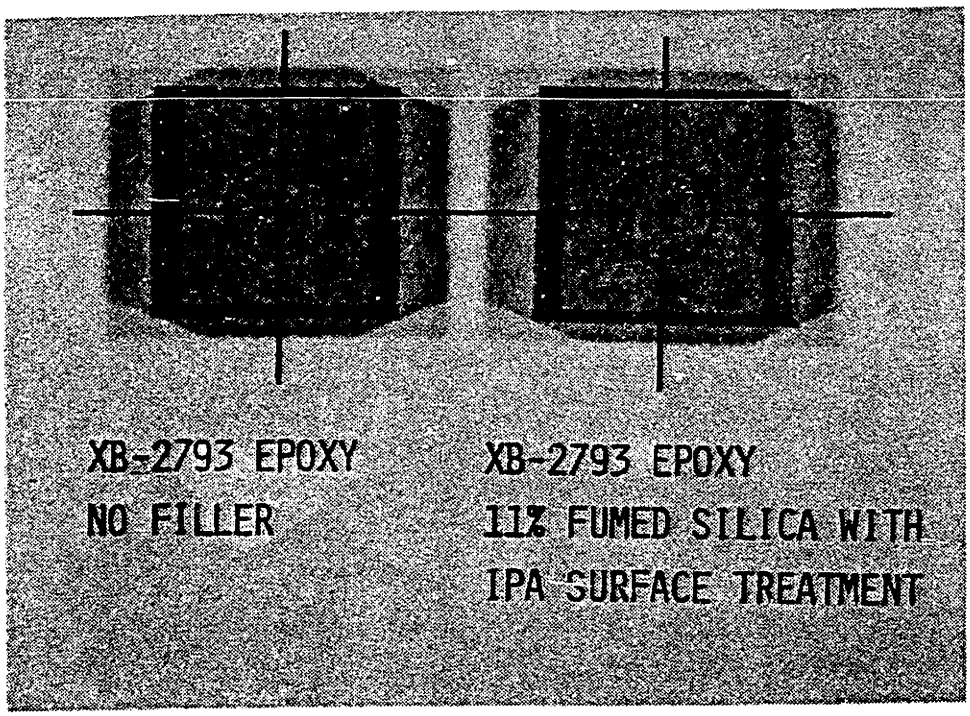

Figure D-17 Sample of isopropyl alcohol treated fumed silica in hydantoin epoxy (XB-2793) is still transparent with 11% wt silica concentration.

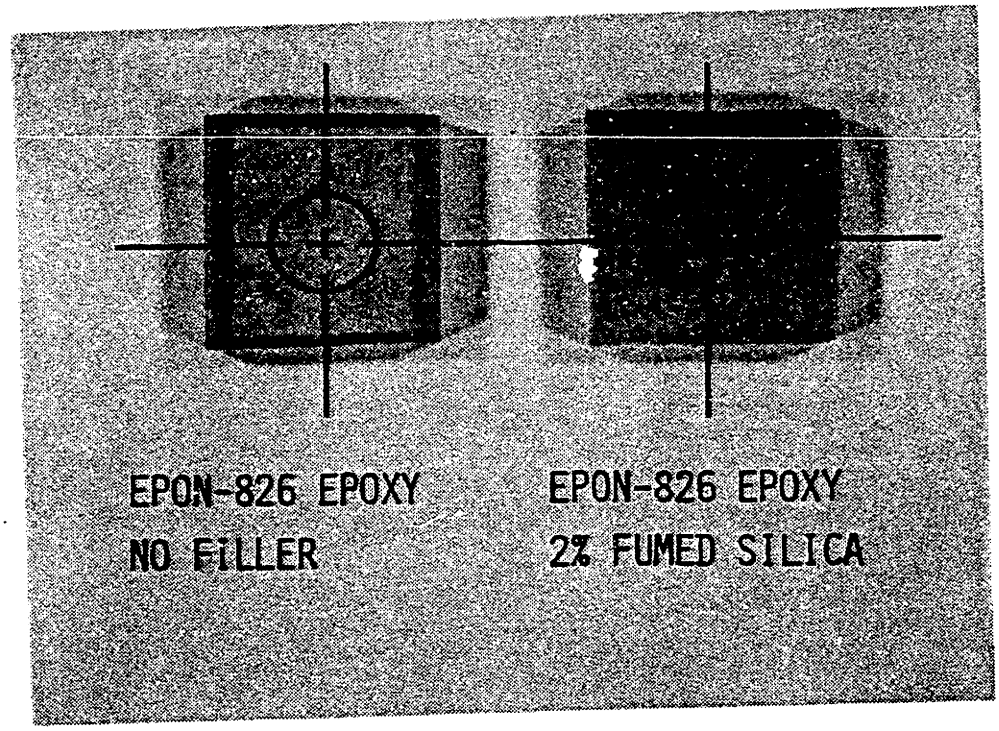

Figure D-18 Sample of fumed silica in DGEBA epoxy (epon-826) is liss transparent than the fumed silica filled hydentoin epoxy as shown in figure E-17, even with only 2% wt silica.

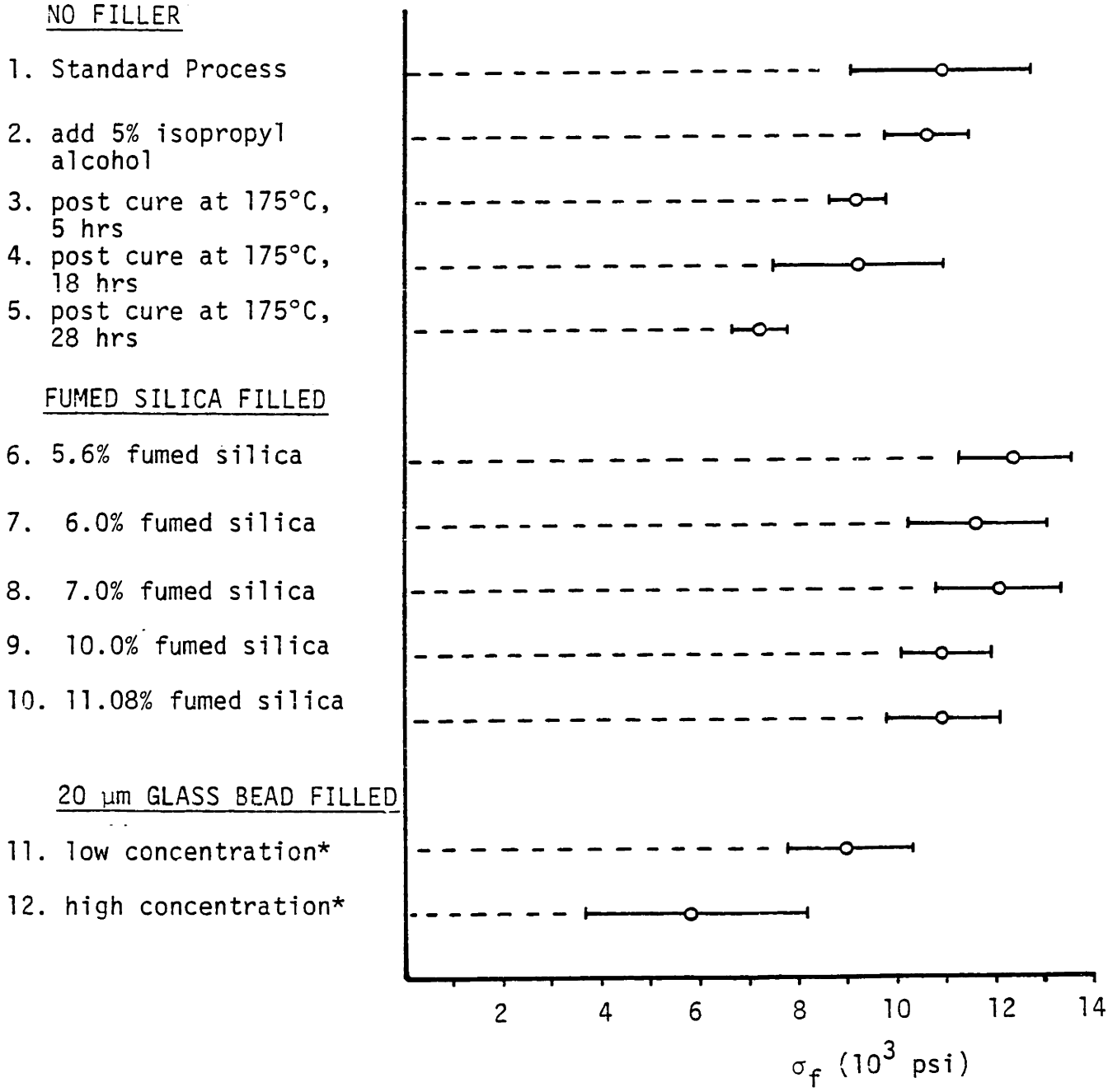

*5% glass beads were initially mixed in batch 11 and 12. Both batches have less than 1% glass beads in the test samples, due to settling during the curing process.

Figure D-19 Fracture strength of epoxy with different curing process and with different particulate fillers.

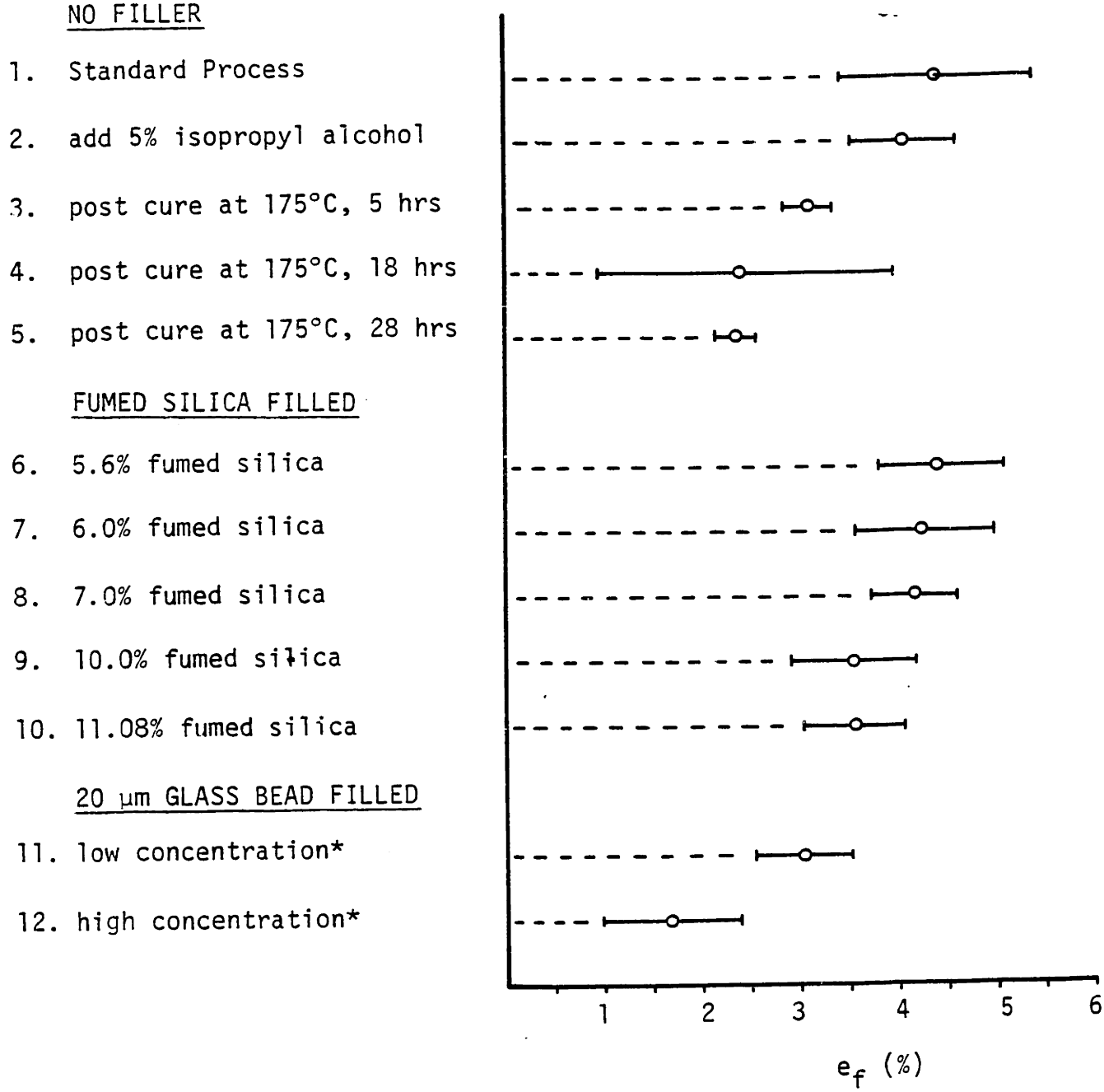

*5% glass beads were initially mixed in batch 11 and 12. Both batches have less than 1% glass beads in the test samples, due to settling during the curing process.

Figure D-20 Fracture strain of epoxy with different curing process and with different particulate fillers.

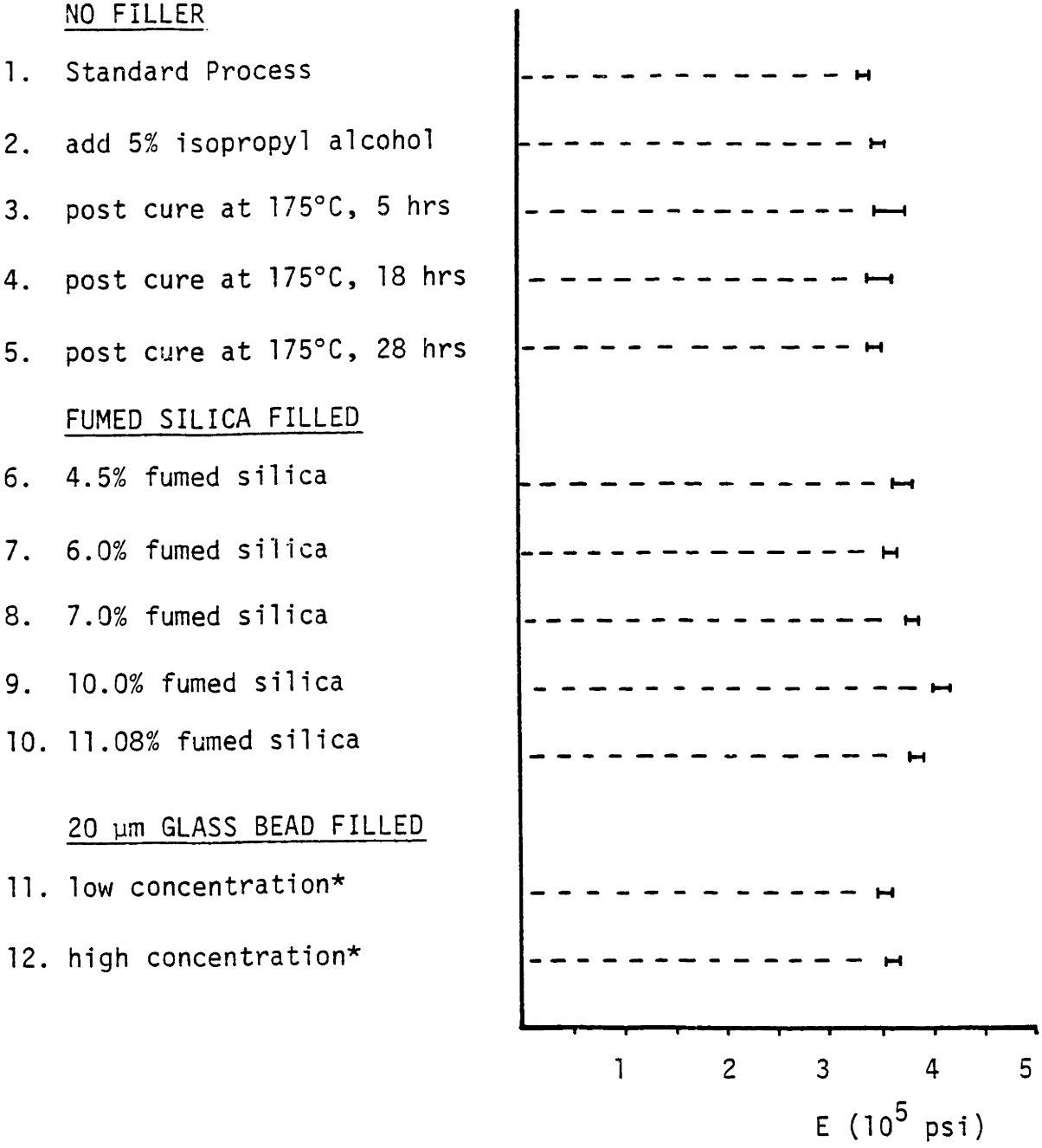

*5% glass beads were initially mixed in batch 11 and 12. Both batches have less than 1% glass beads in the test samples, due to settling during the curing process.

Figure D-21 Modulus of epoxy with different curing process and with different particulate fillers.

Appendix E

TEMPERATURE RISE AT SLIDING CONTACT

The temperature rise at the sliding interface due to frictional heating can be modeled as follows. In our plane on cylinder sliding wear test arrangement (shown in figure E-1), the frictional heat generated at the sliding interface can be considered as a stationary heat source to the test sample and a moving heat source to the rotating steel cylinder. This heat transfer problem was discussed by Jaeger [E-1]. An approximate form of Jeager's solution, given by Cook [E-2] is presented here. For a band heat source of width 2a (figure E-1), the maximum and average flash temperature increases at the sliding interface relative to the temperature in the assumed semi-infinite body are,

For the moving band heat source:

for $\frac{v \cdot a}{\kappa} > 10$ (high speed):

$$\theta_{max} \approx 1.6 \frac{qa}{k} \left(\frac{v \cdot a}{\kappa}\right) \qquad (E-1)$$

$$\theta_{avg} \approx \frac{2}{3} \theta_{max}$$

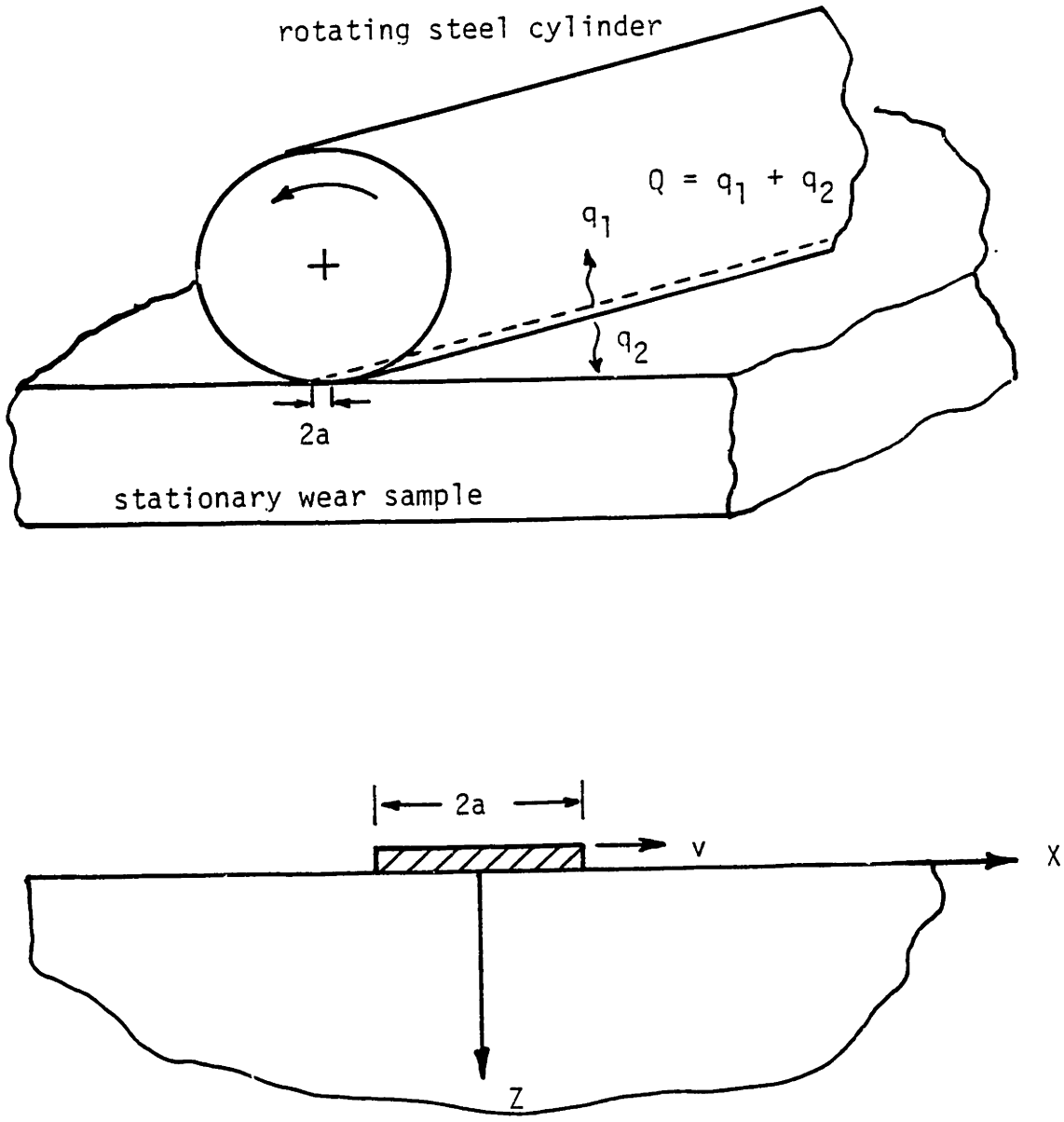

Figure E-1 Model of the sliding contact as a band heat source.

for $\frac{v \cdot a}{\kappa} < 0.5$ (low speed):

$$\theta_{max} \approx 0.64 \frac{qa}{k} \ln \left[\frac{6.1\ \kappa}{v \cdot a}\right]$$

$$\theta_{avg} \approx 0.64 \frac{qa}{k} \ln \left[\frac{5.0\ \kappa}{v \cdot a}\right] \qquad \text{(E-2)}$$

For the stationary band heat source:

$$\theta_{max} \approx 1.1 \frac{q : a}{h}$$

$$\theta_{avg} \approx 0.95 \frac{q : a}{k} \qquad \text{(E-3)}$$

Where q is the heat transfer from the heat source to the semi-infinite body and k and κ are the thermal conductivity and the thermal diffusivity respectively . Notice that the temperature rise is a function of the non-dimensional parameter (va/K). In order to solve the above equations, it is assumed that the temperature increases are the same at both the stationary and the moving bodies. The sum of the frictional heat that is transferred to the stationary and moving bodies is equal to the frictional work,

$$Q_{total} = q_1 + q_2 = W_{friction} = \mu \cdot L \cdot u \qquad \text{(E-4)}$$

The contact band width, 2a, can be estimated from applied load, sample dimensions, and hardness of the material. Listed in table E-1 are some materials with very different thermal properties. Figures E-2 and E-3 show the results of the analysis for epoxy sliding against steel at different loads and speeds. The temperature rise of epoxy sliding against the materials listed in table E-1 are shown in figure E-4. It should be noted that the low thermal conductivity of materials such as glass and polymers results in a much higher interfacial flash temperature than is found in more conventional materials.

References

E-1. Jaeger, J.C., "Moving Source of Heat and the Temperature at Sliding Contacts," Proc. Roy. Soc., New South Wales, 56, p. 203 (1942).

E-2. Cook, N.H., Course 2.865 notes. Mech. Eng. Dept., M.I.T.

Material	k Thermal Conductivity (Btu/hr ft °F)	κ Thermal Diffusivity (ft^2/hr)
Silver	244	6.6
Aluminum	118	3.26
Stainless Steel	9.4	0.17
Glass (Silica)	0.78	0.025
Epoxy	0.11	0.005

Table E-1 Thermal properties of some materials.

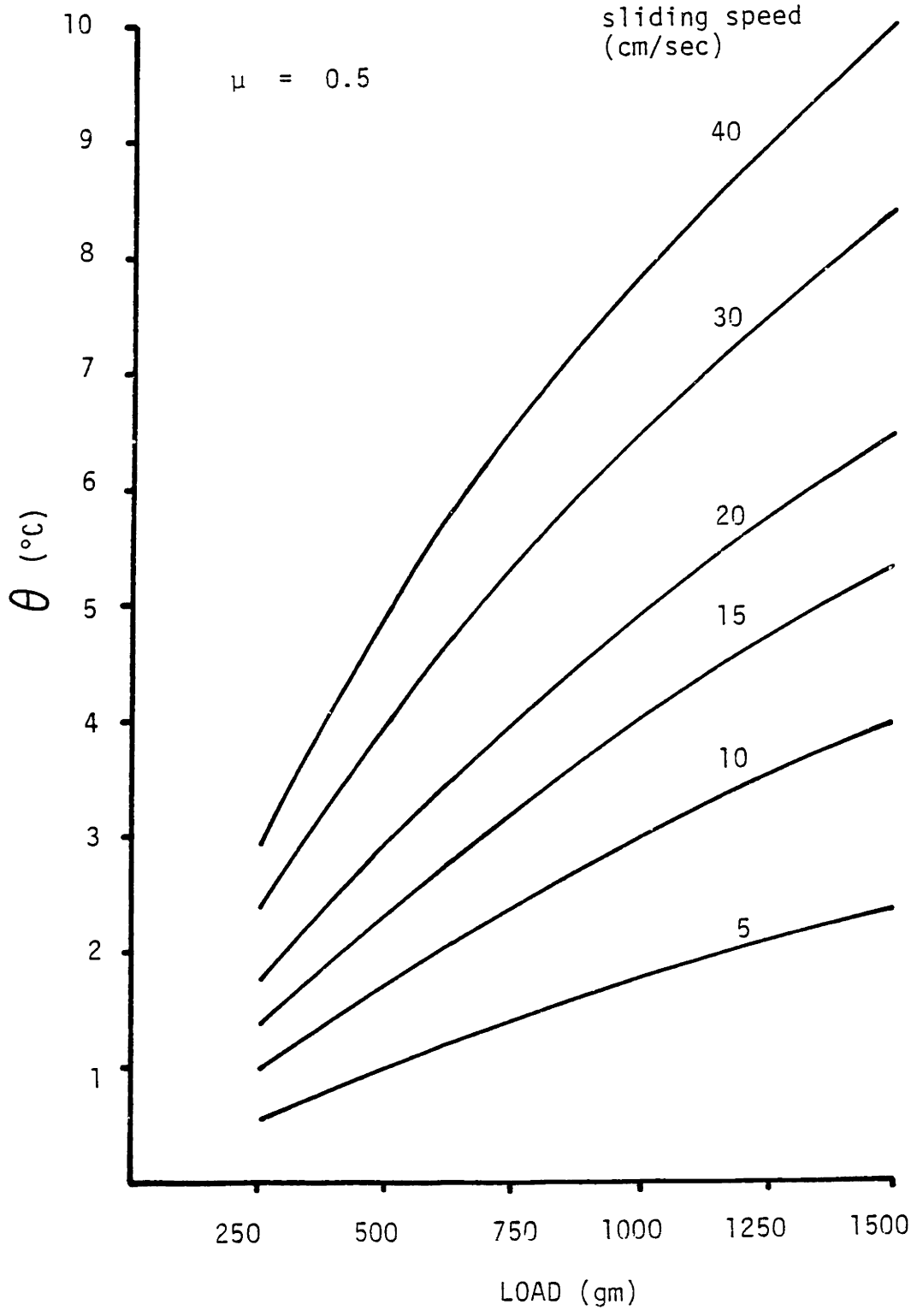

Figure E-2 Average temperature rise at sliding contact of epoxy against steel. Assume friction coefficient μ = 0.5.

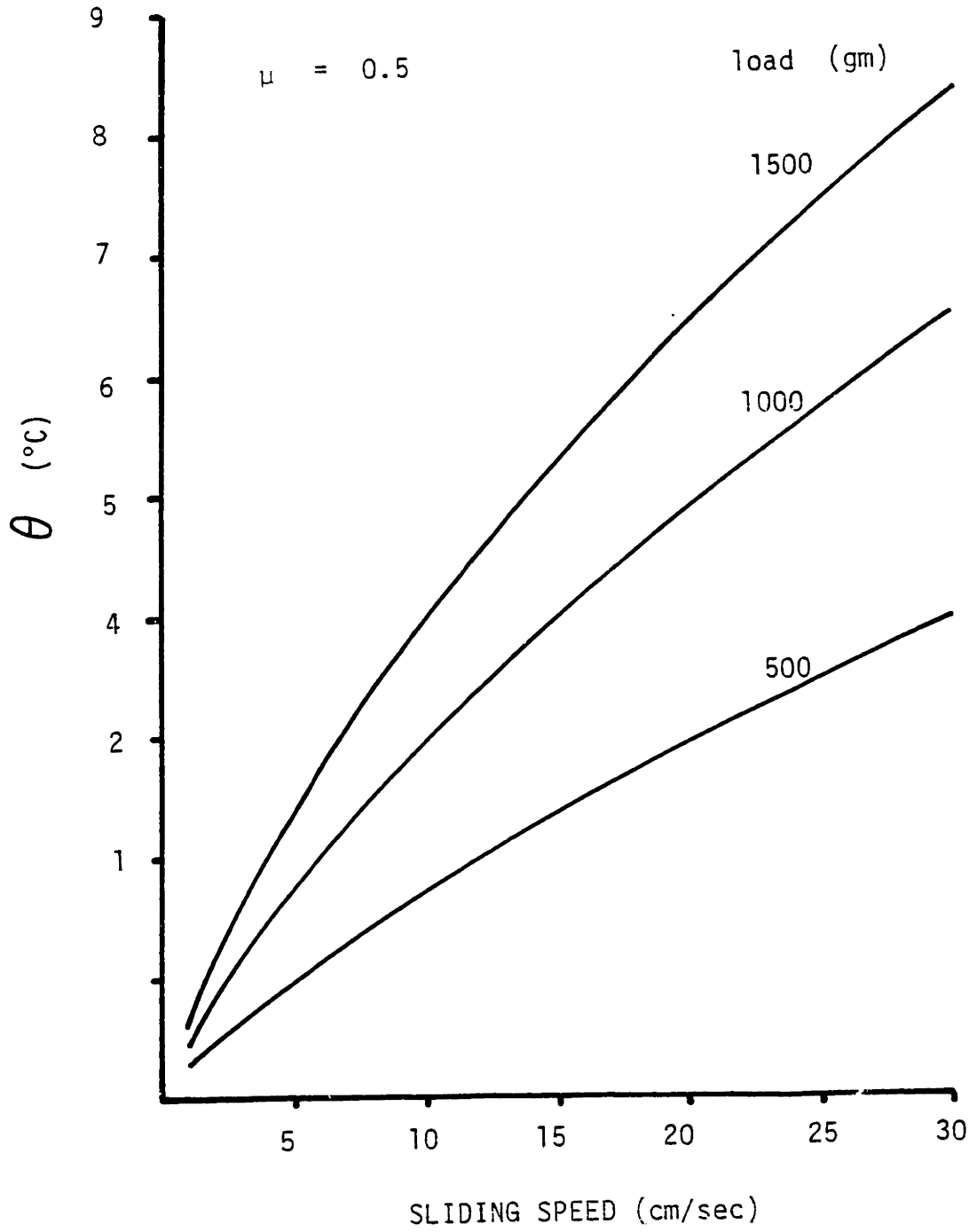

Figure E-3 Average temperature rise at sliding contact of epoxy against steel. Assume friction coefficient $\mu = 0.5$.

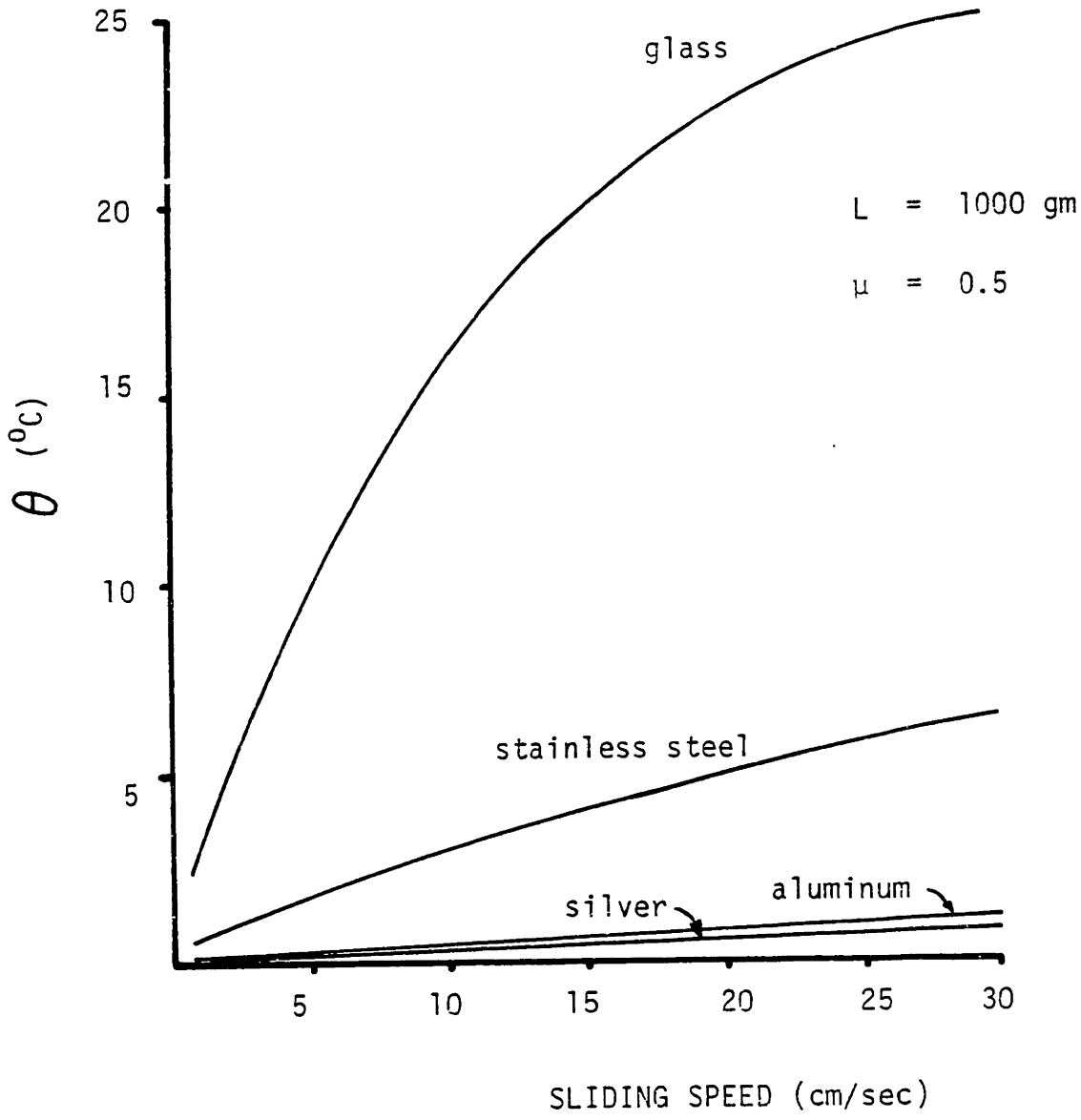

Figure E-4 Average temperature rise at sliding contact of epoxy against different materials assume normal load L = 1000 gm, friction coefficient μ = 0.5.

Appendix F

MICROGRAPHS OF WEAR PARTICLES

Documented here are scanning electron micrographs of wear particles collected from wear tests at environmental temperatures of 21°C and 105°C under different loads and sliding speeds. Readers may refer to figures V-4 and V-5 for the sample temperature developed under these tests conditions.

Comparing these micrographs to the wear data shown in figures V-6 through V-10, small fragmented wear particles were generally found associated with tests that result in low wear. Plate and sheet like large wear particles result from tests with high wear rate. The following is a list of the wear particle micrographs.

Figure F-1 Wear particles of unfilled epoxy tested at 21°C

Figure F-2 Wear particles of unfilled epoxy tested at 105°C

Figure F-3 Wear particles of fumed silica filled epoxy tested at 21°C

Figure F-4 Wear particles of fumed silica filled epoxy tested at 105°C

Figure F-5 Wear particles of crushed silica gel filled epoxy tested at 21°C

Figure F-6 Wear particles of crushed silica gel filled epoxy tested at 105°C

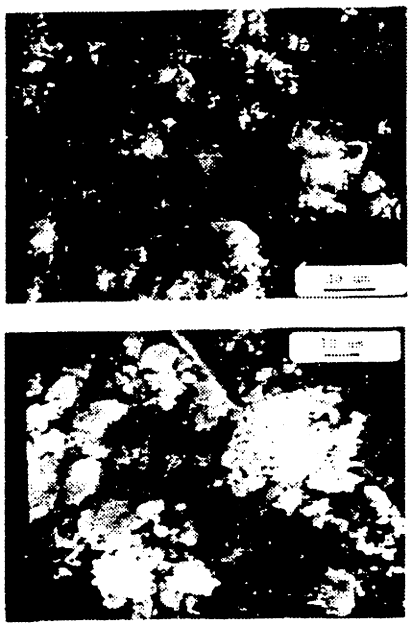

500 g
7.48 cm/sec

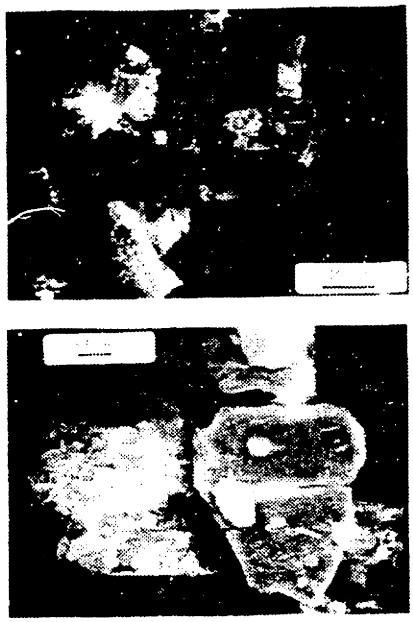

1000 g
7.48 cm/sec

500 g
14.96 cm/sec

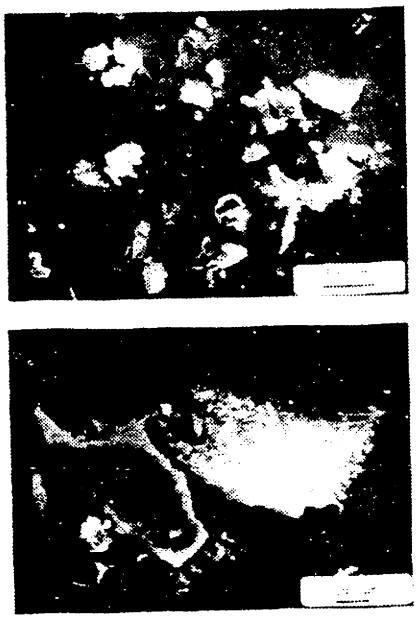

1000 g
14.96 cm/sec

Figure F-1 Wear particles of unfilled epoxy tested at 21°C.

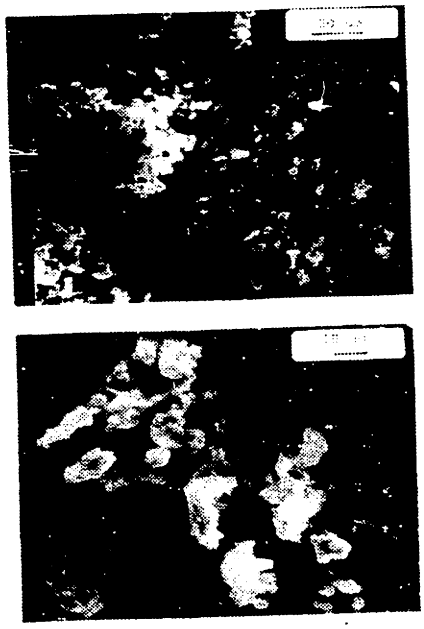

500 g
7.48 cm/sec

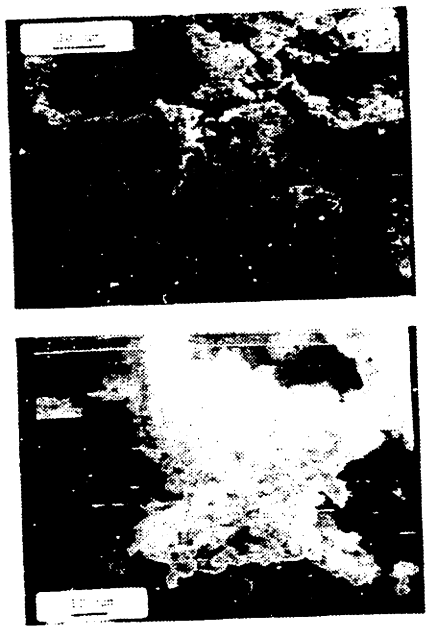

1000 g
7.48 cm/sec

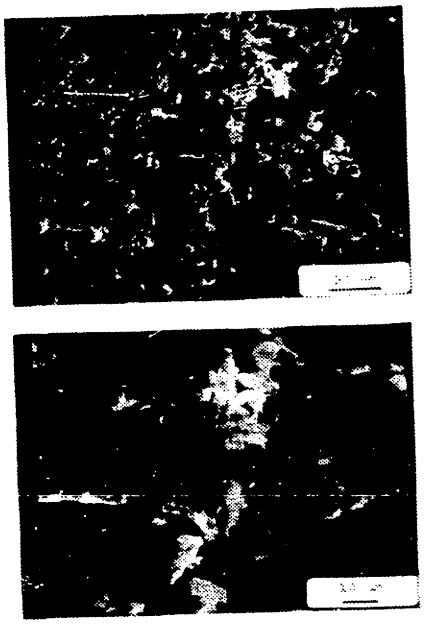

500 g
14.96 cm/sec

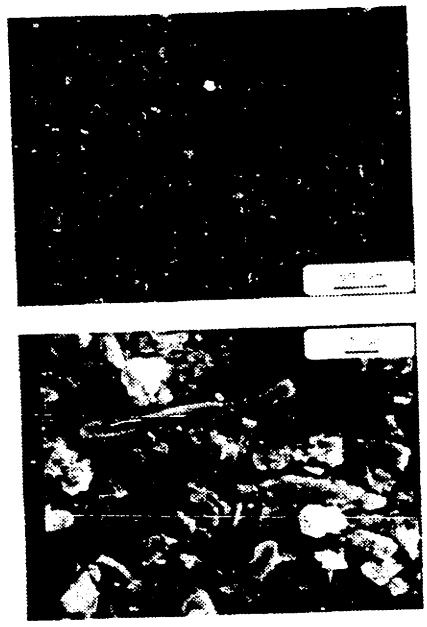

1000 g
14.96 cm/sec

Figure F-2 Wear particles of unfilled epoxy tested at 105°C.

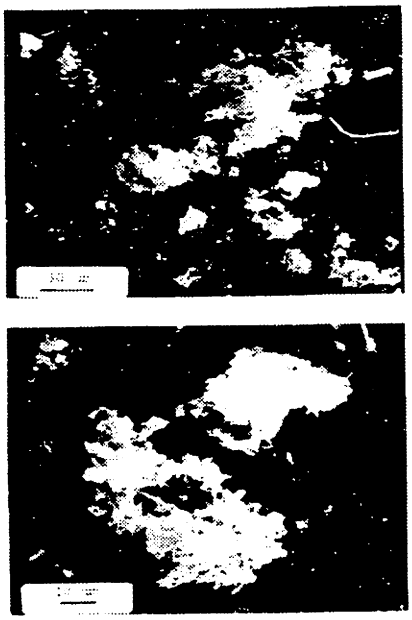

500 g
7.48 cm/sec

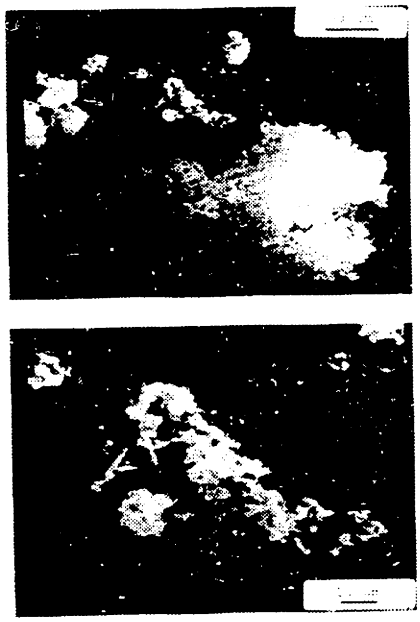

1000 g
7.48 cm/sec

500 g
14.96 cm/sec

1000 g
14.96 cm/sec

Figure F-3 Wear particles of fumed silica filled epoxy tested at 21°C.

500 g
7.48 cm/sec

1000 g
7.48 cm/sec

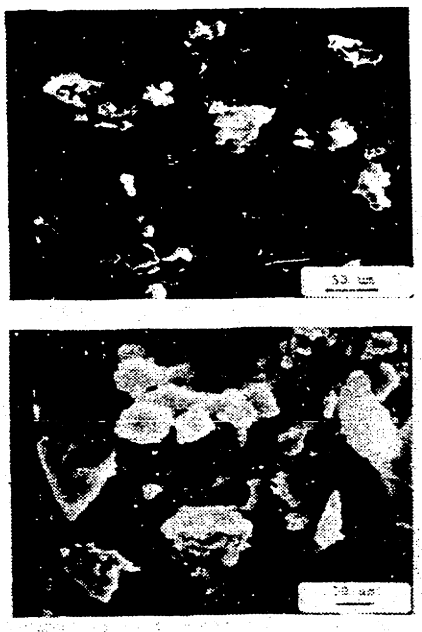

500 g
14.96 cm/sec

1000 g
14.96 cm/sec

Figure F-4 Wear particles of fumed silica filled epoxy tested at 105°C.

500 g
7.48 cm/sec

1000 g
7.48 cm/sec

500 g
14.96 cm/sec

1000 g
14.96 cm/sec

Figure F-5 Wear particles of crushed silica gel filled epoxy tested at 21°C.

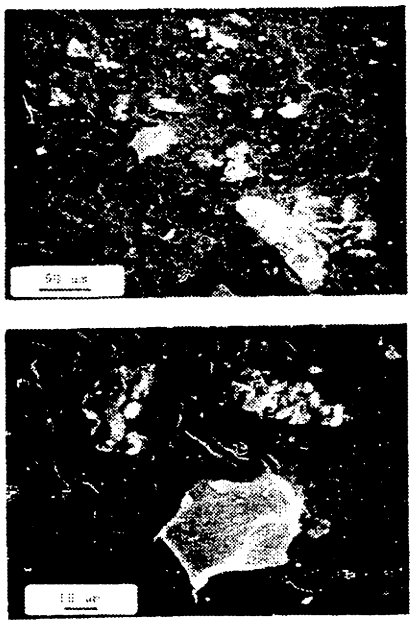

500 g
7.48 cm/sec

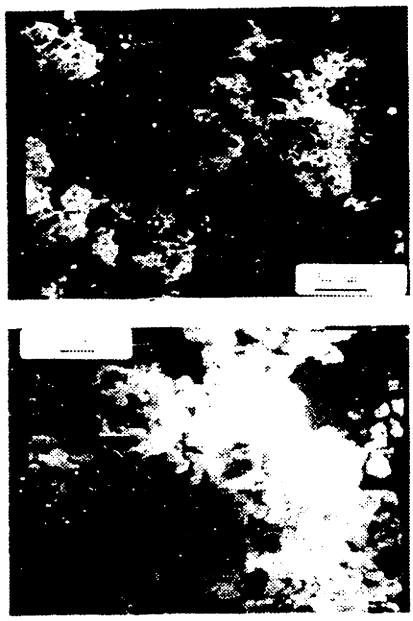

1000 g
7.48 cm/sec

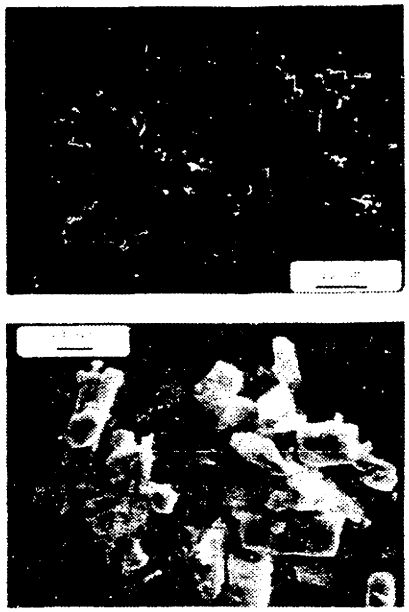

500 g
14.96 cm/sec

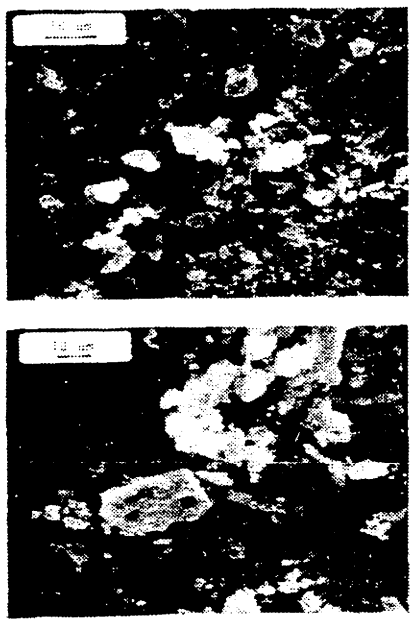

1000 g
14.96 cm/sec

Figure F-6 Wear particles of crushed silica gel filled epoxy tested at 105°C.

Appendix G

MICROGRAPHS OF WEAR TRACKS

Documented here are scanning electron micrographs of wear tracks of samples tested at environmental temperature of 21°C and 100°C under different loads and sliding speeds. Readers may refer to figures V-4 and V-5 for the sample temperature developed under these test conditions. The sliding direction (motion of the counterface) is from top to the bottom of the micrographs. The following is a list of the wear track micrographs.

Figure G-1 Wear tracks of unfilled epoxy tested at 21°C

Figure G-2 Wear tracks of unfilled epoxy tested at 105°C

Figure G-3 Wear tracks of fumed silica filled epoxy tested at 21°C

Figure G-4 Wear tracks of fumed silica filled epoxy tested at 105°C

Figure G-5 Wear tracks of crushed silica gel filled epoxy tested at 21°C

Figure G-6 Wear tracks of crushed silica gel filled epoxy tested at 105°C

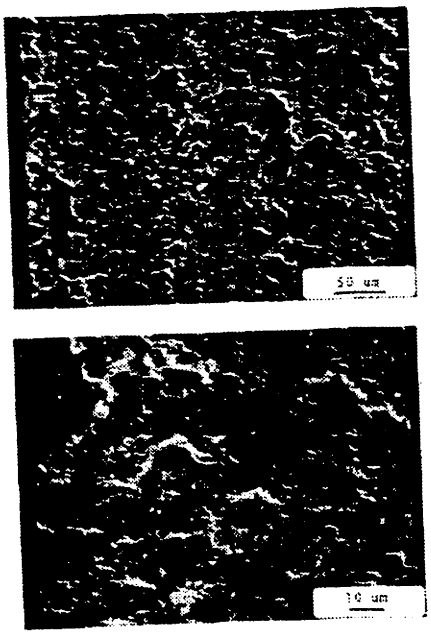

500 g
7.48 cm/sec

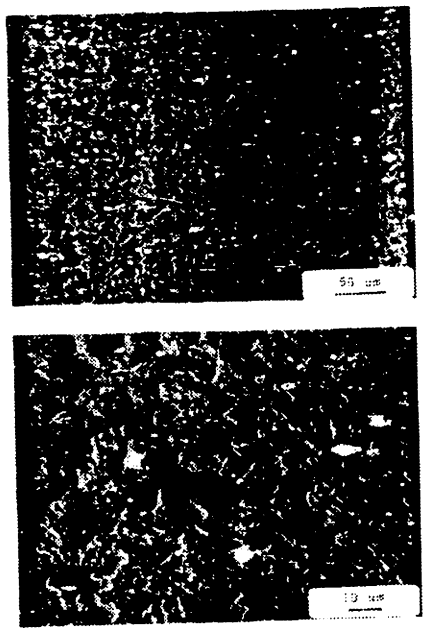

1000 g
7.48 cm/sec

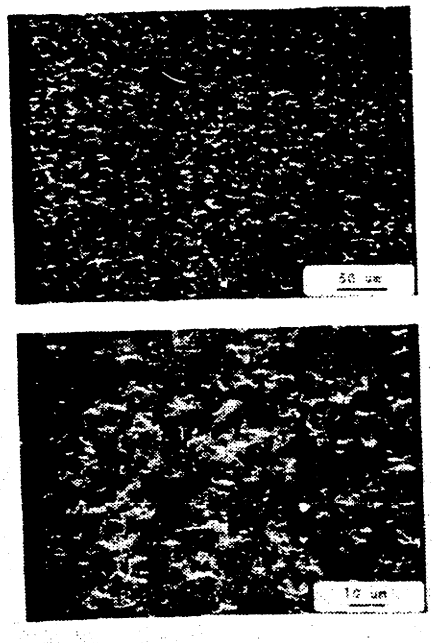

500 g
14.96 cm/sec

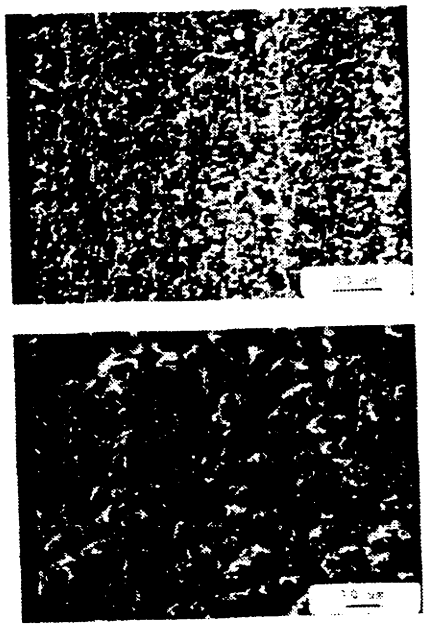

1000 g
14.96 cm/sec

Figure G-1 Wear particles of unfilled epoxy tested at 21°C.

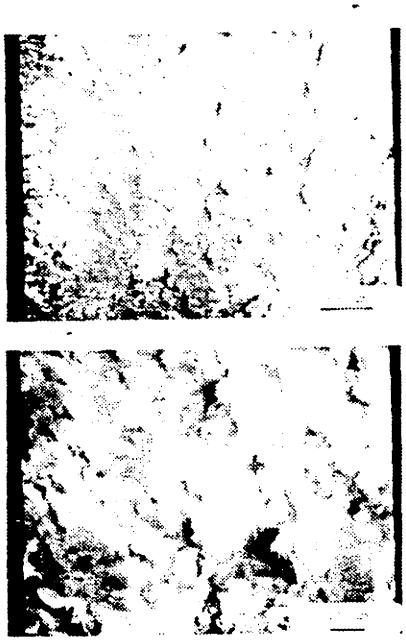

500 g
7.48 cm/sec

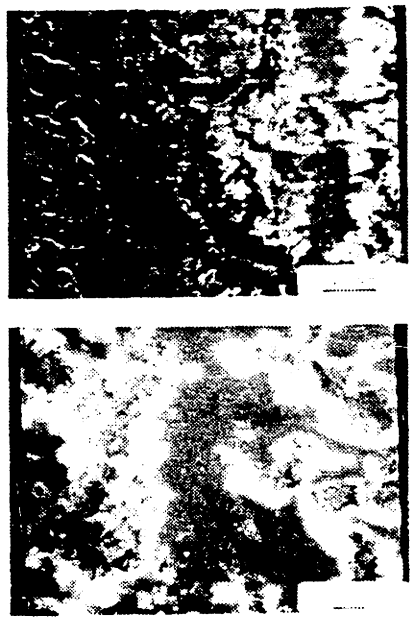

1000 g
7.48 cm/sec

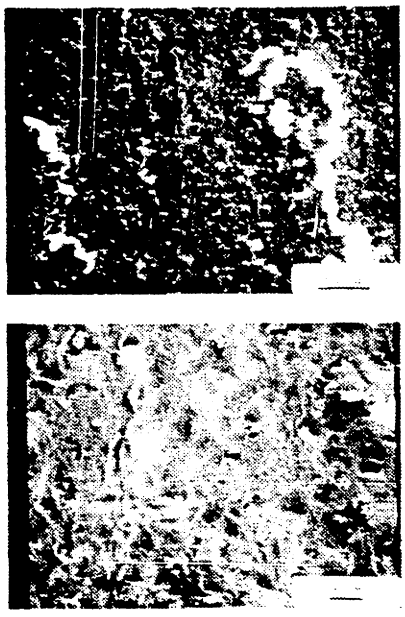

500 g
14.96 cm/sec

1000 g
14.96 cm/sec

Figure G-2 Wear track of unfilled epoxy tested at 105°C.

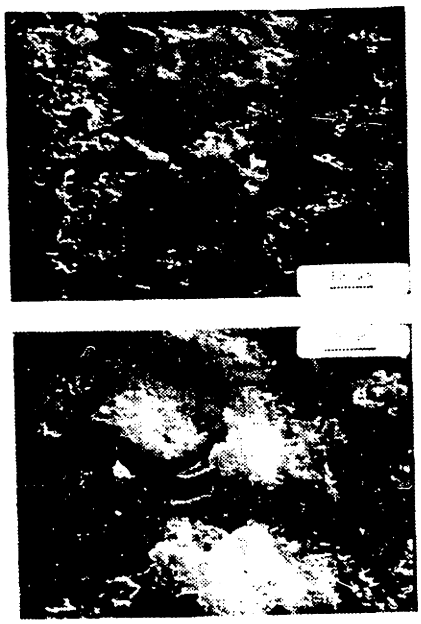

500 g
7.48 cm/sec

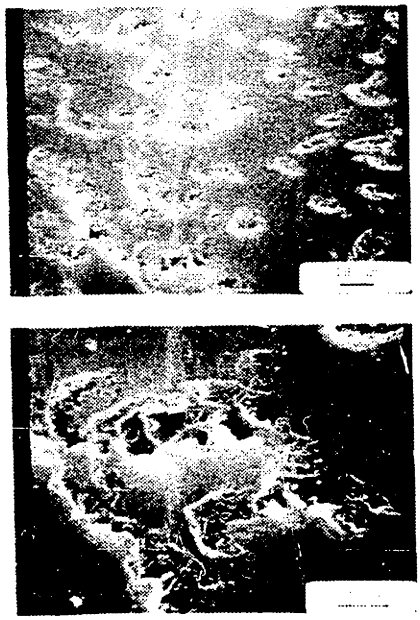

1000 g
7.48 cm/sec

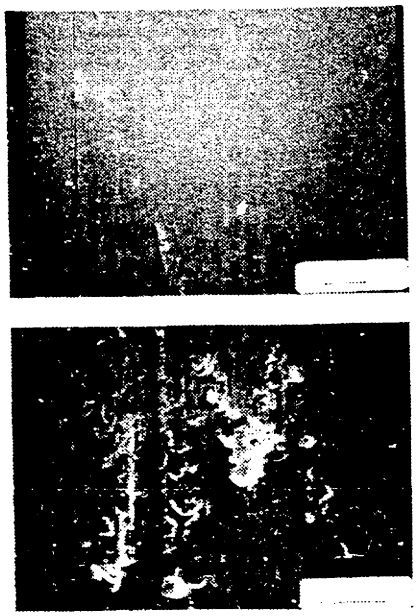

500 g
14.96 cm/sec

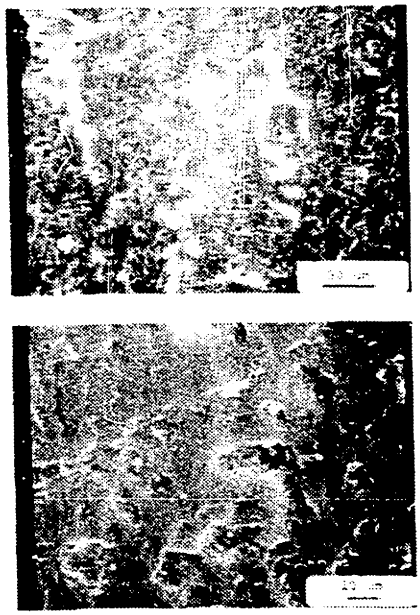

1000 g
14.96 cm/sec

Figure G-3 Wear track of fumed silica filled epoxy tested at 21°C.

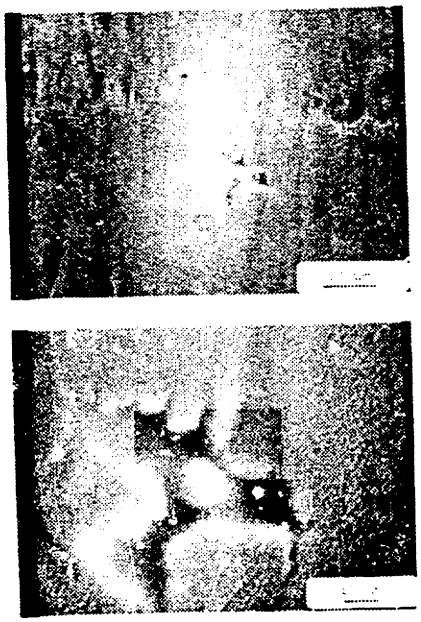

500 g
7.48 cm/sec

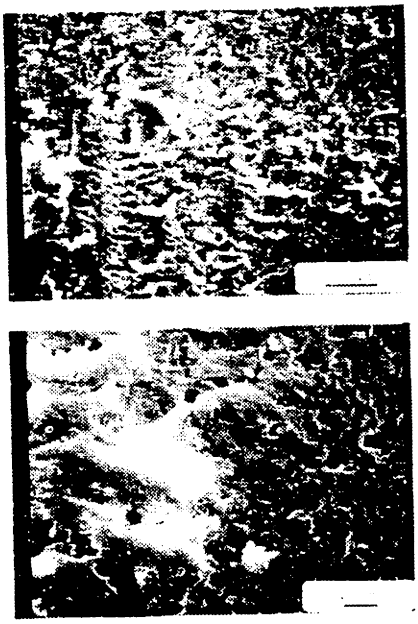

1000 g
7.48 cm/sec

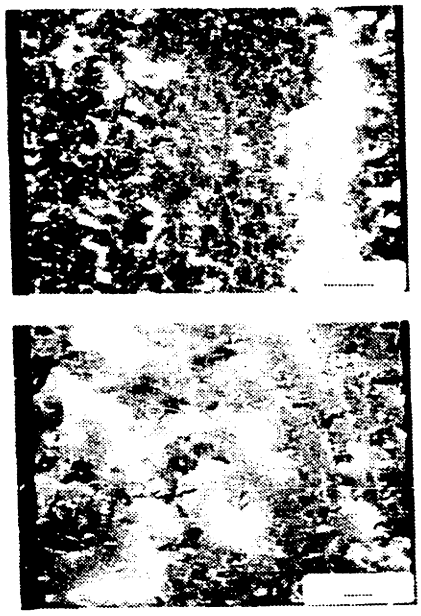

500 g
14.96 cm/sec

1000 g
14.96 cm/sec

Figure G-4 Wear track of fumed silica filled epoxy tested at 105°C.

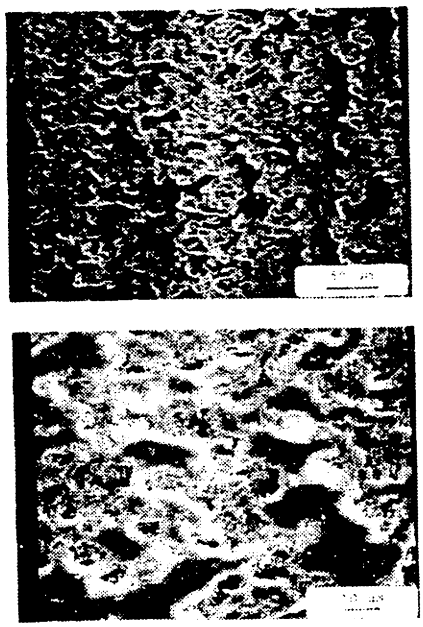

500 g
7.48 cm/sec

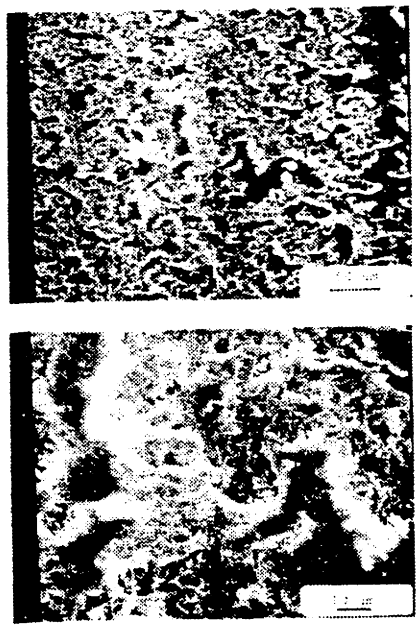

1000 g
7.48 cm/sec

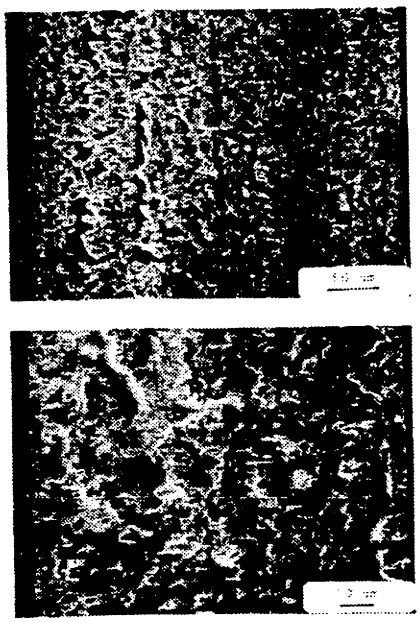

500 g
14.96 cm/sec

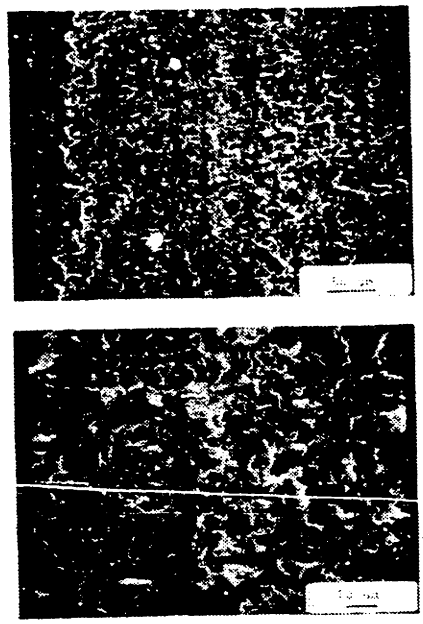

1000 g
14.96 cm/sec

Figure G-5 Wear particles of crushed silica gel filled epoxy tested at 21°C.

500 g
7.48 cm/sec

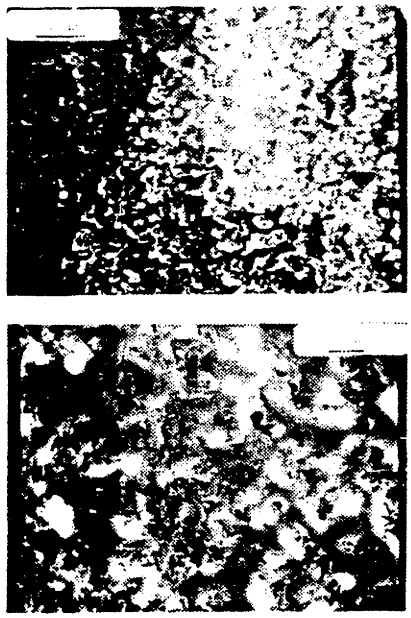

1000 g
7.48 cm/sec

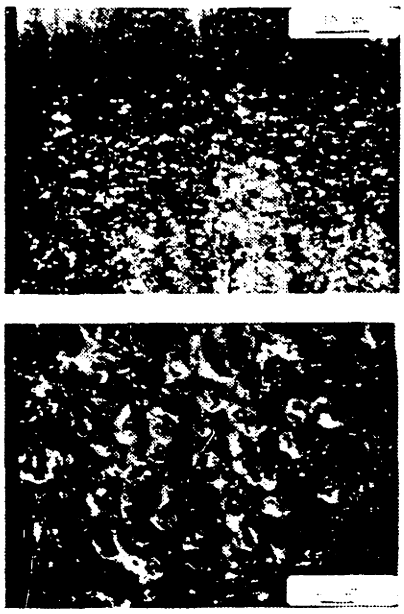

500 g
14.96 cm/sec

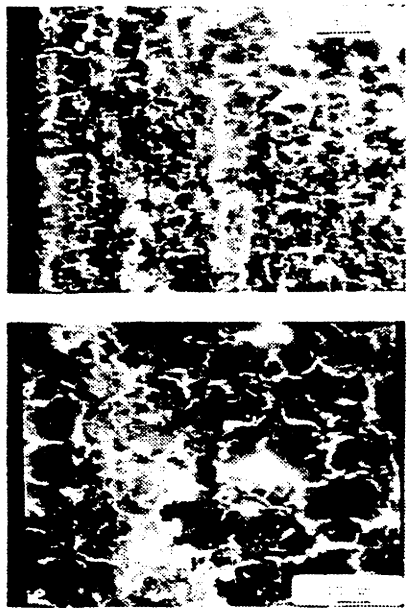

1000 g
14.96 cm/sec

Figure G-6 Wear track of crushed silica gel filled epoxy tested at 105°C.